Mapping of Eelgrass (*Zostera marina*) at Sidney Spit, Gulf Islands National Park Reserve of Canada, Using High Spatial Resolution Remote Imagery

by

Jennifer D. O'Neill
BSc, University of Victoria, 2006

A Thesis Submitted in Partial Fulfillment of the
Requirements for the Degree of

Master of Science

in the Department of Geography

Mapping of Eelgrass (*Zostera marina*) at Sidney Spit, Gulf Islands National Park Reserve of Canada, Using High Spatial Resolution Remote Imagery

by

Jennifer D. O'Neill
BSc, University of Victoria, 2006

Supervisory Committee

Dr. M. Costa, Co-supervisor (Department of Geography)

Dr. T. Sharma, Co-supervisor (Department of Geography, Adjunct)
(Parks Canada)

Dr. R. Canessa, Member (Department of Geography)

Supervisory Committee

Dr. M. Costa, Co-supervisor (Department of Geography)

Dr. T. Sharma, Co-supervisor (Department of Geography, Adjunct) (Parks Canada)

Dr. R. Canessa, Member (Department of Geography)

Abstract

The main goal of this thesis was to evaluate the use of high spatial remote imagery to map the location and biophysical parameters of eelgrass in marine areas around Sidney Spit, a part of the Gulf Islands National Park Reserve of Canada (GINPRC). To meet this goal, three objectives were addressed: (1) Define key spectral variables that provide optimum separation between eelgrass and its associated benthic substrates, using *in situ* hyperspectral measurements, and simulated IKONOS and Landsat 7ETM+ spectral response; (2) evaluate the efficacy of these key variables in classification of the high spatial resolution imagery, AISA and IKONOS, at various levels of processing, to determine the processing methodology that offers the highest eelgrass mapping accuracy; and (3) evaluate the potential of "value-added" classification of two eelgrass biophysical indicators, LAI and epiphyte type.

In situ hyperspectral measurements acquired at Sidney Spit in August 2008 provided four different data sets: above water spectra, below water spectral profiles, water-corrected spectra, and pure endmember spectra. In Chapter 3, these data sets were examined with first derivative analysis to determine the unique spectral variables of eelgrass and associated benthic substrates. The most effective variables in discriminating eelgrass from all other substrates were selected

using data reduction statistics: M-statistic analysis and multiple discriminant analyses (MDA). These selected spectral variables enabled eelgrass classification accuracy of 98% when separating six classes on above water data: shallow (< 3 m deep) eelgrass, deep (> 3 m) eelgrass, shallow sand, deep sand, shallow green algae, and spectrally deep water. The variables were located mainly in the green wavelengths, where light penetrates to the greatest depth: the slope from 500 – 530 nm, and the first derivatives at 566 nm, 580 nm, and 602 nm. The same data were classified with 96% accuracy after correcting for the water column, using the ratios 566:600 and 566:710. The only source of confusion for all data sets was between green algae and eelgrass, presumably due to their similar pigment composition. IKONOS and Landsat 7ETM+ simulated datasets performed similarly well, with 92% and 94% eelgrass classification accuracy respectively.

In Chapter 4, the efficacy of the selected features was tested in the classification of airborne hyperspectral AISA imagery and satellite platform multispectral IKONOS imagery, and compared with various other classifiers, both supervised and unsupervised: K-means, minimum distance (MD), linear spectral unmixing (LSU), and spectral angle mapper (SAM). The selected features achieved the highest eelgrass classification accuracies in the study, when combined with atmospheric correction, glint correction, and optically deep water masking. AISA achieved eelgrass producer and user accuracies of 85% in water shallower than 3 m, and 93% in deeper areas. IKONOS achieved 79% for shallow waters and 82% for deep waters. Endmember classification also showed accuracies over 84% and 71% in AISA and IKONOS imagery respectively. Again, the largest source of confusion was between eelgrass and green algae, as well as between exposed vegetation (sea asparagus and green algae) and exposed eelgrass.

Incompatibilities of the automatable processing steps (Tafkaa, LSU and SAM) made automated mapping less accurate than supervised mapping, but suggestions are made toward improvement.

The value-added classification of eelgrass LAI and epiphyte type produced poor results in all cases except one; epiphyte presence / absence could be delineated with 87% accuracy.

Before applying the findings of this study, one must consider the spatial scale of the intended management goal and select imagery with suitable spatial resolution. Tidal variations, as well as seasonal variability in water conditions and eelgrass phenology must also be considered as they may affect classification accuracies.

Table of Contents

Supervisory Committee ii
Abstract iii
Table of Contents v
List of Tables vii
List of Figures viii
List of Symbols xii
Acknowledgements xv
1 Introduction 1
1.1 Eelgrass mapping background 4
1.2 Study Site - Marine areas around Sidney Spit, a part of the Gulf Isalnds National Park Reserve of Canada (GINPRC) 7
1.3 Remote Sensing Theory 9
2 Methodology 23
2.1 Field methods 23
2.2. Spectra Processing 31
2.3 Remote Imagery 34
3 Variable reduction of *in situ* hyperspectral measurements over shallow coastal benthic substrates for use in remote mapping of eelgrass (*Zostera marina*) 37
3.1 Introduction 37
3.2 Methods 41
3.3 Results 45
3.4 Discussion 63
3.5 Conclusion 74

4 Mapping of eelgrass (*Zostera marina*) at Sidney Spit, Gulf Islands National Park Reserve of Canada, using high spatial resolution airborne and satellite imagery 79
4.1 Introduction 80
4.2 Methodology 82
4.3 Results 95
4.4 Discussion 108
4.5 Conclusion 115
5 Conclusions 122
Bibliography 132
A Ancillary Figures and Tables 154
B Chromophoric Dissolved Organic Matter (CDOM) Measurements 158
C Chlorophyll-a (Chl-a) and Accessory Pigments Measurements 160
D Total Suspended Matter (TSM) Measurements 161
E Spatial Distribution of Water Optical Constituents 163
F Tafkaa Input: Parameter and AISA / IKONOS Header Files 164
G Numerical classification accuracy results 167

List of Tables

Table 2.1. Benthic covertypes present at the Sidney Spit study site and number of spectral samples acquired for each. 25
Table 2.2 Spectral and spatial specifications of IKONOS and Landsat ETM+ satellite sensors (Modified from GeoEye, 2006). 35
Table 3.1 Cases for which data reduction was performed. 44
Table 3.2. Water optical constituents profile for Sidney Spit field sites. 46
Table 3.3 List of indices used in M-statistic and MDA analysis: (a) Spectral slopes and ratios showing potential for separating eelgrass from other substrates, as per visual analysis of first derivative spectra (b) common vegetation indices, and (c) first derivative values known to be effective. 51
Table 3.4 Set 2 bands selected by the MDA for each processing level 53
Table 3.5. Set 2 (MDA result) separability of shallow eelgrass (<3m) spectra from other benthic substrate spectra acquired from above water. A dark box represents good separability (M-statistic > 1) and an empty box denotes poor separability (M-statistic < 1). The value in the box is the M-statistic result. 67
Table 3.6 Separability of deep eelgrass (>3m) spectra from and other benthic substrate spectra acquired from above water. A dark box represents good separability (M-statistic > 1) and an empty box denotes poor separability (M-statistic < 1). The value in the box is the M-statistic result. 68
Table 3.7 Separability of eelgrass spectra from and other benthic substrate spectra acquired from above water and corrected for water column attenuation. A dark box represents good separability (M-statistic > 1) and an empty box denotes poor separability (M-statistic < 1). The value in the box is the M-statistic result. 68
Table 4.1. Number of sites visited in the survey of benthic substrates, and division of sites into classification training and testing sites. E = eelgrass, Ag = green algae, Ab = brown algae, S = sand, Asp = sea asparagus, dW = optically deep water, d = deep, s = shallow, and e = exposed. * there were no brown algae training sites present in the IKONOS image due to large pixel size and small patch size of brown algae (~1 x 1m). 83
Table 4.2 Reduced variable band set defined in the previous chapter and applied here during each supervised maximum likelihood classification case. R' = first derivative of above water remote sensing reflectance, s = slope. NPCI is the Normalized Pigment Chlorophyll-a Index using bands 680nm and 430nm (Penuelas et al. 1993). For IKONOS the wavelengths represent the centre of the bands. 92

List of Figures

Figure 1.1. Sidney Spit, Sidney Island, British Columbia is part of the Gulf Islands National Park Reserve. The red line delineates a portion of the western boundary of the Reserve (Modified from Parks Canada, 2005). 8
Figure 1.2. Paths of radiance received by a satellite remote sensor. Path 1 contains the desired radiance information from the target, while paths 2-6 introduce atmospheric noise to the radiance measured by the sensor, L_T. (Adapted from Jensen, 2007)..... 10
Figure 1.3. An example of pure endmember in situ spectra of eelgrass in the visible range. Variations are due to eelgrass blade age and epiphyte cover. Reflectance is shown as albedo, which is the ratio of radiance from the substrate, to the irradiance incident upon it in the water column (Modified from Werdell & Roesler, 2003). 11
Figure 1.4. Spectral change of eelgrass blades with age. Reflectance is shown as albedo, which is the ratio of radiance from the substrate, to the irradiance incident upon it in the water column. (Modified from Werdell & Roesler, 2003). 12
Figure 1.5. Example of in situ hyperspectral (a) sand and (b) clay/silt spectra in the visible range. The absorption feature around 676nm is caused by the accessory pigments of detritus and benthic diatoms. (Modified from Werdell & Roesler, 2003). 13
Figure 1.6. Spectral absorption properties of pure water, chromophoric dissolved organic material (CDOM), and suspended matter (TSM) in the water column (modified from Kirk, 1986). 14
Figure 1.7. Reflectance spectra for varying concentrations of suspended inorganic matter. Note that with increasing concentration, reflectance increases at all wavelengths, but is biased toward the longer visible wavelengths (500 – 700nm) (from Chen et al., 1991). 15
Figure 1.8. Absorption spectra for chlorophyll-a and accessory pigments chlorophyll-b and carotenoids. (Modified from Whitmarsh and Govindjee, 1999). 16
Figure 1.9. Empirical Line Calibration: A best-fit least squares regression line for a single sensor band, using two spectral reference targets (Modified from Smith and Milton, 1995). 21
Figure 2.1. Location of ground-truth survey sites and spectral acquisition sites at Sidney Spit, GINPRC……..26
Figure 2.2 Radiometers used to acquire in situ field spectra above and below water from the boat. The HyperSAS LSsky and LT sensors (a) were mounted on a frame on a tripod viewing over the side of the boat, the ES cosine collector (b) was mounted vertically on a 2m dowel at the highest point on the boat, and the HyperPRO Ed profiler (c) was connected by a line to a downrigger mounted on the same side of the boat. 29
Figure 2.3 Acquisition of endmember, or "pure," spectra with the HyperSAS sensor. Substrates were placed four layers deep, in an area three times the diameter of the sensor field of view. Sensor height was 31cm for covertypes, and 10cm for epiphytes. 30
Figure 2.4 Relative spectral responsivity for the visible and NIR bands of (a) IKONOS and (b) Landsat ETM+. The radiance measured at a specific band (e.g., blue band) is a weighted

average of the radiance at each wavelength in the bandwidth, where the weight is the relative responsivity value (y-axis) (Modified from GeoEye, 2008 and NASA 2009 respectively).. 35
Figure 2.5 Overview of field data acquisition and data processing steps described in Chapter 2, and where each of these components is applied in the remainder of the study. 36
Figure 3.1 Mean temperature and salinity profiles during field acquisition. 45
Figure 3.2 Average pigment profile as measured by HPLC methods, in percent of total. 47
Figure 3.3 Kd spectra derived from E_u and E_d in-water profiles at various sites around Sidney Spit over six days, August 14-18 and 31, 2008. 47
Figure 3.4 (a) Average above-water reflectance with 95% confidence interval for each benthic substrate type and (b) major reflectance (grey) and absorption (black) features for each benthic substrate with 95% confidence interval, as derived by first derivative analysis..... 49
Figure 3.5 Average spectra of eelgrass, biofouled with diatoms and red algae, Smithora, for (a) above water spectra with 95% confidence interval (dotted lines); (b) water-corrected spectra 95% confidence interval (dotted lines); and (c) endmembers. (c) also shows eelgrass with no biofouling. (d) shows endmember spectra of epiphytes only, scraped from eelgrass blades. 50
Figure 3.6 Data reduction steps and accuracy of Set 2 for each classification case (letters denote sections of the methodology text): (i) Above water HyperSAS data; (ii) Water column corrected HyperSAS data; (iii) Endmemeber data; (iv) LAI, percent cover and epiphyte classification; and (v) IKONOS and Landsat ETM+ above water data simulated from HyperSAS data. 55
Figure 3.7 Plot of first two canonical discriminant functions for (a) shallow water (< 3m) substrate classification, (b) deep water (> 3m) classification, (c) all depth classification and (d) all depth classification with the addition of a red edge index. 56
Figure 3.8 Average spectra (thick lines) ±95% confidence interval (thin lines) of each benthic type corrected for the attenuating effects of the water column using Maritorena et al.'s (1994) equation (Eq. 2.10). Grey lines represent the water corrected above-water spectra ad black lines represent the in situ pure endmember spectra for comparison 58
Figure 3.9 Percent error of the water attenuation correction for each substrate. 58
Figure 3.10: (a)The depth at which the HyperSAS sensor can distinguish each covertype from spectrally deep water for the lowest (thin lines) and highest (thick lines) Kd's found at the study site. Calculated as per Dekker et al. (2005). (b) Lowest, highest and average Kd values found at the study site. 59
Figure 3.11 Endmember spectra of healthy and senescent green algae and biofouled, non-biofouled and senescent eelgrass. Classifications exhibit confusion between healthy green algae and non-biofouled eelgrass as well as senescent green algae and bio-fouled eelgrass. 60
Figure 3.12: Average eelgrass in situ above water spectra (a & b) and water corrected spectra (c & d) spectra grouped by percent cover and LAI classes. 61
Figure 3.13 MDA classification of eelgrass in situ spectra into low, medium and high LAI classes: graphical representation of the efficacy of the model based on the first two canonical discriminant functions (total accuracy 80%). 62

Figure 3.14 Average (a) shallow and (b) deep covertype spectra for the hyperspectral field sensor (solid line) compared with the multispectral IKONOS (solid bar) and LandsatETM+ (dotted bar) sensors simulated from the HyperSAS data. 63
Figure 4.1 RGB composite of the (a) hyperspectral AISA image (R = 650, G = 550, B = 450nm) (2 x 2 m resolution) and (b) multispectral IKONOS image (R = 665 nm, G = 550nm, B = 480nm) (4 x 4 m resolution). 84
Figure 4.2 Endmember libraries for (a) the AISA above water image (HyperSAS above water measurements); (b) the AISA water corrected image (HyperSAS endmember measurements); and (c) the IKONOS above water image (simulated from HyperSAS above water measurements) 92
Figure 4.3. Image processing steps. 94
Figure 4.4. Top: (a) Eelgrass and (b) optically deep water spectra AISA and (B) IKONOS imagery after sea surface glint and atmospheric corrections ELC and Tafkaa. In situ spectra are presented for comparison. Bottom: The percent error of ELC and Tafkaa corrections with glint correction when compared with in situ spectra. 96
Figure 4.5 Before and after Hedley et al (2005) glint correction of AISA imagery demonstrated here in a portion of heavily glint affected optically deep water with false colour AISA imagery (top), an image x-profile of optically deep water showing 550nm (blue line), 668nm (green line) and 748nm (red line) Rrs values (middle) and a single deep water spectrum (bottom). 97
Figure 4.6 (a) Spectra of medium density eelgrass beds with epiphytes at varying depths extracted from the Maritorena water column corrected AISA image; and (b) depth restriction at which the AISA sensor can no longer distinguish between each substrate and deep water (solid lines) and average Kd value for the scene (dotted line) derived from in situ in water spectral profiles. 98
Figure 4.7 Visibility threshold (depth at which each covertype can no longer be discerned from deep water) of AISA and IKONOS sensors at the time of image acquisition, calculated using Equation 4.9. 98
Figure 4.8 AISA user and producer eelgrass classification accuracies for (a) shallow (<3m depth) and (b) deep (>3m depth) eelgrass at various levels of image correction. 101
Figure 4.9 IKONOS user and producer eelgrass classification accuracies for (a) shallow (<3m depth) and (b) deep (>3m depth) eelgrass at various levels of image correction. 101
Figure 4.10 Total accuracies for all (a) AISA and (b) IKONOS classifications. 101
Figure 4.11 Classifier results for the AISA image with various processing 102
Figure 4.12 Classifier results for the IKONOS image with various processing 103
Figure 4.13. Classification results with the best accuracies and substrate distribution: (a) AISA_ELC_GC_ML; (b) IKONOS_ELC_GC_ML for the shallow (< 3 m) areas; and (c) IKONOS_ELC_GC_MD for the deep (> 3 m) areas. Where ELC = empirical line calibration, GC = glint correction, ML = maximum likelihood classification of selected

spectral indices, and MD = minimum distance classification of full spectral resolution data. 104
Figure 4.14: AISA user and producer LAI classification accuracies in shallow (<3m) water using (a) three LAI classes and (b) two LAI classes. U = user accuracy, P = producer accuracy. 106
Figure 4.15: IKONOS user and producer LAI classification accuracies in shallow (<3m) water using (a) three LAI classes and (b) two LAI classes. U = user accuracy, P = producer accuracy. 107
Figure 4.16: AISA user and producer epiphyte type classification accuracies in shallow (<3m) water using (a) three epiphyte classes: red algae, diatom, none and (b) two epiphyte classes: epiphyte presence absence. 108
Figure 4.17: IKONOS user and producer epiphyte type classification accuracies in shallow (<3m) water using (a) three epiphyte classes: red algae, diatom, none and (b) two epiphyte classes: epiphyte presence absence 108
Figure 5.1 Most accurate eelgrass map produced in this study. Image processing steps were: atmospheric correction, glint correction, optically deep water masking, and maximum likelihood classification of the selected spectral variables.....126
Figure 6.1 M-statistic results for the above-water dataset describing the separability of each benthic class and (a) shallow eelgrass (<3m) original $R_{rs}(0+)$ data; (b) shallow eelgrass $R_{rs}(0+)$ first derivative data; (c) deep eelgrass (>3m) original $R_{rs}(0+)$ data; and (d) deep eelgrass $R_{rs}(0+)$ first derivative data. An M-statistic > 1 indicates good separation. 154
Figure 6.2 M-Statistic results of above water dataset indices for the shallow (< 3 m) dataset (white and light grey bars) and the deep (> 3 m) dataset (dark grey and black bars). 155
Figure 6.3 M-statistic results of water column corrected data set (a) original and first derivative data and (b) indices for separating eelgrass from sand and green algae 155
Figure 6.4 M-statistic results of endmember data set (a) original and first derivative data and (b) indices, for separating green algae from biofouled eelgrass (black) and non-biofouled (manually cleaned) eelgrass (grey). 156
Figure 6.5 M-statistic results for separating Sparse (20-70% cover) and Dense (> 70% cover) percent cover classes in shallow (< 3 m) eelgrass using (a) the original $R_{rs}^{(0+)}$ data (thick lines) and first derivative $R_{rs}^{(0+)}$ (thin lines) data; and (b) indices. Results are shown for both above water data ($R_{rs}^{(0+)}$) and water corrected data (R_{rs}^{b}). 156
Figure 6.6 M-statistic results of the above water dataset for the separation of three LAI classes in shallow (<3m) eelgrass using (a) the original Rrs(0+) data (thick lines) and first derivative Rrs(0+) (thin lines) data; and (b) indices. L/M = Low vs. Medium LAI, L/H = Low vs. High LAI, and M/H = Medium vs. High LAI classes values. 157
Figure 6.7 M-statistic results between epiphyte type classes (diatom and red algae) in shallow (<3m) eelgrass for above water data and water corrected data (a) original and first derivative data and (b) indices. 157

List of Symbols

Symbol	Name	Units
λ	wavelength	nm
L	radiance	$\mu W\ cm^{-2}sr^{-1}nm^{-1}$
L_T	total at-sensor radiance	$\mu W\ cm^{-2}sr^{-1}nm^{-1}$
L_{sky}	sky radiance	$\mu W\ cm^{-2}sr^{-1}nm^{-1}$
L_{atm}	atmospheric radiance	$\mu W\ cm^{-2}sr^{-1}nm^{-1}$
L_p	path radiance	$\mu W\ cm^{-2}sr^{-1}nm^{-1}$
L_{sfc}	surface glint radiance	$\mu W\ cm^{-2}sr^{-1}nm^{-1}$
L_w	water-leaving radiance	$\mu W\ cm^{-2}sr^{-1}nm^{-1}$
L_b	radiance from the target substrate	$\mu W\ cm^{-2}sr^{-1}nm^{-1}$
L_u	upwelling radiance below the air-water interface	$\mu W\ cm^{-2}sr^{-1}nm^{-1}$
E_0	solar irradiance at the top of the atmosphere	$\mu W\ cm^{-2}nm^{-1}$
E_S	downwelling solar irradiance	$\mu W\ cm^{-2}nm^{-1}$
E_{sky}	diffuse sky irradiance	$\mu W\ cm^{-2}nm^{-1}$
E_d	downwelling irradiance below the air-water interface	$\mu W\ cm^{-2}nm^{-1}$
T_θ	atmospheric transmittance at an angle θ to the zenith (θ_0 or θ_v)	
θ_0	solar zenith angle	
θ_v	sensor scan angle	
ρ’	Proportionality factor relating sea surface reflected sky radiance to total sky radiance	
W	wind speed	$m\ s^{-1}$
R	reflectance	
R_{rs}	remote sensing reflectance	sr^{-1}

$R_{rs}^{(0+)}$	Above-water remote sensing reflectance	sr^{-1}
$R_{rs}^{(0-)}$	remote sensing reflectance just beneath the air-water interface	sr^{-1}
$R_{rs}^{dp(0-)}$	remote sensing reflectance of optically deep water just beneath the air-water interface	sr^{-1}
R_{rs}^{b}	remote sensing reflectance of the benthic target	sr^{-1}
R_{rs}^{DT}	sensor detecting threshold in remote sensing reflectance terms	sr^{-1}
R_{rs}' or R'	first derivative of remote sensing reflectance curve	
τ	aerosol optical thickness	
Chl-a / Chl-b	Chlorophyll-a / Chlorophyll-b	$mg\ m^{-1}$
TSM	total suspended matter	$g\ m^{-3}$
TOC	total organic carbon	%
CDOM	chromophoric dissolved organic matter	
a_{CDOM}	absorption from CDOM	m^{-1}
A	absorbance	
l	path length	m
c_T	beam attenuation coefficient (in water)	
a_T	total absorption coefficient (in water)	
b_T	total backscattering coefficient (in water)	
K_d	downwelling diffuse attenuation coefficient (in water)	
z	water depth	
α	Fresnel reflection albedo for irradiance from sun and sky	
ρ	Fresnel reflectance index of seawater	
$s\lambda - \lambda$	Slope between two wavelengths	
ELC	empirical line calibration	
E	eelgrass	
Ag	green algae	
Ab	brown algae	

S	sand	
Asp	sea asparagus	
dW	optically deep water	
LAI	leaf area index	$m^2 m^{-2}$
M	M-statistic	
MD	minimum distance classifier	
ML	maximum likelihood classifier	
LSU	linear spectral unmixing classifier	
SAM	spectral angle mapper classifier	

Acknowledgements

There are several people that I must thank for their assistance in this project. I would first like to thank my supervisor, Maycira Costa, for introducing me to ocean remote sensing and giving me the opportunity to undertake this research. I have learned much through the care, support, and patience she has shown me throughout, especially in these final busy months of writing and structuring. I would also like to thank Eduardo Loos, who spent many a patient hour showing me the ins and outs of the field equipment and answering my barrage of questions.

A giant thank-you to my field helpers Terri Evans, Thiago Silva, Eddie Loos, Sarah Loos, and Tanya Bryan. The work would not have been possible without you, nor would it have been nearly as fun. A special debt of gratitude is also owed to Joel Blair, whose help with ground-truthing was indispensable and whose advice, support, and mindfulness helped me over many major hurdles.

I thank Parks Canada for providing boat time and the friendly wardens who drove the boat. I am grateful for their expertise and the outstanding patience they expressed while I asked them to do such things as “hold position over this exact spot of eelgrass, counter to the current, while pointing away from the sun.” Repeatedly! Also, thank-you to Leanna Boyer and Nikki Wright of the Seagrass Conservation Working Group for showing me the ropes of eelgrass mapping.

Much appreciation to Ricardo Rossin for his help with the HPLC procedures and troubleshooting, to Olaf Niemann, for his help in procuring the airborne data, and to the kind folks in Dr. Niemann’s Hyperspectral-LiDAR Research Laboratory: Fabio Visintini and Rafael Loos, for their georeferencing expertise and enthusiastic ear for many questions.

To the members of the Spectral Lab, including Eduardo Loos, Thiago Silva, Nicholas Komick, and Terri Evans, thank-you for all of your help, insight, perspective and most importantly, providing a glimmer of sanity when I needed it. Last, but certainly not least, a major thanks goes out to my friends and family, who put up with not seeing me for large chunks of time during the busy stages, supported me and kept me motivated through the tougher times, and celebrated the successes by my side, in stride.

Funding for this research was provided by NSERC postgraduate scholarship and on the water logistics were provided by Parks Canada. The AISA image was acquired by Terra Remote Sensing. Tafkaa was provided by Marcos Montes at the Naval Research Lab, Washington, D.C.

Chapter 1:

Introduction

Seagrasses are perennial flowering marine plants, occurring both intertidally and subtidally in soft benthic substrates of sheltered coastal regions. As photosynthetic organisms, prefer clear, oxygenated water and are limited to the photic zone and (Short and Coles, 2001). Of the class Monocotyledons and order Alismatales, they encompass the four families, *Posidoniaceae, Zosteraceae, Hydrocharitaceae,* and *Cymodoceaceae,* contain about sixty species worldwide (Larkum et al., 2006), and cover approximately 0.1 – 0.2% of the global ocean (Duarte, 2002).

Eelgrass, *Zostera marina,* is a species of seagrass that occurs throughout the northern coast of the Atlantic and Pacific Oceans (den Hartog 1971). It grows in complex spatial patterns, from sparse scattered patches to large continuous meadows both intertidally and subtidally (+2 m to -5 m relative to chart datum) (Larkum et al., 2006). Eelgrass, and seagrass in general, is widely recognized for its ecological and conservation value in coastal ecosystems (Hemming and Duarte, 2000; Jackson et al., 2001). First, it creates physical and chemical stability. It is a baffle against wave and current action (Fonseca and Cahalan, 1992), a sediment stabilizer (Mateo et al., 2003), an oxygenator of water and pore water (Hemminga & Duarte, 2000) and together with its epiphytes (Penhale & Smith, 1977), a major determinant of the balance of oxygen, carbon, nitrogen and phosphorous within the ecosystem (Hemminga & Duarte, 2000; Apostolaki, 2010). Second, eelgrass provides protection for many marine organisms, including out migrating juvenile salmon (*Onchorhynchus* spp.), Pacific herring (*Clupea harengus*), and complex macroinvertebrate assemblages (Mazzella et al., 1989; Sewell *et al.,* 2001, Borg et al., 2006). Third, the beds are a food source for the organisms inhabiting them. In many ecosystems, detritus derived from eelgrass has been identified as the fundamental source of nutrition for

coastal animals (Phillips, 1984; Thistle et al., 2010). The diets of fish utilizing eelgrass beds have been found to be 56% (by weight) comprised of sources within the eelgrass beds, including eelgrass shoots (Ganter, 2000), crustaceans, gastropods, and detritus (Adams, 1976). It is therefore not surprising that historical fish abundance has been linked to eelgrass presence (Phillips, 1984; Murphy et al., 2000), thus defining it as an exceptionally important resource to sustainable commercial fisheries (Adams, 1976). Lastly, in addition to nourishing its inhabitants, eelgrass also creates far-reaching ecosystem links. For instance, seagrass production can be buried in sediments or exported to neighbouring ecosystems, thus contributing to approximately 15% of the total organic carbon stored in marine ecosystems (Duarte and Chiscano 1999).

Due to this foundational role of seagrass in coastal ecosystem functioning and its well documented response to changes in water quality (Batiuk et al. 1992; Dennison et al. 1993), seagrass has been used worldwide as an indicator of coastal ecosystem health (Sewell *et al.*, 2001), and restoration success (Moore et al., 2000).When beds are lost, the shoreline extent and profile are significantly altered and ecosystem functioning negatively affected (Christiansen et al., 1981; Johnson et al, 2005).

Despite its importance, eelgrass populations have experienced worldwide decline (Orth & Moore 1983; Orth & Moore, 1984, Duarte et al., 2002; Orth et al. 2010). An estimated 2–5% of seagrass ecosystems are lost annually due to anthropogenic pressures (Duarte et al., 2002). This loss has been attributed not only to the physical pressures of increased coastal human populations and shoreline development (Duarte, 2002; Burkholder et al., 2007), vessel anchoring, and dredging (Duarte, 2002), but also to the light shading pressures of sedimentation, nutrient loading, and eutrophication (Burkholder et al., 2007), caused by intense aquaculture (Holmer et al., 2008), fish farming (Marba et al., 2006; Diaz-Almela et al., 2008; Apostolaki et al., 2009, Apostolaki, 2010), upland development and agriculture (Short & Wyllie-Echeverria, 1996), and increased pollution levels (Nienhuis, 1983; Giesen *et al*, 1990; Dejong & Dejong, 1992; den Hartog, 1994). The light shading pressures diminish eelgrass productivity by reducing the availability of photosynthetically active radiation (Moore and Wetzel, 2000; Zimmerman, 2003).

Additional eelgrass loss is predicted in response to climate change (Duarte, 2002; Najjar et al., 2010). For instance, on the west coast of North America, drier summers, wetter winters, greater autumn and winter riverine flow, and more frequent extremes in temperature and precipitation are predicted (Barnett et al. 2005; IPCC 2007b; Johannessen & Macdonald, 2009).

Eelgrass mortality is expected to rise in response to the ensuing higher sea temperature (Bintz et al., 2003; Sedinger et al., 2006; Moore and Jarvis, 2008), CO_2 (Thom, 1996; Palacios and Zimmerman, 2007), and epiphytic growth (Bintz et al., 2003; Short and Neckles, 1999), as well as altered estuarine flow (Stevenson et al.,1993; Greve et al., 2003) and erosion due to rising sea level and increased storms (Duarte, 2002). Furthermore, once seagrasses are under environmental stress, they are more susceptible to disease (Burdick et al. 1993). For example, in 1931–1932, "Wasting disease," a disease caused by infection with the protist *Labyrinthula zosterae*, led to the sudden destruction of 90% of the *Zostera marina* beds along the entire east coast of North America (Short et al. 1987; Muehlstein 1989; Muehlstein et al. 1991) and a significant decline of species in Europe (Cottam et al. 1944; Cottam and Munro 1954; Rasmussen 1977). The scale of the epidemic has been postulated by many authors to be linked to already stressed eelgrass (Young 1938; Rasmussen 1977; Vergeer & den Hartog 1994) and spurred the earliest attempts at transplanting seagrass (Cottam & Munro 1954; Rasmussen 1977).

Seagrass loss is projected to accelerate as human pressure on the coastal zone grows (Duarte, 2002). Knowing the temporal and spatial dynamics of eelgrass habitat is becoming exceedingly important in understanding estuarine processes, separating anthropogenic disturbances from natural trends, and identifying suitable areas for protection and rehabilitation, each toward the common goal of mitigating additional loss (Duarte, 2002; Dekker *et al.*, 2005; Ferwarda et al., 2007). Metrics that are commonly used to assess eelgrass habitat are patch size (Irlandi 1997), number of patches (Salita et al. 2003), shoot density (Bell & Westoby 1986a,b), biomass (Adams 1976), percent cover (Heck & Orth 1980), leaf height (Bell & Westoby 1986a,b; Thistle et al., 2010), maximum depth (Robinson & Yakimishyn, 2005), and epiphyte biomass and epiphyte species (Robinson & Yakimishyn, 2005). Mapping of these eelgrass metrics and distribution has historically been conducted by teams of divers and surveyors, and has therefore been limited by accessibility, time, and cost (Ackleson and Klemas, 1987; Dekker *et al.*, 2005). A proposed alternative method for eelgrass mapping is the use of remote imagery, which can cost- and time- effectively cover large and inaccessible areas nearly instantly and frequently (Chavez, 1996; Dekker *et al.*, 2005). The general objective of this research was to assess the feasibility and limitations of using various remote optical sensors - specifically hyperspectral field measurement, airborne hyperspectral AISA, and multispectral satellite sensors IKONOS and Landsat ETM+ - to map the location and biophysical attributes of eelgrass

at Sidney Spit, Gulf Islands National Park Reserve (GINPRC), British Columbia. To meet this objective, two components were addressed. First, the unique spectral characteristics of eelgrass and its associated benthic substrates were defined using *in situ* hyperspectral measurements, as described in Chapter 3. Second, these spectral characteristics were then applied in classification trials of the high spatial resolution data acquired by AISA and IKONOS at various levels of processing to determine the highest accuracy method of mapping eelgrass, as covered in Chapter 4. Chapter 5 summarizes the findings of both components and presents recommendations for their implementation in eelgrass mapping. Chapter 2 outlines methodology common to both Chapters 3 and 4. Any methodology unique to a chapter is presented as part of the respective chapter. The remainder of this chapter provides a brief literature review of eelgrass mapping techniques (Section 1.1), the biological and physical processes at the study site (Section 1.2), theoretical background for oceanographic remote sensing in shallow coastal waters (Section 1.3), and the optical properties of water column constituents (Section 1.4).

1.1 Eelgrass mapping background

Before remote sensing was possible, eelgrass mapping was carried out as area surveys from a boat (Young & Kirkman, 1975; Environment Canada, 2002), snorkel and land-based transects (Hyland et al., 1989; Dennison & Abal, 1999; Environment Canada, 2002), and towed underwater videography (Norris et al., 1997; Environment Canada, 2002; Precision Identification, 2002; Stevens & Connolly, 2005). These manual methods are the most commonly employed at present because they are well characterized and require little equipment. However, this approach is neither time nor cost effective enough to map large areas and therefore return time is very infrequent. Accuracy is also variable and often undefined due to variation in training of the mapper. In many cases, eelgrass delineation is dependent on the continued availability of skilled community or academic volunteers (Wright, 2002).

Initial forays into remote eelgrass mapping were made by aerial photograph interpretation when they became available in the late 1930s (Orth and Moore, 1984; Zharikov et al., 2005), first by delineating manually with a stereoscope (Ferguson et al., 1993), and then by automated classification methods on digitally scanned photographs (Chauvaud et al., 1998), and eventually digital photographs when the technology became available (Lathrop et al., 2006). Total

accuracies as high as 86% (Chauvaud et al., 1998) and a minimum discernable unit of 1 m^2 (Ferguson et al., 1993; Ferguson & Korfmacher, 1997) have been reported for aerial photography. However this accuracy is dependent on shallow, clear, calm water and bright sediment to contrast with vegetation (Ferguson et al. 1993), as well as significant *a priori* knowledge of the area. Many studies have been qualitative and/or do not quantify classification accuracy (e.g. the Orth, (1976) and Orth et al. (1979) studies of recovery after the 1930s wasting event). The benefits of aerial photography are flexible acquisition times, flexible and suitable image scale and spatial resolution (as fine as 0.1 x 0.1m – Andrefouet et al., 2002), fast processing return time (Lathrop et al., 2006), and the ability to acquire imagery below cloud cover (Ferguson et al., 1993). However the disadvantages are the high cost of the flight, low spectral resolution (3 bands - options of true colour RGB or false colour near-infrared), distortion of the photograph edges, and georeferencing difficulties due to the small area covered by a single photograph and the general featurelessness of large tracts of the coastal benthos (Ferguson et al. 1993). Lastly, radiometric response tends to be inconsistent between images, making it difficult to establish generalized rule-based classifications (Lathrop et al., 2006).

In 1972 multispectral satellite imagery became available, offering a lower-cost alternative to aerial photography. However the spatial resolution was much coarser. For example, the first Landsat sensor, Landsat MSS (Multispectral Scanner) launched in 1972, was 80m x 80m, and the current Landsat ETM+ (Enhanced Thematic Mapper Plus) is 30m x 30m resolution. The resulting high sub-pixel heterogeneity limited eelgrass delineation to presence/absence of large meadows and the effectiveness of the imagery in benthic classification depended on spectral location of the few (usually 2 or 3) visible bands. Several authors have found moderate success with Landsat. The majority of benthic mapping studies using Landsat have produced overall accuracies between 65% to 75% (Ferguson and Korfmacher, 1997; Mumby & Edwards, 2002; Bouvet et al., 2003; Dekker et al., 2005; Schweizer et al., 2005; Roelfsema, 2009), but some have been as low as 37% for complex substrates (Mumby et al., 1997; Mishra et al. 2005). One study derived overall accuracy for eelgrass specifically as 59% (Mumby & Edwards, 2002). Another derived a model of eelgrass biomass that explained 64% of biomass variation (Schwiezer et al, 2005).

The advent of high spatial resolution sensors such as SPOT (Satellite Pour l'Observation de la Terre) (10x10 m), IKONOS (4 x 4 m and 1 x 1 m), and Quickbird (1 x 1 m) enabled more

detailed classification of eelgrass spatial distribution but were still limited to two to four spectral bands to characterize differences between substrates. Various authors have attempted benthic classification with IKONOS, resulting in overall accuracies of 69 to 84% and eelgrass overall accuracies ranging from 56% to 89% (Mumby & Edwards, 2002; Andrefouet et al., 2003; Purkis, 2005; Fornes et al. 2006). SPOT has shown 87 to 96% overall accuracy (Pasquilini et al. 2005) and Quickbird has shown 81% overall accuracy (Mishra et al. 2006).

Development of digital airborne hyperspectral digital scanning sensors such as CASI (Digital Compact Airborne Spectrographic Imager) and AISA offered the combination of benefits from both satellite image and aerial photo acquisition. First, georeferencing of continuous flight lines of imagery is much more accurate than with punctual images, especially as geolocational information can be acquired simultaneously and attributed to the image. Second, airborne scanning data can be acquired below cloud cover, and with the flexibility of time, elevation, solar-sensor geometry, flight direction etc. Lastly and most importantly, imagery can be acquired at both high spatial (1 m x 1 m) and high spectral (e.g. 1nm continuous) resolution, enabling substrate spectral signatures to be fully characterized. With this full characterization, unique spectral regions can be identified to maximize substrate separation and increase classification accuracy. With this high level of spectral detail, substrate subcategories have been remotely delineated with success, such as eelgrass leaf area index (Dierssen et al., 2003) and species composition (Fyfe, 2003). In comparative analysis, airborne scanning has shown significant advantage over satellite sensors when detecting a large number of classes. For example, Mumby et al. (1997) showed 81% accuracy with vs. 37% with Landsat or SPOT when over 9 classes, including eelgrass were present. Mumby et al. (1998) showed 89% accuracy with CASI when four classes, including eelgrass were present. As a more local example, Su et al (2006) mapped eelgrass in Puget Sound with overall eelgrass accuracy of 92% using 5 x 5 m multispectral airborne scanning.

As ideal as it is, digital airborne scanning still has the disadvantage of high cost. Cost and accuracy-wise, the ideal sensor for eelgrass mapping would be a high spatial resolution multispectral satellite sensor with a small number of bands located in key wavelengths that are specific to the separation of submerged substrates.

1.2 Study Site – Marine areas around Sidney Spit, Gulf Islands National Park Reserve of Canada (GINPRC)

Benthic Substrates

Sidney Island is a 8.9km^2 island, located approximately 4 km east of Sidney, British Columbia (Figure 1.1). The 1.8km long sand spit and lagoon on its north-eastern extreme outline the 1.78km^2 Sidney Spit protected area, part of the GINPRC (Parks Canada, 2010). The waters immediately east and west of the sand spit are underlain by shallow sloping sandy substrate and fringing beds of intertidal *Zostera marina.* Subtidal *Z. marina* inhabits sandbars approximately 500 metres west of the spit. A shallow lagoon southwest of the spit and bordered on its west side by Hook Spit, contains a large and very well protected eelgrass bed that is entirely exposed during lowest tide events. In 2004, an eelgrass assessment by Parks Canada in the lagoon produced the following average metrics: density = 300 shoots/m^2 and biomass = 198.8 g m^{-2}, which were in agreement with average values for the Gulf Islands. Leaf area index was 2.24 m^2 m^{-2}, a slightly higher mean than the Gulf Island sites mean of 1.8 m^2 m^{-2} (Robinson & Yakimishyn, 2005). Total eelgrass meadow extent was estimated from orthophotos at 183, 000m^2 in 2006 (Robinson and Martel, 2007). At least 15 fish species inhabit the eelgrass meadows, as determined by beach seine (Robinson & Yakimishyn, 2005). A graduate student thesis research project (Leatherbarrow, 2006) mapped eelgrass distribution using towed underwater video around the areas of anchoring activity at Sidney Spit in the summer of 2005. The study found eelgrass distribution to be confined to shallower than 2.0m below chart datum, suggesting that light availability due to water clarity was the limiting factor. The study also revealed that boaters frequently anchor in the eelgrass beds.

Epiphytic algae, filamentous diatoms and *Smithora spp.*, colonize the eelgrass blades variably throughout the site. In 2004, the eelgrass epiphyte loading at Sidney Spit was found to be lower than average among Gulf Islands, and composed mainly of filamentous diatoms, and only small amounts of *Smithora spp.* (Robinson & Yakimishyn, 2005). The observations of this study in 2008 revealed spatial dependent high coverage by both epiphyte types. The other major submerged substrates are green algae (*Ulva fenestrata* and filamentous green algae) and sandy bottom. The halophyte *Salicornia virginica* (sea aparagus) is found in large stands in the

extreme south of the lagoon. Brown algae *Fucus spp., Sargassum muticum,* and *Laminaria saccharina* are present but were not found at high areal coverage (< 1m^2) at the time of sampling.

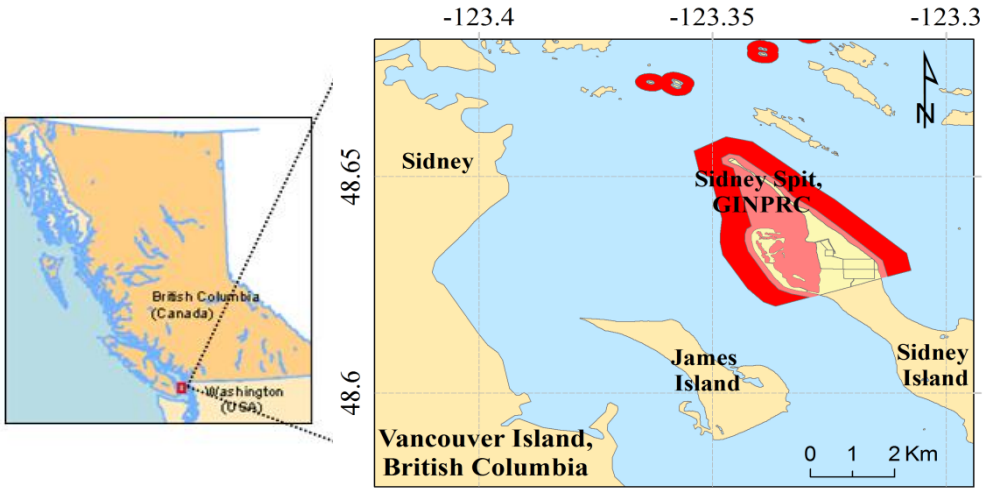

Figure 1.1. Sidney Spit, Sidney Island, British Columbia is part of the Gulf Islands National Park Reserve of Canada (GINPRC). Pale red area is designated as Marine protected area within the park and and dark red is Marine Extension (Modified from Parks Canada, 2010).

Water constituents

The Gulf Islands are bordered on the West by Vancouver Island, on the South by the Strait of Juan de Fuca to the South, and on the Northeast by the remaining Gulf Islands and the Strait of Georgia (Figure 1.1). In the Strait of Georgia, the dominant source of fresh water and particles is the Fraser River, which contributes approximately 73% of the 158 × 109 m^3yr^{-1} of water and 64% of the 30 × 109 kg yr^{-1} of particles (Johannessen et al., 2003), with highest inputs in late summer and early autumn (Johannessen et al., 2006). While this riverine input influences the northern eelgrass meadows of the Gulf Islands (Bennett Bay on Mayne, Island Cabbage Island, and Tumbo Island), the Sidney Spit waters appear to have constituent properties in between the warmer, riverine Strait of Georgia and the colder, oceanic Strait of Juan de Fuca (Robinson & Martel, 2006). Temperature and salinity recorded by Robinson & Martel in August 2006 were ~13.5 °C and ~29 ppt respectively. Since there is little documentation of CDOM (chromophoric dissolved organic material) and TSM (total suspended matter) for the Sidney Spit area, the most oceanic central portions of the Strait may be the most comparable, with $a_{CDOM}(443)$ ranging from 0.22 – 0.48 m^{-1} and TSM concentrations from 1.76 – 3.47 g m^{-3} in

mid-July (Komick et al., 2009). Nitrate input is also primarily from the Strait of Juan de Fuca, which provides a surface range of 25-30 μM while the Fraser River contribution is minor at < 5 μM (Pawlowicz et al. 2005). Surface chlorophyll and CDOM vary on a seasonal cycle with phytoplankton production. Concentrations are high in the spring due to increased solar radiation and taper off to low levels by late summer when nutrients in the euphotic zone become depleted (Johannessen et al., 2008; Masson and Peña, 2009). There is a high degree of fine silt-clay particle settling at Sidney Spit (>10% higher than other locations within the park) due to very low current flows (Robinson & Yakimishyn, 2005). This silt can be assumed to lead to higher TSM values during tidal flux.

1.3 Remote Sensing Theory

Passive remote sensing of a target depends on measurements of solar electromagnetic radiance reflected off of a target substrate and measured by the sensor as a radiance spectrum ($L(\lambda)$). When the target of interest is a submerged substrate, the characteristics of this radiance spectrum are not representative of the target surface alone; The total observed radiance at the sensor ($L_T(\lambda)$) is a combination of the desired substrate radiance ($L_b(\lambda)$) and spectral information derived from absorption and scattering interactions in the atmosphere ($L_{atm}(\lambda)$) (Werdell & Roesler, 2003), off the water surface ($L_{sfc}(\lambda)$) (Hochberg et al., 2003; Hedley et al., 2005) and within the water column ($L_w(\lambda)$) (Lyzenga, 1978):

$$L_T(\lambda) = L_b(\lambda) + L_{atm}(\lambda) + L_{sfc}(\lambda) + L_w(\lambda) \quad (1.1)$$

These attenuation paths are depicted in Figure 1.2. To derive the pure spectra of a submerged substrate, these interactions must be accounted for and removed from the total spectral signal in respective order:

$$L_b(\lambda) = L_T(\lambda) - L_{atm}(\lambda) - L_{sfc}(\lambda) - L_w(\lambda) \quad (1.2)$$

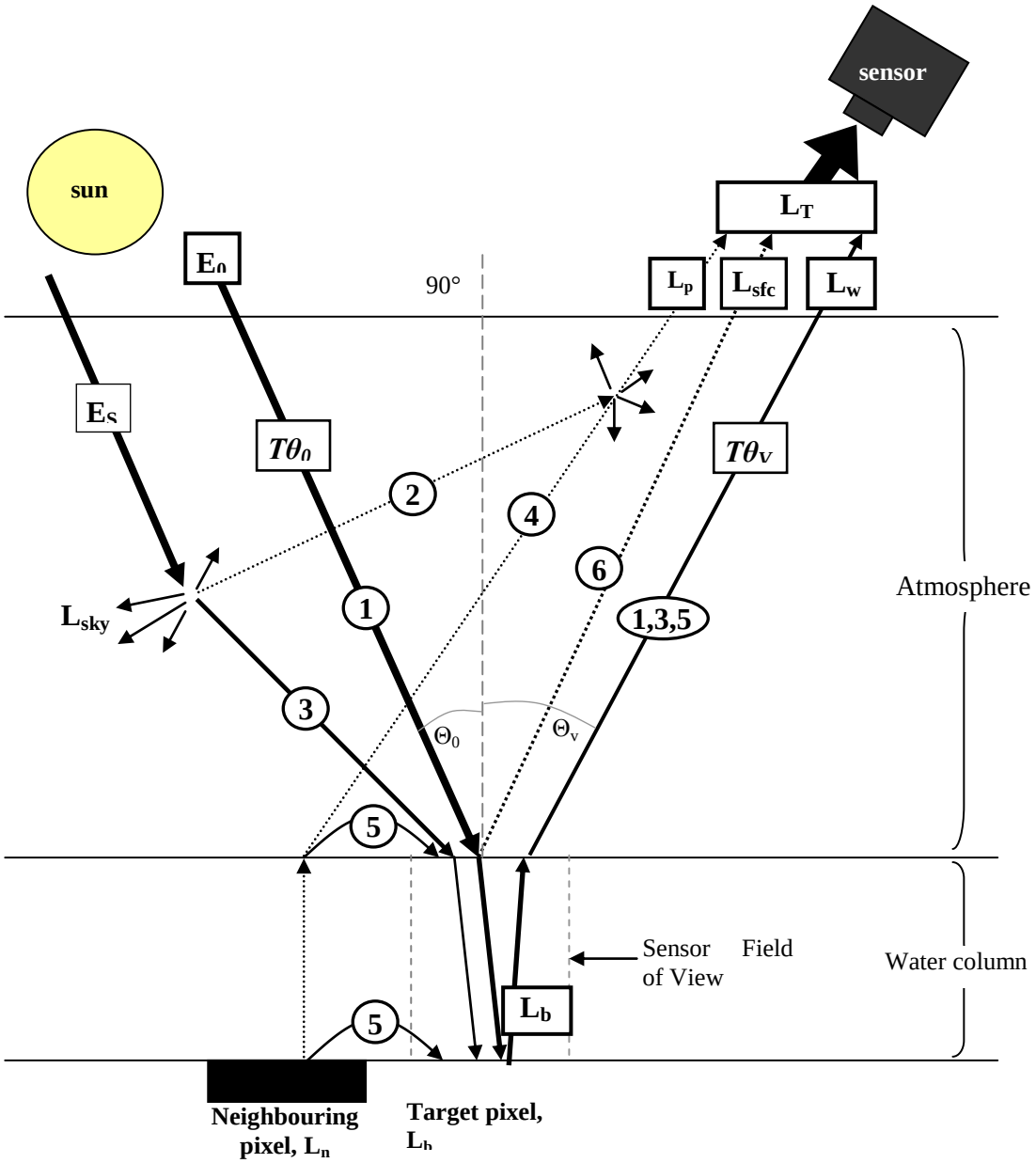

Figure 1.2. Paths of radiance received by a satellite remote sensor. Path 1 contains the desired radiance information from the target, while paths 2-6 introduce atmospheric noise to the radiance measured by the sensor, L_T. (Adapted from Jensen, 2007)

where E_0 = solar irradiance at the top of the atmosphere (μW $cm^{-2}nm^{-1}$), E_S = downwelling solar irradiance (μW $cm^{-2}nm^{-1}$), L_{sky} = diffuse sky radiance (μW $cm^{-2}sr^{-1}nm^{-1}$), T_θ = atmospheric transmittance at an angle θ to the zenith (θ_0 or θ_v), θ_0 = solar zenith angle, θ_v = scan angle (nadir view angle of the satellite sensor), L_b = average target reflectance, L_n = average background reflectance form a neighbouring pixel, L_W = water-leaving radiance of the target (μW $cm^{-2}sr^{-1}nm^{-1}$), (i.e. free of atmospheric effect, as a radiometer would produce), L_p = path radiance due to multiple scattering (μW $cm^{-2}sr^{-1}nm^{-1}$), composed of skylight and radiance from neighbouring pixels, L_{sfc} = radiance due to specular reflection off of the water surface (surface glint), L_T = total radiance at the sensor (μW $cm^{-2}sr^{-1}nm^{-1}$).

The following sections describe the characteristics of the terms in Eq. 1.2.

1.3.1 Optical properties of substrates, L_b

Absolute and relative reflectances in the visible wavelengths of an exposed substrate spectrum are a result of both the total and the relative concentrations of substrate pigments. Increasing the concentration of any photosynthetic pigment causes a progressive increase in visible range absorption, particularly at its characteristic absorption features (Curran *et al.*, 1991). Near Infrared (NIR) reflectance is characteristic of the cell structure of vegetation, increasing with vegetation density, but varying with species (Jensen, 2007). In this section, a description of the spectral behaviour of each substrate is provided. When the substrate is submerged, spectral influences of the water column and its constituents come into play and this is described in *Section 1.3.2.*

Eelgrass (Zostera marina)

Eelgrass contains the primary photosynthetic pigment chlorophyll-a and accessory pigment chlorophyll-b, which absorb light in the red and blue wavelengths. It lacks carotenoid absorption in the 500 to 600nm range, which creates a broad reflectance peak in the green region (Werdell & Roesler, 2003). Eelgrass growing in shallow water also contain photoprotective anthocyanins that absorb in the range of 500 – 550nm and reflect in the 600 – 640 nm region (Gausman, 1982; Fyfe, 2003). Examples of eelgrass spectra are shown in Figure 1.3 (Werdell & Roesler, 2003).

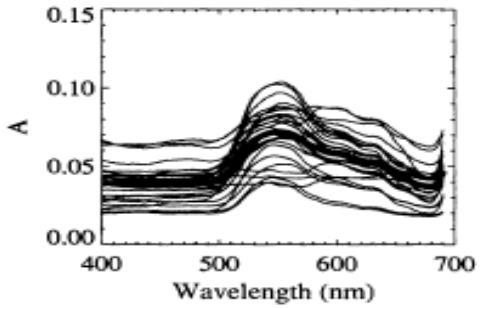

Figure 1.3. An example of pure endmember in situ spectra of eelgrass in the visible range. Variations are due to eelgrass blade age and epiphyte cover. Reflectance is shown as albedo, which is the ratio of radiance from the substrate, to the irradiance incident upon it in the water column (Modified from Werdell & Roesler, 2003).

Spectral variations among eelgrass samples (Figure 1.4) are a result of blade age and epiphyte cover. The youngest blades, generally found at the centre of an eelgrass bed, have the highest chlorophyll-a concentration and therefore higher reflectance values in the green region (Werdell & Roesler, 2003). As blades age, they acquire epiphytes (Neckles et al., 1993; Drake et al., 2003) and exhibit a spectrally independent increase in reflectance in the blue and red wavelengths. As the oldest blades on the outermost edges of the bed senesce, pigments are lost and reflectance decreases across the spectrum (Werdell & Roesler, 2003) (Figure 1.4).

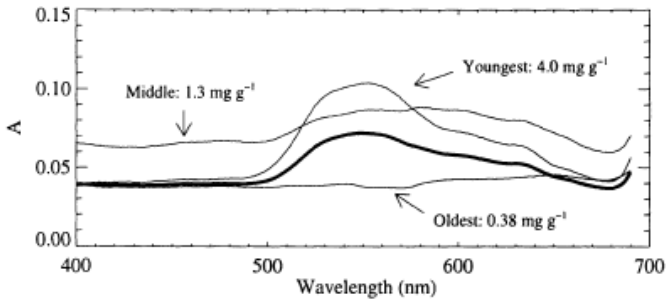

Figure 1.4. Spectral change of eelgrass blades with age. Reflectance is shown as albedo, which is the ratio of radiance from the substrate, to the irradiance incident upon it in the water column. (Modified from Werdell & Roesler, 2003).

Green algae

The pigment composition of green algae is very similar to eelgrass except it does not contain anthocyanins, has higher concentrations of lutein, and contains the additional accessory pigment β-carotene, which absorbs in the blue spectral wavelengths 400 – 505 nm (Rowan, 1989). Therefore, it is expected to have higher absorption in the blue and in the shorter green wavelengths.

Sand and silt

Sand has a much higher albedo compared with eelgrass and deep water. A sand spectrum is relatively featureless, with reflectance values increasing steadily toward longer wavelengths (Figure 1.5a). Clay and silt have a lower mean albedo brightness and a lower mean red to blue ratio (A_{700}:A_{400}) than sand, owing to its finer grain-size, which allows higher organic and bacterial content and therefore higher absorption (Werdell & Roesler, 2003) (Figure 1.5b).

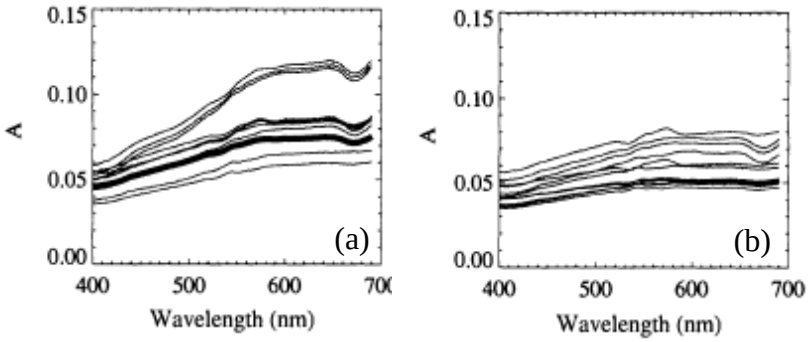

Figure 1.5. Example of in situ hyperspectral (a) sand and (b) clay/silt spectra in the visible range. The absorption feature around 676nm is caused by the accessory pigments of detritus and benthic diatoms. (Modified from Werdell & Roesler, 2003).

1.3.2 Optical Properties of the Water Column, L_{water}

Early oceanographic remote sensing involved derivation of chlorophyll-a algorithms for open ocean waters. To do so, three assumptions were made: (1) the water contained only pure water and chlorophyll-*a*; (2) Any other water constituents covaried with chlorophyll-a or were spectrally negligible; and (3) the water was optically deep, meaning the benthic substrate could not be detected (Gordon and Morel, 1983; Morel and Maritorena 2001; Darecki and Stramski, 2004). This type of water was termed "Case 1."

Coastal waters are referred to as Case 2 waters and are optically more complex, with additive absorption and scattering contributions from all major water constituents: pure water, chlorophyll, accessory photosynthetic pigments, CDOM, and suspended matter, which vary independently of one another (Gordon and Morel 1983; IOCCG, 2000). Shallow coastal waters, such as the ones explored in this research, are not optically deep and therefore include the additional optical component of the seafloor. The optical behaviour of each Case 2 optical water constituent is described in the following section.

(i) Pure Water

Pure water absorbs electromagnetic energy very efficiently, resulting in very low reflectance (less than 1% of incident radiance). The high absorption features of water in the infrared region of the spectrum (Figure 1.6) together with the low signal-to-noise ratio of optical

sensors in the ultraviolet range limit optical studies of water to the visible range (400 - 700nm) and a small portion of the near infrared range (700-800nm) (IOCCG, 2000; Mueller et al., 2003).

(ii) Total Suspended Matter, TSM

Suspended matter in marine environments consists of both organic and inorganic particles. The organic portion is comprised of detritus, phytoplankton cells, and land runoff, while the inorganic portion is derived from mineralogical terrigenous sources. High reflectance in the red and near infrared (NIR) wavelengths and high absorption in the blue wavelengths (Figure 1.6) are characteristic of suspended matter (Babin et al, 2003). Increasing the concentration of suspended matter causes a wavelength-independent increase in reflectance that is biased in the red and near-infrared ranges (Figure 1.7). This signature interferes with atmospheric and sun glint correction applications that assume NIR reflectance of water is zero, and that all NIR reflectance present in an image water pixel results from atmospheric scattering or sun glint (Hocherg *et al.*, 2003; Hedley & Mumby, 2005; Lavender et al., 2005). Suspended matter is a significant optical component in coastal waters with eelgrass due to proximity to land and the slowing of the surrounding current by eelgrass beds, which encourages greater deposition of sediment and detritus (Holt et al., 1997).

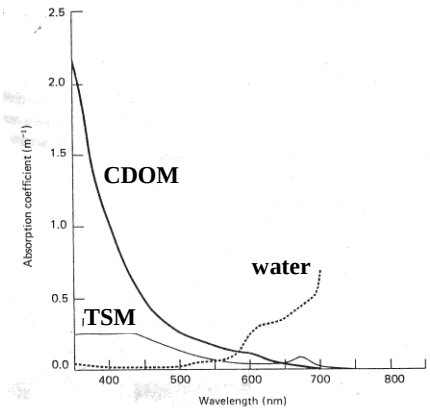

Figure 1.6. Spectral absorption properties of pure water, chromophoric dissolved organic material (CDOM), and suspended matter (TSM) in the water column (modified from Kirk, 1986).

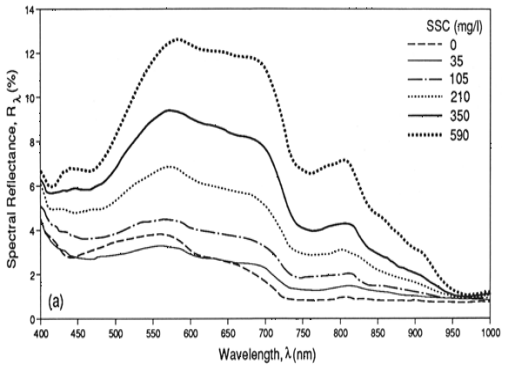

Figure 1.7. Reflectance spectra for varying concentrations of suspended inorganic matter. Note that with increasing concentration, reflectance increases at all wavelengths, but is biased toward the longer visible wavelengths (500 – 700nm) (from Chen et al., 1991).

(iii) Chromophoric Dissolved Organic Material (CDOM)

CDOM is created by the decomposition of organic matter into humic and fulvic acids (Carder *et al.*, 1989). Its concentration in coastal water occurs independently of chlorophyll-a concentration because it is derived not only from primary production of phytoplankton, but also from terrigenous sources (Twardowski & Donaghay, 2001). Scattering by CDOM is negligible, however very high absorption is exhibited in the shorter wavelengths, exponentially decreasing toward the longer wavelengths (Kirk, 1986) (Figure 1.8). This absorption feature overlaps with that of the photosynthetic pigment chlorophyll-*a*, presenting issues for separation of the blue reflectance signal into the contribution from each optical component.

(iv) Photosynthetic Pigments

Phytoplankton require photosynthetic pigments to harvest solar energy and drive photosynthesis. Though all pigments are optically active, the dominant pigment is usually chlorophyll-a, which exhibits high absorption in the blue wavelengths, and slightly weaker absorption in the red wavelengths (Kirk, 1986) (Figure 1.8). Accessory pigments have characteristic absorption features in other wavelength ranges (Figure 1.8), allowing the photosynthetic organism to harvest solar energy additional to that captured by chlorophyll-a.

Some accessory pigments include chliorophyll-b, -c, and -d; phycoerythrin, phycocyanin, phycobiliproteins, and carotenoids. (Kirk, 1986).

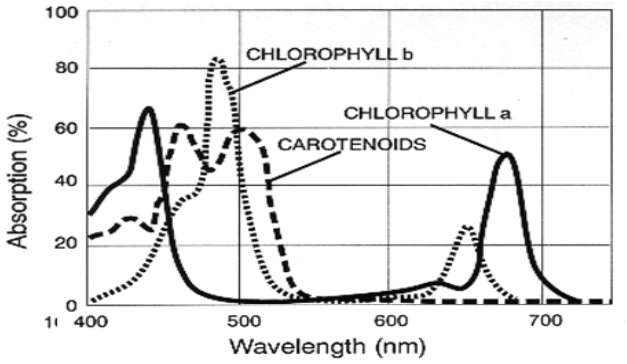

Figure 1.8. Absorption spectra for chlorophyll-a and accessory pigments chlorophyll-b and carotenoids. (Modified from Whitmarsh and Govindjee, 1999).

Characterizing and correcting for attenuation by the water column

The above-mentioned absorption and scattering properties of the water column for any given wavelength can be specified in terms of the total absorption coefficient $a_T(\lambda, z)$ and total scattering coefficient $b_T(\lambda, z)$, which describe the proportion of radiant flux lost by absorption and scattering, respectively, over an infinitesimally thin horizontal plane (Kirk, 1986). These are termed the inherent optical properties of water because they are independent of the geometry of the light field, and depend solely on water constituent composition. Total attenuation per unit distance is termed the beam attenuation coefficient $c_T(\lambda, z)$ and is defined as (Kirk, 1986):

$$c_T(\lambda, z) = a_T(\lambda, z) + b_T(\lambda, z) \quad (1.3)$$

The total absorption coefficient (a_T) is an additive combination of absorption by water, CDOM, suspended organic material, and suspended inorganic material. Similarly, total backscattering coefficient (b_T) is an additive combination of backscattering by water, suspended organic material, and suspended inorganic material.

$$a_T(\lambda, z) = a_W(\lambda, z) + a_{CDOM}(\lambda, z) + a_{org}(\lambda, z) + a_{inorg}(\lambda, z) \quad (1.4)$$

$$b_T(\lambda, z) = b_{org}(\lambda, z) + b_{inorg}(\lambda, z) \quad (1.5)$$

The rate of attenuation of irradiance with depth for a given composition of water is defined by the vertical diffuse attenuation coefficient, K (K_d for downward irradiance and K_u for upward irradiance). K is termed an apparent optical property of water because it is dependent on the geometry of the light field, i.e. the irradiance spectrum (Kirk, 1986). In practice it is assumed that $K_u = K_d$ (denoted K) and is only weakly dependent on depth (Mobley, 1994; Hedley & Mumby, 2003).

$$K_d = (d \ln E_d) / dz = -(1/E_d)(dE_d/dz) \quad (1.6)$$

$$K_u = (d \ln E_u) / dz = -(1/E_u)(dE_u/dz) \quad (1.7)$$

where z = depth in metres, E_d = downwelling irradiance, and E_u = upwelling irradiance.

K can be used to remove the attenuation of the water column from above-water spectra and achieve reflectance spectra of benthic substrates as they would appear in the absence of the water column (R_{rs}^{b}) (Maritorena 1994; Hedley & Mumby, 2003; Brando et al., 2009). This methodology is described in *Chapter 2, Section 2.2.2.*

1.3.3 Optical Properties of the Sea Surface, L_{sfc}

The spectral signal is attenuated at the air-water interface both when entering and leaving the water column. Downwelling irradiance is lost through reflection and refraction off of the surface in a direction out of the sensor's field of view, and upwelling radiance is lost by refraction back down into the water column.

Refraction at the air-water interface

Because water and air have different densities, the velocity of light is different through each. When a beam of light obliquely encounters a boundary between the two mediums, it will change speed and therefore change direction. A beam of light incident on the water surface from above will be slowed by the water and refract toward vertical. A beam of light approaching the air-water interface from under water will speed up in air and be refracted in the opposite way; further from vertical. A beam incident to the interface perpendicularly, will not be refracted. To

convert from reflectance just above the water surface $R^{(0+)}$, to reflectance just below the surface $R^{(0-)}$,

$$R^{(0-)} = R^{(0+)} \cdot \frac{(1+\alpha)}{(1-\rho)} \tag{1.8}$$

where α= Fresnel reflection albedo for irradiance from sun and sky (standard value 0.043), and ρ= Fresnel reflectance index of seawater (standard value 0.021) (Fargion & Mueller, 2000).

Reflection at the air-water interface (spectral glint)

A small portion of the solar beam incident on the water surface will be reflected off of the surface and back into the atmosphere. The proportion of light that is reflected rather than transmitted across the surface varies with incidence angle, from 2% for vertically incident light, to 100% for light at grazing incidence (Kirk, 1986). Reflectance off of a flat water surface occurs at an angle equal to the incidence angle and is termed specular reflectance (Path 6 in Figure 1.2). Specular reflectance is responsible for "sun glint" in remote imagery when the sensor view angle is equal to the solar incidence angle or in wind-roughened water when the wave angle causes the solar beam to be reflected directly into the sensor (Hochberg et al., 2003). Sun glint is wavelength independent and obscures the water reflectance signal by increasing radiance in all wavelengths with a pattern characteristic of the irradiance spectra (Philpot, 2007). Glint corrections are effective over optically deep water and shallow waters with substrate reflecting in the visible range (400 – 700nm), however errors occur over substrates with NIR reflectance, including eelgrass. Because the corrections rely on the assumption that all NIR reflectance present in an image water pixel results from sun glint, the NIR signal crucial to recognizing shallow eelgrass beds is removed, and the information is lost (Hedley et al., 2005). Therefore in the case of eelgrass mapping, it is crucial to avoid sun glint by ensuring optimal solar, sensor, and water surface geometry. To ensure best compromise between high pixel brightness and low sun glint, it is recommended to acquire data over calm water, at a sensor view angle 10 – 20° from the sun specular point, avoiding the sun glint cone (Abileah, 2007).

1.3.4 Optical Properties of the Atmosphere, L_{atm}

Water absorbs electromagnetic energy very efficiently, this resulting in a very low reflectance signal. Therefore the scattering and absorption by even a small amount of moisture and/or particulate in the overlying atmosphere adds significant attenuation to satellite optical data acquired over water (Dekker et al., 2005). In the atmosphere, scattering is additive and is the most dominant (Chavez, 1988). It is facilitated by aerosols, which can be suspended liquid or particulate matter, and can be partitioned into three major types depending on aerosol size: (1) Raleigh (molecular), (2) Mie (aerosol), and (3) non-selective scattering. Rayleigh (molecular) scattering is caused by gas molecules 0.1 times the size of the wavelengths they scatter. Rayleigh scattering is inversely proportional to the fourth power of the wavelength ($1/\lambda^4$), and therefore selectively scatters very short visible wavelengths of radiant energy, giving the sky a blue appearance to the eye (Young, 1982). Mie (aerosol) scattering is caused by aerosols such as dust, pollen, smoke, ash, water vapour, and salts with diameter length 0.1 to 10 times the wavelengths they scatter. These larger aerosols selectively scatter longer, particularly red, visible wavelengths (Klein and Isacks, 1997). Non-selective scattering is caused by large particles such as water droplets that are over 10-times the size of the wavelengths they scatter. Non-selective scattering increases radiance values over the entire visible range, yielding a white appearance to the eye (i.e. haze, fog, and clouds) (Jensen, 2007).

Atmospheric absorption is multiplicative (Chavez, 1988) and is dominated in the optical region (400 – 1000nm) by water and ozone absorption features. Water vapour and the atmospheric gases: water (H2O), carbon dioxide (CO2), oxygen (O2), methane (CH4), nitrous oxide (N2O), carbon monoxide (CO), nitrogen dioxide (NO2), and ozone (O3) selectively absorb energy in wavelengths greater than 800nm. According to Montes *et al.* (2004), for sensors measuring below 1000nm, it is only necessary to consider the absorption effects of NO2, O3, H2O, and O2.

As a result of atmospheric attenuation, two separate radiative components reach the water surface: a direct solar radiation component (E_s) maintaining directionality as it existed outside the atmosphere (Path 1 in Figure 1.2) and a diffuse solar radiation component (or skylight, L_{sky}) that reaches the water surface at multiple angles due to atmospheric scattering (Path 3 in Figure

1.2) (Sathyendranath, 2000). Radiation that is not lost by specular reflection off of the surface (Section 1.3.3 and Path 6 in Figure 1.2) is available for transmission through the water column.

Before reaching the sensor, some radiation is scattered into the field of view by the atmosphere (Path 2 in Figure 1.2) and neighbouring pixels (Paths 4 and 5 in Figure 1.2), adding a noise, which is termed path radiance, $L_p(\lambda)$. So we see that L_{atm} of Eq. 1.1 and 1.2 is divided into three components (Figure 1.2):

$$L_{atm}(\lambda) = E_s(\lambda) + L_{sky}(\lambda) + L_p(\lambda) \quad (1.9)$$

Different atmospheric correction methods have been developed for the removal of L_{atm} from L_{tot}. In this study two atmospheric corrections were used: the empirical method, Empirical Line Calibration and the radiative transfer modelling method, *Tafkaa.*

The Empirical Line Calibration (ELC) method relies on above-water hyperspectral *in situ* spectra (i.e. L_w, a combination of $L_b + L_{sfc} + L_{water}$, Figure 1.2) measured over various targets within the image bounds at the time of image acquisition. These *in situ* measurements are considered to be atmospherically correct upon acquisition, as they were normalized to E_s. The image data are then forced to match the atmospherically correct *in situ* measurements by applying a best-fit (least squares) regression line between the image DN or radiance values and their corresponding *in situ* reflectance measurements for each sensor band (Che and Price, 1992) (Figure 1.9). The resulting regression lines can be expressed mathematically as

$$\text{Rrs} = \text{S x L} + \text{“y-offset”} \quad (1.10)$$

$$\text{or re-arranging, Rrs} = (\text{L} - \text{“x-offset”}) \cdot (1/\text{S}) \quad (1.11)$$

The “x-offset” is representative of atmospheric radiance and the inverse slope (1/S) is representative of the downwelling irradiance (Es). Therefore by applying the band-specific regression line equations to each pixel, atmospheric radiance is subtracted, and illumination effects are removed by normalizing to irradiance, yielding atmospherically corrected above water remote sensing reflectance values ($R_{rs}^{(0+)}$).

$$\text{Remote sensing reflectance (Rrs)} = \frac{\text{Image Radiance} - \text{Atmospheric Radiance}}{\text{Downwelling Irradiance}} \quad (1.12)$$

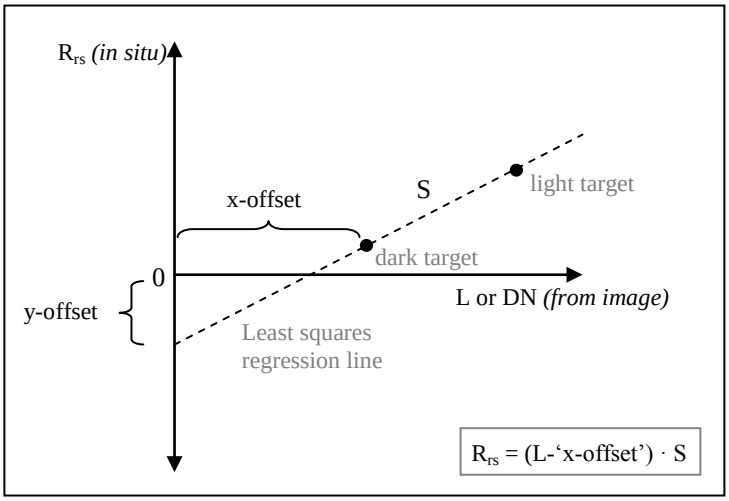

Figure 1.9. Empirical Line Calibration: A best-fit least squares regression line for a single sensor band, using two spectral reference targets (Modified from Smith and Milton, 1995).

The ELC correction has specific requirements for *in situ* measurements. Each target site should have low spectral variation across the entire spectra, and be spectrally homogeneous, vegetation-free, Lambertian, horizontal, and have a large enough area to be resolved in the image (Che and Price, 1992; Smith and Milton, 1999). Karpoulzi and Malthus (2003) recommend a target area three times larger than the spatial resolution of the image. Additionally, *in situ* measurements should be made at the very least at a 'spectrally dark' target (usually deep water), and a 'spectrally bright' target (e.g., dry sand), to ensure the correction will be representative of the entire reflectance range of the image (Freemantle *et al.*, 1992; McArdle *et al.*, 1992).

A major disadvantage of atmospheric correction with *in situ* measurements, such as ELC, is that the coefficients derived between image and field measurements are specific to the place and time of image acquisition and therefore cannot be used to compare data temporally or between locations. ELC also assumes that the atmosphere is uniform across the image, whereas water vapour often varies greatly over a small scale (Smith and Milton, 1999).

Radiative transfer models do not require *in situ* spectral measurements, but instead rely on sun-sensor geometry, meteorological and atmospheric aerosol variables at the time of image acquisition to mathematically characterize the amount of atmospheric attenuation to be removed. Lookup tables are used to match a pre-defined atmospheric constituent profile to the image, and then remove the radiance characteristics of that profile using radiative transfer codes such as LOWTRAN (Kneizys *et al., 1988),* MODTRAN (Berk *et al.,* 1989), and 5S or 6S (Second Simulation of the Satellite Signal in the Solar Spectrum) (Vermote *et al.* 1997). Radiative transfer modelling often produces better results than other correction methods; however, a vast number of atmospheric models exist, in an array of requirements and computational complexity levels. It is important for atmospheric correction of coastal waters to ensure the chosen model accounts for high absorbance aerosol (salts), highly reflective suspended sediments, and sun glint (Shi and Wang, 2007). As mentioned, the atmospheric correction radiative transfer model selected for this study was *Tafkaa*, which was developed by the United States Naval Research Laboratory in the late 1990's specifically for imagery acquired over turbid shallow coastal waters (Gao et al., 2000). *Takfaa* models atmospheric absorption using a high-resolution database of gas absorption coefficients, temperature, and pressure profiles with ATREM (ATmosphere REMoval) radiative transfer code, and models scattering from an aerosol profile measured *in situ* (Gao et al., 2000; Montes et al., 2004a). Inputs to the model are date, time, coordinates, elevation, sensor altitude, temperature, ozone amount, relative humidity, wind speed, and aerosol optical depth (AOD) measured by a sun photometer station. Tafkaa has been applied successfully to hyperspectral imagery acquired by low altitude airborne sensor PHILLS (Portable Hyperspectral Imager for Low Light Spectroscopy) (Davis et al., 2002), high altitude (20km) airborne sensor AVIRIS (Airborne Visible/Infrared Imaging Spectrometer) (Gao et al., 2000; Goodman et al., 2003; Montes et al., 2003; Montes et al., 2004b), and NASA EO-1 satellite sensor Hyperion (Ungar, 1997; Montes et al., 2004b) over sandy bottoms of Chesapeake Bay and the Florida Keys and coral reef systems of the Hawaiian Islands, French Frigate Shoals and Kaneohe Bay. Versions of Tafkaa have also been developed for multispectral sensors such as the SeaWiFS (Sea-viewing Wide Field-of-view Sensor) and MODIS (Moderate-resolution Imaging Spectroradiometer) (Montes et al., 2003).

Chapter 2

Methodology

This chapter outlines the field and laboratory methodologies that were common to both Chapter 3 and Chapter 4. Any methodology unique to a chapter is presented in the methodology section of that chapter. Figure 2.5, found at the end of this chapter, provides an overview flowchart of how the field data acquisition and data processing steps described here are applied in the remainder of the study.

2.1 Field methods

Field methods encompassed the acquisition of benthic substrate distribution and properties, water samples, and *in situ* spectra. The following sections describe the details of the acquisition processes. Figure 2.4, found at the end of this chapter, summarizes the relationship among all methodology, including field methods, spectra processing, and remote imagery processing.

2.2.1 Benthic substrate properties

Training of a benthic classification scheme and validation of a final benthic substrate map requires the results of classified pixels to be compared with ground-truthing at the same locations in the field. The ground-truth data was supplied by means of an extensive benthic survey within the study site, conducted from July 30 to August 3, 2008, the week previous to *in situ* spectra acquisition. Additional sites were visited on July 7, 2010 to increase the deep substrate sample size, under the assumption that benthic substrate presence/absence had remained similar since field collection in 2008. Additionally, a multibeam bathymetry layer with 5 m x 5 m horizontal spatial resolution and 1 m vertical resolution was provided by Parks Canada.

Initially, a map of known benthic cover polygons was established using an August 2006 AISA image and boat reconnaissance, thus defining six major cover classes, eelgrass *Zostera marina* (E), green algae (Ag) (*Ulva fenestrata* and filamentous algae), sand (S), brown algae (Ab) (present in very small amounts), sea asparagus (Asp), and optically deep (>30 metres) water

(dW) *(Table 2.1)*. Polygons were split by depth: less than 3 metres (shallow substrate, denoted *s*) and greater than 3 metres (deep substrate, denoted *d*). This depth stratification was based on previous field data (2006, 2008, not published) that showed clear spectral shape and magnitude differences above and below 3 metres depth, and was later corroborated during the field data analysis *(Chapter 3)*. Subsequently, a stratified random sampling method was used to define field sites within these polygons (Green *et al.,* 2000), defining a total of 559 sites. Ground-truth sites for difficult to access deep substrates were conducted by random underwater videography transects within the substrate polygons. The number of ground-truth sites surveyed for each substrate is presented in Table 2.1. The location of each ground-truth site is presented in Figure 2.1. At each site, the percent cover of each benthic substrate was estimated within a randomly placed 0.5m x 0.5m quadrat.

At 66 of the 245 eelgrass sites, an eelgrass survey was conducted in accordance with Environment Canada's (2002) goal level 4, the highest detail eelgrass mapping level, inclusive of both eelgrass distribution and water properties analysis. Five biophysical parameters were recorded at each site: percent cover, epiphyte type, shoot density (number of shoots per m^2), and the length and width of three random blades per quadrat (Kirkman, 1996; Green et al., 2000, Environment Canada, 2002). If the shoot count in the quadrat exceeded 100, a $0.0625m^2$ (0.25m x 0.25m) quadrat was used (Environment Canada, 2002). From these measurements, LAI was calculated for each shallow (<3m depth) eelgrass site according to the following equation:

$$\mathrm{LAI} = \frac{\mathrm{No.\,of\ Shoots} \times \mathrm{Average\ Leaf\ length\ (m)} \times \mathrm{Average\ Leaf\ Width\ (m)}}{\mathrm{Area\ (m^2)}} \qquad (2.1)$$

Six photographs were taken at each site; one of the quadrat at nadir, one in each cardinal direction, and one of three eelgrass shoots overlain on a white laminated card for estimation of epiphyte load as percent cover (Yakimishyn and Robinson, 2005).

In addition to spectrally separating eelgrass from other benthic covertypes, a goal of the study was to look for spectral differences between eelgrass sub-categories: Leaf Area Index (LAI), percent cover, and epiphyte type. While percent cover and epiphyte type could be visually determined from photographs taken during spectral acquisition, LAI required measurements of length, width and shoot density (Eq. 2.1). As time was restricted to the relatively short tide and sun angle window, it was not viable to measure eelgrass biometrics concurrent with spectral

acquisition. Instead, a photographic index for determining Leaf Area Index similar to Kutser (2007) was developed from the eelgrass survey. A total of 66 eelgrass photographs from the survey were paired with their respective LAI values. The photographs were then organized into low (LAI < 1, n=30), medium (LAI 1-2, n=29), and high (LAI > 2, n=7) LAI categories after Dierssen (2003) to form a photographic reference library. The eelgrass spectral acquisition sites could then be assigned an LAI value by visually comparing the field photos, taken concurrent with spectral acquisition, with the three LAI photo index categories.

Table 2.1. Benthic substrates present at the Sidney Spit study site and sample numbers for each. E = eelgrass, Ag = green algae, Ab = brown algae, S = sand, Asp = sea asparagus, dW = optically deep water, epi = epiphyte. d= deep, s = shallow, e = exposed.

Field photo	Common name	Latin name	Abbrv	Ground-truth sites (n)	Above-water spectra (n)	Endmember spectra (n)
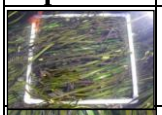	**Eelgrass (total)**	***Zostera marina***	**sE dE**	245 shallow 58 deep	20 shallow 4 deep	26
	**Eelgrass with no epiphyte**	-	**-**	26 shallow 9 deep	0 shallow 0 deep	10
	**Eelgrass with diatom epiphyte**	***Bacillari-ophyceae***	**-**	16 shallow 9 deep	16 shallow 0 deep	6 on eelgrass 6 epiphyte only
	**Eelgrass with red algae epiphyte**	***Smithora spp.***	**-**	20 shallow 9 deep	4 shallow 4 deep	10 on eelgrass 15 epiphyte only
	**Green algae: Sea Lettuce**	***Ulva fenestrata***	**sAg**	97 shallow 0 deep	6 shallow 0 deep	13
	**Green algae**: **Filamentous**	***Enteromorpha prolifera***	**sAg**	60 shallow 0 deep	2 shallow 0 deep	9
	**Brown Algae**	***Sargassum muticum & Fucus spp.***	**sAb**	6	0	6
	**Sea Asparagus**	***Salicornia sp.***	**eAsp**	8	0 (exposed)	1
	**Sand**	-	**sS dS**	55 shallow 31 deep	6 shallow 3 deep	12
	**Spectrally deep water (>30m)**	-	**dW**	-	7	-

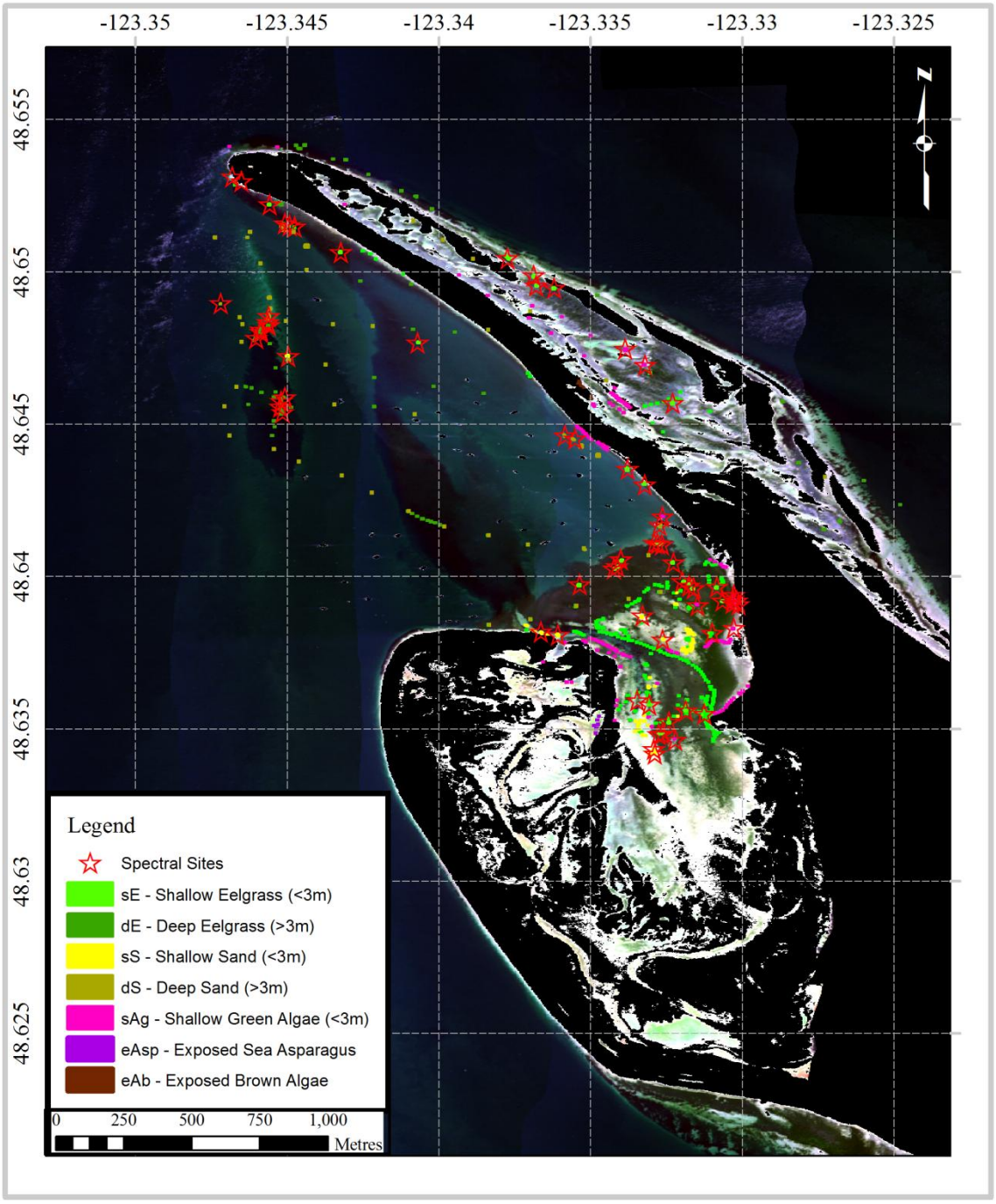

Figure 2.1. Location of ground-truth survey sites, and spectral acquisition sites at Sidney Spit.

Discrete water samples - acquisition and analysis

At 26 stations, triplicate water samples were collected from subsurface (0.5 m) water using 5 L Niskin bottles for analysis of total suspended matter (TSM), total organic carbon (TOC), coloured dissolved organic matter (CDOM), photosynthetic pigment chlorophyll-*a* (chl-a) concentration, and accessory pigment concentration. For TSM analysis, 1L of each water

sample was filtered through a pre-combusted and pre-weighed 0.7 µm Whatman GF/F filter. The filters were then dried at 60°C for 6 hour intervals until constant mass was reached. TSM was then calculated in mgL^{-1} (Clesceri *et al.*, 1998):

$$\text{TSM} = \text{Final mass} - \text{Initial mass} \tag{2.2}$$

TOC was determined by loss on ignition (LOI) methods, igniting the filters at 500°C for 1 hour intervals until constant mass was reached (Heiri, et el. 2001). TOC was then calculated as percentage of TSM:

$$(\text{Mass after combustion} - \text{Mass before combustion}) / \text{Mass before combustion} \times 100\% \tag{2.3}$$

CDOM was determined by filtering 1 L of each sample through a 0.2 µm Pall Supor® membrane disc filter. The filtrate was stored at -30°C in pre-rinsed (deionised water) and pre-combusted (450°C) amber bottles. Absorbance, $A(\lambda)$, of each sample was measured between 250 and 875 nm (Chen and Gardner, 2004; Kowalczuk *et al.* 2005) using a 10-cm quartz cuvette in an Ocean Optics S2000 single-beam spectrophotometer. Absorbance measurements were baseline-corrected by subtracting the mean $A(\lambda)$, between the interval of 650 and 700 nm where CDOM absorption is negligible. These values were then converted to absorption ($a_{CDOM}(\lambda)$, values using Beer-Lambert's Law (Kirk, 1994):

$$a_{CDOM}(\lambda) = 2.303 \cdot \left(\frac{A(\lambda)}{l}\right) \tag{2.4}$$

where l is the cuvette length in metres (0.01m). Absorption at 440nm ($a_{CDOM}(440nm)$) was reported as the proxy for CDOM concentration and deionised water was used as the reference standard.

For the determination of chl-a (a proxy for phytoplankton concentration) and nine accessory pigment concentrations (chl-b, chl-c2, chl-c3, β-carotene, Fucoxanthin Peridinin, Diadino, Alloxanthin, Zeaxanthin), 1L of each water sample was filtered through 0.7 µm Whatman GF/F filters and stored folded in Falcon tubes in the freezer at -80°C (Jeffrey *et al.*,

1997). Pigment concentrations were then determined by reverse-phase high-performance liquid chromatography (HPLC) with a Dionex Summit P680A HPLC (Arar, 1997). Certified pigment standards by Sigma-Aldrich Canada Inc. and DHI Water and Environment were used.

2.2.2 In situ spectra acquisition

Thirty eelgrass, 12 green algae, 9 sand, and 6 optically deep water sites were documented from a boat during spectral acquisition on August 14-18 and 31, 2008. The following data were collected at each of the field sites: (1) GPS location; (2) above water photos and underwater videography for substrate identification, density, and LAI estimation; (3) above-water hyperspectral measurements for deriving spectral variables; (4) in-water hyperspectral measurements for calculating diffuse downwelling attenuation coefficients, K_d, (5) depth and Secci depth; (6) wind speed to correct radiometric measurements for stray light added by the water surface; and (7) water samples to determine the water constituent composition: total suspended organic and inorganic material (TSS), coloured dissolved organic material (CDOM), and pigment composition.

In situ spectra measurements were conducted according to three strategies: above-water, pure spectral endmember, and in-water spectra as follows.

(1) Above-water in situ spectra

Above-water *in situ* radiance spectra (n=48) were measured over the four major substrates, eelgrass *Zostera marina*, green algae (*Ulva fenestrata* and filamentous algae), sand, and optically deep water (>30 metres). The number of ground-truth sites surveyed for each substrate is presented in *Table 2.1*. The majority of spectral measurement sites were over eelgrass beds, since eelgrass was the substrate of focus for this study. Spectra were collected over a range of (a) depth, from approximately 1.0 m to 6.0 m, (b) eelgrass stand density, from 0 - 624 shoots/m^2**,** and (c) epiphytic algae density and type (filamentous diatoms (n=16) and red algae *Smithora spp.*(n=8)).

Total water leaving radiance was measured 1m above the water surface using a Satlantic HyperSAS mounted on a tripod in the boat (Figure 2.2a) and total irradiance was measured with a Satlantic OCR-3000 sensor (Satlantic, 2003a,b) mounted on a dowel on the highest position of the boat (Figure 2.2b). Total water-leaving radiance ($L_T(\lambda)$, 40° from nadir), sky radiance

($L_{sky}(\lambda)$, 40° from zenith) and total irradiance ($E_S(\lambda)$, cosine collector at zenith, Figure 2.2b) were measured continuously (1 spectra every 2 seconds) for a period of 40 seconds, while effort was made to maintain L_T sensor viewing geometry at 90° to the sun to avoid specular reflection into the sensor (Mobley, 1999; Hooker *et al.,* 2004). The radiance sensors had a half-angle FOV of 3°, two-nanometre spectral resolution and a spectral range of 350 - 800nm. All measurements were made in clear weather with no precipitation, less than 20 percent cloud cover, low wind speeds (< 10 m s^{-1}), and solar zenith angle between 30° and 60° (Hooker *et al.,* 2004; Gordon, 2005; Wang 2006). Two stations were omitted due to erroneous radiance values caused by patchy overcast conditions and foam on the water surface.

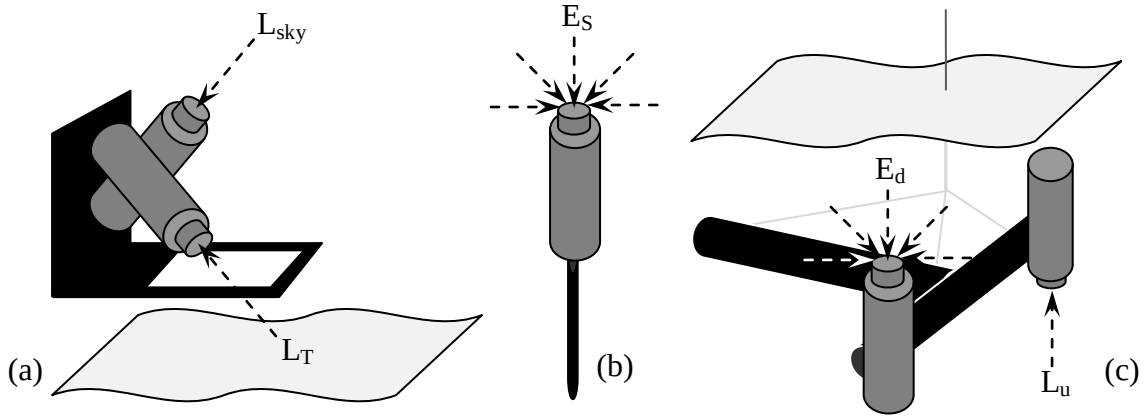

Figure 2.2 Radiometers used to acquire in situ field spectra above and below water from the boat. The HyperSAS LSsky and LT sensors (a) were mounted on a frame on a tripod viewing over the side of the boat, the ES cosine collector (b) was mounted vertically on a 2m dowel at the highest point on the boat, and the HyperPRO Ed profiler (c) was connected by a line to a downrigger mounted on the same side of the boat.

(2) Endmember in situ spectra

Endmember spectra were collected for all benthic substrates and transported in seawater in a cooler. Within thirty minutes of collection, three or more samples of each substrate were laid flat, four layers thick, on black canvas and measured with the HyperSAS radiometer (Figure 2.3). In the case of eelgrass, blades were measured before and after removing epiphytes with a soft brush. The freed epiphytes were also measured independently. Measurements were made at 31cm height with the same sensor-solar geometry configuration as the above-water spectra, and

samples were three times the diameter of the field of view to ensure that the canvas did not impact the spectra. Each sample was rearranged and measured three times and then averaged. These measurements represent the "pure" spectra of each cover type without the spectral influence of water optical constituents and adjacent/underlying substrates. It is important to note, however, that these endmember measurements do not preserve the natural geometry of *Zostera marina* or algae blades supported in the water column, as viewed by a remote sensing platform.

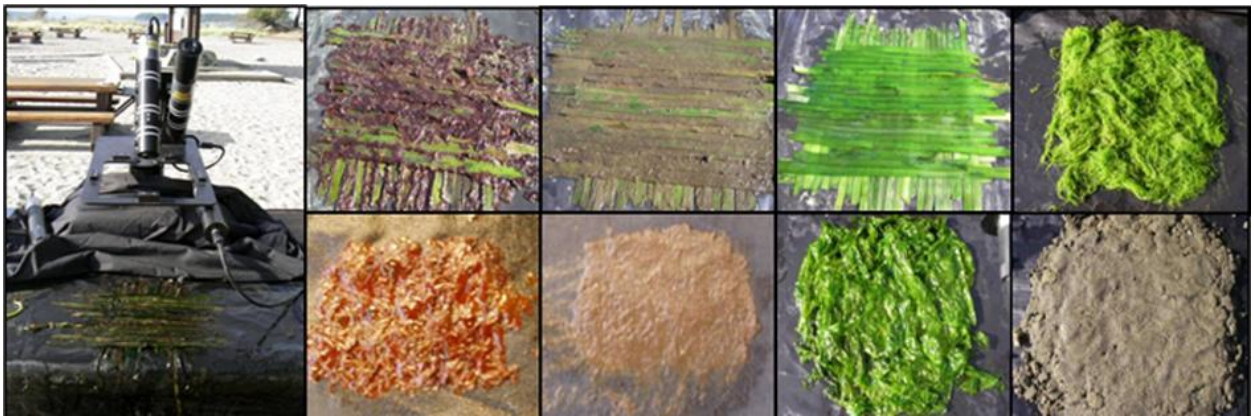

Figure 2.3 Acquisition of endmember, or "pure," spectra with the HyperSAS sensor. Substrates were placed four layers deep, in an area three times the diameter of the sensor field of view. Sensor height was 31cm for covertypes, and 10cm for epiphytes. Top row left to right: biofouled eelgrass Zostera marina with Smithora epiphyte; biofouled eelgrass with diatom epiphyte; non-biofouled eelgrass brushed clean of epiphytes; filamentous green algae. Bottom: Smithora epiphyte; diatom epiphyte; green algae Ulva fenestrata (sea lettuce); sand.

(3) In-water in situ spectral profiling

Under-water spectral measurements were taken at 25 of the sites using a Satlantic Hyperpro profiler with CTD lowered through the water column with a boat-mounted downrigger (Figure 2.2c). The profiler acquired down-welling irradiance ($E_d(\lambda)$, cosine collector) at two-nanometre spectral resolution with a spectral range of 300 - 800nm, every 0.1m depth, while the E_s cosine collector simultaneously acquired downwelling irradiance above the water (Figure 2.2b). $E_d(\lambda)$ spectra were used to derive the diffuse downwelling attenuation coefficient, K_d, (Eq. 2.14), which is required for the water column correction method (Maritorena et al., 1994) applied to the *in situ* above-water spectra, and for determining the depth limit of spectral detection of eelgrass (Dekker et al., 2005).

2.2. Spectra Processing

Above-water Spectra - glint correction and radiance to reflectance conversion

Spectra were acquired at a rate of one spectrum every two seconds over an interval of approximately 40 seconds, for a total sample size of n=20 per site. To remove possible sun glint outliers from the above-water spectral measurements, L_T spectra containing values exceeding 1.5 standard deviations from the mean spectrum of the site were removed from the dataset (Hooker *et al.*, 2002). The remaining radiance measurements were converted to above-water remote sensing reflectance ($R_{rs}(\lambda)$) according to Eq. (2.5), (2.6), and (2.7) (Ruddick *et al*., 2006*)* based on modified Fresnel reflectance glint correction algorithm S95, which removed any remaining sky-glint and standardized for variability in solar angle, irradiance, and sea surface state among measurements (Mobley, 1999; Hooker, 2002). All remaining remote sensing reflectance spectra from the acquisition interval were then averaged. Note that for the remainder of the text, the wavelength symbol (λ) will be omitted from all spectral terms for simplicity. However, all spectral quantities are wavelength dependent unless otherwise stated.

$$R_{rs}^{(0+)}(\lambda) = \left(L_T(\lambda) - \rho' \cdot L_{sky}(\lambda)\right) / E_S(\lambda) \quad (2.5)$$

$$\rho' = 0.0256 + 0.00039W + 0.000034W^2, \text{ when } L_{sky}(750) / E_S(750) < 0.05 \quad (2.6)$$

$$\rho' = 0.0256, \text{ when } L_s(750) / E_S(750) \geq 0.05 \quad (2.7)$$

where ρ' is the proportionality factor relating the amount of sky radiance reflected off of the sea surface to the total sky radiance, and is dependent on wavelength (λ), wind speed (W), and the proportion of cloud cover present in the sky radiance distribution as defined by the ratio $L_s(750)/E_S(750)$, which represent sky radiance and radiance at 750 nm respectively. When sky conditions are clear ($L_{sky}(750)/E_S(750) < 0.05$), ρ' varies with wind-generated surface roughness, which increases reflections off of the water surfaces. Under cloudy conditions, ρ' is independent of wind speed because the diffuse light limits glint (Mobley 1999, Ruddick *et al.*, 2006).

Every spectrum has a slightly different ρ' value, which can only be estimated through modelling and not known with certainty, and therefore a vertical offset error was inherent in each spectra. To correct this error, each spectrum was offset by a constant value equal to its mean

reflectance value from 750-800nm, which standardized each spectrum to a NIR value of zero in this range. The validity of this method was verified by simulating a case 1 IOP model in Hydrolight (Mobley & Sundman, 2000a,b) with chl = 2.1 µg/L and average ooid sand bottom at 0.5 m depth (personal communications Mobley, 2009). The calculated NIR reflectance values were zero beyond 750nm. Further, all *in situ* spectra were cropped below 400nm to avoid low signal-to-noise data (Cho et al, 2008) and match the calibrated range of imagery to which the results of this study will be further applied.

Above-water Spectra – water column removal

The Maritorena et al. (1994) water attenuation correction was applied to the HyperSAS above water remote sensing reflectance, $R_{rs}^{(0+)}(\lambda)$, by first converting it to reflectance just below the water surface, $R_{rs}^{(0-)}(\lambda)$ (Lee et al., 2002):

$$R_{rs}^{(0-)} = \frac{R_{rs}^{(0+)}}{0.52 + [1.7 \cdot R_{rs}^{(0+)}]} \tag{2.8}$$

then following Brando et al. (2009), solving for the reflectance of the substrate at depth 0, i.e., water attenuation corrected substrate spectra, R_{rs}^{b}, (Eq. 2.10) in Maritorena's (1994) equation (Eq. 2.9),

$$R_{rs}^{(0-)} = R_{rs}^{dp(0-)} + \left(R_{rs}^{b} - R_{rs}^{dp(0-)}\right) \cdot e^{-2K_d z} \tag{2.9}$$

$$R_{rs}^{b} = \frac{R_{rs}^{(0-)} - R_{rs}^{dp(0-)} \cdot (1 + e^{-2K_d z})}{e^{-2K_d z}} \tag{2.10}$$

where z is the substrate depth, K_d is the diffuse downwelling attenuation coefficient of the water, and $R_{rs}^{dp(0-)}$ is the reflectance of optically deep water (>30m depth). The efficacy of the water column correction was assessed by comparing the resulting spectra to measured endmember spectra of the same benthic class.

The depth limit for this correction was assumed to be the same as the average depth at which eelgrass can no longer be discernable from deep water (i.e. becomes optically "deep"). Following Dekker *et al* (2005), the detectability threshold of a given submerged substrate occurs

when the second term of Maritorena's equation (Eq. 2.9) equals the detecting threshold of the sensor in reflectance terms (R_{rs}^{DT}), as expressed below:

$$\left[R_{rs}^{b} - R_{rs}^{dp(0-)}\right] \cdot e^{-2K_d z} = R_{rs}^{DT} \tag{2.11}$$

R_{rs}^{DT} is defined as the wavelength-dependent standard deviation of a homogeneous *in situ* reflectance measurement of optically deep water. The detectability depth limit of each substrate was computed by solving for z in *Equation 2.8*:

$$z = \frac{1}{2K_d} \cdot \ln\left[\frac{R_{rs}^{b} - R_{rs}^{dp}}{R_{rs}^{DT} - R_{rs}^{dp}}\right] \tag{2.12}$$

Beyond this depth, the substrate is no longer discernable from deep water

Endmember spectra processing

No sun-glint and NIR correction were necessary for endmember spectra as they were not submerged. The measured radiance spectra were converted to reflectance as follows:

$$R_{rs} = L_T / E_S \tag{2.13}$$

In-water spectra processing and diffuse attenuation coefficient caclulation

Initially, the E_d profiles were checked for tilt and the E_s measurements were checked to ensure low variability during the acquisition interval. E_d and E_s measurements were then synchronized for time. The water attenuation coefficients, K_d, were calculated for each site according to Kirk (1994):

$$K_{d(\lambda)} = \frac{-1}{z} \cdot \ln\left[\frac{E_d \cdot z_{2(\lambda)})}{E_d \cdot z_{1(\lambda)})}\right] \tag{2.14}$$

where E_d is downwelling irradiance, z_2 is 1.5m depth, and z_1 is 1.0m depth measured with the HyperPro profiling optical sensor. Calculating a general vertical downwelling attenuation for the entire column assumes a uniform water column in regard to inherent optical properties (Werdell and Roesler, 2003; Conger et al., 2006). *In situ* temperature and salinity profiles were checked to ensure no water stratification was present at the time of image acquisition, this indicating homogeneous distribution of water attenuators (Kirk, 2003). The 1.0 to 1.5 m interval was the shallowest measurement common to all profiles in the dataset, and was used to standardize the

K_d calculation across all sites. Water properties were assumed to be constant throughout the study site as K_d spectra had low variance throughout all sample sites (Further discussion in *Chapter 3*).

2.3 Remote Imagery

Three remote sensors were used in this study: high spatial resolution airborne hyperspectral sensor AISA, high spatial resolution satellite multispectral sensors IKONOS and medium spectral resolution multispectral satellite sensor Landsat ETM+. The following section provides a description of each.

AISA

AISA is a hyperspectral sensor system that can be installed in small aircrafts. The sensor used in this study was the AisaDUAL system, which has a spectral range of 400 – 2500 nm, spectral resolution of 2.13nm (498 bands) (Spectral Imaging, 2008). Swath width and spatial resolution are variable depending on the flight elevation, but spatial resolution can be achieved as fine as 1m x 1m. Imagery was acquired at 2m x 2m spatial resolution for this study because the study site's close proximity to an airport restricted long periods of flight below 1500 metres altitude.

IKONOS

IKONOS is a commercial satellite fitted with a high spatial resolution multispectral optical sensor. It was launched on September 24, 1999 and has available imagery dating back to January 1, 2000. Since it is sun-synchronous, each overpass occurs at relatively the same time every three to five days (10:30am local time) (GeoEye, 2006). IKONOS collects data in three visible and one NIR band (Table 2.2) at 4-metre spatial resolution with an 11km x 11km swath, or scene, width. The band specifications are outlined in Table 2.2 and the relative spectral responsivity at each wavelength is depicted in Figure 2.4. From the relative spectral responsivity, the sensor's bandwidths and centres can be visualized. Additionally, the relative spectral responsivity factors of IKONOS are required as weighting factors when convolving hyperspectral *in situ* data into a simulation of IKONOS measurements (described in Chapter 3).

Landsat ETM+

The Landsat Enhanced Thematic Mapper Plus (Landsat 7ETM+) is a medium spatial resolution multispectral sensor carried onboard the Landsat 7 satellite, which is jointly managed by NASA and the U.S. Geological Survey. It was launched July 1999 and has a 16-day repeat cycle. Landsat 7ETM+ acquires data in three visible and one NIR spectral band (Table 2.2) at 30-metre spatial resolution with an 11km x 11km swath, and 170 km north-south by 183 km east-west scene size (USGS 2010). The relative spectral responsivity at each wavelength is depicted in Figure 2.4.

Table 2.2 Spectral and spatial specifications of IKONOS and Landsat ETM+ satellite sensors (Modified from GeoEye, 2006).

IKONOS Band	Wavelength Range (nm)	Band Centre (nm)	Spatial Resolution	LANDSAT ETM+ Band	Wavelength Range (nm)	Band Centre (nm)	Spatial Resolution
1 (blue)	445 - 516	480	4m	1 (blue)	450-520	479	30m
2 (green)	506 - 595	550	4m	2 (green)	530-610	561	30m
3 (red)	632 - 698	665	4m	3 (red)	630-690	661	30m
4 (NIR)	757 - 853	805	4m	4 (NIR)	780-900	834	30m

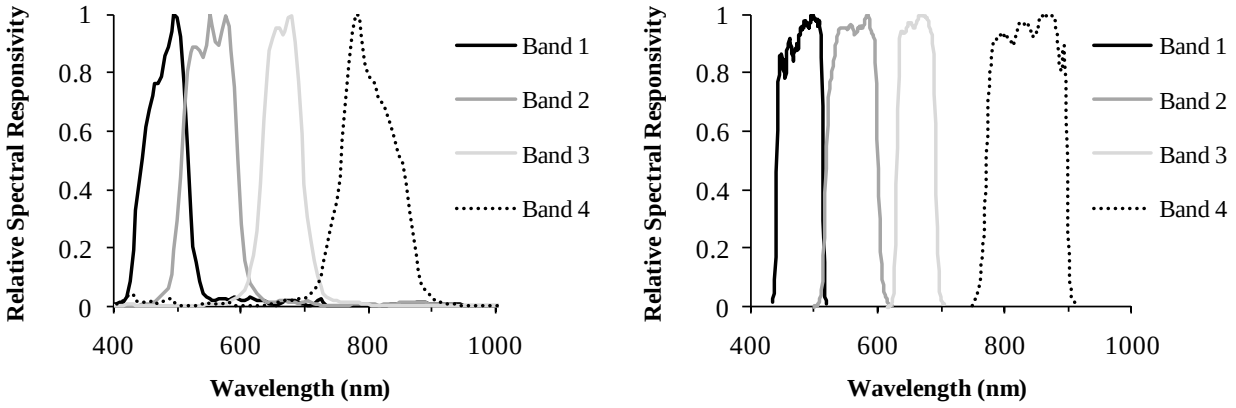

Figure 2.4 Relative spectral responsivity for the visible and NIR bands of (a) IKONOS and (b) Landsat ETM+. The radiance measured at a specific band (e.g., blue band) is a weighted average of the radiance at each wavelength in the bandwidth, where the weight is the relative responsivity value (y-axis) (Modified from GeoEye, 2008 and NASA 2009 respectively).

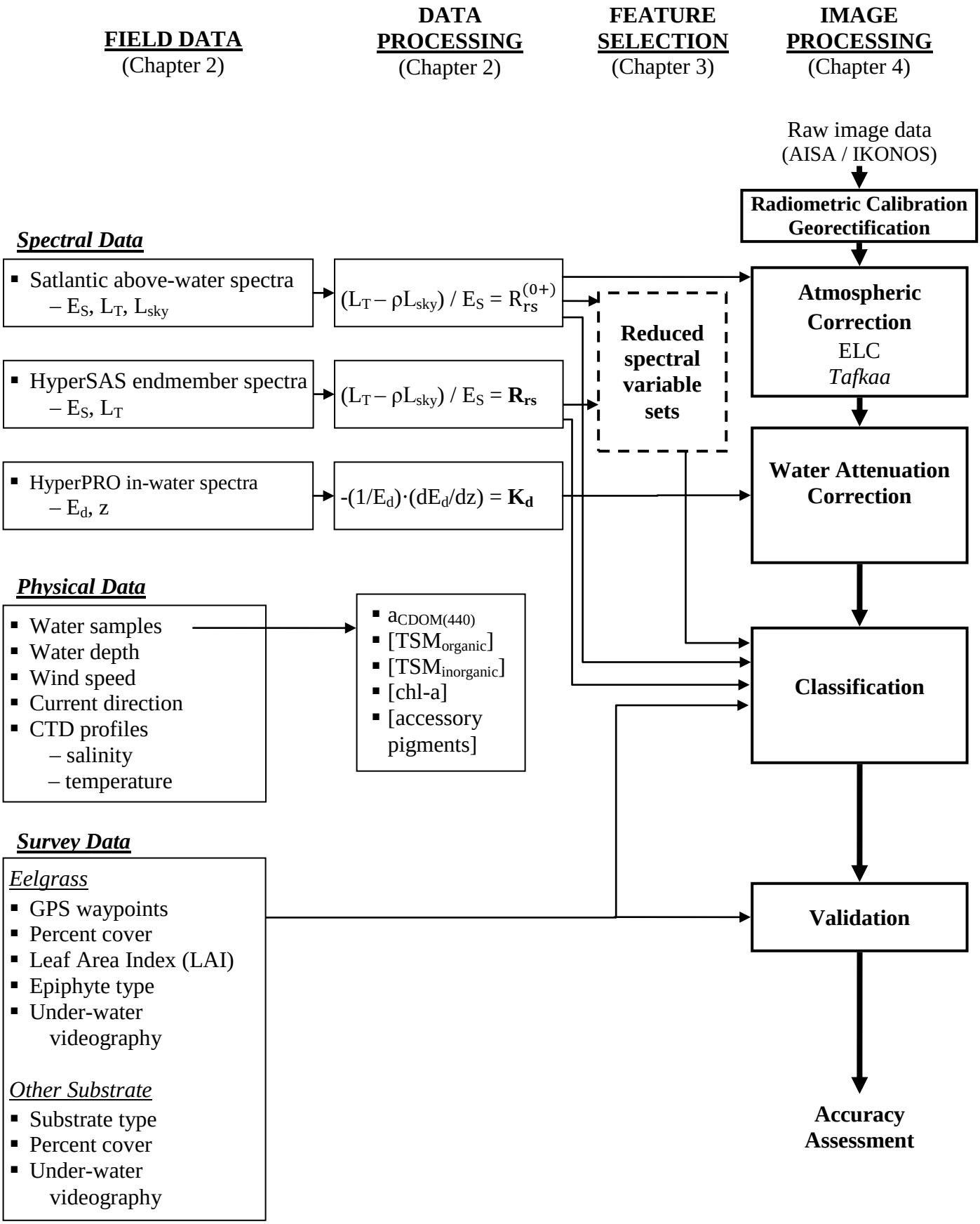

Figure 2.5 Overview of field data acquisition and data processing steps described in Chapter 2, and where each of these components is applied in the remainder of the study.

Chapter 3

Variable reduction of *in situ* hyperspectral measurements over shallow coastal benthic substrates for use in remote mapping of eelgrass (*Zostera marina*)

Abstract

Eelgrass (*Zostera marina*) is a keystone component of, and effective sentinel for environmental change within, inter- and sub-tidal ecosystems. Despite its ecological and conservation value, it has exhibited worldwide population decline in response to anthropogenic pressures. Eelgrass delineation and continuous monitoring is therefore an integral part of coastal ecosystem management. A proposed tool for this purpose is remote imagery, which can cost- and time- effectively cover large and inaccessible areas frequently. However, to effectively apply this technology, an understanding is required of the spectral behaviour of target substrates. In this study, *in situ* hyperspectral measurements were used to define key spectral variables that provide the greatest spectral separation between *Zostera marina* and associated shallow submerged substrates. The effectiveness and depth constraint of eelgrass classification using these variables was assessed. For eelgrass classification of an above water reflectance dataset, the selected variables were: slope500-530nm, first derivatives (R') at 566nm, 580nm, and 602nm, yielding 98% total accuracy. For classification of a water column corrected dataset, the selected variables were ratios 566:600nm and 566:710nm, yielding 97% total accuracy. The potential of using satellite data for eelgrass classification was evaluated by simulating IKONOS and Landsat ETM+ reflectance. The selected variables were blue, green, blue:red, and green:red for both, yielding 92% and 94% total eelgrass classification accuracy, respectively. The depth constraint for eelgrass identification with the field spectrometer was found to be five to six metres on average, with a range of three to 15 metres depending on the characteristics of the water column.

3.1 Introduction

Eelgrass (*Zostera marina*) is an important component of inter- and sub-tidal ecosystems and is widely recognized for its ecological and conservation value (Hemming and Duarte, 2000; Jackson et al., 2001). First, it provides physical stability by anchoring sediment (Mateo et al., 2003) and baffling the shoreline against wave and current action (Fonseca and Cahalan, 1992).

Second, it mediates biochemical balance by oxygenating water and pore water (Hemminga & Duarte, 2000) and determines the balance of carbon, nitrogen and phosphorous within the ecosystem and beyond (Hemminga & Duarte, 2000; Apostolaki, 2010). Eelgrass may be responsible for up to 15% of the total organic carbon stored in marine ecosystems (Duarte and Chiscano 1999) and not just in its immediate vicinity; far-ranging ecosystem links are established by burial of this carbon in sediments and exportation to neighbouring ecosystems. Third, eelgrass provides a fundamental nursery ground and food source for many marine organisms (Phillips, 1984; Thistle et al., 2010). Many species find refuge within the beds, including complex macroinvertebrate assemblages and several species of commercially important fish, such as out migrating juvenile salmon (*Onchorhynchus* spp.) and Pacific herring (*Clupea harengus*) (Mazzella et al., 1989; Sewell *et al.*, 2001, Borg et al., 2006). The diets of fish utilizing eelgrass beds have been found to be 56% (by weight) comprised of sources within the beds (Adams, 1976) and historical fish abundance has been linked to eelgrass presence (Phillips, 1984; Murphy et al., 2000; Johnson et al., 2010). Accordingly, eelgrass has been identified as a detrimentally important resource to sustainable commercial fisheries (Adams, 1976). Its keystone importance and fast responsiveness to changes in water quality have established it worldwide as an early harbinger of environmental change and indicator of coastal ecosystem health (Sewell *et al.*, 2001).

Eelgrass populations have experienced worldwide decline. An estimated 2–5% of seagrass ecosystems are lost annually due to anthropogenic pressures (Duarte et al., 2002). The loss has been attributed to two major forces: (1) the direct pressures of a growing coastal human population such as shoreline development (Duarte, 2002; Burkholder et al., 2007) and vessel anchoring; and (2) the light shading pressures of sedimentation, nutrient loading, and eutrophication (Burkholder et al., 2007) caused by intense aquaculture (Holmer et al., 2008), fish farming (Marba et al., 2006; Diaz-Almela et al., 2008; Apostolaki et al., 2009), upland development and agriculture (Short & Wyllie-Echeverria, 1996), and increased pollution levels (Nienhius, 1983; Giesen *et al,* 1990; Dejong & Dejong, 1992; den Hartog, 1994), which diminish the available photosynthetically active radiation (Moore and Wetzel, 2000; Zimmerman, 2003). Further eelgrass loss is predicted in response to climate change (Duarte, 2002; Najjar et al., 2010).

Eelgrass loss is projected to accelerate as human pressure on the coastal zone grows (Duarte, 2002). Baseline knowledge and continued monitoring of temporal-spatial eelgrass distribution is exceedingly important in mitigating additional loss, as it allows separation of anthropogenic disturbances from natural trends and identification of suitable areas for protection and rehabilitation (Duarte, 2002; Dekker *et al.,* 2005; Ferwarda et al., 2007). Mapping of eelgrass and associated substrate has traditionally been accomplished by boat- and land-based surveys, which are limited by accessibility, time, and cost (Ackleson and Klemas, 1987; Dekker *et al.,* 2005). A proposed alternative method is remote imagery, which can cost- and time-effectively cover large and inaccessible areas nearly instantly and frequently (Chavez, 1996; Dekker *et al.,* 2005). However, the effective application of this technology requires a firm understanding of the spectral behaviour of eelgrass and associated substrates. Submerged eelgrass can only be detected by a remote sensor if (1) eelgrass spectral properties are distinct from those of surrounding cover types (sand, macroalgae, epiphytes, detritus, etc.); (2) the unique spectral characteristics can be separated from the spectral influence of the atmosphere and water column; (3) the spectral resolution of the sensor is adequate to resolve the unique spectral characteristics; and (4) the spatial resolution of the sensor is adequate to capture the spatial patterns (i.e. patchiness) of the eelgrass meadow (Hedley & Mumby, 2003).

The success of requirement (1) can be influenced by the properties of water column. With increasing depth eelgrass and surrounding substrate become less spectrally separable, as the optical properties of the water column constituents begin to dominate the signal (Dekker et al., 2006; Ferwerda et al., 2007). The degree of this dominance is wavelength and constituent dependent. In coastal, Case 2, waters, three major optical constituents cause wavelength independent attenuation of light: chromophoric dissolved organic material (CDOM), phytoplankton photosynthetic pigment chlorophyll-*a (*Chl-*a),* and total suspended matter (TSM), which can be separated in organic and inorganic fractions. CDOM and chl-a reduce the reflectance signal; CDOM markedly absorbs light in the blue wavelengths and chl-a has major absorption peaks in both the blue and red wavelengths. TSS increases the reflectance signal in the red region and causes a green peak shift to longer wavelengths (Kirk, 1994; Mobley, 1994). The attenuation caused by each of these water constituents acts additively to diminish available light with increasing depth, particularly in the photosynthetically active portions of the spectrum.

The success of requirement (1) can also be affected by epiphytic loading, which can

remarkably change the reflectance of eelgrass. Studies have shown that heavy epiphyte loads can absorb up to 63% of incident light in the peak chlorophyll absorption bands leading to greater reflectance slopes at 440nm and 680nm then at 550nm (Drake et al., 2003). Reflectance in the 575 – 630nm region is markedly increased (Fyfe, 2003) while green light is physically blocked by non-photosynthetic material accumulation (Drake et al., 2003) and absorbed by non-chlorophyte epiphytes (Mazzella and Alberte, 1986). These affects additively lead to flattening of the eelgrass spectra and increased variability in green reflectance values (Werdell and Roesler, 2003; Fyfe, 2003). Further, two unique features are produced by epiphyte chlorophyll-*a* and -*c;* a reflectance peak at 590nm (Fyfe, 2003) and a small absorption feature at 632nm (Meleder et al., 2003; Murphy *et al.*, 2005).

The characteristics of the remote sensor have an additional impact on the detectability of eelgrass, as higher spatial and spectral resolution offer greater discernable spatial and spectral detail and a greater understanding of the key optical differences among covertypes. Greater resolution however, comes with the expense of processing time as it introduces very large data volumes and high data redundancy. Data reduction methods can be used to address volume and redundancy issues, decreasing processing time and increasing classification accuracy by removing unnecessary information and retaining only spectral variables offering the greatest spectral distinction among cover classes (Richards & Jia, 2005).

In this light, the goal of this study was to explore the feasibility of using spectral data from three remote sensors, *in situ* hyperspectral HyperSAS, IKONOS, and Landsat ETM+, to classify eelgrass distribution at Sidney Spit, GINPRC. The questions asked of each dataset were:

1. *Can submerged eelgrass be spectrally distinguished from other submerged substrates?*
2. *If so, what spectral bands and/or band "indices" (slopes and ratios) offer the best separation between substrates with the least redundancy? Statistical data reduction methods were used to identify a band set of key wavelengths and/or wavelength indices.*
3. *Using the selected set of indices, how accurate is the eelgrass classification produced by each sensor?*
4. *Can differences in eelgrass density and epiphyte types be detected? What are the major indices?*
5. *What is the maximum depth at which the sensor can detect eelgrass?*

To address these questions, IKONOS and Landsat ETM+ data were simulated based on measured *in situ* hyperspectral reflectance.

3.2 Methods

Field work was conducted in July and August 2008 to gather information about eelgrass distribution, water optical constituents, and *in situ* spectral data. Details of each procedure can be found in *Chapter 2*, as indicated below.

3.2.1 *In situ* data collection

Ground-truthing, *in situ* spectra acquisition, eelgrass categorization, and water constituent analysis are found in *Chapter 2, Section 2.2.1*.

3.2.2. *In situ* spectra processing

Above-water spectra, endmember spectra, and in-water spectra processing methods are in *Chapter 2, Section 2.2.2.* This includes radiance to reflectance conversion for all spectra; glint correction and water column removal on above-water spectra; and diffuse attenuation coefficient (K_d) derivation from in-water spectra.

3.2.3 Data Reduction and variable selection

Calculating Indices

The substrates were grouped into six classes, defined by substrate type and depth. The defined classes were optically deep water (>30m), deep sand and deep eelgrass (>3m); shallow sand, shallow eelgrass and shallow green algae (<3m). No green algae sites could be found deeper than three metres and hence representative spectra are absent from this study.

Shallow/deep stratification was defined at 3 m because preliminary analysis of the *in situ* spectra for each substrate showed noticeable reflectance magnitude differences beyond this depth, particularly in the 700 - 750nm region. This threshold is also in agreement with previous *in situ* measurements and radiative transfer models (Roelfsema *et al.*, 2006) as well as image analyses (Brando & Dekker, 2003; Phinn *et al.*, 2005; Phinn et al., 2008), which found seagrass species and broad cover classes to be inseparable deeper than three metres. Stratifying submersed

coastal classification into separate depth ranges has been shown to benefit the classification process by ensuring that dense shallow beds of eelgrass are not confused with sparse deep beds (Phinn *et al.,* 2005).

Three consecutive methods were adopted for defining major spectral features in the HypersSAS measured *in situ* spectra with the purpose of separating the different substrates. First, visual inspection of spectra was used to form a preliminary list of reflectance peaks and valleys that appeared capable of separating eelgrass from other substrates. Second, the first derivative curve for each spectral curve was calculated (*Eq 3.1*) to establish the exact location where the major features occurred. The first derivative is defined as follows:

$$R_{rs}^{(0+)'} = (R_{rs}^{(0+)}{}_{n+1} - R_{rs}^{(0+)}{}_{n}) / (\lambda_{n+1} - \lambda_{n}) \qquad (3.1)$$

where $R_{re}^{(0+)'}$ = above-water remote sensing reflectance first derivative (line segment slope), denoted R' from here on in the text, n = band number, and λ = wavelength in nm (Becker *et al.*, 2005). The mean and the 95% confidence interval of each key feature location were calculated for each cover class and compared between cover classes (Figure 3.4). If a peak or valley location of a specific covertype did not overlap with that of any other covertype, it was considered unique to that covertype.

It has been observed that while the spectral measurements of a single substrate can be variable in reflectance magnitude, spectral shape is typically retained (Vahtmae et al., 2006). Therefore, the third step incorporated spectral shape by calculating the ratios and slopes (denoted *λ: λ and s λ- λ* respectively and here forth termed "indices") between absorption and reflectance features from the first derivative analysis. The results were compiled into a list of 23 indices (Table 3.3a). Fourteen common vegetation indices and two literature documented first derivative values were also calculated and added to the list (Table 3.3b&c) along with the first derivative values at each wavelength.

Statistical analyses: M-statistic and multiple discriminant analysis

Due to the high volume of data it produces, hyperspectral measurement provides detailed information but also contains high redundancy and yields long data processing times. Furthermore, classical discriminant analysis (further in text) is valid only if there are less than n-

1 bands in the band set (where n = number of training samples) (Bandos et al., 2009). Since the original spectra, first derivative spectra, and indices total over 350 available variables, a dataset reduction was necessary. A two step reduction approach was used: M-statistic and multiple discriminant analysis (MDA).

In the first step of spectral data reduction, all cases of eelgrass-other substrate class pairing were defined (i.e. Eelgrass-sand, eelgrass-green algae, etc.). The M-statistic (*Eq 3.2*) was then calculated at every band and index (together termed variables) for each eelgrass-substrate pairing case, retaining only those variables with the highest M-statistic values (i.e. the greatest separation between a pair of covertypes). These retained variables were termed "Set 1" *(Figure 3.4)* and the number of variables contained in each Set 1 depended on the substrate pair case. The M-statistic is a measure of class separability. It normalizes the difference between the means of two benthic classes ($\mu_{1(\lambda)} - \mu_{2(\lambda)}$) by the sum of their standard deviations ($\sigma_{1(\lambda)} + \sigma_{2(\lambda)}$) at the specified variable, as follows (Kaufman and Remer, 1994):

$$M_{(\lambda)} = \frac{\mu_{1(\lambda)} - \mu_{2(\lambda)}}{\sigma_{1(\lambda)} + \sigma_{2(\lambda)}} \tag{3.2}$$

A large M-statistic indicates good separation between the two classes as within-class variance is minimized and between-class variance maximized. Following Kaufman and Remer (1994), M > 1.0 indicates good class separation and M < 1.0 indicates poor separation. Since the M-statistic assesses separability for each benthic class pair independently, it offers the beneficial option of focusing only on pairs involving eelgrass. Selecting variables that are important solely to eelgrass classification ensured that in the next reduction step, the multiple discriminant analysis (MDA) did not compromise eelgrass classification accuracy for the classification accuracy of other substrates.

In the second step, a MDA with stepwise variable selection was run on the Set 1 variables to eliminate remaining redundancy, selecting the model with the minimum number of variables and maximum discriminating ability (Fisher, 1936; Bandos et al., 2009). This new reduced set of variables is termed "Set 2." A Set 2 was derived through MDA for each of the following cases:

Table 3.1 Cases for which data reduction was performed.

	Case name	Data Set		Depth		Class type	No. of classes
		$R_{rs}^{(0+)}$	R_{rs}^{b}	< 3m	> 3m		
1	Above-water shallow	■		■		substrate	3
2	Above-water deep	■			■	substrate	3
3	Above-water all depths	■		■	■	substrate	6
4	Above-water % cover	■		■		% cover	2
5	Above-water LAI	■		■		LAI	3
6	Above-water epiphyte	■		■		epiphyte type	2
7	Water-corrected model		■	■	■	substrate	6
8	Water-corrected % cover		■	■		% cover	2
9	Water-corrected LAI		■	■		LAI	3
10	Water-corrected epiphyte		■	■		epiphyte type	2

The potential classification accuracy of each Set 2 was evaluated with a test classification, where its MDA model equations were applied to the dataset. Rather than separating the dataset into training and testing data, leave one out cross-validation (LOO-CV) was used, whereby each case was classified using a discriminant function derived from all cases except the given case. This maximized the number of samples in both the test (n) and training (n-1) sets while eliminating bias in the classification accuracy value (Efron, 1981). Because substrate sample sizes were unequal, prior probabilities of class membership were assigned based on sample sizes, i.e., a greater probability of belonging to a larger class size. All models and classification tests were run with 500 bootstrap samples stratified by substrate at a confidence level of 95%.

3.2.4 IKONOS and Landsat 7ETM+ Simulation

For further understanding of the possible results attainable from imagery based classification, the spectral responses of IKONOS and Landsat ETM+ were simulated from the hyperspectral *in situ* SAS spectra using their relative spectral response (RSR) coefficients (GeoEye, 2008; USGS, 2008). The simulation was limited to bands 1 through 3 due to the 350-

797 nm spectral range of the HyperSAS field instrument. With the three possible band ratios (480:550, 550:665, 480:665) a total of six variables were analysed by stepwise MDA.

3.3 Results

3.3.1 Characterization of water optical constituents and light attenuation

Lab analysis results for the *in situ* water constituent distribution are summarized in Table 3.2. Appendices B - D shows all of the results in detail. Mean salinity and temperature at Sidney Spit were 11.5°C and 29ppt (Figure 3.1), which were comparable with Robinson and Yakimishyn's (2005) measurements of ~13.5°C and ~29ppt around the same time of year.

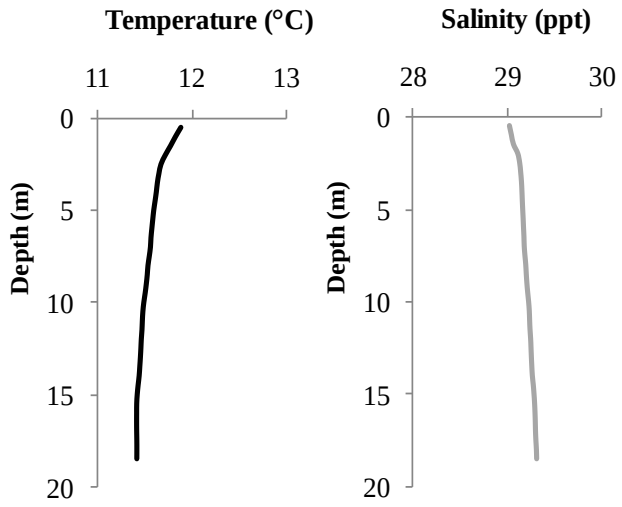

Figure 3.1 Mean temperature and salinity profiles during field acquisition.

The measured chl-a range of 1.28 – 7.23 µg m^{-3} was in agreement with mid-July surface measurements made by Robinson & Yakimishyn (2005) at Sidney Spit (1.66 µg m^{-3}) and Komick et al. (2009) in the central, most oceanic, portions of the Strait of Georgia in late July (1.55 - 6.48 µg m^{-3}). CDOM (0.18 – 0.33 m^{-1}) and TSS (2.25 – 6.08 g m^{-3}) were also in agreement with Komick et al. (2009) (0.22 – 0.48 m^{-1} and 1.76 - 3.47 g m^{-3} respectively) although our TSS had greater variability. As expected, the organic fraction comprised nearly half (average 47.6%) of the total suspended matter at this site due to organic detritus produced by the eelgrass beds. Higher TSS values were

typically found closer to shore, while CDOM and chl-a did not appear to follow a clear spatial pattern (see Appendix E for spatial distribution maps).

The average pigment distribution is shown in Figure 3.2. The most prevalent pigment was chlorophyll-*a*, followed by fucoxanthin, and then chlorophyll-*c*, a pigment composition characteristic of diatom species (Rowan, 1989). Peridinin and diadino, marker pigments of dinoflagellates, were present in varying amounts, with typically higher concentrations in more open, deep waters and as little to none in the shallow lagoon. Some areas of the lagoon however had noteworthy levels of alloxanthin, a marker for Cryptophyceae (Antajan and Gasparini, 2004). Chl-a concentrations Strait of Georgia region are known to vary from <1 mg m^{-3} in the winter to 10 to 50 mg m^{-3} in the early spring phytoplankton bloom (Li et al. 2000).

The relative magnitude of the diffuse downwelling attenuation coefficients, K_d *(Figure 3.3)*, is related to the distribution of water constituents. The characteristic blue absorption by CDOM, blue and red absorption by chlorophyll and red reflectance by TSS (Liedtk et al., 1995) cause higher K_d values in these ranges. Water attenuates NIR exponentially, resulting in rapid K_d increase beyond 710nm. The lowest K_d values occur between 500 – 600 nm because of lower attenuation by pigments and water constituents in these wavelengths. K_d had slight spatial variation, but with no discernible pattern, i.e. K_d was not significantly different between near shore and deep water sites.

Table 3.2. Water optical constituents profile for Sidney Spit, GINPRC, field sites.

	Average	**Range**
$a_{CDOM}(440)$	0.24 m^{-1}	0.18 - 0.33 m^{-1}
TSM	4.03 g m^{-3}	2.25 - 6.08 g m^{-3}
TOC	47.60%	32.7 - 65.3%
chl-*a*	2.44 mg m^{-1}	1.28 - 7.23 mg m^{-1}
$K_d(440)$	0.59	0.15 - 1.22
$K_d(550)$	0.42	0.04 – 1.09
$K_d(650)$	0.71	0.19 – 1.48

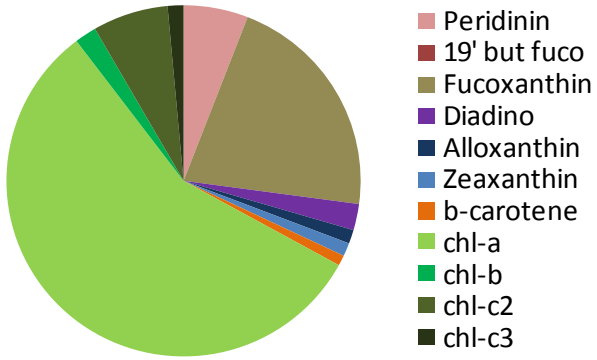

Figure 3.2 Average pigment profile as measured by HPLC methods, in percent of total.

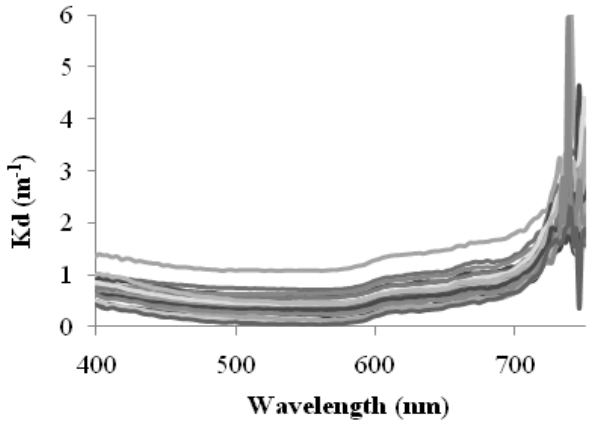

Figure 3.3 Kd spectra derived from E_u and E_d in-water profiles at various sites around Sidney Spit, GINPRC, over six days, August 14-18 and 31, 2008.

3.3.2 Spectral characteristics of the benthic substrates

Eelgrass and its associated substrates were spectrally distinct and the spectral shapes and relative magnitudes were in agreement with the *in situ* measurements of other studies for both above-water measurements (Call et al., 2003; Dierssen et al., 2003; Kutser et al., 2006; Vahtmae et al., 2006) and pure endmember measurements (Maritorena et al., 1994; Andréfouët et al., 2004; Fyfe, 2003; Hochberg & Atkinson, 2003; Louchard et al., 2003; Dekker et al., 2005; Thorhaug et al., 2007). The signal reaching the sensor is a combination of all matter the light has interacted with. Accordingly, the characteristic attenuation features of the water column and constituents were found in all measured spectra, and were most exaggerated in deeper waters. Generally, characteristic blue absorption (400-500nm) by CDOM and blue and red absorption by

phytoplankton chlorophyll decreased reflectance in this part of the spectrum, and fluorescence caused a reflectance peak at 685nm (Maritorena et al., 2000). TSS caused red reflectance that was evident in the masking of various benthic red absorption features as depth increased. The characteristic water absorption features appeared at 520nm, 570-600nm and 700-760nm (Morel, 2007).

The most marked differences among benthic classes occurred in the green spectral range between 500-600nm, evident in both the original magnitude spectra (Figure 3.4) and first derivative spectra (Appendix A, Figure 6.2 & 6.3). In regard to the magnitude in this range, shallow substrate showed higher reflectance than deep substrates. Of the shallow substrates, sand had the highest magnitude, followed by green algae, non-biofouled eelgrass, and biofouled eelgrass in decreasing order. Of the deep substrates, deep sand showed higher magnitude, while deep water and deep eelgrass showed similar lower magnitudes. Spectra for all substrates were generally characterized by a broad green peak at the photosynthetic pigment absorption minimum between 560 and 575nm; however, for shallow eelgrass and shallow sand peaks it occurred an average of 5nm after the other benthic types (570 vs. 565nm). Green peak slopes for all vegetation (algae and eelgrass) became steeper with decreasing water depth, and overall, green algae slopes were steeper than that of eelgrass. Eelgrass and green algae exhibited a small shoulder at 470-480nm interrupting the ascending slope.

A marked absorption feature in the blue range (400-500nm) was present for all substrates, due to water constituents, particularly CDOM and chl-a, but was strengthened in vegetation classes by chlorophyll-*a* and -*b*, and lutein, and by the additional accessory pigment β-carotene in green algae. This translated into a s500-530 in the HyperSAS (or 480:550 in the simulated IKONOS and Landsat ETM+) that was steeper for green algae than for eelgrass *(Figure 3.4).* A second major absorption feature appeared in the red region at 662-669nm for all except sand, which occurred at 675nm. This feature is characteristic of chlorophyll-*a,* and *–b* and was most pronounced in shallow cover classes where the red reflectance of TSS is minimized by a short water column. The presence of epiphytic diatoms on eelgrass and green algae was signified by the unique chlorophyll*–a* and *–c* absorption trough between 630-640nm and decreased reflectance from 530-566nm caused by absorption by fucoxanthin (Meleder et al., 2003). The vegetation red-edge occurred in the range of 670-705nm and in all shallow substrates, the 685nm

phytoplankton chlorophyll fluorescence peak was masked by a NIR peak between 705-710nm, 696-709nm, and 687-697nm respectively *(Figure 3.4b).*

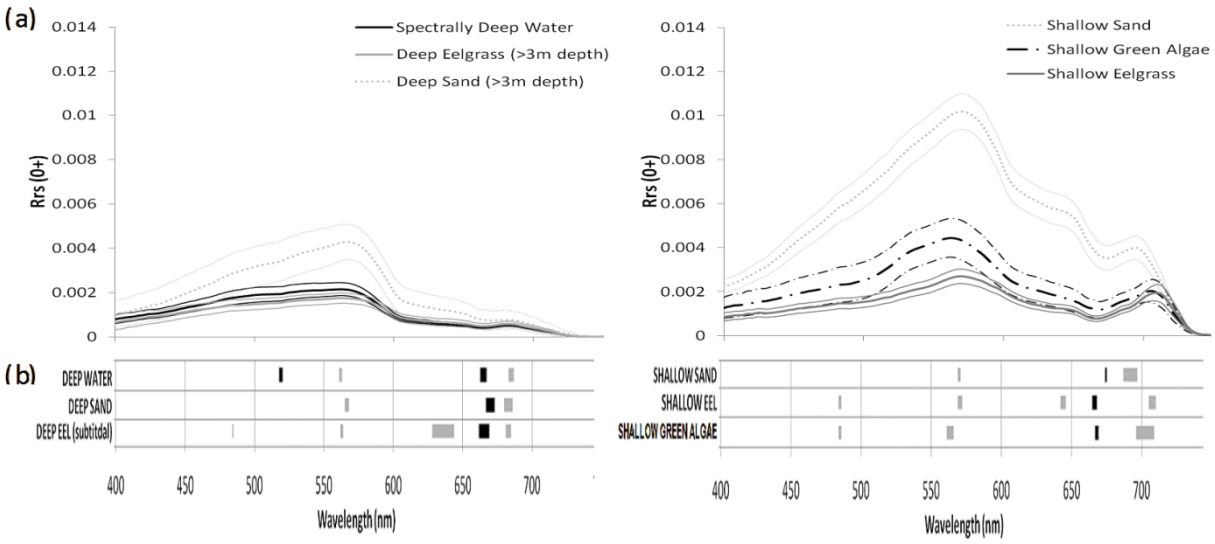

Figure 3.4 (a) Average above-water reflectance with 95% confidence interval for each benthic substrate type and (b) major reflectance (grey) and absorption (black) features for each benthic substrate with 95% confidence interval, as derived by first derivative analysis.

The average spectra of each epiphyte type (Figure 3.5) showed that the major spectral differences between the two epiphyte type were higher blue absorption due to α and β-carotene and lutein, higher green absorption due to billiproteins phycoerythrin and phycocyanin (Rowan, 1989), higher red absorption due to chlorophyll-a and b, and greater NIR reflectance of the red algae, perhaps due to its broader surface area. Biofouled eelgrass exhibited a shift of the tall green peak into a broad red peak (Figure 3.5c), with diatoms showing major reflectance features at 582nm, 602nm and 645nm, and absorption features related to chlorophyll-a and –c at 586nm, 632nm, and 670nm (Figure 3.5c). Red algae epiphyte reflectance features were found to occur at 586nm and 652nm with absorption at 618nm and 670nm, due to absorption by biliproteins (Rowan, 1989), but trended closer to that of diatoms when senescing (Figure 3.5d).

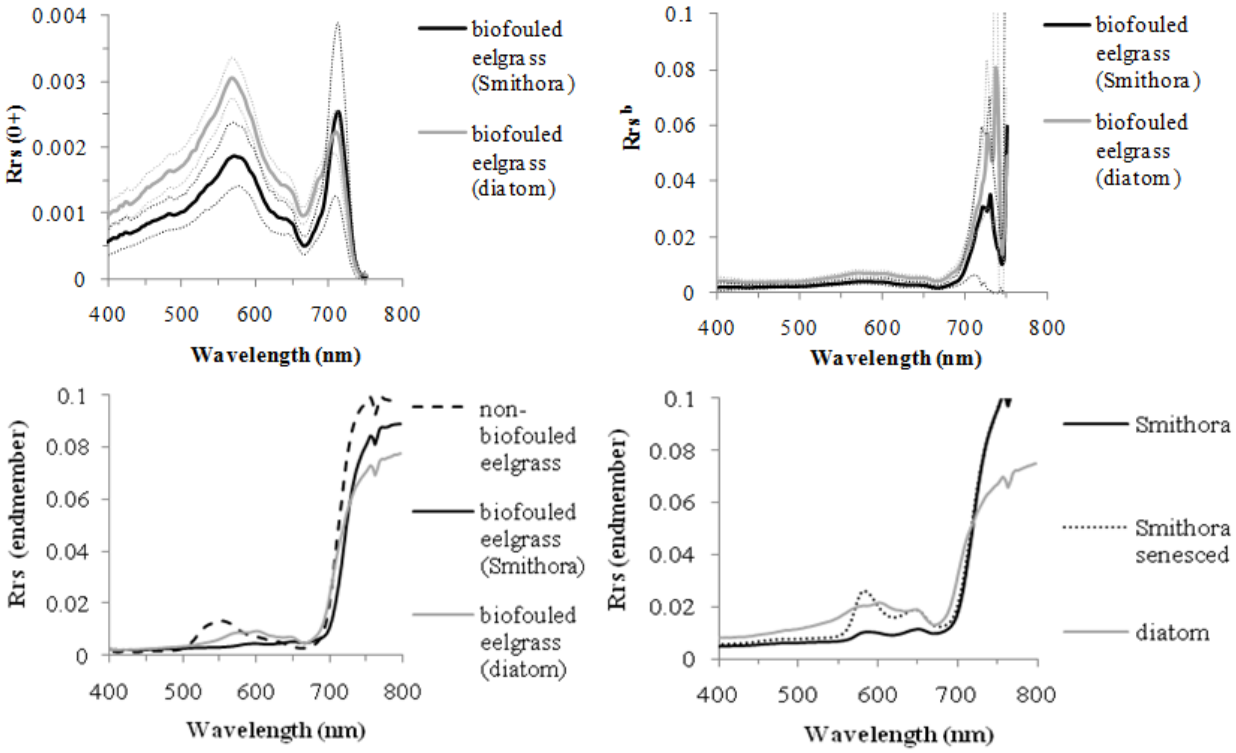

Figure 3.5 Average spectra of eelgrass, biofouled with diatoms and red algae, Smithora, for (a) above water spectra with 95% confidence interval (dotted lines); (b) water-corrected spectra 95% confidence interval (dotted lines); and (c) endmembers. (c) also shows eelgrass with no biofouling. (d) shows endmember spectra of epiphytes only, scraped from eelgrass blades.

3.3.3 Statistical Analysis: Data Reduction

Indices

Twenty-three indices resulted from the calculation of slopes and ratios between major absorption and reflectance features. Both slope (denoted, sλ-λ) and ratio (denoted λ: λ) were calculated for each feature pair, except in the case where a slope did not make mathematical sense (e.g., between reflectance peaks at 566nm and 670nm).

Table 3.3 List of indices used in M-statistic and MDA analysis: (a) Spectral slopes and ratios showing potential for separating eelgrass from other substrates, as per visual analysis of first derivative spectra (b) common vegetation indices, and (c) first derivative values known to be effective.

(a) Wavelengths	Slope(s) Ratio(r)	Description	Reference
480, 490	s,r	Chl blue absorption	This study
500, 530	s,r	Green peak – ascending edge to 530nm shoulder	This study
536, 566	s,r	Greek peak – ascending edge shoulder to max	This study
500, 566	r	Max blue absorption: max green reflectance	This study
566, 600	s,r	Green peak – descending edge	This study
620, 640	s,r	Chl b & water red absorption – descending slope	This study
630, 640	s,r	Detect diatom epiphytes	This study
650, 660	s,r	Chl red absorption –descending edge	This study
566, 670	r	Chl max green reflectance: max red absorption	Viollier et al. 1985 (672:550)
566, 694	r	Green peak : sand NIR peak	This study
566, 710	r	Green peak : vegetation NIR peak	Lichtenthaller et al. 1996
570, 710	r	Green peak : vegetation NIR peak	This study
670, 700	s,r	Red edge. correlated with chlorophyll-a	Gitelson et al. 1993; Murphy et al, 2005
668, 710	r	red edge	Jordan, 1969 (RVI)
690, 710	r	NIR peak position	Lichtenthaller et al. 1996

(b) Vegetation Index	Calculation	Reference
NIR/B	(R710 – R436) / (R710+R436)	Kromkamp et al, 2006
B/G	(R570 – R436) / (R570 + R436)	Kromkamp et al, 2006
G/R	(R570 – R666) / (R570 + R666)	Kromkamp et al, 2006
Log R/IR	Log710/Log666	Kromkamp et al, 2006
SAVI	[(NIR – RED) / (NIR + RED + L)](1+L) where L=0.5 or 0.25	Kromkamp et al, 2006
SAVI 2	NIR / (RED +b/a) where a&b are gain and offset values of a sand RED/NIR regression	
NDVI	(NIR – RED) / (NIR + RED)	Rouse et al, 1973
Macrophyte index (MCI)	(R710/R666) / (R566/R666) (macrophytes present when >2)	Kromkamp, 2006
PVI	NIR – aRED – b / SQRT(1+a^2) where a&b are gain and offset values of a sand RED/NIR regression	Richardson & Wiegard, 1997
NPCI	(R680 – R430) / (R680 + R430)	Penuelas et al. 1993; Murpy et al 2004
PRI	(R530 – R566) / (R530 + R566)	Gamon, 1997; Thorhaug 2006
Chl_NDI	(R710 – R700) / (R710 + R700)	Gitelson & Marzlyak, 1994; Thorhaug 2006
SIPI	(R710 – R450) / (R710 – R666)	Penuelas and Filella, 1998; Thorhaug, 2006
562:647	R562 / R647	Murphy et al. 2005

(c) First Derivative	Description	Reference
R'632	Diatom presence	Murphy et al. 2006
R'710	Red Edge	This study

The following sections describe the results of data reduction for each processing case. The lettering of each title (i.e. *i., ii., iii...*) corresponds with those depicted in the methodology flow chart, which can be found in Figure 3.6.

(i) Above-water dataset (no water column correction) - eelgrass classification

Figures 6.1 and 6.2 of Appendix A show the M-statistic separability results for shallow eelgrass and deep eelgrass versus the other benthic classes. The results showed that the first derivative variables were more effective at separating covers, given the higher M-statistic values for first derivative variables. No wavelength in the original spectra could effectively differentiate between eelgrass and green algae in shallow water or between deep eelgrass and deep water. First derivative variables however, did produce M-statistics greater than one for these pairs. In shallow water (< 3 m), Set 1 variables (the result of M-statistic) for differentiating eelgrass from sand were R'506, R'532, R'592, *s*500-530; and for separating eelgrass from green algae were *s*566-600 and R'524, R'580, *s*500-530, *s*566-600, and 536:566. The vegetation indices were unable to separate eelgrass from green algae samples. In deep water (> 3 m), Set 1 variables were R'580, and 566:600 for differentiating deep eelgrass from optically deep water; R'474, R'530, R'596, 480-490, 566-600, and *s*R500-R530 for deep eelgrass from deep sand.

Set 1 of the shallow and deep water groups were each further reduced using stepwise multiple discriminant analysis (MDA). The remaining reduced variable set (Set 2) for each group are reported with total classification accuracy in Table 3.4 and Figure 3.6. Shallow water Set 2 variables were sR500-R530, R'566, R'580, and R'602 for a total classification accuracy of 97.1% due to a misclassification of one out of eight *Ulva* samples as shallow eelgrass. Deep water Set 2 variables were sR500-R530, R'580, and R'602 for a total classification accuracy of 100.0%. Note that caution should be taken in interpreting this result as the sample size of deep eelgrass was small (n = 4), and therefore the 100% accuracy attained by the model is likely a high estimate. The Set 2 variables for each depth group were pooled to test their combined efficacy in a single classification. The stepwise MDA retained all four variables in the model for

a total classification accuracy of 97.9%, misclassifying only the same Ulva sample as the shallow model did. User and producer accuracies are reported in Table 3.4 and Figure 3.6.

Table 3.4 Set 2 bands selected by the MDA for each processing level. * Two accuracy values indicate shallow / deep eelgrass accuracy.

	Processing Level									
	Above-water data set $R_{rs}^{(0+)}$						**Water corrected data set** R_b			
	Shallow Model	Deep Model	All Depths Model	LAI Model	Percent Cover Model	Epiphyte Model	All Depths Model	LAI Model	Percent Cover Model	Epiphyte Model
*s*500-530	■	■	■							
*r*566:600							■			
*r*650:660									■	
*r*566:710							■			
*r*570:710									■	
*r*668:710			■							
NPCI				■	■					
Chl_NDI								■		
R'566	■		■							
R'580	■	■	■			■				
R'600									■	
R'602	■	■	■							
R'604					■					
R'680										■
R'700				■						
Prod Acc.	95%	100%	100%/100%*	-	-	-	100%	-	-	-
User Acc.	100%	100%	95%/100%*	-	-	-	95%	-	-	-
Total Acc.	97%	100%	98.0%	80%	75%	100%	97%	75%	9%	90%

To understand further the results of the MDA analysis, the canonical functions of each model were derived. The composite variables (also termed canonical functions) of the defined MDA model are re-projected combinations of the selected variables, which offer the greatest separation between covertypes (McGarigal et al., 2000; Richardson et al., 2004). If a variable contributes highly (i.e. its structural coefficient shows high correlation) to a canonical function that is responsible for most of the variation in the model, that variable is very important in separating the benthic classes. The results show that the first two canonical functions of the final pooled all-depths model explain 94.3% of the total variance between benthic classes (Figure 3.7c). The structure coefficients indicate that Function 1 is responsible for 84.2% of the variance.

Note that the x-axis of Figure 3.7c indicates that Function 1 separates the data into three distinct clusters: eelgrass and deep water; green algae and deep sand; and shallow sand. Function 1 is highly correlated with R'602 (r = -0.632) and s500-530 (r = 0.630), which are the absorption regions of water, chlorophyll-*b*, β-carotene, and lutein (Rowan, 1989). Therefore these constituents appear to be major factors in the separability of the three substrate clusters and also the constituents responsible for the most separability in the model. Similarly, Function 2, which explains 10.1% of the total variance, separates eelgrass from the cluster of shallow green algae, deep water, and deep sand. Function 2 is correlated with R'580 (r = 0.782) and R'566 (r = 0.674), suggesting that green peak location, chlorophyll concentration, and anthocyanin concentration are possible important factors for separating these substrates, a supposition supported in the literature (Gausman, 1982; Fyfe, 2003).

In addition to the statistically selected variables, a NIR band was added to the model. The literature suggests that it is necessary for a benthic classification scheme to include one NIR band to assist in identifying vegetation at the surface of the water (e.g., exposed / floating seagrass and macro algae) (Zacharias et al. 1992). The models did not select an NIR band, presumably because the dataset included no exposed vegetation samples. The red edge variable 668:710nm was included to check for any possible effects on the classification of submerged vegetation. It was found not to affect the accuracy of the model (Figure 3.6).

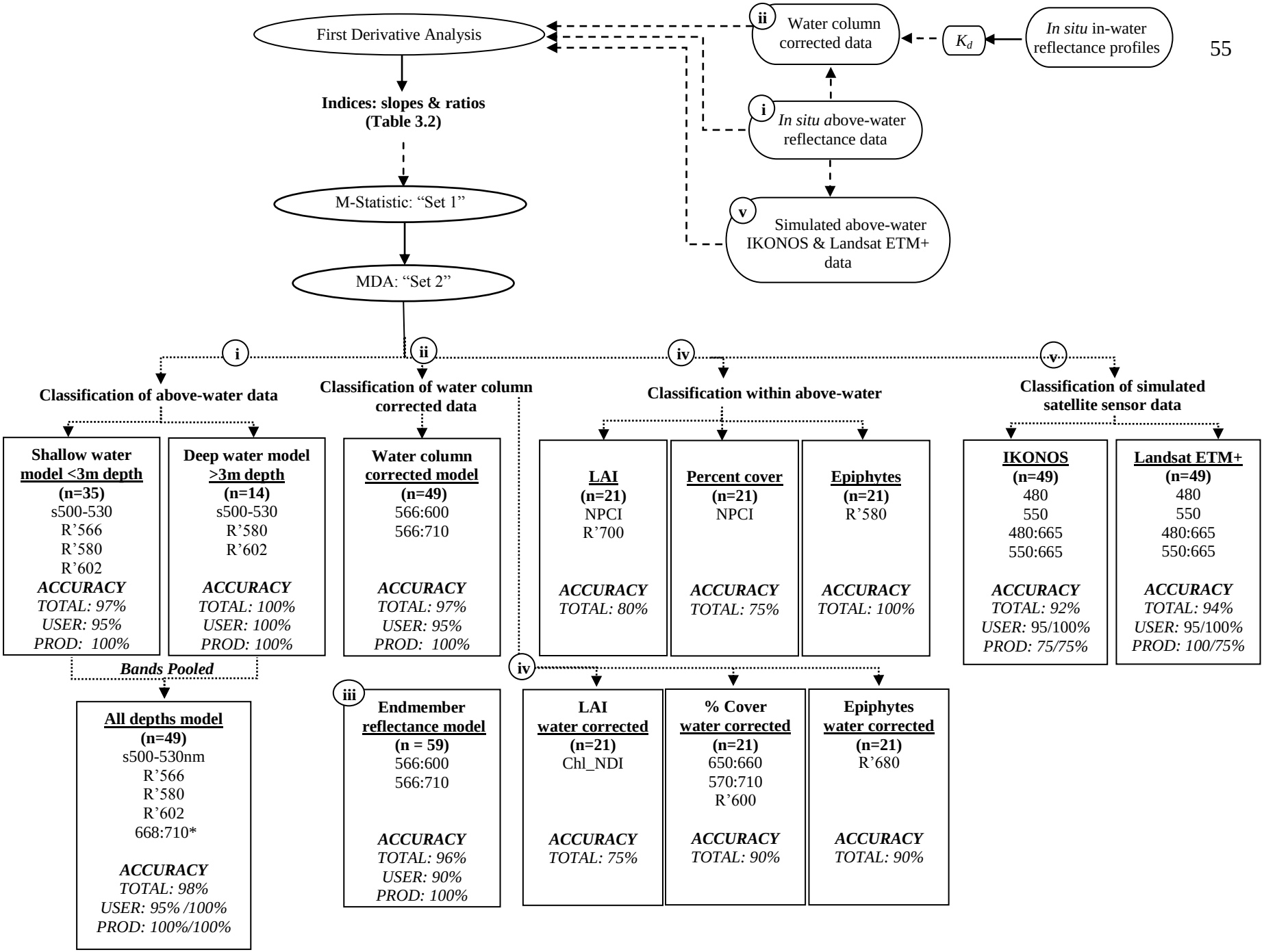

Figure 3.6 Data reduction steps and accuracy of Set 2 for each classification case (letters denote sections of the methodology text): (i) Above water HyperSAS data; (ii) Water column corrected HyperSAS data; (iii) Endmemeber data; (iv) LAI, percent cover and epiphyte classification; and (v) IKONOS and Landsat ETM+ above water data simulated from HyperSAS data.

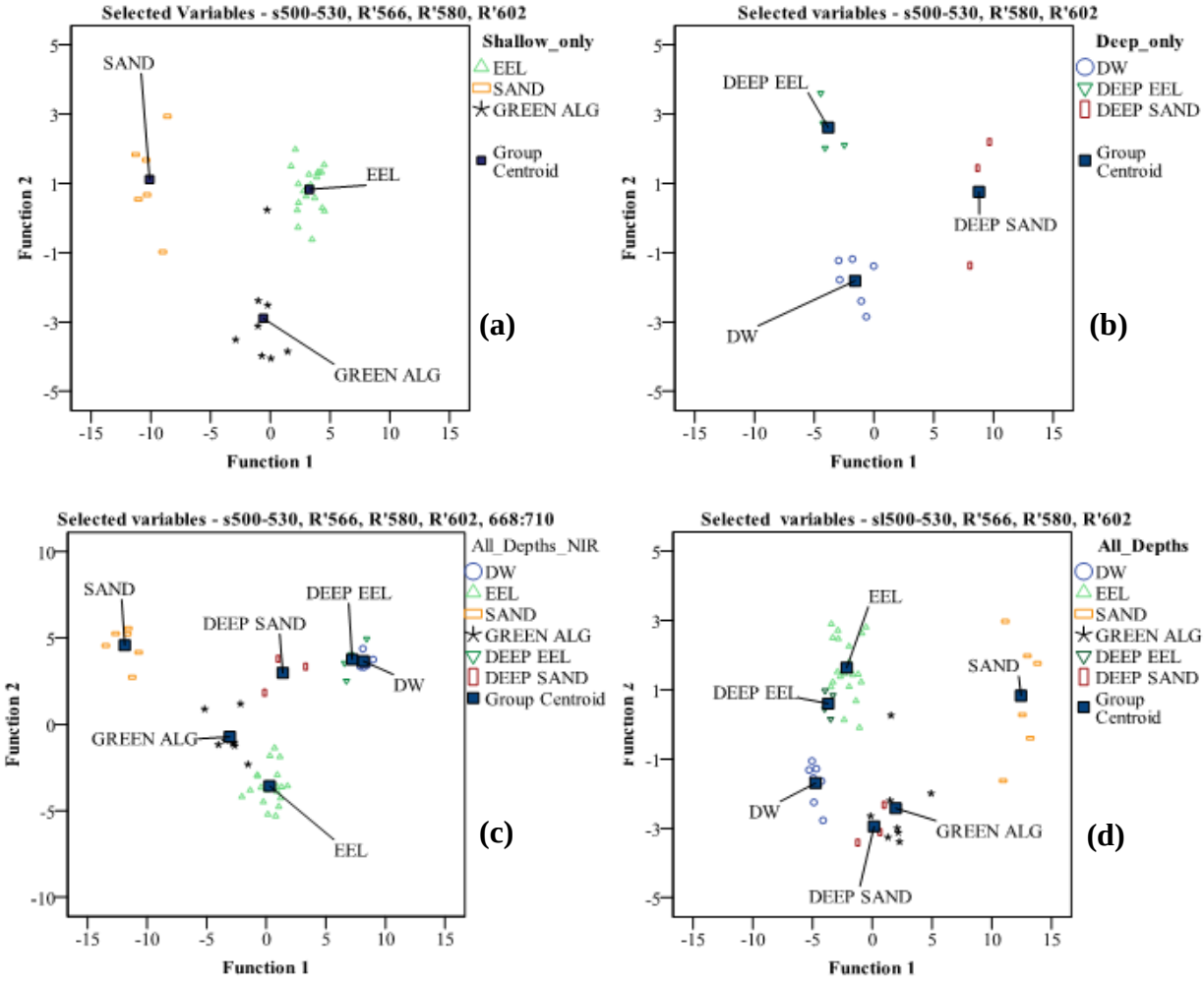

Figure 3.7 Plot of first two canonical discriminant functions for (a) shallow water (< 3m) substrate classification, (b) deep water (> 3m) classification, (c) all depth classification and (d) all depth classification with the addition of a red edge index.

(ii) Water column corrected dataset - eelgrass classification

Results for the corrected spectra after applying the Maritorena et al. (1994) model are shown in Figure 3.8. Generally, the water correction increased reflectance of substrate spectra by one order of magnitude, which is in agreement with endmember spectra. For the covertypes shallower than 3 metres, all corrected spectra averages were within 1standard deviation of their respective endmember. Specifically, corrected magnitudes were within 20% error between 480 - 660nm for eelgrass and 500 – 700nm for sand and green algae (Figure 3.9). The only exception was a 30% error for green algae from 520 to 620nm. Since above water spectral measurements

and endmember samples were collected at different locations, this spectral difference could be due to difference in senescence stage. Generally, the loss of chlorophyll during senescence causes a flattening in the 520 to 620 nm region as red absorption and green reflectance decrease (Werdell & Roesler, 2003). In the blue wavelengths there was an overall, there was over correction of the blue wavelengths for all shallow benthic substrates (Figure 3.9). This overcorrection was less for eelgrass when the depth variable was reduced by 0.5 metres in compensation for blade height, however the compensation instead resulted in an underestimation of the long red and short NIR range (Figure 3.9). All deep eelgrass and deep sediment (> 3m) spectra were significantly over corrected at all wavelengths and held no similarity in spectral shape to their respective endmembers. This suggests that the water column correction is not suitable for substrates deeper than 3 metres when K_d is greater than $K_d(440) = 0.82\ m^{-1}$, $K_d(550) = 0.72\ m^{-1}$, and $K_d(650) = 1.06\ m^{-1}$, which is the highest K_d found in a deep water class during this study and the high K_d used in the minimum depth threshold calculation. Magnitudes are however within 20% error between 550 – 590nm (Figure 3.9); the portion of the spectrum where K_d is lowest and therefore light penetrates furthest (Figure 3.10). This observation is supported by calculations of the HyperSAS depth limit for substrate detection (Dekker, 2006) (Chapter 2, Eq. 2.11 & 2.12). The minimum bound of the depth threshold for sand is approximately 4 metres at 600nm and drops to 3 metres by 700 nm, while for eelgrass with epiphytes it drops from approximately 3 metres at 600 nm to 2.5 metres at 700 nm (Figure 3.10).

It is important to note that slight differences between the water corrected spectra and endmember spectra may be attributed to endmember spectra not capturing the natural orientation of eelgrass and green algae blades. For example, the green peak of water corrected green algae (Figure 3.8c) may have been dampened compared to the endmember because the vertical orientation of the blades was introducing underlying sediment into to the field of view.

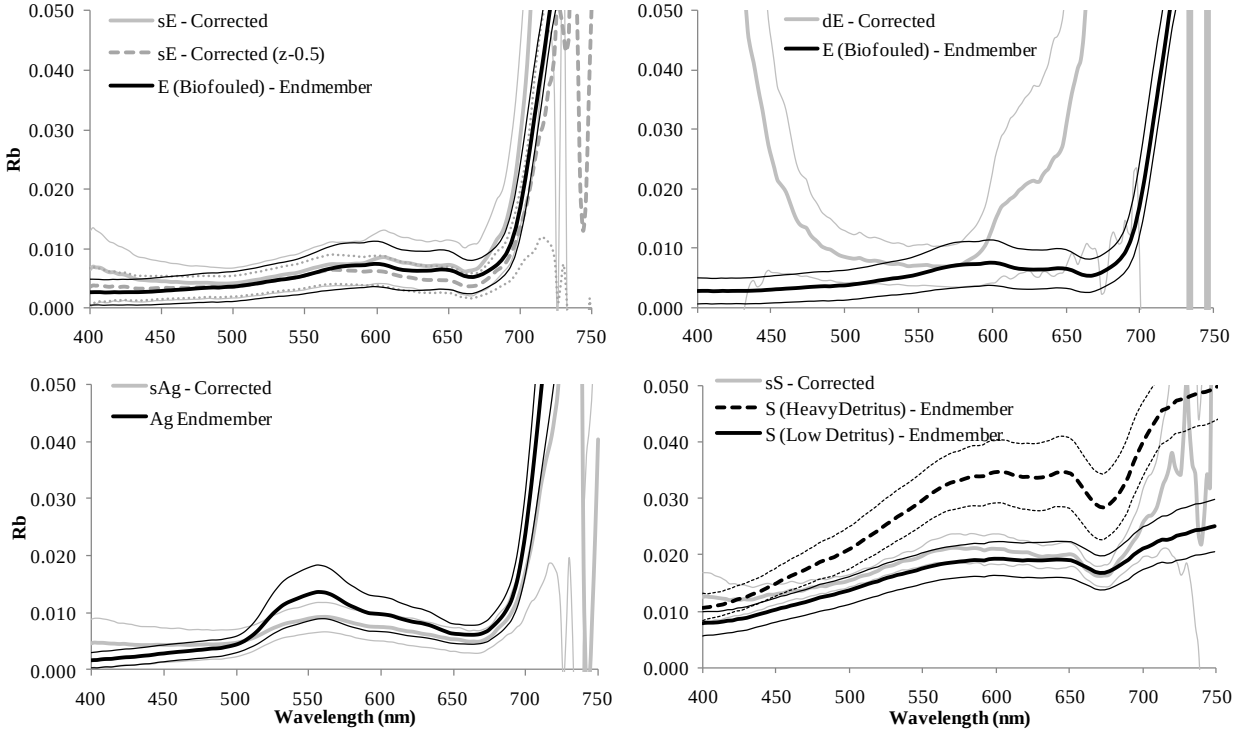

Figure 3.8 Average spectra (thick lines) ±95% confidence interval (thin lines) of each benthic type corrected for the attenuating effects of the water column using Maritorena et al.'s (1994) equation (Eq. 2.10). Grey lines represent the water corrected above-water spectra ad black lines represent the in situ pure endmember spectra for comparison. See Table 2.1 for substrate abbreviations. sE (z-0.5m) is the correction of eelgrass sites with 0.5 metres removed from the depth measurement in compensation for the general height of eelgrass blades.

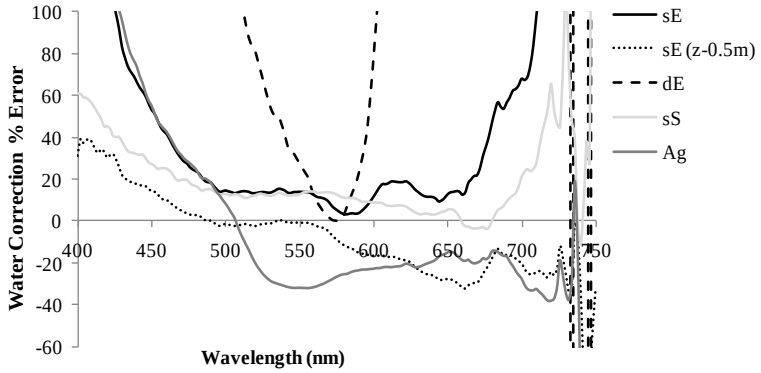

Figure 3.9 Percent error of the water attenuation correction for each substrate.

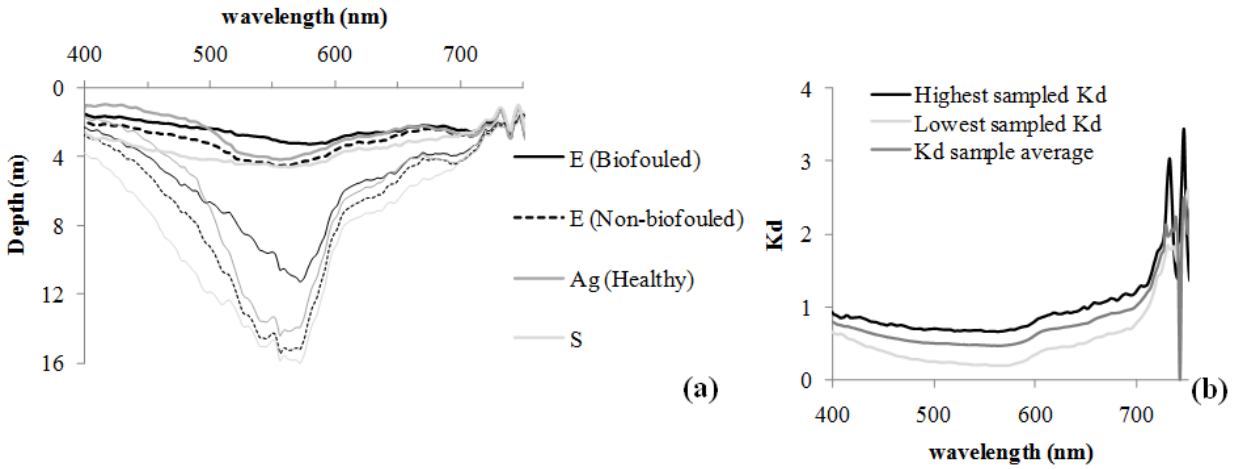

Figure 3.10: (a)The depth at which the HyperSAS sensor can distinguish each covertype from spectrally deep water for the lowest (thin lines) and highest (thick lines) Kd's found at the study site. Calculated as per Dekker et al. (2005). (b) Lowest, highest and average Kd values found at the study site.

The poorly corrected (deep water > 3 m) spectra were removed and the M-statistic and stepwise MDA were applied to the remaining water column corrected set. The defined Set 2 variables were 566:600 and 566:710 with a total classification accuracy of 97.1%, misclassifying only one green algae sample as eelgrass.

(iii) Endmember dataset – eelgrass classification (validation of water corrected model)

Since the shallow (< 3 m) water corrected spectra were similar in shape and magnitude to the endmembers (Figure 3.8 & 3.9) and the endmember sample number was relatively larger (n = 59), the endmember data set was used as a check for the Set 2 selected variables in the water corrected model (566:600 and 566:710). These two variables were entered together into a MDA classification of the endmember data set, with a resulting total accuracy of 96%, with two green algae (both senescent) erroneously classified as eelgrass. When spectra of "non-biofouled" eelgrass were added to the endmember classification, total accuracy was reduced to 78% because six of the nine epiphyte-free eelgrass samples were erroneously grouped as green algae and seven of twenty-two green algae samples were grouped as eelgrass. Conversely, 100% of the fifteen biofouled eelgrass samples were correctly classified. Therefore, if eelgrass beds with little to no epiphyte coverage are present in the site, the classification is likely to exhibit more confusion between eelgrass and green algae; This is supported by the fact that the only variable

to provide an M-statistic greater than one for the separation of epiphyte-free eelgrass and green algae was 650:660 with a value of 1.1. If eelgrass is heavily covered by epiphytes, confusion between eelgrass and green algae is minimized. Figure 3.11 shows the relative similarity of non-biofouled eelgrass and healthy green algae.

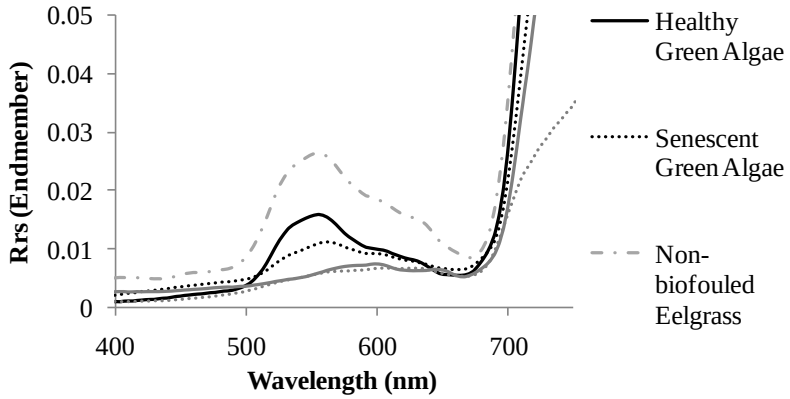

Figure 3.11 Endmember spectra of healthy and senescent green algae and biofouled, non-biofouled and senescent eelgrass. Classifications exhibit confusion between healthy green algae and non-biofouled eelgrass as well as senescent green algae and bio-fouled eelgrass.

(iv) LAI, percent cover, and epiphyte type - eelgrass classification

Shallow eelgrass sites were separated into two broad percent cover groups according to visual estimation based on field photos taken concurrent with spectral sampling (Chapter 2): sparse cover (20-60% cover, n=5) and dense cover (>60% cover, n=19), following Su et al (2006). Shallow eelgrass sites were also separated into three Leaf Area Index (LAI) classes according to the photographic index created from field sampling *(Chapter 2, Section 2.2.1)*: low LAI <1 (n=4), medium LAI = 1-2 (n=12), and high LAI > 2 (n=9) (Dierssen et al., 2003). Lastly, shallow eelgrass sites were separated into two epiphyte type classes: diatoms (n=16) and red algae (n=4). Spectral characterization for percent cover, LAI, and epiphyte type are shown in Figures 3.12a, 3.12b, and 3.5, respectively.

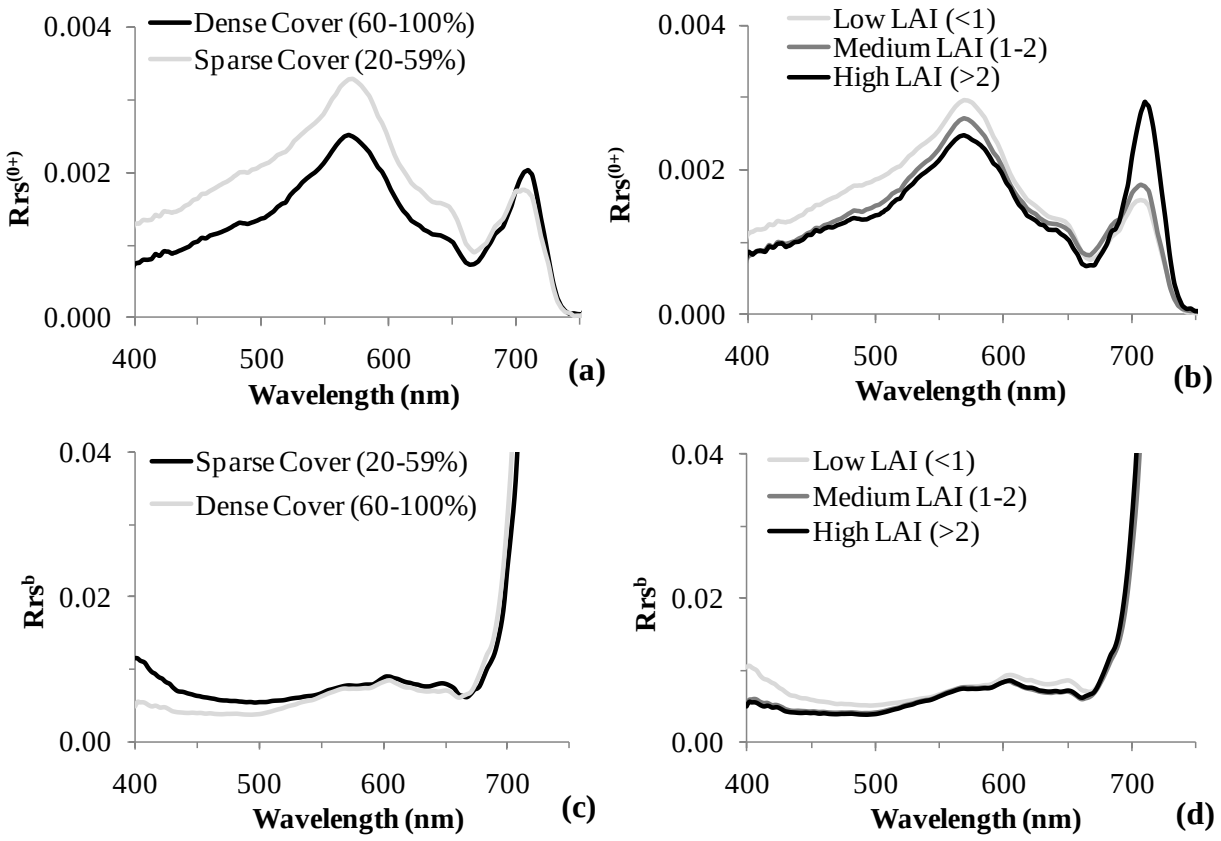

Figure 3.12: Average eelgrass in situ above water spectra (a & b) and water corrected spectra (c & d) spectra grouped by percent cover and LAI classes.

The M-statistic analysis of eelgrass percent cover revealed the NPCI index to be the only variable greater than one. The NPCI index yielded a total classification accuracy of 75%. The M-Statistic and MDA analyses of the water corrected dataset selected a model with 650:660, 570:710 and R'600 for a total classification accuracy of 90%, however sparse eelgrass producer accuracy (n=4) was only 50%. Total, producer, and user accuracy are reported in Table 3.4 and Figure 3.7.

The M-statistic for LAI indicated no original band was effective for separating LAI groups while first derivative spectra and some vegetation indices performed slightly better. Low and Medium LAI groups were separated by the NPCI index; Medium and High were separated by (in order of efficacy) R'700, R'440, R'464; while Low and High were separated by R'604, R'464, R'440, the NPCI index, and 500:530. The stepwise MDA analysis of the three LAI

groups selected a model with the NPCI index and R'700 for a total classification accuracy of 80%. The stepwise LAI MDA run on water corrected eelgrass spectra selected chl_NDI index, resulting in a total classification accuracy of 75%. A plot of the first two canonical functions of the above-water selected MDA model (Set 2), which represent 100% of the variance between LAI classes, is shown in Figure 3.13. The plot indicates separation between low and medium classes with only slight overlap, while high LAI is separated fairly poorly. Two of four samples are located closer to the medium and sparse centroids than to the dense centroid.

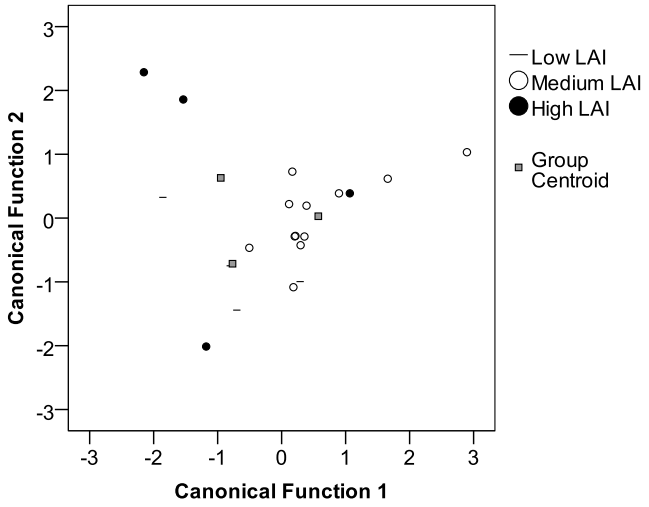

Figure 3.13 MDA classification of eelgrass in situ spectra into low, medium and high LAI classes: graphical representation of the efficacy of the model based on the first two canonical discriminant functions (total accuracy 80%).

The M-statistic analysis of epiphyte type suggested the original wavelengths are ineffective while R'476, R'528, R'580, R'604, and s566-600 were most effective at separating the two groups. The stepwise MDA analysis selected a model with only R'580, producing a total classification accuracy of 100%. Similar analyses on water column corrected spectra selected R'680 with a total classification accuracy of 90%. Total, producer's and user's accuracies for all models are recorded in Table 3.4 and Figure 3.7.

The LAI, percent cover and epiphyte models resulted in high accuracies: 80%, 75% and 100% respectively with above water data and 75%, 90%, 90% respectively with water-corrected data. However since the sample number was relatively low (n=24), caution should be used in interpreting these results. For instance, the percent cover water-corrected model misclassified two out of a total of four sparse samples as dense, resulting in a producer's accuracy of 50%.

(v) IKONOS and Landsat ETM+ Simulation – eelgrass classification

The simulated Landsat ETM+ and IKONOS spectra slightly underestimated the peak green reflectance and overestimated the red reflectance due to the large bandwidths of the sensors (Figure 3.14 & Figure 2.3). MDA was applied to individual bands and the band ratios for both IKONOS and Landsat 7ETM+ simulated spectra. The MDA analysis for IKONOS selected 480, 550, 480:665 and 550:665 for a total accuracy of 92% (shallow eelgrass user/producer accuracy = 95%/75%; deep eelgrass = 100%/75%). The MDA for Landsat 7ETM+ selected the same bands for a total accuracy of 94% (shallow eelgrass user/producer accuracy = 95%/100%; deep eelgrass = 100%/75%). Although IKONOS and Landsat ETM+ bands are very similar, the accuracy results were slightly different; a result that could be due to the narrower visible bands and slightly shorter wavelength placement of the red band of Landsat ETM+ compared with the IKONOS bands.

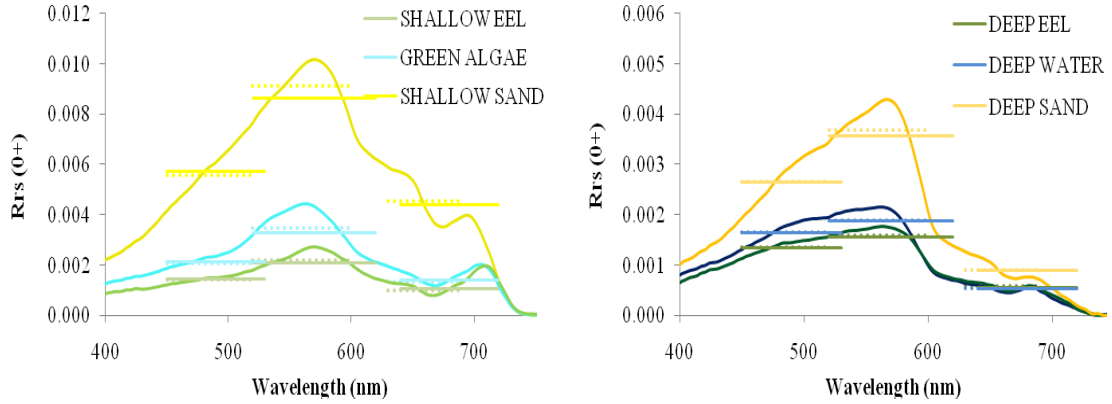

Figure 3.14 Average (a) shallow and (b) deep covertype spectra for the hyperspectral field sensor (solid line) compared with the multispectral IKONOS (solid bar) and LandsatETM+ (dotted bar) sensors simulated from the HyperSAS data.

3.4 Discussion

3.4.1 Above water model (without water correction)

According to Fyfe's (2003) guidelines, an appropriate seagrass classification band set should be composed of narrow bands (5 - 15 nm) that are either centred at or shouldering both sides of the major absorption and reflectance features of all covertypes present, including seagrass that is both non-fouled (suggesting 500, 550, 620, and 675 nm) and fouled (575, 590, and 640 nm), one reference band of low separability such as a blue band, and one NIR band to

discern exposed and floating vegetation. Additionally, each band should be narrower then the spectral feature it represents and should not overlap with any other spectral feature. All models defined in this study were consistent with these recommendations; however our results showed that the substrates were most effectively separated by relative measures of reflectance (indices) rather than by absolute reflectance magnitudes of single wavelengths. This suggests that spectral shape defined a covertype more effectively than spectral magnitude; an observation also made by Vahtmae et al. (2006).

Among the various considered indices, the results of the MDA indicated that s500-530, R'566, R'580, and R'602 were the most statistically significant for accurately discriminating eelgrass from other classes. This result was based on *in situ* above water hyperspectral reflectance for both a two-stage classification stratified by depth (less than and greater than 3m) and a single classification addressing all six depth-covertype classes simultaneously. Therefore, assuming adequate atmospheric correction, it should be possible to retrieve an eelgrass distribution map for Sidney Spit from remote imagery by applying a discriminant analysis, for example Maximum Likelihood classifier, on the above listed indices without first stratifying the image by depth or masking out optically deep water. To calculate these indices would require ten bands of 4nm bandwidth: R500, R530, R554, R568, R578, R582, R600, R604, R668, R710nm. These bands are in agreement with suggestions recommended by Fyfe's (2003) work. Further, based on these *in situ* hyperspectral results, an effective eelgrass classification could be obtained in the absence of a bathymetry map. The classification accuracy should be robust to atmospheric interference because it avoids the blue wavelengths. Accuracy may however not be robust for waters with higher K_d values. As K_d increases, i.e. higher attenuation of the reflectance signal, the spectral curves of all substrates become more similar to the spectra of optically deep water. The increased attenuation also further limits the depth to which the sensor can optically resolve a substrate (Figure 3.10).

The spectral variables selected by statistical analysis offer the greatest separation between substrates, while limiting redundancy. The following describes the possible for the statistical selection of the specific variables. In the visible wavelengths, absolute and relative reflectances of an exposed substrate are a result of both the total and the relative concentrations of substrate pigments. Increasing the concentration of any photosynthetic pigment causes a general increase in visible spectra absorption, particularly at its characteristic absorption features (Curran *et al.*,

1991). However, when the substrate is submerged, the spectral influences of the water column and its constituents come into play. CDOM absorbs strongly in the blue wavelengths while phytoplankton chlorophyll absorbs strongly in the blue and red wavelengths. Inorganic particulate and substrate tend to increase overall visible reflectance, especially in the red wavelengths (Liedtk et al., 1995; Babin et al., 2003). NIR reflectance is characteristic of the cell structure of vegetation, increasing with vegetation density, but varying with species (Jensen, 2007). When submerged, NIR reflectance becomes negligible beyond the first metre of depth due to absorption by water (Kirk, 1986, Mobley, 1994). With this understanding of the optical spectral behaviour of different water optical constituents and vegetation, an analysis of the final selected variables is provided. Tables 3.5, 3.6, and 3.7 provide a summary of the selected variables and the substrate pairs for which each one offers good (M-statistic > 1) separation.

The selected slope between 500 and 530 (*s*500-530) is likely related to absorption by CDOM, chlorophyll, and lutein (an xanthophyll) in the blue spectra in relation to green reflectance. On one hand, the blue absorbing pigments chlorophyll-a, -b, and lutein (432nm, 475nm, and 440 – 460nm respectively, (Snodderly *et al.,* 1983) are present in both green algae and eelgrass. On the other hand, green algae contains the higher lutein concentrations and the additional blue-green (400-505nm) absorbing accessory pigment β-carotene (Rowan, 1989), thus resulting in a steeper spectral curve between 500 - 530 nm than that of eelgrass (Figure 3.4 & 3.8). However, the role of β-carotene is likely minor compared to the strong spectral influence of epiphytes in the 500-530nm region. In addition to physically blocking eelgrass green reflectance, diatoms have a primary accessory pigment, Fucoxanthin, with a major absorption feature at 500 – 590 nm. This is in agreement with the biofouled/ non-biofouled eelgrass and green algae endmember spectra (Figure 3.11). The 500 - 530nm slope is even flatter for eelgrass colonizing shallow water possibly due to one or more of the following: a shorter water column and therefore less blue absorption from CDOM and phytoplankton chl-a, the presence of photoprotective anthocyanins that absorb in the range of 500 – 550nm (Gausman,1982), or possible greater epiphyte coverage in shallow waters (personal observation). Shallow sand exhibited the steepest s500-530 due to its characteristically high green and red reflectance (Miller, 2002) relative to blue absorption by CDOM and chl-a in the water column. Additionally, the s500-530 provided poor separation between deep eelgrass and optically deep water (Table 3.6) because the

attenuating effects of the deeper water column obscured the absorption / reflectance features of eelgrass.

Another selected variable, the first derivative value at 566nm (R'566), represents the peak of green reflectance, which occurred at slightly longer wavelengths in shallow eelgrass and all depths of sand. In eelgrass, this could be due in part to the absorptive effects of anthocyanins at the range 500 – 550 nm displacing the derivative. For sand it is likely due to its characteristic mineral high reflectance in the green to red wavelengths (Maritorena et al., 1994). The green peak of deep (> 3 m) covertypes was probably skewed to shorter wavelengths due to strong attenuation by water, which occurs at 570-600nm (Morel et al., 2007).

The first derivative values at 580 nm and 602 nm mark represent, respectively, the descending slope of the green peak and the inflection point of the red absorption feature. They were both significantly flatter for eelgrass, likely due to epiphyte presence, which increased reflectance between 566 -640nm (Fyfe, 2003), and photoprotective anthocyanins reflecting in the 600 – 640nm region (Gausman, 1982). R'580 provided good separation between eelgrass and every substrate regardless of depth. R'602 provided separation between all covertypes that R'566 did not, and vice versa (Table 3.5 & 3.6).

Lastly, the manually introduced 668:710 ratio identified the vegetation "red edge." The red edge is a steep positive slope that occurs at around 700 nm due to the combined effects of red absorption by chlorophyll and NIR reflectance by plant or algal cell structure (Seager et al. 2005). Because NIR is attenuated exponentially at the water surface (Mobley, 1994), the red edge is characteristic only of shallow vegetation. Therefore a low 668:710 ratio was seen only in shallow (< 3 m) eelgrass and algae, enabling separation of shallow eelgrass from all other substrates except shallow green algae. Although our results showed that this ratio had no effect on the accuracy of the final model, it likely has potential in separating exposed and floating vegetation from shallow vegetation (Zacharias et al, 1992; Fyfe, 2003).

The variables selected for the water corrected data set were different than those selected for the above-water data set. The selected indices were 566:600 and 566:710. The green to red ratio 566:600 separates eelgrass from green algae *(Table 3.7).* It should be noted that this ratio does not separate non-biofouled eelgrass from green algae (M-statistic = 0.29, Appendix A, Figure 6.4b). The ratio is negative for green algae and non-biofouled eelgrass due to red absorption by chl-a relative to green reflectance (Figure 3.8c & 3.11). The ratio is positive for

biofouled eelgrass due to epiphyte dampening of green reflectance and characteristic increase of red reflectance at 590 nm (Fyfe, 2003) *(Figure 3.8a & 3.11).* The green to NIR ratio 566:710, separates eelgrass and sand *(Table 3.7)* based on presence versus absence of the red-edge characteristic of vegetation *(Figure 3.8 a & d).* These ratios hold similarity to some of the variables selected for the above-water data. The 566:600 ratio represents substrate constituents similar to the R'566 and R'580 variables of the above-water model while the 566:710 functions similarly to the 668:710 ratio. It can be inferred that the remaining above-water variables, s500-530 and R'602, are more dependent on attenuation features created by water constituents.

In summary, the band set selected here based on above water spectra is consistent with Fyfe's (2003) recommendations. Its bands, calculated within a 4nm interval, are narrow and do not overlap. It targets the peak (R'566) and shoulders (s500-530 & R'580) of the green reflectance peak maxima, the red absorption feature (R'602 & 668:710), the epiphyte reflectance region (R'580), and the vegetation NIR reflectance feature / red edge (668:710). In the case of water corrected data, its bands target the green reflectance peak maximum and eelgrass epiphyte reflectance features (566:600) as well as the vegetation NIR reflectance feature / red edge (566:710). Comparison of the indices selected for above-water data with those selected for water-corrected data suggests that the relative attenuating effects of the water column play a significant role in the above-water variable s500-530 and R'602.

Table 3.5. Set 2 (MDA result) separability of shallow eelgrass (<3m) spectra from other benthic substrate spectra acquired from above water. A dark box represents good separability (M-statistic > 1) and an empty box denotes poor separability (M-statistic < 1). The value in the box is the M-statistic result.

Band	shallow sand	shallow green algae	deep eel	deep sand	deep water
s500-530	5.73	1.63	1.90	0.49	1.76
R'566	0.56	1.40	2.51	0.68	2.80
R'580	2.10	1.64	0.33	3.21	1.05
R'602	5.70	0.64	0.56	2.46	0.25
668:710	2.06	0.34	1.45	1.44	1.49

Table 3.6 Separability of deep eelgrass (>3m) spectra from and other benthic substrate spectra acquired from above water. A dark box represents good separability (M-statistic > 1) and an empty box denotes poor separability (M-statistic < 1). The value in the box is the M-statistic result.

Band	shallow sand	shallow green algae	shallow eel	deep sand	deep water
s500-530	11.45	2.91	1.90	4.55	0.09
R'566	1.62	0.56	2.51	1.47	1.10
R'580	3.86	2.93	0.33	6.60	2.10
R'602	8.93	1.19	0.56	4.22	0.26
668:710	1.35	0.95	1.45	0.86	0.75

Table 3.7 Separability of eelgrass spectra from and other benthic substrate spectra acquired from above water and corrected for water column attenuation. A dark box represents good separability (M-statistic > 1) and an empty box denotes poor separability (M-statistic < 1). The value in the box is the M-statistic result.

Band	sand	green algae
566:600	0.78	1.23
566:710	1.76	0.77

3.4.2 Water attenuation corrected model

Maritorena et al.'s (1994) water column correction performed well for sites shallower than 3 metres, resulting in spectral curves with similar shape to endmember spectra and magnitude within 20% error for a large portion of the visible range (480 - 660nm for eelgrass and 500 – 700nm for sand and green algae) (Figure 3.8 & 3.9). Generally, the water correction of the eelgrass spectra revealed clearer epiphyte features in the red region. The corrected green algae spectra showed a flatter green peak than the endmember likely caused by differences in senescent stage and biofouling between field sites and endmembers - both of which affect green reflectance (Drake et al., 2003; Werdell & Roesler, 2003). The corrected sediment spectra on average showed greater similarity to the low detritus sand spectra than to the heavy detritus sediment endmember spectra. This could be a result of correction inaccuracies and/or lower detritus density at the measured field sites.

The application of the Maritorena et al (1994) method to sites deeper than 3 m was unsuccessful, except in the green spectral region. This result is consistent with findings in the literature, where 4.5 m was the maximum depth to which plausible reflectance spectra have been derived with water correction (Heege et al., 2003). Since the depth variable of Maritorena's equation is part of the exponential term, the water correction proved very sensitive to depth errors, similar to the findings of others (Dierssen et al., 2003; Werdell and Roesler, 2003; and Conger et al., 2005). As such, the height of the eelgrass canopy can cause depth discrepancies in excess of one metre, or 0.5 metres on average as measured in the field. When a correction of 0.5 metres (z-0.5m) was applied on all shallow eelgrass samples, the blue and NIR spectral ranges showed lower percent error (within 20%) for the entire spectrum (Figure 3.9). however, it did appear to under-correct the red region, but since this region is a major epiphyte marker, the discrepancy may be due to biofouling differences between *in situ* spectra and endmember spectra.

The higher success of the water correction method in the green region was most likely due to the depth limit for which the HyperSAS sensor could detect the bottom signal. Dekker et al. (2005) method was used to calculate this depth limit, defined as the depth at which each substrate was no longer spectrally different from deep water (Figure 3.10a), given the water attenuation properties at the time (expressed as K_d). At the wavelength of furthest light penetration (566nm – lowest K_d), the depth restriction of the HyperSAS, based on the average K_d measured in the field, was 4.6 metres for biofouled and 6.3 metres for non-biofouled eelgrass. Assuming the range of field measured K_d values (Figure 3.10b*)*, the depth restriction can range from a minimum of 3.1 metres to a maximum of 15.2 metres in the green (Figure 3.10a). The depth restriction gets steadily shallower in the red and blue ranges to approximately 3 metres (Figure 3.10a) due to the relatively higher K_d values of these ranges, as seen in the water corrected spectra (Figure 3.8).

The depth restriction for benthic identification will vary depending on the transparency of the water and the magnitude of substrate reflectance. If measurements are taken when the water column is relatively clear (for instance, $K_{d(566nm)}$= 0.20), eelgrass may be mapped up to a depth of 15.0 m if not biofouled and 11.0 m if biofouled. If water is more turbid (e.g. $K_{d(566nm)}$= 0.47), the mapping may be limited to shallow intertidal areas of 3 m depth or less. On average, the depth limit was 4.5 - 6.0 m. This is a mid-range value among benthic mapping depth limits found by

other authors, which range from one to three metres in modelled CDOM-rich waters ($a_{CDOM}(400)$ = 15, chl = 6µg L^{-1}, TSM = 6 mg L^{-1}) (Vahtmae et al., 2006), ~ 2 m in TSM rich waters (TSM = 12.6) (Dekker et al., 2005) and temperate case 2 waters (Ackleson & Klemas, 1987) with Landsat, 3 m in turbid waters with Landsat (Roelfsema et al., 2006), and 6 m in moderate Case 1 waters with IKONOS (Purkis, 2005), to 11 m in modelled medium Case 1 waters ($a_{CDOM}(400)$ = 1.5, chl = 2 µg L^{-1}, TSM = 2 mg L^{-1}) (Vahtmae et al., 2006) and 18 m in very clear tropical case 1 waters with IKONOS, SPOT and CASI (Mumby & Edwards, 2002). Note that the satellite sensors should have shallower depth limits due to higher sensor noise and atmospheric influence (Dekker et al., 2005).

The M-statistic and MDA were applied on the shallow water-corrected data to determine if water correction offered an advantage, in regard to classification accuracy, over the lesser effort process of classifying above-water data. The selected Set 2 bands for the water corrected dataset provided the same accuracy in shallow areas (97%) as the above-water model, misclassifying only one green algae sample as eelgrass. The 566:710 separated vegetated and non-vegetated areas based on NIR signal, while the 566:600 ratio capitalized on the epiphyte reflectance feature in eelgrass at 600nm, its value being negative for eelgrass, positive for green algae, and close to one for sediment. Since classification of water corrected data was achieved with only two spectral indices, it has the benefit of requiring significantly fewer raw bands than the non-corrected model (three versus ten), but with the disadvantage of being restricted to 3 metres depth.

3.4.3 Endmember model

The above-mentioned variables selected for the water-corrected model (566:600 and 566:710) performed similarly well in classification of the endmember spectra (total accuracy 96%). Error was caused by two senescent green algae samples, misclassified as eelgrass. The endmember classification also showed high confusion between healthy green algae and non-biofouled eelgrass, indicating that successful eelgrass delineation depends in part on epiphyte presence. This is because separation of eelgrass and green algae by this model depends on the 566:600 ratio (Table 3.7). Healthy green algae and non-biofouled eelgrass have a negative value caused by high green reflectance and red absorption by chl-a. Loss of chl-a in senescent green algae and presence of epiphytes on eelgrass cause a flattening of the curve, making the ratio

closer to one or even positive. Therefore separation is most effective between healthy green algae and biofouled eelgrass or healthy eelgrass and senescent green algae. The difficulty of spectrally separating non-biofouled eelgrass from green algae is further illustrated by the fact that the only variable to provide an M-statistic greater than one for the separation of epiphyte-free eelgrass and green algae was 650:660 with a value of 1.07. Since a suitable band set for remote imagery should target the full range of spectral features that characterize each cover type, whether fouled or non-biofouled (Fyfe, 2003), it is suggested that these bands be added to the overall band during classification of water corrected imagery if excessive eelgrass-green algae confusion is found upon preliminary accuracy assessment.

3.4.4 LAI and percent cover

Generally, as LAI and percent cover increased, NIR reflectance increased (Figure 3.12). Blue and red reflectance decreased due to increased absorption across the entire visible spectrum possibly caused by increased chlorophyll-*a*, which is in agreement with observations on seagrass in the Bahamas (Dierssen *et al.*, 2003) and on mudflat microphytobenthos in the North Sea (Kromkamp, 2006). However, converse to Dierssen et al.'s findings, the 510:530 ratio and 555 nm magnitude showed no relationship with LAI in water column corrected spectral sets. Rather, the most effective variables for LAI determination were sensitive to chlorophyll-*a* through the red edge (R'700 and chl_NDI) and red-blue or NIR-blue reflectance relationships (NPCI and NIRB), while for the percent cover model, the blue-red reflectance relationship (NPCI) was selected. These findings are in agreement with Kromkamp (2006), who found that the red and NIR based indices were most sensitive to spectral shape changes caused by increases in chlorophyll-a concentration.

LAI models for above water and water column corrected data sets performed equally well with total accuracies of 80.0%. All misclassifications occurred in the adjacent class to the correct class (i.e. two sparse classified as medium, one medium classified as sparse), suggesting possible error intrinsic with valuating LAI by photographic index (Kutser et al., 2007). In ideal circumstances, LAI would be enumerated *in situ* immediately after spectral measurement and a regression approach used to derive an LAI model (Dierssen et al., 2003).

3.4.5 Epiphytes

The two types of epiphytes showed different effects on the eelgrass spectra. Diatom epiphytes caused decreased reflectance in the visible portion of the spectrum due to absorption by chlorophyll in the blue and red spectral regions, decreased eelgrass green reflectance due to physical blocking of eelgrass reflectance and absorption by accessory pigment fucoxanthin at 500-590 nm (Rowan, 1989), and a blue shift of the red edge due to higher red reflectance. The major reflectance features of epiphytic diatoms were located at 582 nm, 602 nm and 645 nm, which are close to, although shifted approximately 5 nm to the right, of Fyfe's (2003) findings of 575 nm, 590 nm, and 640 nm. Absorption features related to chlorophyll-*a* and –*c* are at 586nm, 632nm, and 670nm, and are consistent with Méléder (2003).

Red algae epiphytes resulted in greater absorption of visible light than diatoms did, possibly due to higher pigment content and larger surface area compared with diatoms, and conversely, a NIR shift of the red edge (Figure 3.5). Its major reflectance features were found to occur at 586nm and 652nm with absorption at 618nm and 670nm due to absorption by biliproteins (Glazer et al., 1976; Rowan, 1989), but trended closer to that of diatoms when senescing (Figure 3.5).

It follows that the only spectral features that are spectrally distinct between the two epiphyte types regardless of senescence stage are the 602nm reflectance of diatoms and the NIR shifted red edge of red algae. In above-water HyperSAS measurements, these separate peaks could not be resolved; however the green peak of eelgrass with diatoms was located at a slightly shorter wavelength (568 nm) than eelgrass with red algae (572 nm). Water corrected spectra do show the distinct epiphyte peaks of red algae and diatoms; however diatom peaks existed in all samples, possibly because of their presence in the water column, as indicated in the photosynthetic HPLC composition (Figure 3.2). MDA models selected variables related to these described differences, mainly the high visible spectra absorption and high red reflectance of red algae in above-water spectra (R'580), and high visible spectra absorption and red edge difference of red-algae in water-corrected spectra (668:710).

3.4.6 Landsat and IKONOS

For both simulated Landsat and IKONOS, the best models for eelgrass classification selected the same variables, and their eelgrass classifications performed with similar accuracy.

This was due to the nearly identical band placement and bandwidth. However, when it comes to classification of imagery, the difference in spatial resolution between the two sensors will likely have an impact. The low spatial resolution of Landsat (30 m) will detect more substrate heterogeneity within a pixel, ensuring more spectral mixing than IKONOS (2 m spatial resolution). As the simulation does not account for this spatial mixing, the MDA method is anticipated to perform more poorly on Landsat than implied here, as shown by Mumby et al. (1997), Mumby et al. (1998), and Mumby and Edwards (2002). The authors found that while hyperspectral 5 m resolution CASI and multispectral 1 m resolution IKONOS resulted in seagrass classification at accuracy levels between 85-90%, Landsat accuracy was only 59%. It is possible that classification techniques that consider spectral mixing within a pixel, such as spectral angle mapper (SAM) and linear spectral unmixing (LSU), may produce more accurate results for this coarse spatial resolution. Nonetheless, regardless of classification accuracy, one must consider whether 30m is a proper resolution for resolving eelgrass distribution dynamics, especially at Sidney Spit where patch dimensions were commonly less than 5 x 5 m. Medium resolution imagery such as Landsat has produced limited results for mapping and monitoring small features less than 10m (Johansen *et al.*, 2008; Call et al, 2003; Luczkovich et al. 1993; Zainal et al. 1993), and for many eelgrass mapping studies, it was found that mapping elongate strips and small eelgrass patches required a pixel size less than 10 m – 15 m (Phinn et al., 2008; Kirkman, 1996; Dekker et al., 2005; Cracknell, 1999). Additionally, Clark et al. (1997) advised that 1 m spatial resolution was requisite to resolve and map meadow "blow-outs," important indicators in eelgrass bed dynamics.

Therefore the applicability of Landsat, or any other medium resolution sensor to seagrass mapping may vary depending on the size and extent of eelgrass beds, and the management goal in mind. 30m pixel size may be functional for presence/absence baseline data, but meadow patchiness, species delineation, and epiphyte detection require greater spatial detail (Kirkman,1996; Habeeb, 2007). In exception to this, Dekker *et al.* (2005) were able to detect seagrass species change using Landsat TM with 76% accuracy, but only in large meadows with depths shallower than 0.5m.

3.5 Conclusion

The spectral separability of eelgrass from other submerged substrates was demonstrated in this study based on reflectance values from the three sensors, *in situ* hyperspectral and simulated IKONOS and Landsat 7ETM+, by identifying the spectral variables (bands, slopes, and ratios) for which between-class variability was maximized. The efficacy of defined key spectral regions in identifying eelgrass was also assessed in classification of the spectral data at the two pre-processing scenarios, above water and water corrected, aiming to mimic different levels of image processing. The same was done for the separability of eelgrass percent cover, LAI, and epiphyte types. The results of this study suggested specific combinations of wavebands that could be used to map eelgrass distribution with remote imagery, a non-destructive approach that permits repeated measurements in a specific location. The defined indices could be used to select a suitable multispectral sensor or to reduce large volumes of airborne or satellite hyperspectral data for effective remote eelgrass mapping.

Generally, 95% accuracy can be achieved for mapping eelgrass distribution by applying a discriminant analysis classification procedure to a land-masked image with the following set of five indices as inputs: *s*500-530, R'566, R'580, and R'602 and 668:710. It would not be necessary to segregate the image by depth or mask out optically deep water. If Maritorena et al.'s (1994) water column correction is applied, the input indices were 566:600 and 566:710, however, only shallow areas (< 3 m) can be accurately mapped (97%). Because this water correction is highly sensitive to small errors in depth, more reliable and consistent results may be achieved with a depth independent method such as Lyzenga's (Lyzenga, 1978; Lyzenga, 1981) method successfully used by Ciraolo *et* al (2006) and Mumby et al (1998), or the variant of Beer's Law derived by Dierssen *et al* (2003). Nonetheless, these methods are expected to have the same depth limitations as the Maritorena et al. (1994) method. The three metre depth restriction of the water correction method is equal to the depth limit of the sensor for resolving a benthic substrate, which depends on the benthic reflectance, water constituent composition and the sensor noise. These results are similar to results from Werdell and Roesler (2003), Dierssen et al. (2003), and Conger et al. (2005).

LAI classification of above water eelgrass spectra was possible with 80% accuracy if using the NPCI index and R'700, and percent cover classification was possible with 75% when using NPCI. Classification of diatom and red algae epiphyte types was possible with 100%

accuracy above water using R'580 and 90% on water corrected spectra using R'680. However, sample size was small for all classifications within eelgrass (n=24) and should be noted with scrutiny.

All of these high accuracy results are very encouraging, but they are based on punctual hyperspectral *in situ* measurements, and thus covering small areas. For large scale mapping of eelgrass, satellite imagery provide better spatial data. Our results suggest that the achievement of high accuracy (~93%) for both IKONOS and Landsat simulated reflectance is possible. However, the larger pixel size and henceforth higher within-pixel spectral heterogeneity will likely negatively affect the classification when performed on Landsat imagery. Also, the availability of the NIR should improve the classification accuracy for both sensors, in the case of exposed vegetation. Further, the classifications should be resilient to slight atmospheric correction errors, as they are independent of the blue wavebands where atmospheric interference is greatest. Finally, effort should be made to collect imagery during times of the year when water diffuse attenuation coefficients are known to be low so that the spectra of deep subtidal eelgrass beds are not strongly affected by water optical constituents.

The key wavelengths identified in this study are recommended for application with analysis of airborne and satellite imagery when the goal is delineating the spatial distribution of eelgrass. Applying these key wavelengths in the programming of airborne sensors, or the development of coastal based satellite spectral sensors, would yield an effective separation between eelgrass *Zostera marina* and associated benthic cover in the shallow coastal waters of Sidney Spit, GINPRC, and possibly in other temperate coastal areas. Working with the suggested spectral variables, and within the time and location constraints of the model (to be determined), the possibility is presented of mapping eelgrass in 'real-time' and constructing historical eelgrass distribution maps as far back as suitable imagery is available; in the case of IKONOS since January 1, 2000 and for Landsat ETM+ since April 15, 1999. Landsat MSS imagery is available as far back as 1972, although with 80 x 80 m spatial resolution. These maps could be used as baseline inventory data and, when merged with other ancillary data layers (e.g., estuarine water flow and sediment loads, salinity, temperature, fish and invertebrate distributions), be used to report on the structure and functioning of coastal ecosystems (Strittholt et al., 1996; Johansen et al., 2009).

The following points should be considered in the application of our findings:

(1) K_d variability:

The value of K_d changes with varying concentrations of suspended sediment, dissolved organic matter, and phytoplankton. If the water optical constituents, and therefore K_d, of the water at the time of image acquisition are far different than the ones measured in this study (Table 3.2), the selected spectral indices for the above water classification may be less effective. The classification of water corrected spectra may, however, remain reliable with fluctuating K_d, at least to the tested maximum of $K_d(440) = 0.82\ m^{-1}$, $K_d(550) = 0.72\ m^{-1}$, and $K_d(650) = 1.06\ m^{-1}$, and only areas shallower the three metres. Methods for deriving K_d values from imagery exist (Boss and Zaneveld 2003) and could be used as input to the water column correction algorithm.

(2) Presence of brown algae:

Since very little incidence of brown algae was present at the Sidney Spit study site, it is not represented in the selected variables. The efficacy of the variables may change should it be used in an area with high occurrence of brown algae. Since the main differences between brown algae species and green vegetation is higher red and lower green reflectance, it is possible that the selected indices, located mainly in the green and red portion of the spectrum should capture the variation. However confusion may occur between brown algae and diatom epiphytes.

(3) Exposed eelgrass:

Due to the logistics of data collection from a boat, spectral measurements of exposed eelgrass could not be obtained. The classification models could be improved by adding *in situ* spectra of exposed eelgrass spectra, which would have much higher reflectance values than submerged vegetation at all wavelengths, particularly in the NIR region. To minimize the lack of exposed eelgrass representation on the bands/ indices selection, the ratio 668:710 was included in the model. This ratio incorporates the NIR region and captures the red-edge, an important feature in identifying exposed vegetation. This ratio did not change the accuracy of classifying submerged data, but in the case of a dataset with exposed vegetation, it may be of benefit (Fyfe, 2003).

(4) Statistical analysis:

Although MDA is robust to departures from multivariate normality, and in the case of this dataset, the departures were fairly small, it still remains that the results should be interpreted with more care (Williams, 1983; cited by Richardson et al., 2004). Therefore the MDA is used in

this case for exploratory analysis rather than statistical testing. Additionally, the use of a stepwise variable selection method may have limited the spectral variable selection, since stepwise analysis does not allow variables back into the model once they have been removed. A neural network technique such as Tabu search (Glover 1989, 1990; Glover et al., 1993) considers more variable combinations and would be more likely to arrive at the best model.

Sample sizes have been listed throughout the discussion and should be noted with scrutiny, especially for classification within eelgrass. For example, the sparse class in the percent cover model contained only four samples. Models could be improved upon by increasing the sample size and forming equal size classes.

(5) Tidal effects:

LAI estimation is more beneficial than percent cover estimation because it provides an absolute quantitative measure. It can be combined with leaf area-to-mass relationships to derive biomass, or with leaf growth rates to be translated into Net Primary Productivity (Dierssen et al., 2003), both of which can be further integrated into carbon budget modelling to assess the impact of natural disturbances, climate change, and management strategies. Percent cover, on the other hand, fluctuates with tidal state. Eelgrass blades assume a vertical orientation at slack tide and become nearly parallel to the substrate in high tidal flux or when exposed on the surface. But the eelgrass bed orientation issue is two-fold. The extreme flattening of blades caused by a strong tidal current is expected to increase the visible reflectance, creating over-estimates of LAI when using a model developed for a slack tide. It is therefore especially important for effective temporal monitoring of eelgrass to always acquire the imagery at the same tidal state. This study took place during slack low tide, however further investigation is recommended into the tidal state that optimizes LAI estimates.

(6) Eelgrass phenology:

Species discrimination in the remote sensing of vegetation is achievable as long as the species and substrates under study are spectrally distinct over space and time (Fyfe, 2003). For example, high classification accuracies at Sidney Spit are owed in part to the large spectral magnitude differences between eelgrass and sand. Classification of an area where substrates are spectrally darker and more closely resemble the reflectance of submerged eelgrass may not perform as well (Ackleson and Klemas, 1987). Likewise, plant phenology and water properties inevitably vary over time and among locations. Classification at a time when eelgrass is largely

senescent or sparse may also result in different accuracies. Therefore it is recommended that these models be tested on data gathered at Sidney Spit over different seasons and at additional areas in the Gulf Islands National Park to confirm whether these models are local- and time-specific, or more widely applicable.

Chapter 4

Mapping of eelgrass (*Zostera marina*) at Sidney Spit, Gulf Islands National Park Reserve of Canada, using high spatial resolution satellite and airborne imagery

Abstract

Eelgrass, a fundamental part and key indicator of coastal ecosystem health, has exhibited worldwide decline in response to anthropogenic pressures. It is therefore important that eelgrass distribution be known and monitored as part of an effective coastal ecosystem management strategy. A proposed alternative to current manual mapping methods is the use of remote imagery, which can cost- and time- effectively cover large and inaccessible areas nearly instantly and frequently. The purpose of this study was to explore and compare the efficacy of high spatial resolution airborne (AISA) and satellite (IKONOS) imagery in mapping eelgrass location and biophysical parameters at Sidney Spit, GINPRC. The primary objective was to determine the optimal combination of spectral and spatial resolution, and image processing level for accurately resolving bed location, leaf area index (LAI), and epiphyte type. A two-metre resolution hyperspectral AISA image and a four-metre resolution multispectral IKONOS image were acquired over Sidney Spit in August 2008. Concurrently, *in situ* above-water hyperspectral remote sensing reflectance, underwater videography, and water samples for optical constituent analysis were collected. The *in situ* spectra, treated as spectral "truths," were statistically analyzed to select the key bands and band ratios unique to eelgrass (presented in Chapter 3). Both images were subjected to varying combinations of image processing steps: atmospheric correction, surface glint correction, deep water masking, and water depth removal. Each processed product was then classified using various supervised and unsupervised methods, with full spectral range and with the reduced variable dataset determined in Chapter 3. In the case of both AISA and IKONOS images, the highest classification accuracies were achieved with atmospheric correction, glint correction, deep water masking, and maximum likelihood (ML) classification of the indices: slope500-530nm, first derivatives of 556nm, 580nm, and 602nm for AISA and 480nm, 550nm, 480:665 and 550:665 for IKONOS. The one exception was that deep (> 3 m) areas of IKONOS were better classified with minimum distance classification (MD). AISA achieved eelgrass producer and user accuracies of 85% in water shallower than 3 m, and 93% in deeper areas. IKONOS achieved 79% for shallow waters and 82% for deeper areas. Endmember classification showed accuracies over 84% and 71% in AISA and IKONOS imagery respectively. The largest source of confusion was between eelgrass and green algae, and between exposed vegetation and exposed eelgrass. LAI and epiphyte type classifications produced poor results in all cases except one; epiphyte presence / absence could be delineated with 87% accuracy. This study resulted in recommendations for remote eelgrass mapping and monitoring within the Gulf Islands National Park Reserve.

4.1 Introduction

Eelgrass, *Zostera marina,* is a fundamental part of coastal ecosystem health. It functions as a shoreline baffle against wave and current action (Fonseca and Cahalan, 1992), a sediment stabilizer (Mateo et al., 2003), a water and pore water oxygenator (Hemminga & Duarte, 2000), and a major determiner of oxygen, carbon, nitrogen and phosphorous balance within the ecosystem (Hemminga & Duarte, 2000; Apostolaki, 2010). Eelgrass also serves a nursery ground and food source for many marine organisms including out migrating juvenile salmon (*Onchorhynchus* spp.), Pacific herring (*Clupea harengus*), Dungeness crab (*Cancer magister*), rare invertebrate species, and black brant geese (*Branta bernicla*) (Mazzella et al., 1989; Sewell *et al.,* 2001, Borg et al., 2006). Accordingly, several studies have shown a link between historical fish abundance and eelgrass presence (Phillips, 1984; Murphy et al., 2000; Johnson et al., 2010) and justifiably, eelgrass has been used worldwide as an indicator of coastal ecosystem health (Sewell *et al.,* 2001), and is a resource of detrimental importance to sustainable commercial fisheries (Adams, 1976).

Despite its far-ranging importance, eelgrass has exhibited worldwide decline in response to anthropogenic pressures such as sea surface temperature change and light restriction due to sedimentation and eutrophication (Nienhius, 1983; Orth & Moore, 1983; Giesen *et al,* 1990; Dennison *et al.*, 1993; Dejong & Dejong, 1992; den Hartog, 1994; Sedinger *et al.*, 2006). It is therefore important that eelgrass distribution be known and monitored as part of an effective coastal ecosystem management strategy. Due to the time sensitive nature of the issue, this monitoring must be done cost- and time-effectively (Dekker, 2005). Eelgrass distributions are currently mapped manually by snorkelling diving, underwater video, and transect surveys; a labour-intensive process involving large time investments and accuracy levels that are difficult to define (Environment Canada, 2002; Roelfsema, 2009). A proposed alternative is the use of remote imagery, which is more time and cost effective, can cover large areas nearly instantly with a frequent return rate, can be acquired in hard to access areas, and could possibly be automated. Therefore, the ease of a reasonably accurate routine optical remote assessment procedure could lead to improved spatial and temporal coverage of coastal monitoring programs aimed at investigating eelgrass distribution dynamics and its role in the larger coastal ecosystem (Werdell and Roesler, 2003).

Identification of a target covertype such as eelgrass with remote imagery is dependent on the target having a spectral signature unique among its surrounding covertypes, and being perceivable by the sensor's spectral sensitivity. This target spectral signature is altered on its way to the sensor by attenuation in the atmosphere, at the water surface, and within the water column (Kirk, 1994). Image processing techniques such as atmospheric, surface glint, and water column corrections are often necessary to compensate for these attenuations prior to classification in order to achieve suitable mapping accuracy (Lyzenga, 1978; Guzzi et al., 1987; Maritorena et al., 1994; Hedley et al., 2005).

Many researchers have demonstrated success in remote benthic classification at varying levels of image processing, specifically, for seagrasses (Pasqualini et al., 196; Armstrong, 1993; Mumby et al., 1997; Lunden and Gullstrom, 2003; Dekker et al., 2005; Forster & Jesus, 2006; Gullstrom et al., 2006; Peneva et al., 2008; Fyfe 2009; Roelfsema et al., 2009), for macroalgae (Andrefouet et al., 2004, Gower et al., 2006; Kutser et al., 2006; Vahtmae et al., 2006) and for corals (Holden & Ledrew, 1998, 1999; Hochberg & Atkinson, 2000; Call et al., 2003; Hedley et al., 2004; Mumby et al., 2004; Phinn et al., 2005; Mishra et al., 2006; Lobitz, 2008). However the vast majority of these studies take place in Case 1 waters, which, being void of constituents other than phytoplankton, are relatively transparent. Mapping becomes more challenging in the more complex temperate Case 2 waters, which contain coloured dissolved organic material, suspended organic and inorganic particles, and phytoplankton, each of which attenuate the incident and reflected light uniquely (Dekker, 1992; Kirk, 2003). These turbid waters make the benthic substrates more difficult to detect and remain a challenge for benthic mapping (Phinn et al., 2005; Vahtmae, 2006).

Additionally, the majority of benthic mapping studies have been conducted with multispectral scanners (e.g., Ackleson & Klemas, 1987; Ferguson & Korfmacher, 1997; Andrefouet et al., 2002; Bouvet et al, 2003; Lunden & Gullstrom, 2003; Purkis, 2005; Shweizer et al, 2005; Dekker et al., 2006; Fornes et al., 2006; Mishra et al, 2006; Su et al., 2006). Hyperspectral sensors are now available that, by measuring radiance at hundreds of spectral wavelengths, offer far greater spectral detail for characterizing spectral signatures. Hyperspectral sensors have shown improvements in benthic classification accuracy (Mumby et al. 1997; Dierssen et al., 2003), but have the downfall of being much more expensive than multispectral sensors. The best scenario is a multispectral sensor with bands placed at key wavelengths, where

eelgrass exhibits unique spectral characteristics (Fyfe, 2003). To explore the degree of cost-benefit gains with increased spectral resolution, this study compared the capacity of the airborne hyperspectral sensor AISA (>200 bands), with the four band multispectral satellite sensor IKONOS to map eelgrass and its biophysical properties at Sidney Spit, GINPRC. These sensors were also selected for their high spatial resolution (2 x 2 m and 4 x 4 m, respectively) in consideration of the spatial scale of eelgrass bed dynamics, where beds can be as small as a couple metres in diameter.

The specific objectives were as follows:

(1) Classify the AISA and IKONOS images according to a pre-determined benthic classification scheme at varying stages of the correction process and validate with ground truth samples to assess the accuracy of eelgrass delineation. The stages were: georectification, atmospheric correction, surface glint correction, water attenuation correction, and optically deep water masking.

(2) Classify the eelgrass class from the most accurate substrate map by LAI and epiphyte species (two metrics commonly used to assess eelgrass habitat (Chapter 1)), at coarse (two-class) and fine (three-class) levels of detail.

4.2 Methodology

4.3.1 Field survey

Ground-truth data was supplied by means of an extensive benthic survey of the study site, conducted from July 30 to August 3, 2008, and described in Chapter 2, Section 2.2.1. Additional sites were visited on July 7, 2010 to increase the deep (> 3 m) substrate sample size, under the assumption that benthic substrate presence/absence had remained similar since field collection in 2008. The number of sites surveyed for each substrate is presented in Table 4.1.

Table 4.1. Number of sites visited in the survey of benthic substrates, and division of sites into classification training and testing sites. E = eelgrass, Ag = green algae, Ab = brown algae, S = sand, Asp = sea asparagus, dW = optically deep water, d = deep, s = shallow, and e = exposed. * there were no brown algae training sites present in the IKONOS image due to large pixel size and small patch size of brown algae (~1 x 1m).

			Training / Validation Sites (~20%/80%)	
Substrate Classes	**Substrate Abbrev.**	**Ground-truth Survey Sites**	**AISA**	**IKONOS**
Shallow Eelgrass	(sE)	265	51 / 235	28 / 138
Deep Eelgrass	(dE)	19	4 / 15	3 / 13
Green Algae	(sAg)	129*	24 / 105	13 / 55
Shallow Sand	(sS)	49	10 / 39	6 / 20
Deep Sand	(dS)	32	6 / 26	2 / 7
Brown Algae	(sAb)	7	2 / 5	*
Exposed Sea Asparagus	(eAsp)	6	2 / 4	2 / 6

**** 84 Ulva fenestrata , 23 Enteromorpha spp., and 22 filamentous green algae***

AISA Value-Added Eelgrass Classes	**Abbrev.**	**Training / Validation Pixels (~20%/80%)**		
Eelgrass LAI: Coarse	(sE_{LAI})	***Low (<1)***	***High (>1)***	
		4 / 19	13 / 52	
Eelgrass LAI: Fine		***Low (<1)***	***Med (1-2)***	***High (>2)***
		4 / 19	6 / 20	7 / 32
Eelgrass Epiphyte Type:	(sE_{EPI})	***Absent***	***Present***	
		4 / 16	8 / 35	
Eelgrass Epiphyte Type: Fine		***Absent***	***Diatom***	***Red Algae***
		4 / 16	5 / 24	3 / 11

IKONOS Value-Added Eelgrass Classes	**Abbrev.**	**Training / Validation Pixels (~20%/80%)**		
Eelgrass LAI: Coarse	(sE_{LAI})	***Low (<1)***	***High (>1)***	
		3 / 9	6 / 22	
Eelgrass LAI: Fine		***Low (<1)***	***Med (1-2)***	***High (>2)***
		3 / 9	4 / 14	2 / 8
Eelgrass Epiphyte Type:	(sE_{EPI})	***Absent***	***Present***	
		3 / 9	6 / 16	
Eelgrass Epiphyte Type: Fine		***Absent***	***Diatom***	***Red Algae***
		3 / 9	4 / 12	2 / 4

4.3.2 Imagery Acquisition

Hyperspectral, high spatial resolution AISA airborne imagery was acquired over Sidney Spit by Terra Remote Sensing on August 16, 2008 at 12:14 during low tide (0.42m) (Figure 4.1a). The AISA sensor flew at an elevation of 1500 metres, acquiring six flight-lines with a pixel size of 2 x 2m and a swath width of 592m. The sensor was programmed at 2nm spectral resolution from 408nm to 2494nm. Sun glint was minimized by flying in a direction as close as possible to perpendicular with the incident solar angle (Mobley, 1999; Kay et al., 2009).

An IKONOS satellite image was acquired on August 31, 2008 at 11:12 local time (Figure 4.1b). Tidal height was 0.75m and was within one hour of low tide. IKONOS is a multispectral sensor with three visible bands and one NIR band, a pixel size of 4 x 4m, a swath width of 11.3km, and 11-bit data (Geoeye, 2006).

Figure 4.1 RGB composite of the (a) hyperspectral AISA image (R = 650, G = 550, B = 450nm) (2 x 2 m resolution) and (b) multispectral IKONOS image (R = 665 nm, G = 550nm, B = 480nm) (4 x 4 m resolution).

4.3.3 Image Processing

A flow diagram of all image processing steps can be found in Figure 4.3. In summary, prior to classification, the images were geometrically corrected, land masked, and atmosphere corrected through two methods: Empirical Line calibration (ELC) and radiometric transfer model *Tafkaa* (Montes et al., 2004), followed by cloud masking, surface glint correction, and water attenuation correction. Lastly, five different classification approaches were applied to the images: K-Means, Minimum Distance (MD), Maximum Likelihood (ML), Linear Spectral Unmixing (LSU), and Spectral Angle Mapper (SAM). The accuracy of each approach was tested at each of the following processing levels: (1) raw data, (2) atmosphere and surface glint corrected data, and (3) atmosphere, surface glint, and water attenuation corrected data. Finally, "value-added" eelgrass classifications were then attempted for LAI and epiphyte type. Detailed description of the processing steps is provided in the following section.

Step 1: Georectification, land mask, and spectral smoothing

AISA: The six flight lines were geometrically corrected with Hyperbatch, a custom software developed by the Hyperspectral and LiDAR Research Group at the University of Victoria, which used the airplane's positional measurements and a LiDAR DEM collected side by side with the radiance data. The flight lines were geographically matched manually to one another to minimize residual geo-locational error (average RMSE = 0.30pixels, or 0.60m) and then mosaicked together. A land mask was defined as all pixels with a blue (450nm) band digital number greater than 2200. All remaining land vegetation pixels were masked out manually using knowledge of the area, but this could also be achieved with a bathymetry layer at Mean Lower Low Water level of zero. To remove scene noise, data were then spectrally smoothed with a Gaussian smoothing window of 10nm.

IKONOS: The IKONOS image was geometrically corrected by the data provider, Pacific Geomatics, using satellite orbit model, BC TRIM (British Columbia Terrain Resource Information Management) vectors, and field measured ground control points provided by this research.

Step 2: Atmospheric Correction

AISA and IKONOS: Two atmospheric corrections were applied to the imagery and their efficacy compared; the empirical-based ELC (Teillet *et al.,* 1990) and the radiative transfer model-based method *Tafkaa* (Montes et al. 2004). *Tafkaa* was developed by the US Naval Research Laboratory (NRL) for atmospheric correction of images acquired over oceans (Montes and Gao, 2000; Montes et al., 2004). The efficacy of each atmospheric correction was evaluated by comparing corrected image spectra with *in situ* spectra measured at the same location and similar tidal heights.

The ELC was conducted in ENVI image processing software. In this method, acquired *in situ* remote sensing reflectance measurements were considered to be atmospherically correct as they were corrected for downwelling sun and sky irradiance (Eq. 2.5 - 2.7). The corrected image output was generated by applying a best-fit (least squares) regression line for each band between the original image radiance values and the corresponding *in situ* reflectance measurement. The inputs were the average values from a 3 x 3 pixel region of interest (ROI) selected in the original radiance image and its corresponding *in situ* remote sensing reflectance spectrum (Karpouliz and Malthus, 2003) for each of: one dark region (optically deep water) and one bright region (shallow sand, 0.75m depth) to encompass the full brightness range of the image (Karpouliz and Malthus, 2003; Smith and Milton, 1999). The remaining image pixels were then adjusted using the regression line for each band.

Tafkaa corrects for atmospheric attenuation by modeling the atmospheric absorption and scattering effects present at the time of acquisition. Atmospheric absorption is modelled from a high-resolution database of gas absorption coefficients, temperature, and pressure profiles with ATREM (*Atmosphere* REMoval) radiative transfer code (Gao et al. 1993; CSES, 1999), while scattering is calculated from an aerosol profile measured *in situ* (Montes et al., 2004). Inputs to this model were date, time, coordinates, elevation, sensor altitude, temperature, ozone amount, relative humidity, wind speed, and aerosol optical depth (AOD) measured by the AERONET (AErosol RObotic NETwork) sun-photometer on nearby Saturna Island (Holben et al. 1998). Specific inputs for each image can be found in Appendix F.

Step 3: Cloud masking

AISA: There were no clouds present in the AISA image.

IKONOS: The low-altitude cloud mask was defined for IKONOS similar to Montes et al, (2004) as all pixels where

$$R_{rs}^{(0+)}(805nm) > 0.1sr^{-1} \quad (4.1)$$

Where $R_{rs}^{(0+)}$ is the above water remote sensing reflectance value for a given pixel.

Step 4: Sun glint correction

Sun glint is caused by sunlight reflecting directly off of the water surface and into the sensor (specular reflection) and is a result of sun sensor geometry and the waves redirecting the sun's irradiance (Hedley et al., 2005). Hedley et al. (2005) algorithm was applied for sun glint removal, using the longest available NIR wavelength, 748nm. The method assumes no water leaving reflectance in the NIR region, and that glint present in the visible wavelengths is linearly related to NIR reflectance. The slope of the linear regression, b_i, between the reflectance at each visible band *i* ($Rrs_i^{(0+)}$) and the reflectance at 748nm ($Rrs_{748nm}^{(0+)}$) served as the proportionality factor used to yield the amount of glint in the pixel. The glint reflectance was then removed from the visible reflectance to obtain the glint-free value, $Rrs'^{(0+)}_i$, as follows:

$$Rrs'^{(0+)}_i = Rrs_i^{(0+)} - b_i\,(Rrs_{748nm}^{(0+)} - \text{Min}\ Rrs_{748nm}^{(0+)})$$

Where Min $Rrs_{748nm}^{(0+)}$ is the minimum $Rrs_{748nm}^{(0+)}$ value found in the whole image and represents a pixel containing no sun glint (Hedley et al., 2005).

Because this method assumes the water leaving signal at NIR wavelengths is zero, pixels contain shallow vegetation with NIR signals greater than that of deep water were masked out to avoid over-correction. The mask pixels were defined as:

$$\text{NDVI} > 0 \text{ and } \text{Rrs}^{(0+)}_{(748\text{nm})} > 0.001\text{sr}^{-1} \quad (4.2)$$

where NDVI is the normalized difference vegetation index (Rouse et al., 1974):

$$\text{NDVI} = [\,Rrs_{710nm}^{(0+)} - Rrs_{680nm}^{(0+)}\,] / [\,Rrs_{710nm}^{(0+)} - Rrs_{680nm}^{(0+)}\,] \quad (4.3)$$

Step 5: Water attenuation correction

The attenuating effects of the water column were removed from the image by first converting the above water reflectance, $R_{rs}^{(0+)}$, to reflectance just below the surface, $R_{rs}^{(0-)}$ (Lee et al., 2002),

$$R_{rs}^{(0-)} = \frac{R_{rs}^{(0+)}}{0.52 + [1.7 \cdot R_{rs}^{(0+)}]} \tag{4.4}$$

and then calculating R_{rs}^{b}, the substrate reflectance without water column interference, using Maritorena et al.'s (1994) equation (Eq. 4.5) rearranged (Eq. 4.6) (Brando et al, 2009), as follows:

$$R_{rs}^{(0-)} = R_{rs}^{(0-)dp} + \left(R_{rs}^{b} - R_{rs}^{(0-)dp}\right) \cdot e^{-2K_d z} \tag{4.5}$$

$$R_{rs}^{b} = \frac{R_{rs}^{(0-)} - R_{rs}^{(0-)dp} \cdot (1 + e^{-2K_d z})}{e^{-2K_d z}} \tag{4.6}$$

where z is the substrate depth, K_d is the diffuse downwelling attenuation coefficient of the water, and $R_{rs}^{(0-)dp}$ is the reflectance of optically deep water (>30m depth). The efficacy of the water column correction was assessed by comparing the resulting spectra to endmember *in situ* spectra of the same benthic class.

Step 6: Optically deep water masking

Submerged substrate classification accuracy can be greatly improved by masking deep water (Ackleson and Klemas, 1987; Zainal, 1993). Therefore, classification was attempted on images with both masked and non-masked optically deep water. The optically deep water threshold was defined for each image as the average depth at which eelgrass and sand could no longer be discernable from deep water (i.e. becomes optically "deep"). Following Dekker *et al* (2005), the detectability threshold of a given submerged substrate occurs when the second term of Maritorena et al.'s equation (Eq. 4.5) is equal to the detecting threshold of the sensor in reflectance terms (R_{rs}^{DT}):

$$\left[R_{rs}^{b} - R_{rs}^{(0-)dp}\right] \cdot e^{-2K_d z} = R_{rs}^{DT} \tag{4.7}$$

Where R_{rs}^{b} is the mean endmember spectra of the substrate, $R_{rs}^{(0-)dp}$ is the average optically deep water reflectance just below the surface, K_d is the average diffuse attenuation coefficient

calculated from the HyperPro in-water profile measurements of optically deep water (Eq. 2.14), and R_{rs}^{DT} is the detecting threshold of the sensor, i.e. AISA or IKONOS. R_{rs}^{DT} was defined as the wavelength-dependent standard deviation of reflectance within a homogeneous 33 x 33 pixel optically deep water region (Wettle et al., 2004; Brando et al, 2009). The detectability depth limit of each substrate for each sensor was computed by solving for z in Eq. 4.8 and rounding up to the nearest 0.5 m value:

$$z = \frac{1}{2K_d} \cdot \ln\left[\frac{R_{rs}^{b} - R_{rs}^{(0-)dp}}{R_{rs}^{DT}}\right] \tag{4.8}$$

Where all R_{rs} values are remote sensing reflectance values at wavelength 566nm where K_d was lowest, and therefore light penetrated the furthest (Figure 4.6b). At regions deeper than this threshold, the substrate was no longer discernable from deep water. The threshold was found to be 5.5 m for AISA and 7.5 m for IKONOS, based on non-biofouled eelgrass. The threshold was deeper for IKONOS because the water had a lower $K_{d\,(566nm)}$ value and was therefore more transparent at the time of IKONOS acquisition.

Step 7: Classification and validation

Classifications were run independently for three purposes: (1) substrate classification for delineating eelgrass presence at the three different processing levels mentioned in Section 4.3.3, (2) LAI classification of eelgrass, and (3) epiphyte presence/absence classification of eelgrass. Table 4.1 outlines the following classification scheme: shallow eelgrass (sE), deep eelgrass (dE), shallow sand (sS), deep sand (dS), shallow green algae (sAg), shallow brown algae (sAb), and exposed sea asparagus (eAsp). Substrates were defined by depth range (< 3m and > 3m) as a means of improving classification of substrates existing in a wide bathymetric range and therefore having a large above-water spectral range (Pasqualini et al., 1997). The three metre threshold was defined according to Chapter 3, Section 3.3.3. Classification was performed on the image with and without optically deep water masking (defined in step 6). The shallow and deep eelgrass classes from the highest accuracy classification were then combined and retained as an independent data layer for additional classifications of LAI and epiphyte type, to a coarse two-class level, and a fine three-class level (Dierssen et al., 2003) (Table 4.1).

Five classifiers were applied in each of the three above listed purposes: unsupervised K-Means, supervised minimum distance (MD) classifier on full resolution spectra, supervised maximum likelihood (ML) classifier on pre-determined reduced band sets (Table 4.2) defined in Chapter 3, and two spectral endmember library methods: Linear Spectral Unmixing (LSU) and Spectral Angle Mapper (SAM) (Hedley & Mumby, 2003). Multiple classifiers were chosen because each classifier requires different input and separates classes by different criteria. Since K-Means is able to separate classes based purely on image statistics without training data, it is considered an unsupervised classifier. It does however require ground-truth knowledge to identify the classes that are produced. Minimum Distance and Maximum Likelihood are supervised classifiers, meaning the classification algorithm must first be trained by input in the form of ground-truth data. SAM and LSU are endmember classifiers and are the most independent because they do not require ground-truthing. Instead, they access an endmember spectral library to assign pixels to the most similar class.

Unsupervised K-Means Classifier

K-Means is an unsupervised classification requiring no training data; pixels were clustered into a user-defined number of benthic classes using only image statistics. Class mean vectors begin as evenly distributed in the image spectral space and then are iteratively redefined using the minimum distance technique. Pixels are assigned by closest Euclidean distance, the mean vectors are recalculated from these pixels, and the process is repeated until all the pixels are classified (Tou and Gonzalez, 1974).

Supervised Classifiers - Minimum Distance / Maximum Likelihood

In supervised classification the algorithm is trained to recognize each substrate by assigning training regions of interest (ROIs) to known locations of each, taking care to encompass the spectral range of each cover. Approximately twenty percent of all field data were assigned as training data by random sampling of the surveyed sites (refer to Table 4.1 for sample sizes). In the case of substrates with small sample sizes (i.e. sea asparagus and brown algae), the training set exceeded 20% for the sake of procuring at least two training samples. Using the statistical information from these training ROIs, the classification algorithm assigned the remaining image pixels to the benthic class of the closest spectral match. The supervised classifier, minimum distance (MD), was applied to the full spectral resolution AISA and

IKONOS images. In this method, mean vectors for each substrate are calculated from the training data and each unknown pixel is matched to the nearest mean vector according to Euclidean distance (Richards, 1999).

The supervised classifier, Maximum Likelihood (ML) was applied only to spectrally reduced versions of the images, which included only bands and spectral indices recommended from previous analysis of *in situ* spectra from Sidney Spit (Chapter 3 & Table 4.2). The Maximum Likelihood classifier uses linear discriminant functions to calculate the probability of an unknown pixel belonging to each class and then assigns the pixel to the class of highest probability (Richards, 1999).

Endmember Library Classifiers - Linear Spectral Unmixing / Spectral Angle Mapper

Both linear spectral unmixing and spectral angle mapper are spectral endmember library classifiers, meaning that instead of using image-specific training data to assign a class to a questioned pixel, they utilize a spectral library of various known benthic spectra as a lookup table. The endmember library is scene independent and can therefore be used on multiple images. The averages of the above-water spectra measured *in situ* with the Satlantic HyperSAS spectroradiometer (Chapter 2, Figure 2.1a) served as the spectral library in this case (Figure 4.2 a & b). The end-members included optically deep water, shallow and deep sandy substrate, shallow green algae, and shallow and deep eelgrass. A library of the HyperSAS pure end-members were used for the spectral library when classifying water column corrected data (Chapter 2, Figure 2.2; Figure 4.2 c).

The linear spectral unmixing (LSU) procedure assumes that the measured spectral signal in a single pixel is the linear sum of a set of pure end-member spectra, weighted by their relative abundances (Mather, 1999). The classification algorithm used the spectral library to construct a library of all possible weighted combinations of the covertype spectra. Each questioned pixel in the image was then matched to the most similar spectra in the library. Lastly, the end-member contributing the most reflectance to the matched library spectra was assigned as the benthic cover for the pixel.

The Spectral Angle Mapper (SAM) classifier transforms the shapes of both spectral library and questioned pixel spectra into vectors with dimensionality equal to the number of bands (*n)* in the spectrum (*n*-D space) and direction equal to a mathematical combination of all band reflectance values. The angle is calculated between the questioned pixel vector and each

spectral library class vector. The class with the smallest angular distance to the questioned pixel vector is assigned to the pixel (Kruse et al., 1993). SAM is insensitive to illumination and albedo magnitude effects and classifies data based more so on spectral shape (Kruse et al., 1993). This classifier was included because the findings of Chapter 3 indicated the importance of spectral shape over spectral magnitude.

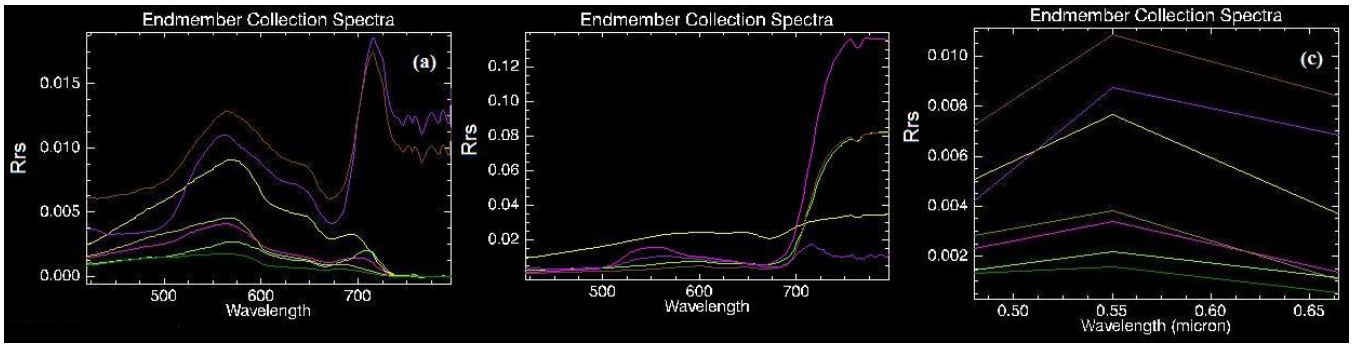

Figure 4.2 Endmember libraries for (a) the AISA above water image (HyperSAS above water measurements); (b) the AISA water corrected image (HyperSAS endmember measurements); and (c) the IKONOS above water image (simulated from HyperSAS above water measurements). Chartreuse = sE, dark green = dE, magenta = sAg, yellow = sS, dark yellow = dS, purple = Asp, dark brown = sAb (see legend of Figure 4.13).

Table 4.2 Reduced variable band set defined in the previous chapter and applied here during each supervised maximum likelihood classification case. R' = first derivative of above water remote sensing reflectance, s = slope. NPCI is the Normalized Pigment Chlorophyll-a Index using bands 680nm and 430nm (Penuelas et al. 1993). For IKONOS the wavelengths represent the centre of the bands.

	Classification case					
Sensor	***Eelgrass delineation*** $(R_{rs}^{(0+)})$	***Water corrected eelgrass delineation*** (R_{rs}^{b})	***LAI classification Level 1*** $(R_{rs}^{(0+)})$	***LAI classification Level 2*** $(R_{rs}^{(0+)})$	***Epiphyte classification Level 1*** $(R_{rs}^{(0+)})$	***Epiphyte classification Level 2*** $(R_{rs}^{(0+)})$
AISA	s500-530 R'566 R'580 R'602	566:600 566:710	NPCI R'700	NPCI R'700	R'580	R'580
IKONOS	480 550 480:665 550:665	n/a	480:665 665	480:665	band set irreducible	band set irreducible

Each classification output was treated with a 3 x 3 pixel majority filter to eliminate speckle before validation (Macleod and Congalton, 1998). Validation was performed by comparing the substrate class or biophysical parameter designated by classification to the true substrate or parameter at that location as determined in the field. Approximately 80 percent of field data (the portion remaining after training data random selection) was used as validation data (Table 4.1). A typical validation matrix was then constructed to calculate user, producer, and total accuracies for eelgrass presence, LAI, and epiphyte type. Producer accuracy is defined as the percentage of testing pixels of a specific substrate that were classified correctly (i.e. how well the training sites were classified or the probability of misclassifying a training site) (Story & Congalton, 1986; Lefèvre, 1992). User accuracy is the percentage of pixels classified as a specific substrate that are truly that substrate (i.e. how well the classification represents ground-truth) (Story & Congalton, 1986). Total accuracy is the percentage of sites of all substrate types classified correctly. Because total accuracy considers all substrates together it gives an idea of how well substrates other than eelgrass are classified.

In calculation of eelgrass accuracy, misclassifications of shallow eelgrass as deep eelgrass, and vice versa, were not treated as classification errors. The rationale for this is as follows: (1) These misclassifications occurred on or near the three metre depth boundary, a boundary that was slightly “fuzzy” because the vertical and horizontal accuracies of the bathymetry layer were one metre and 5x5 m respectively and (2) there were far fewer testing regions for deep eelgrass than for shallow eelgrass. If even a small misclassification of shallow eelgrass as deep eelgrass occurred at the fuzzy three metre boundary and was considered as an error, the user accuracy of deep eelgrass would be disproportionately affected.

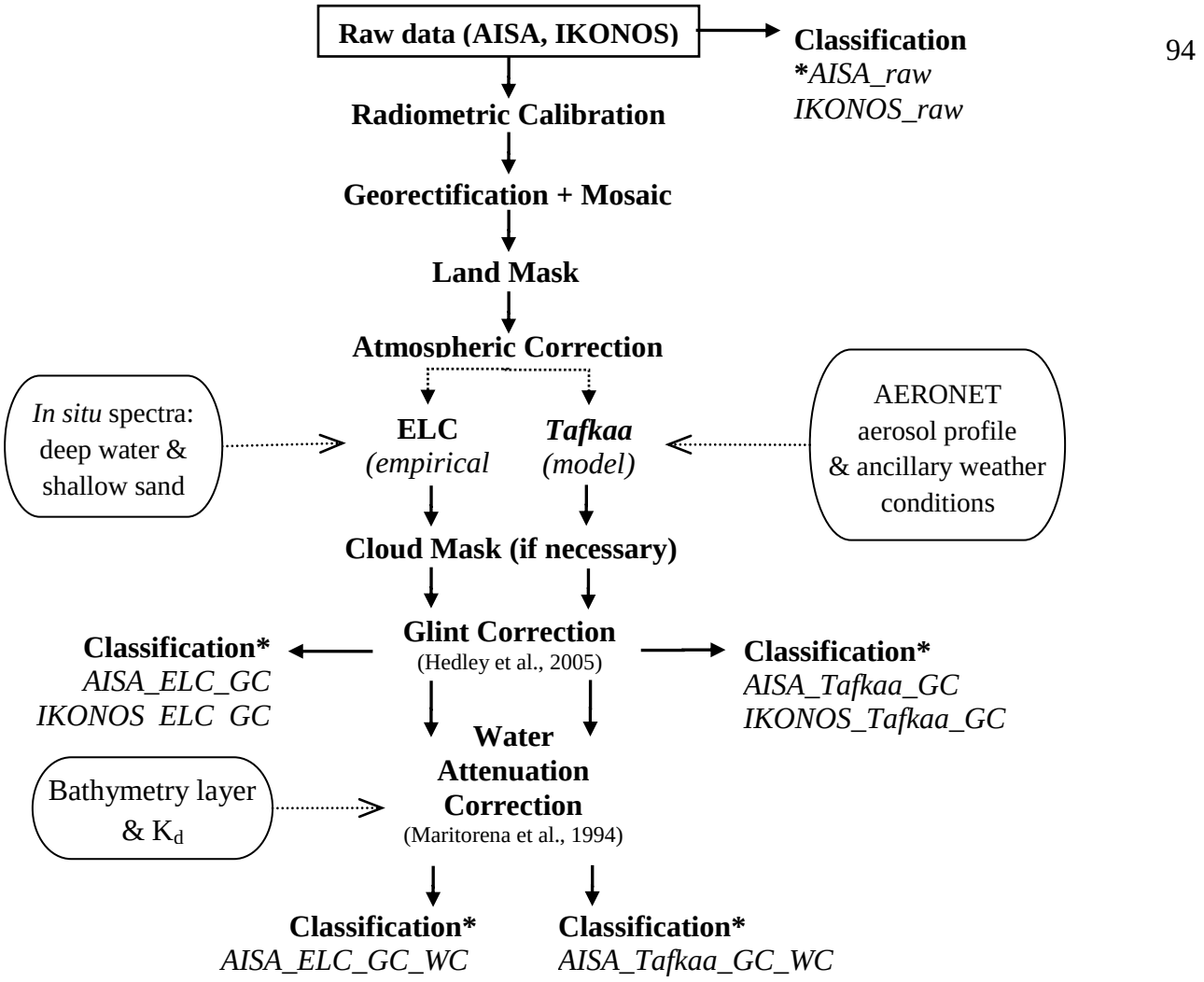

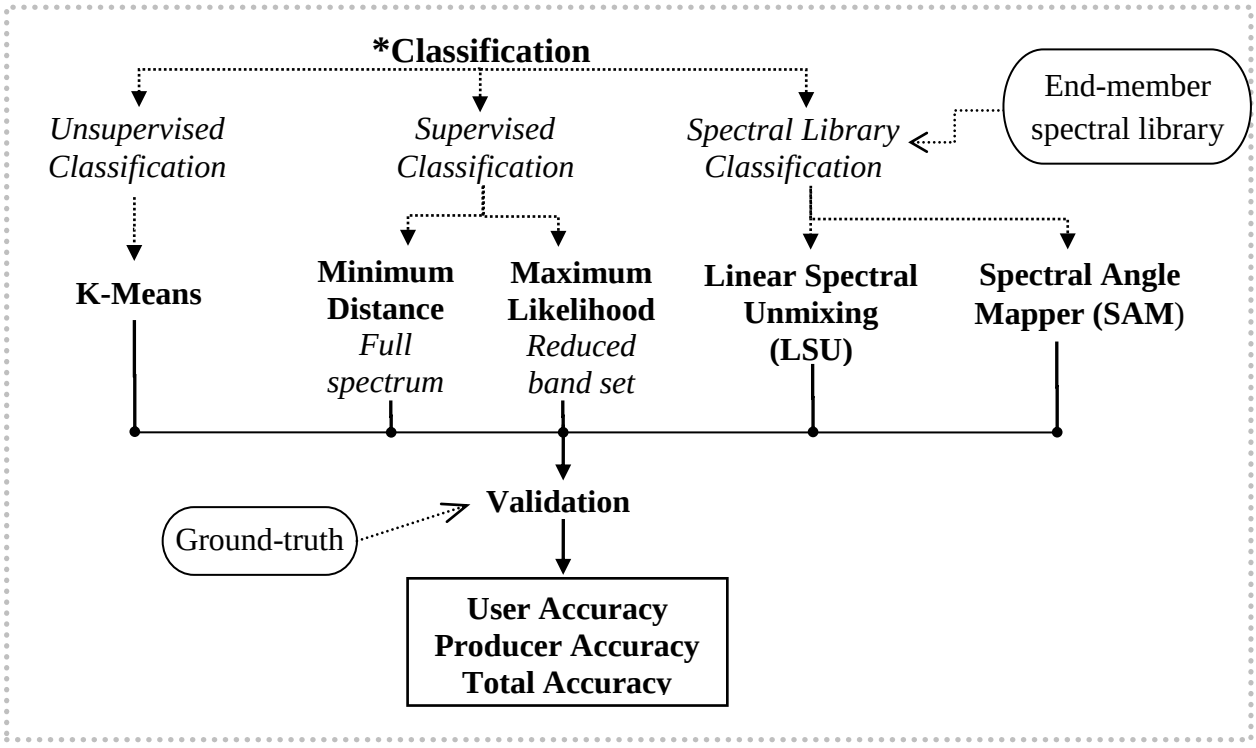

Figure 4.3. Image processing steps.

4.3 Results

4.3.1. Atmospheric correction

The ELC atmospheric correction technique yielded similar spectral shape to *in situ* above-water spectra of optically deep water and submerged substrates for both AISA (Figure 4.4A) and IKONOS (Figure 4.4B). Spectral magnitude differences were observed, especially in the blue and NIR spectra, with the largest departures occurring for eelgrass spectra. In an effort to reduce the observed differences between corrected and *in situ* eelgrass spectra, the ELC method was readjusted considering not only deep water and shallow sand ROIs, but also a shallow eelgrass ROI. The results did not show any improvement, suggesting that the additional error was likely due to differences in tidal height and eelgrass orientation in the water column (i.e. swept flat vs. upright). As an example, the higher magnitude of AISA image spectra compared to the HyperSAS data in Figure 4.4A is likely due to a tidal difference of about 0.15m shallower during acquisition of the AISA image. Note how the NIR signal of the AISA eelgrass spectrum (Figure 4.4A(a)) is much higher than the HyperSAS because the blades were closer to the surface of the water during AISA acquisition.

Overall eelgrass magnitude error was higher for IKONOS than for AISA. The ELC error for AISA was around 50% in the blue and green and 100% in the red, while for IKONOS it remained around 100% for all visible bands. The IKONOS image and HyperSAS spectra were acquired at comparable tidal height, so the higher magnitude errors of eelgrass may be due to differences in blade orientation.

Applying Tafkaa to AISA resulted in similar spectral shape compared to the *in situ* HyperSAS spectra in all regions except the blue range, which was under corrected. This is a known issue with Tafkaa in coastal areas close to urban centres, where elevated levels of blue absorbing NO_2 in the troposphere are not accounted for in the model (Montes et al., 2004). In the case of eelgrass, Tafkaa also overestimated NIR reflectance beyond 700nm, but approximated the slope of the red edge fairly accurately (Figure 4.4A(a)). IKONOS corrected with Tafkaa did not show this over-correction problem in the blue wavelengths. Rather, spectral magnitudes were far overestimated for the entire spectra, with an error range of 200-700% (Figure 4.4B). This is a possible artefact of the broad spectral bands over which Tafkaa must average the atmospheric properties. Better results could likely be obtained with some fine-tuning of the aerosol and

molecular absorption inputs. Despite the sizeable error in magnitude, however, spectral shape similarity with *in situ* spectra was obtained with Tafkaa on IKONOS (Figure 4.4B).

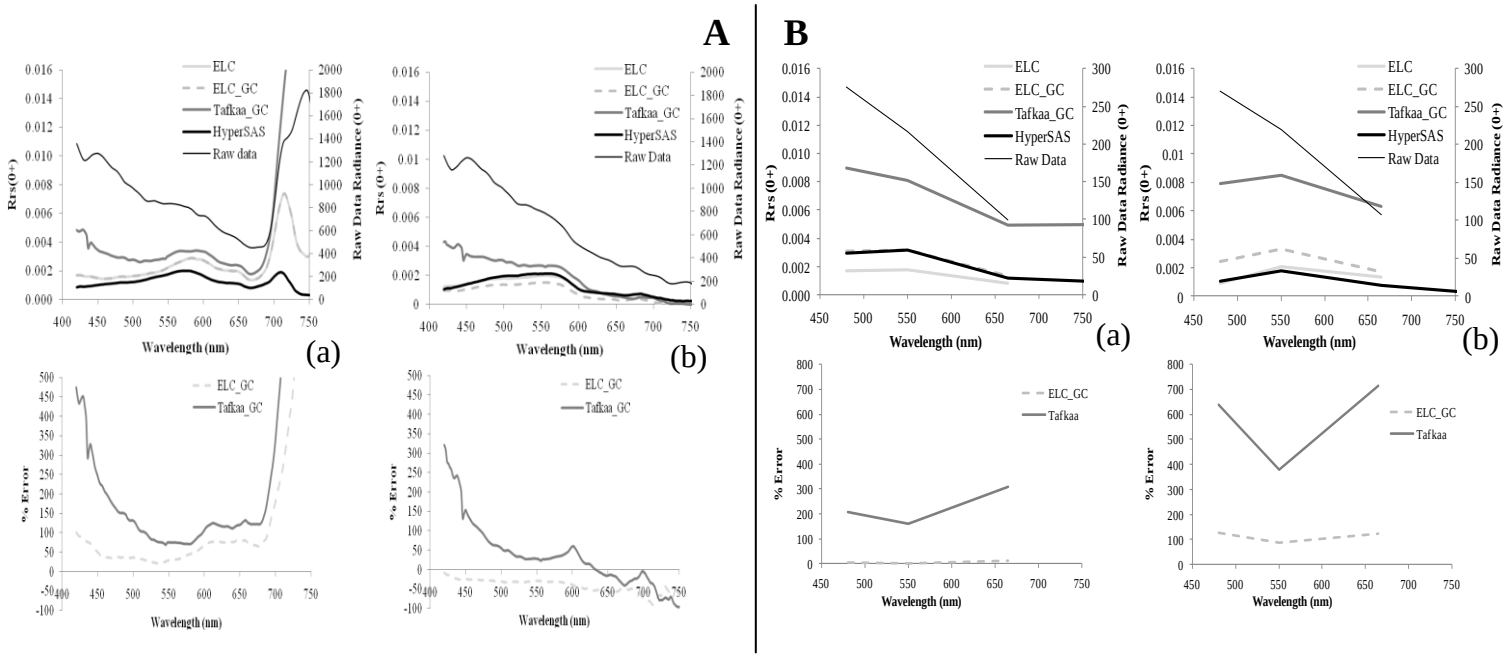

Figure 4.4. Top: (a) Eelgrass and (b) optically deep water spectra AISA and (B) IKONOS imagery after sea surface glint and atmospheric corrections ELC and Tafkaa. In situ spectra are presented for comparison. Bottom: The percent error of ELC and Tafkaa corrections with glint correction when compared with in situ spectra.

4.3.2 Glint Correction

The Hedley et al. (2005) glint correction was effective in removing surface glint from the image (Figure 4.5), thus resulting in spectra with characteristics more closely resembled that of the *in situ* HyperSAS spectra. It did however, cause a slight magnitude underestimate for any non-vegetated areas to which it was applied (Figure 4.4) due to its application after ELC atmospheric correction. ELC forces the image spectra to closely match the field spectra. When the glint correction is applied, reflectance is removed from every pixel, unless its 750-800nm reflectance value is the absolute minimum in the image. Therefore the glint correction causes a slight negative departure from the close magnitude match that ELC has forced. Shallow vegetated areas did not show this underestimate because they were masked before the glint correction.

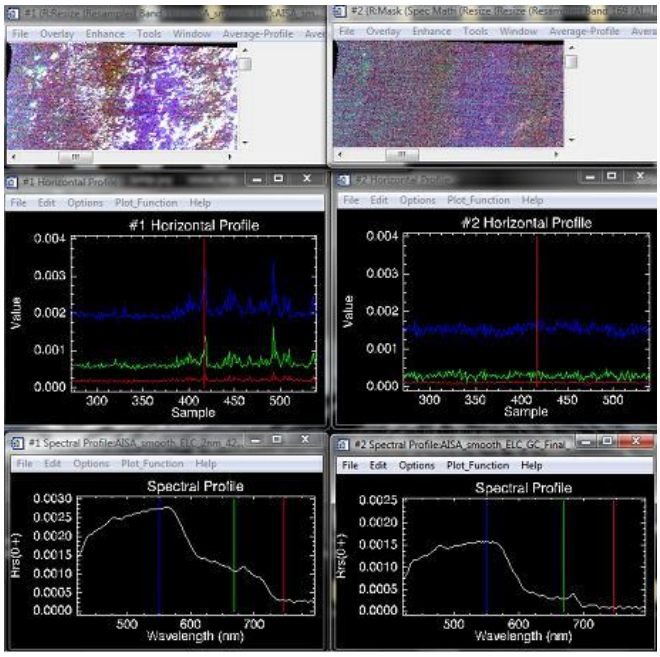

Figure 4.5 Before and after Hedley et al. (2005) glint correction of AISA imagery demonstrated here in a portion of heavily glint affected optically deep water with false colour AISA imagery (top), an image x-profile of optically deep water showing 550nm (blue line), 668nm (green line) and 748nm (red line) R_{rs} values (middle) and a single deep water spectrum (bottom).

4.3.3 Water column removal

The Maritorena et al. (1994) water column correction (Eq. 4.6) provided accurate results up to about three metres depth, in agreement with the *in situ* trial in Chapter 3. Below approximately 2.5 metres depth, the method over corrected spectra in the 400-500nm and over 600nm regions, and the error continually increased with greater depth (Figure 4.6a). Thus, the lowest difference between Maritorena corrected spectra and *in situ* spectra was observed between 500-600nm (Figure 4.6a) where the lowest attenuation of light ($K_{d\ (556nm)} \sim 0.5\ m^{-1}$) was calculated to occur (Figure 4.6b). Due to the lower K_d value, light in this spectral range can penetrate deeper, and therefore the Maritorena correction is effective to a greater depth; to a maximum of 5.5 m (Figure 4.7). Because depth and K_d are found within the exponential term of Eq. 4.6, this method is highly sensitive to even slight errors in either depth or K_d. Similar error was assumed for IKONOS due to similar water conditions and within-pixel depth heterogeneity.

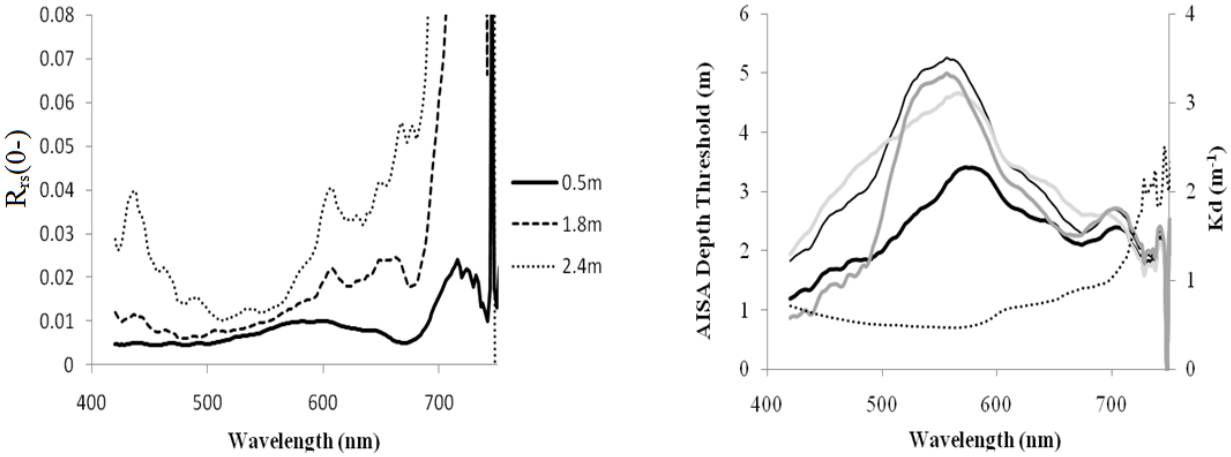

Figure 4.6 (a) Spectra of medium density eelgrass beds with epiphytes at varying depths extracted from the Maritorena water column corrected AISA image; and (b) depth restriction at which the AISA sensor can no longer distinguish between each substrate and deep water (solid lines) and average Kd value for the scene (dotted line) derived from in situ in water spectral profiles. Depth restriction is wavelength dependent and varies inversely with K_d.

4.3.4 Deep water masking

The optically deep water threshold, calculated following Eq. 4.8, was defined as 5.5 metres for AISA and 7.5 metres for IKONOS based on non-biofouled eelgrass. The higher threshold for IKONOS was due to clearer waters on the day of IKONOS acquisition (K_d(556nm) = 0.3 m^{-1} for IKONOS s. 0.5 m^{-1} for AISA) (Figure 4.7).

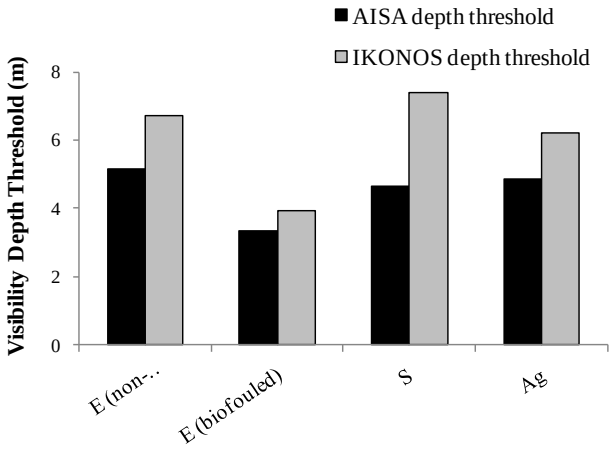

Figure 4.7 Visibility threshold (depth at which each covertype can no longer be discerned from deep water) of AISA and IKONOS sensors at the time of image acquisition, calculated using Eq. 4.8.

4.3.5 Image classification

Eelgrass classification

Producer and user accuracies for all substrate classifications of AISA and IKONOS are reported in Figure 4.8 and 4.9, respectively. Total accuracies for both sensors are reported in Figure 4.10. A numerical report can be found in Appendix G. In the case of both AISA and IKONOS images, the highest producer, user, and total accuracy for eelgrass classification was achieved with the application of deep water masking, atmospheric and glint correction followed by the maximum likelihood (ML) algorithm on the statistically selected indices (Table 4.2; Figure 4.13 a & b). Again, these indices were defined according to M-Statistics and Multiple Linear Discriminant Analysis (MDA) of HyperSAS data in Chapter 3. In this case, total accuracy was over 82% in for AISA and above 69% for IKONOS, regardless of the atmospheric correction method, ELC or Tafkaa (Figure 4.10). Eelgrass producer/user accuracies for the AISA image were 85%/ 96% for shallow (< 3 m) and 98%/ 93% for deep (> 3 m) eelgrass. IKONOS achieved 79%/ 81% for shallow eelgrass. There was an exception in the deep portion (> 3 m) of the IKONOS image, where the ML classification was not effective; eelgrass user accuracy was 59% (Figure 4.9b & 4.13b). In these IKONOS deep regions, the full spectral resolution minimum distance (MD) classification delineated eelgrass more successfully (Figure 4.13c), with an eelgrass user accuracy of 86% (Figure 4.9b).

LSU endmember classification yielded eelgrass accuracies over 84% in AISA imagery and over 71% in IKONOS imagery when atmospherically corrected with ELC (Figure 4.8 & 4.9), but poor performance was achieved for the Tafkaa corrected imagery, as can be seen when comparing the distribution of classes in the final maps (Figure 11 f & p; Figure 121 f & k). For example, the Tafkaa corrected IKONOS LSU classification lacked sAg and eAsp classes (Figure 12 k). Therefore, the eelgrass producer and user accuracies of over 60% (Figure 4.9) were misleading, emphasizing the importance of considering both accuracy values and class distribution together (Congalton & Green, 1999).

The SAM classifier resulted in high confusion between shallow eelgrass, exposed sea asparagus and brown algae of AISA imagery, both in exposed areas and in submerged areas where eelgrass was very near or floating on the surface (Figure 4.11 g & q). SAM also showed high confusion in IKONOS imagery between sea asparagus and eelgrass, but only in exposed

areas (Figure 4.12 g & l). This lack of confusion in submerged shallow eelgrass in this case is likely due to the deeper tidal stage during IKONOS acquisition. SAM worked well in the ELC corrected AISA image for deep areas (Figure 11 g), but for the remaining cases (AISA Tafkaa, IKONOS ELC, and IKONOS Tafkaa), the deep classification (> 3 m) was very poor, designating nearly all pixels as deep eelgrass.

Masking optically deep water (5.5 m for AISA and 7.5 m for IKONOS) had no effect on the eelgrass mapping accuracy of the AISA ML classification, but did improve the MD classification of deep eelgrass (> 3 m). Deep eelgrass producer/user accuracies improved from 35% /77% to 72% /90% when the deep water was masked. Marked improvement was also achieved in the IKONOS image. Deep eelgrass producer/user accuracy increased from 78% /26% to 82% /86% for the MD classifier and from 82% /28% to 100% /59% for ML classification (data not shown).

The lowest accuracy results were obtained with the MD classifier of water corrected imagery. Total accuracy was 25% and shallow eelgrass producer/user accuracies were 8% /96%. The classification was constrained to the 3 m threshold of water correction efficacy and therefore deep eelgrass accuracies were not calculated. ML classification of water corrected imagery showed some improvement over the MD classifier. Total accuracy was 43% and shallow eelgrass accuracies were 22% /81%. The slight improvement may be due to the indices of the ML classification being located in the green portion of the spectrum, where the water corrected spectra show the least error (< 20% error) (Figure 4.6a and Figure 3.9) and in the NIR region, where the water corrected spectra were overestimated, but still relatively proportional to their respective covertypes. On the contrary, the MD applied the classification to the entire full-resolution water corrected spectra where large errors had resulted from the water correction method in the blue and red spectral regions. Despite the accuracy improvement, high confusion remained between eelgrass and the other green substrates, sAg and eAsp (Figure 11 i & j).

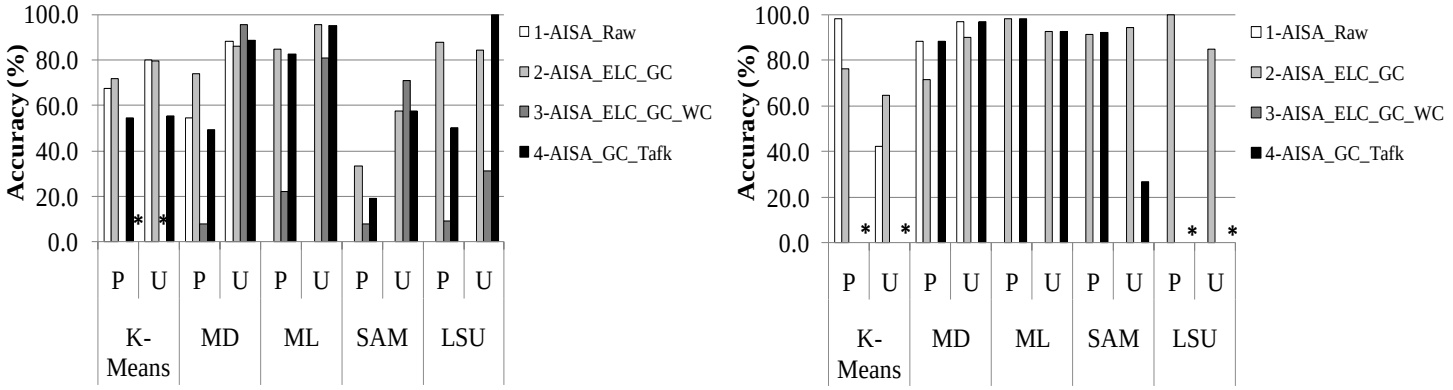

Figure 4.8 AISA user and producer eelgrass classification accuracies for (a) shallow (<3m depth) and (b) deep (>3m depth) eelgrass at various levels of image correction. P = producer accuracy, U = user accuracy. Raw = raw data, ELC = Empirical Line Calibration, Tafk = Tafkaa, GC= glint correction, WC=water correction. * denotes a value of zero. Unmarked missing bars are due to non-applicability of the classifier to the processing scheme (e.g., LSU on raw data).

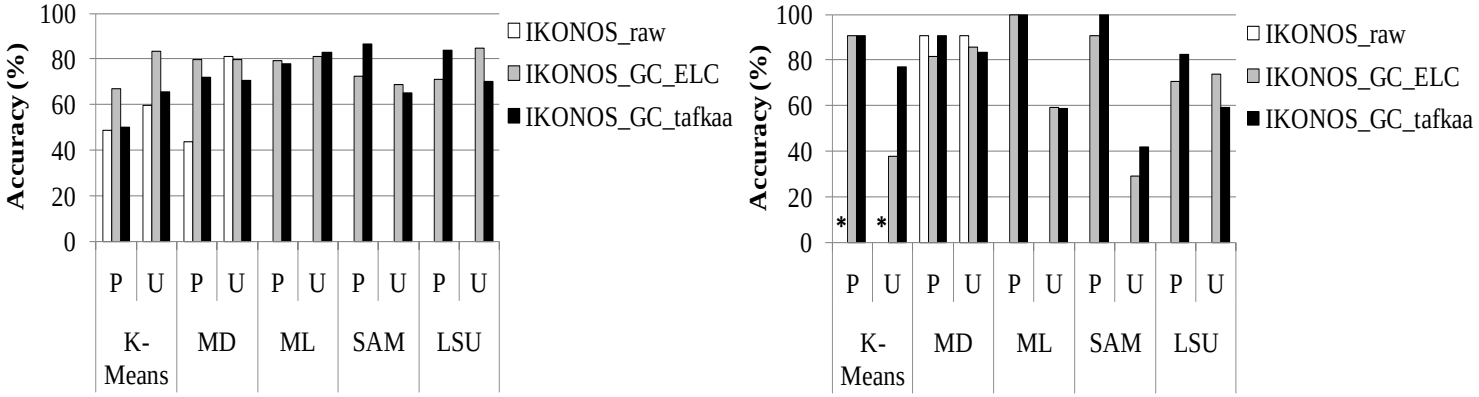

Figure 4.9 IKONOS user and producer eelgrass classification accuracies for (a) shallow (<3m depth) and (b) deep (>3m depth) eelgrass at various levels of image correction. P = producer accuracy, U = user accuracy. Raw = raw data, ELC = Empirical Line Calibration, GC= glint correction. * denotes a value of zero. Unmarked missing bars are due to non-applicability of the classifier to the processing scheme (e.g., ML or LSU on raw data).

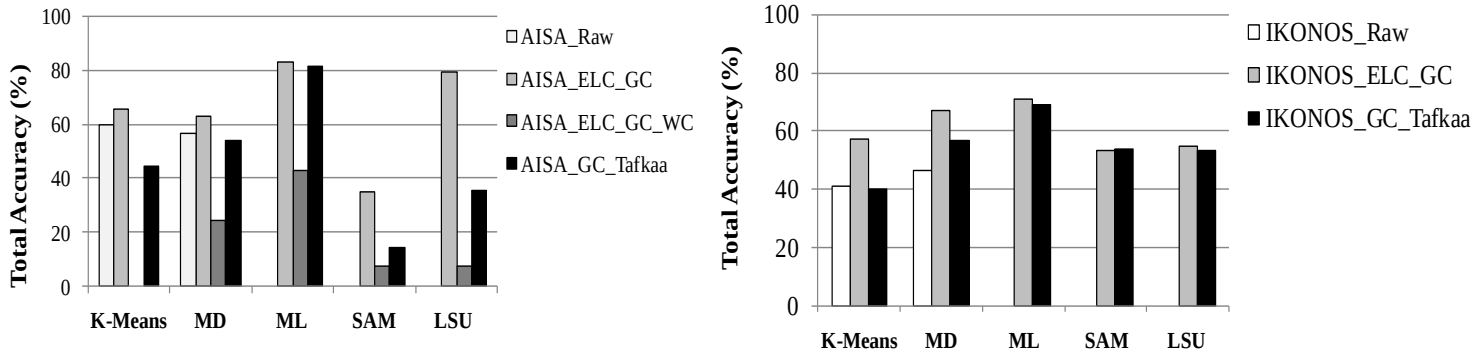

4.10 Total accuracies for all (a) AISA and (b) IKONOS classifications. Raw = raw data, ELC = Empirical Line Calibration, GC= glint correction.

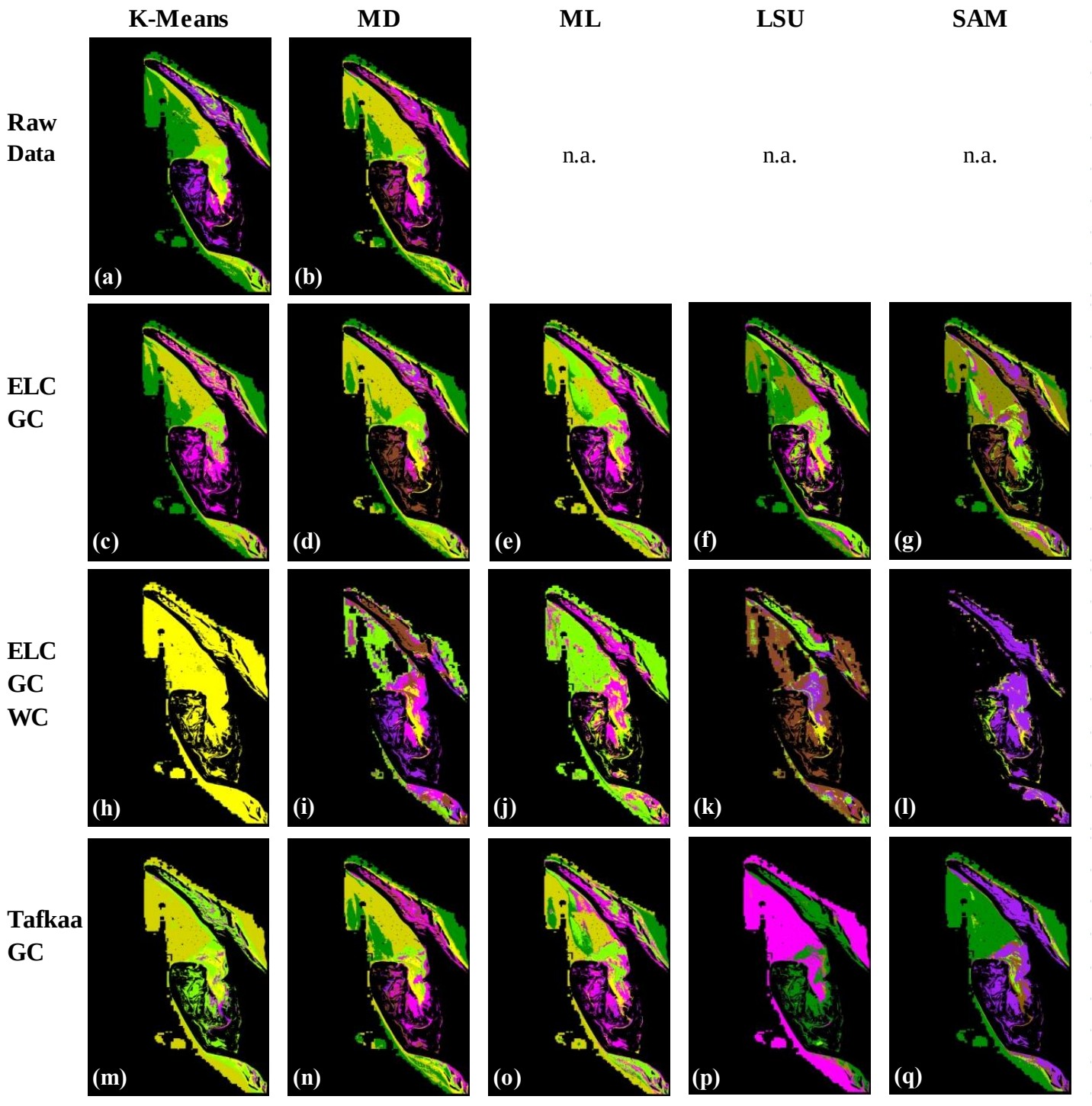

Figure 4.11 Classifier results for the AISA image with various processing. Raw Data = no processing, ELC = empirical line calibration, GC = glint correction, WC = water correction, MD = minimum distance classifier, ML = maximum likelihood classifier, LSU = linear spectral unmixing classifier, and SAM = spectral angle mapper classifier.

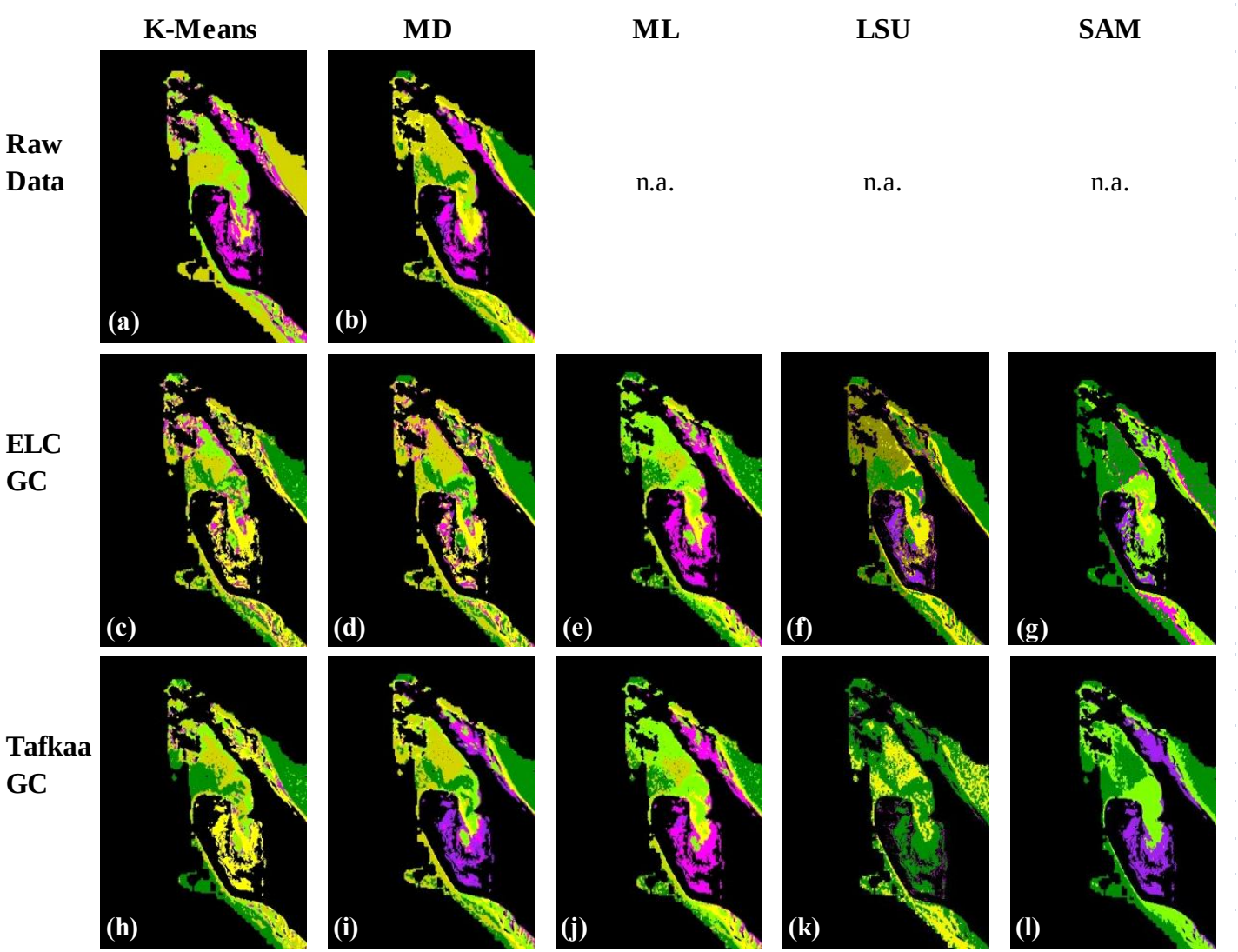

Figure 4.12 Classifier results for the IKONOS image with various processing. Raw Data = no processing, ELC = empirical line calibration, GC = glint correction, MD = minimum distance classifier, ML = maximum likelihood classifier, LSU = linear spectral unmixing classifier, and SAM = spectral angle mapper classifier.

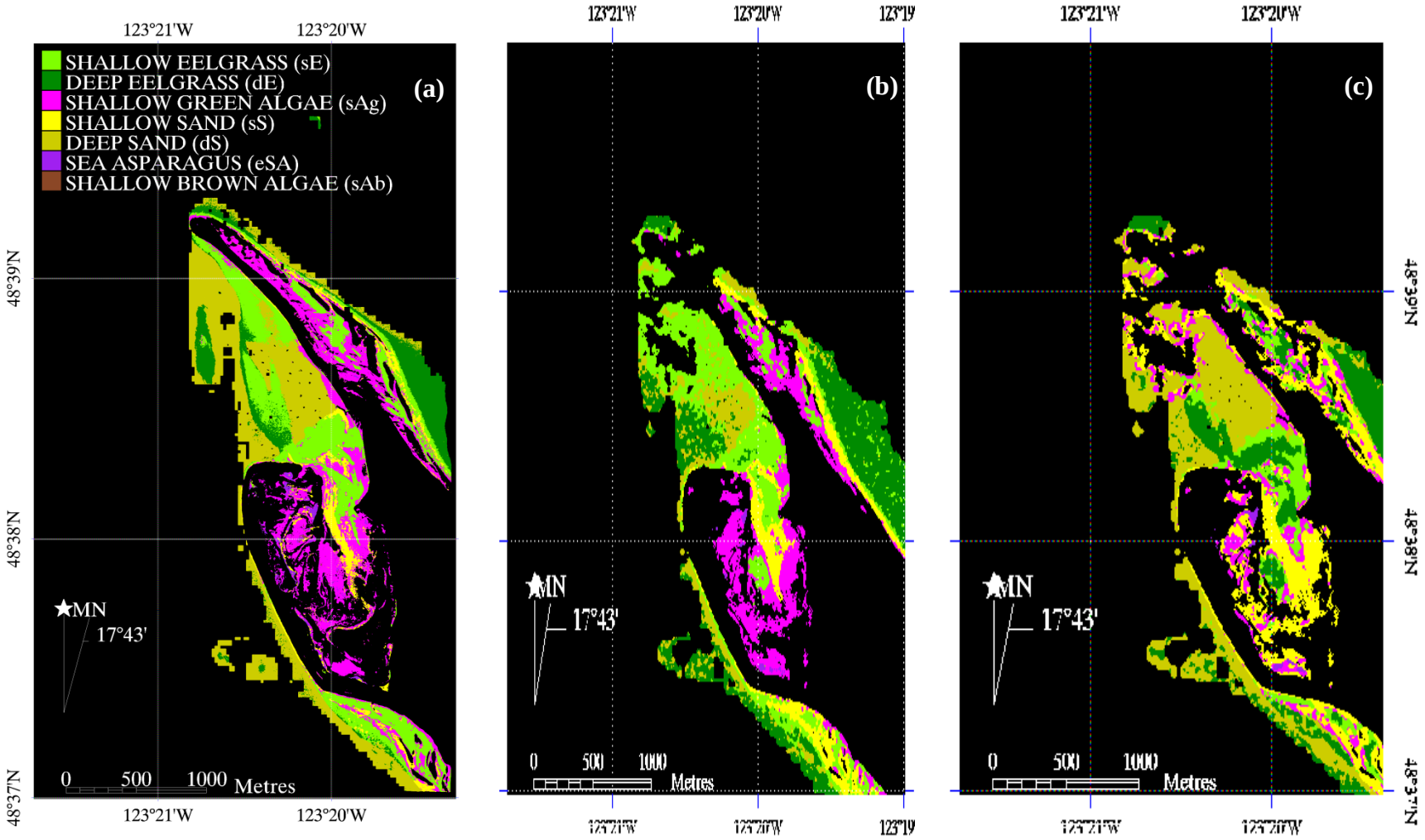

Figure 4.13. Sidney Spit benthic substrate classifications with the best accuracies and substrate distribution: (a) AISA_ELC_GC_ML (85%/ 96% shallow and 98%/ 93% deep eelgrass producer/ user accuracy); (b) IKONOS_ELC_GC_ML for the shallow (< 3 m) areas (79%/ 81% shallow eelgrass producer/ user accuracy); and (c) IKONOS_ELC_GC_MD for the deep (> 3 m) areas (82% / 86% deep eelgrass producer/ user accuracy). Where ELC = empirical line calibration, GC = glint correction, ML = maximum likelihood classification of selected spectral indices, and MD = minimum distance classification of full spectral resolution data.

Sources of confusion in the eelgrass classification

The primary source of classification confusion in both AISA and IKONOS images was between optically deep water and deep (>3metres depth) eelgrass. This is because as depth increases, the spectral signal of the water column becomes dominant in comparison to the signal coming from the substrate, particularly over a dark target like dense eelgrass (Ackleson and Klemas, 1987; Zainal, 1993). Masking optically deep water improved the AISA_MD, IKONOS_MD, and IKONOS_ML classifications. This result is consistent with the findings of others (Ackleson and Klemas, 1987; Zainal, 1993). The AISA ML classification was, however, unaffected by deep water masking, suggesting that the reduced spectral variable set offered a classification with less confusion between deep water and deep eelgrass. The better separation by the reduced spectral variable set (ML) compared to the full-spectrum data (MD) is likely due to the exclusion of redundant spectral ranges where the two covertypes are spectrally similar.

After masking optically deep water, the major source of confusion within the best classifications was between eelgrass and green algae. For ML classification of the AISA imagery, approximately 5% of all sAg wereas misclassified as sE (producer error) while 14% of all pixels classified as sE were actually sAg (user error), regardless of the atmospheric correction method used. The sand class resulted in the least confusion at all depths, with 3% sE-sS producer error and 2% dE-dS producer error. This confusion was mainly near the periphery of the eelgrass bed where sparse density and georeferencing error likely play a role. There was no eelgrass user error attributed to sand, meaning there were no cases where sand was misclassified as eelgrass. This could likely be attributed to the small number ground-truth sand sites located on the periphery of the eelgrass bed. The LSU classification contained slightly more sE-sAg confusion (14% producer and 10% user error), and sE-sS elgrass-sand error to the ML classification.

sE-sAg error was of similar magnitude in the IKONOS ML image (14% producer and 6% user error), however the sand class caused greater confusion at all depths (5% /15% producer/user sE-sS error 15% /0% producer/user dE-dS error). This could be due to the coarser spatial resolution of IKONOS, i.e., within a larger pixel, there is greater benthic heterogeneity, and therefore the pixel reflectance represents a greater mix of substrates. There is also possibly a greater error penalty for pixel geolocation errors, as an error of one pixel places the testing site over a substrate 4 m away compared with 2 m away in AISA.

LAI Classification

The best achievable coarse level LAI classification (two classes: low LAI < 1, high LAI > 1) total accuracy was 79% for AISA (ML) and 71% for IKONOS (ML) (Figure 4.14 & 4.15). However user and producer accuracies were not evenly distributed between low and high classes; many of the high LAI class were erroneously classed as low LAI (e.g., 9% producer accuracy for high LAI in AISA ML classification, Figure 4.14). All classifiers had similarly poor accuracies for low LAI suggesting approximately half of the low LAI samples were misclassified.

The fine level LAI classification (three classes: LAI < 1, LAI = 1-2, LAI > 2) was, at best, 54% for AISA and 43% for IKONOS (Figure 4.14 & 4.15). Confusion occurred largely between adjacent categories, explaining why the course level LAI classification had relatively greater success. Low ML accuracies may be attributed to the relatively small sample size of the dataset used to determine the reduced set of indices for separating LAI classes (Chapter 3).

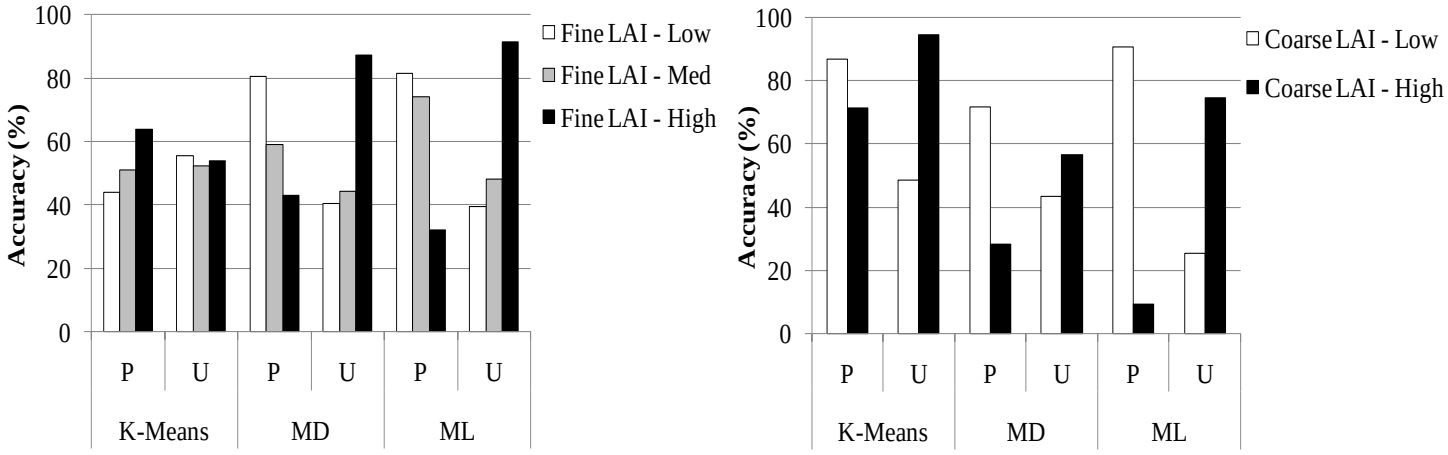

Figure 4.14: AISA user and producer LAI classification accuracies in shallow (<3m) water using (a) three LAI classes and (b) two LAI classes. U = user accuracy, P = producer accuracy.

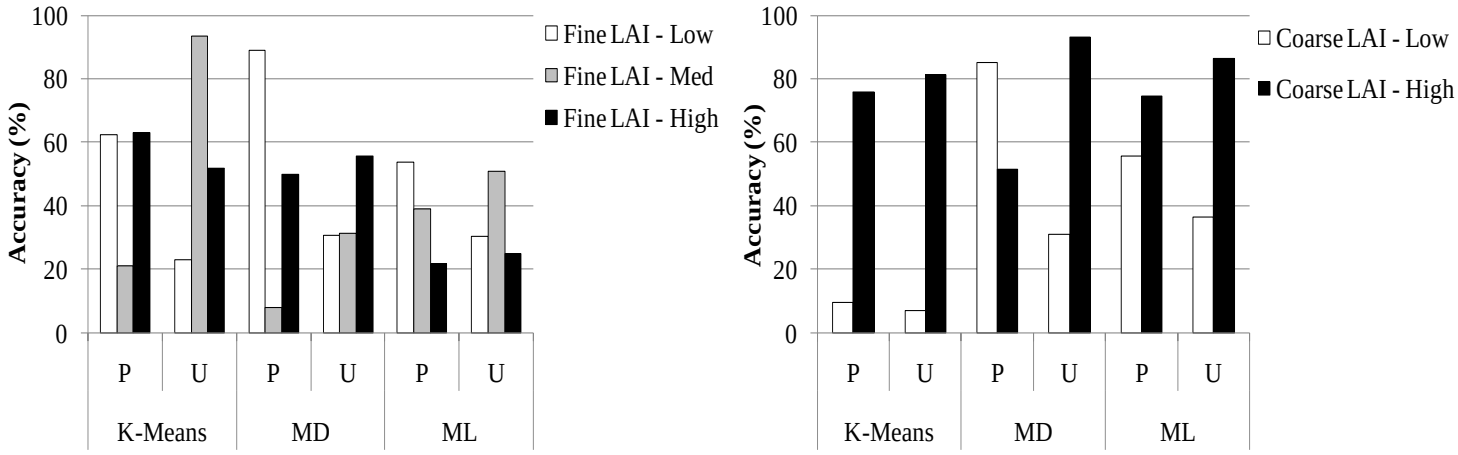

Figure 4.15: IKONOS user and producer LAI classification accuracies in shallow (<3m) water using (a) three LAI classes and (b) two LAI classes. U = user accuracy, P = producer accuracy.

Epiphyte Type Classification

Classification of three epiphyte classes: red algae, diatoms, and absent epiphyte, did not reach over 58% accuracy (Figure 4.16 & 4.17). Results improved greatly in the AISA image with the courser epiphyte classification – epiphyte presence absence. Total accuracy of 87% was achieved with well balanced user and producer accuracies using the ML classifier on the reduced dataset variables 440nm and R'580nm (Figure 4.16). IKONOS had no variable set that improved epiphyte classification and could at best resolve the two classes with 54% accuracy using MD classification (Figure 4.17). In this case the accuracy were not well distributed between the two epiphyte classes: approximately 95% of the "epiphyte absent" class were being misclassified as "epiphyte present."

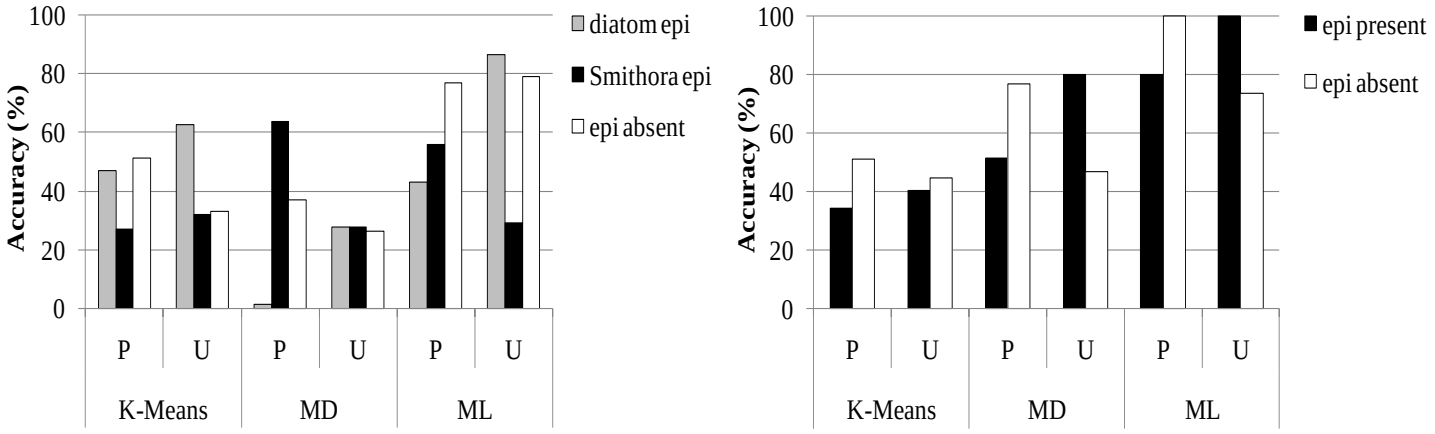

Figure 4.16: AISA user and producer epiphyte type classification accuracies in shallow (<3m) water using (a) three epiphyte classes: red algae, diatom, none and (b) two epiphyte classes: epiphyte presence absence. U = user accuracy, P = producer accuracy.

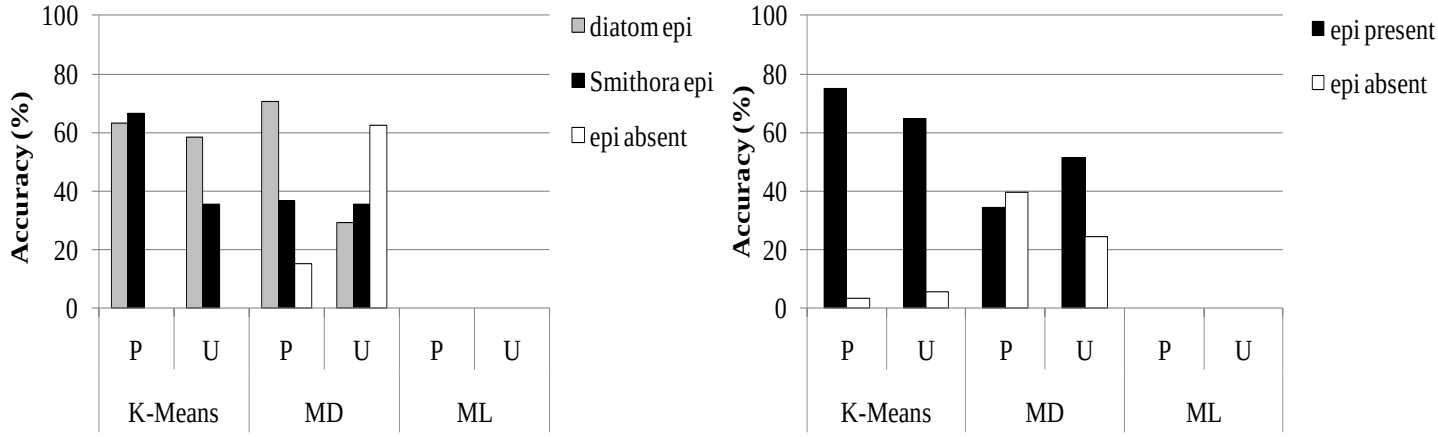

Figure 4.17: IKONOS user and producer epiphyte type classification accuracies in shallow (<3m) water using (a) three epiphyte classes: red algae, diatom, none and (b) two epiphyte classes: epiphyte presence absence. U = user accuracy, P = producer accuracy. The results are absent for ML because no beneficial reduced variable set could be found for the epiphyte type dataset.

4.4 Discussion

4.4.1 Image pre-processing

Two main points are of notable attention in the image pre-processing steps: atmosphere and water attenuation correction. ELC and *Tafkaa* atmospheric corrections generally under corrected eelgrass reflectance, resulting in higher magnitudes compared with *in situ* spectra.

However, both produced spectral shapes that were in reasonable agreement with in situ spectra of all benthic types, excepting Tafkaa under correction in the blue region (Figure 4.4) due to underestimation of [NO_2] in its coastal model (Montes et al., 2004; Gao et al., 2009). It is suggested by Pe'eri et al. (2008) to increase the NO_2 input concentration by a factor of 90 to compensate for the under correction. Further research could test this recommendation. The higher blue reflectance lead to decreased supervised minimum distance and SAM classification accuracies (Figure 4.8 & 4.9), especially in deep water where the signal to noise ratio is much higher (Figure 4.4A(b)). The ML classification of indices was not adversely affected by the blue spectra under correction, as indices in the blue region were purposely avoided during selection (See Chapter 3 for definition of indices).

A major disadvantage of ELC atmospheric correction is that the coefficients derived between image and field measurements are specific to the place and time of image acquisition and therefore can only be applied to images acquired at similar times and locations. ELC also assumes that the atmosphere is uniform across the image, which is often not true, especially in the case of water vapour, which varies greatly over a small scale (Smith and Milton, 1999). *Tafkaa* appears to be a suitable alternative in this regard, as climate and aerosol input are readily available online from radiosonde and sun photometer databases such as AERONET (Holben et al., 1998) and weather stations. Further, water vapour and aerosol depth can be retrieved pixel-by-pixel from the image data if required, provided at least two NIR wavelengths over 1000nm are available (Montes, 2004).

The Maritorena et al (1994) water column correction was unsuccessful in this study. At depths over 2.5 metres, the resulting spectral shapes were nonsensical, and R_{rs}^{b} magnitudes were highly overestimated, especially at wavelengths greater than 600nm, similar to results from Werdell and Roesler (2003), Dierssen et al. (2003), and Conger et al. (2005). The error was likely caused by the coarse one-metre vertical resolution of the bathymetry layer combined with the depth-of-detection limit of the sensor where the signal returning from the sea floor is no longer strong enough to be discriminated from the water column (Conger et al., 2005). The calculated depth of detection limit of AISA for each substrate was was in agreement with the water correction failure beyond 2.5 m (Figure 4.6); Figure 4.6a shows water-corrected biofouled eelgrass sites at various depths. The detection depth limit of biofouled eelgrass in Figure 4.6b is approximately 3.5 metres in the mid-green (566nm) and drops to 2.2 metres in the red (670nm)

and 1.2m in the blue (420nm). Because of water correction failure in the blue, red, and NIR wavelengths, beyond 2.5 m the eelgrass classification accuracy for the water column corrected AISA image was markedly lower in deep areas (> 3 m) than in shallow areas (< 3 m) (Figure 4.8). The ML indices classification of the water corrected AISA image was more successful than the MD full spectrum classification (Figure 4.8) because the indices (566:600 and 566:710) were composed of bands located at wavelengths with relatively deep visibility thresholds, i.e. the green wavelengths and NIR depth threshold peak (Figure 4.6b).

Spatially dependent water column correction error may occur in areas of the image where the assumption of a single K_d value fails, such as turbid areas during tidal flux. Incorrect depth estimation will also adversely affect the correction results. Depth and K_d are found within the exponential term of Eq. 4.6, thus making the method highly sensitive to even slight errors in either variable. This becomes particularly important when estimating the tidal stage, as even a small error will have the effect of over or under estimating reflectance over the entire image. It is also important to note that the presence of eelgrass can cause bathymetry discrepancy of over one metre, causing overcorrection of the signal over eelgrass beds, as seen in Chapter 3 (Figure 3.8).

Previous successes with the Maritorena et al. water attenuation correction (Mumby et al., 1998; Werdell & Roesler, 2003) could be attributed to the clear waters in which it was used. As Werdell and Roesler (2003) noted, accurate substrate spectral retrieval in turbid water is more dependent on the accuracy and precision of the reflectance, attenuation, and depth measurements than retrieval from clear waters. The water correction method was expected to produce even greater error in the IKONOS image, due to its greater within-pixel depth heterogeneity, and was therefore not attempted. Other methods of water attenuation removal are available that are depth-independent (Andrefouet 2003 and Green et al 2000). These corrections may produce more accurate results in the blue and red spectra when correcting shallow water and will be resilient to depth errors, but their applicability will be similarly depth-limited by the sensor's ability to detect the substrate (Figure 4.6a).

4.4.2 Eelgrass classification performance

For both AISA and IKONOS sensors, the best eelgrass classification accuracy was achieved with a supervised maximum likelihood classifier applied on a reduced set of spectral

indices (listed in Table 4.2), after atmospheric correction, surface glint correction, and optically deep water masking pre-processing techniques. The set of spectral indices performed better than the full resolution spectra because (1) the indices are located on major spectral features where between-covertype variation is highest and therefore group separation is greatest; (2) Within a covertype spectral shape tends to be less variable than spectral reflectance magnitude. Since all variables in the reduced set are slopes and ratios, they characterize shape and are more resilient than full resolution spectra to within cover class variability; (3) For the same reason, the indices set was more resilient to atmospheric correction error, as both ELC and *Tafkaa* errors were greater in reflectance magnitude than in shape (Figure 4.4); and 4) The reduced set (AISA only) contained no bands in the blue wavelengths, which are highly sensitive to atmospheric and sensor noise (Montes et al., 2004) as well as absorption by phytoplankton and CDOM in the water column (Kirk, 1994; Vahtmae et al., 2006).

The only case where maximum likelihood classification was unsuitable was in the deep regions (>3m) for IKONOS imagery, where a significant amount of deep sand was erroneously classified as deep eelgrass. There are possible physical reasons for this error. For instance, the slightly deeper tidal stage and low spectral resolution of IKONOS likely make it difficult to distinguish between the deep substrates due to their low inter-class spectral variation (Figure 3.4), and it is possible that reflectance noise was introduced by notable cloud and haze cover at the time of image acquisition. On the other hand, it is also possible that the indices were not adequate for separating deep cover types. First, the IKONOS indices neglected the absolute reflectance in the red band, where sand exhibits a unique reflectance peak. Secondly, hyperspectral measurements showed s500-530 to be one of the best separators between deep sand and deep eelgrass (Chapter 3, Table 3.6 and Figure 6.2 Appendix A). This slope cannot be derived from IKONOS spectra because the blue and green bands are located at 480 nm and 550 nm. The hyperspectral index s500-566, most similar to the IKONOS blue to red slope, was found to be an unimportant variable (M-statistic < 1), as shown in Chapter 3. Fortunately, the MD classifier was found to be much more effective in the IKONOS deep regions (Figure 4.12c). This classification utilized the full spectral resolution IKONOS and yielded well distributed deep area substrate distribution. The shallow regions of the MD classification, however, show more confusion between the shallow and exposed classes, sE, sAg and eAsp. With this in mind, there are two options for IKONOS classification: (1) use the ML classifier in regions of the image

shallower than 3 metres and the MD classifier in regions of the image deeper than 3 metres, or (2) improve the MD classification of shallow waters by adding an exposed or surface eelgrass class.

In this study, AISA classification achieved producer and user accuracies over 85% for shallow eelgrass and 93% for deep eelgrass. IKONOS achieved over 79% for shallow eelgrass and over 82% for deep eelgrass. These accuracies are comparable with the results of authors who have attempted benthic classification with hyperspectral airborne, IKONOS, and other sensors of similar spatial resolution. For example, airborne scanning, CASI, has shown 81% overall accuracy (Mumby et al., 1997) and eelgrass accuracy of 92% using 5 x 5 m multispectral airborne scanning (Su et al., 2006). Overall IKONOS accuracies have ranged from 69 to 84% for four to five classes and eelgrass overall accuracies ranging from 56% to 89% (Mumby & Edwards, 2002; Andrefouet et al., 2003; Purkis, 2005; Fornes et al. 2006). Similar resolution SPOT and Quickbird have shown 87 to 96% overall accuracy (Pasquilini et al. 2005) and 81% overall accuracy (Mishra et al. 2006), respectively.

As expected after analysis of the AISA visibility depth threshold, the Maritorena et al. (1994) water column correction offered no cost-benefit for eelgrass classification in this study. Classification of imagery corrected with the Maritorena et al. method was restricted to areas less than 2.5 metres deep and in those areas yielded lower accuracies than imagery without the correction (Figure 4.6a). Depth restriction is expected to be even shallower at times of increased and unevenly distributed water turbidity, such as phytoplankton bloom or tidal flux.

The main goal of this study was to effectively map eelgrass distribution, and thus user and producer accuracies of the eelgrass class have been the main focus. However high accuracy classification of non-eelgrass substrates could also be a beneficial asset to coastal ecosystem research; the co-occurrence of vegetated and non-vegetated substrate has been shown as an important influencing factor for many aquatic faunal species (Heck & Orth 1980, Orth and Moore, 1984; Irlandi et al. 1995, Hyndes et al. 2003). In this study, total (or overall) accuracies were calculated to determine how well the remaining substrates were classified. The best classification (again, ML classification of glint and atmosphere corrected and deep water masked image) yielded total accuracies of 83% for the AISA image and 70% for the IKONOS image, regardless of atmospheric correction type (Figure 4.10). Accuracies of the glint and atmosphere corrected LSU were 80% /55% (ELC /Tafkaa) for AISA and 55% /53% (ELC/Tafkaa) for

IKONOS. These total accuracies are comparable with the findings of other authors as described in the previous text, but on the lower end of the range (Mumby et al., 1997; Mumby & Edwards, 2002; Andrefouet et al., 2003; Pasquilini et al. 2005; Purkis, 2005; Fornes et al. 2006; Mishra et al. 2006; Su et al., 2006). The total accuracies are somewhat low because since the main focus of the study was to delineate eelgrass, the dataset reduction was applied with the goal of maximizing separation only between eelgrass and other covertypes *(Chapter 3)*. The accuracy for other benthic substrates could be improved by performing data set reduction with a focus on maximizing separation between all substrate pairs, not just eelgrass-substrate pairs. It should be noted however, that maximizing separation between non-eelgrass substrates could improve total accuracy at the expense of eelgrass accuracy. The total classification accuracy of LSU, which does not utilize the reduced variable set, could possibly be improved by increasing the number of samples in the spectral endmember library and therefore encompassing greater substrate variability.

Misclassification occurred primarily between eelgrass and green algae due to pigment composition similarity (Rowan, 1989). This confusion may be addressed by re-classifying only the shallow vegetated areas (defined by the best initial classification) with the inclusion of the 668:710 and 650:660 ratios. The 668:710 ratio defines the red-edge, a feature common to all vegetation and variable by species. The red edge could help to separate exposed vs. submerged vegetation (Zacharias et al. 1992), and therefore aid in separating green algae and eelgrass. Since the pigment composition of eelgrass and green algae are very similar (Rowan, 1989), the two substrates are difficult to separate if eelgrass epiphytes are not present. It is likely that some of the image classification confusion between the two classes may have occurred in beds that were relatively free of epiphytes. In *Chapter 3* the 650:660 ratio was the only index yielding good separation (M-statistic >1) between epiphyte-free eelgrass and green algae, suggesting its inclusion may decrease the image classification confusion between the two classes.

Low LAI classification accuracies may be attributed to an insufficient set of indices for LAI determination, due to the relatively small dataset used to select it (Chapter 3). Additionally, the error between adjacent classes is likely due to the subjective nature of the class breaks between low, medium and high LAI classes. It may be of benefit to develop a regression model rather than a categorical one, such as the study by Dierssen et al. (2003), which found regression models able to explain 70% of LAI variation.

Epiphyte type classification accuracies were also low, except in one case. AISA resolved two epiphyte classes (present and absent) with a total accuracy of 87% when applying ML classification of indices R440nm and R'580nm (Figure 4.16b). However, this method required the collection of training sites. A more independent method is not clear as the unsupervised K-Means classifier appears to delineate LAI more effectively than it does epiphyte type, at least in the AISA image (Figure *4.8*). Constructing an endmember library would be difficult considering the additive effects of eelgrass density and epiphyte loading on the spectral signal. Epiphyte mapping was very poor for IKONOS imagery and is not recommended unless a better model can be found.

Regardless of the accuracy of the eelgrass classification, the spatial resolution of the sensor must also be adequate to capture the spatial patterns of (i.e. patchiness) in the eelgrass meadow and changes in those patterns. The applicability of a particular sensor to seagrass mapping will vary depending on the size and extent of eelgrass beds, and the management goal in mind. For instance, 30m x 30m resolution Landsat, having similar bands to IKONOS, may be sufficient for preliminary exploratory mapping of general vegetation presence/absence along large tracts of coastline (e.g. the British Columbia mainland coast). However high spatial resolution imagery is required for small scale meadow pattern dynamics, loss detection, eelgrass species delineation, and epiphyte bloom detection (Kirkman,1996; Habeeb, 2007).

Eelgrass at Sidney Spit consists of extensive fringing beds flanking the sand spit, a very extensive flat meadow in the lagoon to the south, and patches in between that are commonly less than 5m x 5m. The 4m x 4m resolution of IKONOS should be fine enough to resolve general bed patterns and small patches larger than 4m x 4m, and is certainly the better cost-benefit trade-off for mapping larger areas of the islands for presence/absence data. For studies of ecological dynamics that depend on fine scale eelgrass patch patterns or bed edge change it is recommended that airborne data be used for mapping, or that IKONOS 4m x 4m classification results be refined with its 1m x 1m panchromatic band to infer fine scale patterns (Pasquilini, 2005; GeoEye, 2006). Examples of where 1 m spatial resolution is necessary are when mapping areas with very narrow fringing beds, 1m x 1m patches, or for mapping meadow "blow-outs," important indicators in eelgrass bed dynamics (Clark et al., 1997).

4.4.3 Spatial distribution of eelgrass classification result (AISA)

According to these best classifications (Figure 4.13), there are two large flat meadows of shallow eelgrass; one in the lagoon, and one running along the east side of the sand spit. The entire sand spit, except for an approximate 180 m stretch of the most northern tip, is flanked by an approximately 75 - 100 m wide fringing eelgrass bed on both the east and west sides, enlarging to 300 m wide mid-spit on the west side. Two deep eelgrass beds occur along sandbars running north south; a large one between Hook Spit (west of the lagoon) and Sidney Spit (approximately 350 m west of the ferry dock), and a second smaller one running parallel to the first, approximately 200 m west of the first. A third very large eelgrass bed occurs at the southeast extent of the sand spit and is unfortunately cut off by the image edge. The fringing eelgrass bed and smaller second sand bar bed to the west could not be confirmed in the IKONOS image because the area was obscured by clouds (Figure 4.13b & c). The total area delineated as eelgrass in the AISA image was 1,041,492 m^2, with 232, 628m^2 of it occurring in the lagoon. This total excluded the bed delineated to the southwest of Hook Spit because it was not visited during fieldwork. Eelgrass coverage could not be delineated for the entire area of the IKONOS image because the northern portion of the spit was obscured by clouds. The IKONOS image does indicate that the eelgrass be in the lagoon was 286, 335 m^2.

4.5 Conclusion

It is important that eelgrass distribution be known and monitored as part of an effective coastal ecosystem management strategy. The purpose of this study was to explore and compare the efficacy of high spatial, high spectral resolution airborne (AISA) and high spatial, low spectral resolution satellite (IKONOS) imagery in mapping eelgrass location, LAI, and epiphyte coverage. The optimal combination of spectral resolution, spatial resolution, image pre-processing, and classification technique delivering the highest accuracy for each image was determined. Classification and validation were performed after each step of the image processing process to illustrate the accuracy benefits gained from each processing step. The product with the least time and monetary costs while still retaining acceptable eelgrass classification accuracy is the desired goal for environmental management. The best classification accuracies were found to

be comparable with previous benthic mapping studies using airborne hyperspectral, IKONOS, and similar resolution sensors.

In the case of both AISA and IKONOS images, the highest classification accuracies were achieved with atmospheric correction, glint correction, optically deep water masking, and ML classification of the predetermined indices, with the exception of IKONOS deep (> 3 m) regions, where MD classification was more successful. AISA producer and user accuracies were over 85% for eelgrass shallower than 3 metres, and over 93% for deeper eelgrass. IKONOS achieved 79% for shallow eelgrass and over 82% for deep eelgrass. The AISA indices are located mainly in the green and red wavelengths to capitalize on differences in accessory pigment composition between eelgrass and algae, higher visible reflectance and characteristic red reflectance of sand, the unique features of epiphytes in the red region, and the high transparency of water in this region, as determined in Chapter 3. Failure of the ML classifier to separate deep sand and deep eelgrass in the IKONOS image could be because the IKONOS indices neglect the absolute reflectance in the red band and because one of the most important indices for deep eelgrass-deep sand separation, s500-530 cannot be derived with IKONOS bands. Since the MD classifier was more successful than ML at separating the IKONOS deep substrates, two recommendations were made for effective eelgrass mapping of all depths using IKONOS: (1) use the ML classifier in regions of the image shallower than 3 metres and the MD classifier in regions of the image deeper than 3 metres, or (2) improve the MD classification of shallow waters by adding an exposed or surface eelgrass class.

Endmember classification (LSU) also showed accuracies over 84% and 71% in AISA and IKONOS imagery, respectively, but only for ELC corrected imagery. Endmember classification of Tafkaa corrected imagery performed poorly.

Maritorena et al. (1994) water column removal was ineffective in this location as it was restricted to areas shallower than 2.5 metres and subject to local errors in areas of high turbidity and depth misestimation. Other water attenuation removal methods that use depth independent indices rather than a bathymetry layer are available in the literature (Andrefouet et al., 2003 and Green et al., 2000). These methods may produce more accurate results in the blue and red spectra when correcting shallow water and will be less sensitive to depth errors, but their applicability will still be similarly depth limited by the sensor's ability to detect the substrate. Since the area where eelgrass can be effectively detected depends on water depth and attenuation coefficient,

every effort should be made to acquire imagery at the lowest possible tide, in the months when waters are clearest, and during a time when no major blooms are known to be occurring.

Both sensors yielded poor LAI and epiphyte classification in all cases except for the course presence/absence epiphyte classification, which was 87% accurate. Further research into this "value-added" classification of eelgrass LAI and epiphyte loading should involve an increased ground-truth sample size. A regression analysis may provide more accurate results than discreet LAI classes (Dierssen et al., 2003) and, further, both LAI and epiphyte estimation may be more accurate in water corrected imagery (Dierssen et al., 2003). This possibility could be tested on exposed areas or in a submerged area of less than 2.5m depth (e.g. the lagoon at low tide) corrected with the Maritorena et al. (1994) water correction. Before water correction, the bathymetry layer should be corrected for eelgrass height in the areas where eelgrass beds are present.

Automation

The ultimate goal of remote sensing is automation; retrieving all desired parameters in the absence of *in situ* measurements (Dierssen et al., 2003). This research showed that higher accuracies are achieved with the application of a supervised (Maximum Likelihood) classifier to glint and atmosphere corrected and deep water masked imagery for the purpose of mapping eelgrass in coastal environments. The results are encouraging; Eelgrass accuracies are 85% and up for AISA and 79% and up for IKONOS. However, these achievements rely on the costly input of *in situ* field data every time an image is acquired – above-water spectra for ELC atmospheric correction and locations of known benthic cover for training the supervised classification.

Supervised classification relies on a training input dataset of locations with known covertype for each covertype in the area. There are two options that could be applied to make classification more automated. 1) Construct a database of locations known to have consistent covertype inter-annually. This list would need to be composed of an adequate number of sites per covertype (Congalton and Green, 1999) and regularly maintained; 2) Use an unsupervised classification method such as Spectral Angle Mapper (SAM) or Linear Spectral Unmixing (LSU). These methods utilize a library of pre-established spectral endmembers as a lookup table and therefore can run independently of real-time field measurements. In this study, LSU resulted

in eelgrass accuracies over 84% for AISA but worked poorly for the IKONOS image. An initial time and monetary cost is necessary to define a library that encompasses the complete variation of each covertype.

ELC atmospheric correction requires *in situ* spectra acquired approximately at the time of image acquisition (Che and Price, 1992). Applying the more independent atmospheric correction Tafkaa, which uses radiative transfer modelling, in combination with the LSU classifier is the most automated method. Tafkaa's inputs do not rely on field measurement. Aerosol and weather inputs are readily available through online databases such as AERONET and various weather sites and in the event that these are not available, Tafkaa has the ability to derive atmospheric parameters, provided two or more NIR wavelengths over 1000nm are available (this would not be an option for IKONOS). However, Tafkaa's underestimation of attenuation of blue wavelengths by atmospheric constituents (Figure 4.4) (Montes et al, 2004) causes significant confusion in the two endmember-based classifications for AISA. This can be seen as a drop in eelgrass accuracy between the ELC LSU and the Tafkaa LSU. The accuracy drop was from 85% shallow and deep eelgrass accuracy to 50% shallow and 0% deep eelgrass accuracy (Figure 4.8). Alternatively, one could (1) use an atmospheric correction that more accurately estimates blue wavelengths, (2) attempt LSU or SAM classification of Tafkaa output with data over 500nm only or (3) attempt LSU or SAM classification on the reduced variable data set, which uses no blue bands. If these suggestions were not successful, a fourth option would be to use Tafkaa with ML classification, carried out with known inter-annually constant training sites, since Tafkaa yielded comparable accuracy to ELC for ML classification (Figure 4.8a & 4.8b). This is an especially important recommendation for IKONOS imagery, where endmember classification yielded unsatisfactory results regardless of atmospheric correction.

It is also of interest to automate the process of identifying and masking deep water, as the process has been shown in this study to improve classification accuracy. The identification of optically deep water requires the average deep water reflectance spectrum ($R_{rs}^{(0-)dp}$) and K_d value for an image (Dekker et al., 2005). $R_{rs}^{(0-)dp}$ could be estimated by radiative transfer simulations specific to the study site, or alternatively by inferring water column inherent optical properties from well characterized stations of known benthic cover and a priori knowledge of depth and R_b (Dierssen at al, 2003). $K_{d(490)}$ could be estimated from deep water pixel reflectance and applied to

shallow water pixels using available empirical algorithms (Austin and Petzold 1981; Mobley 1994; Esaias et al. 1998), however these alternatives require further research.

The results of this study are encouraging, but before they can be implemented to reliably map eelgrass for ecological management purposes, there are a few areas that must first be explored through additional research. First, further research should focus on the spectral separation of exposed substrates, an issue that was not explored in the field sampling of this study, and caused some classification confusion, particularly in the IKONOS image. Second, separation between green algae and eelgrass requires more attention, as this was the major source of confusion in all models. Confusion has been shown to occur particularly between senescent green algae and biofouled eelgrass as well as healthy green algae and non-biofouled eelgrass *(Chapter 3).* A more exhaustive *in situ* spectral study characterizing the full spectral variation of these two substrates would be beneficial. Third, the reliability of the procedures recommended in this study must be ensured by testing their resiliency in varied natural conditions. The protocol should be tested on additional imagery acquired during similar seasonal and tidal conditions at Sidney Spit. The methods should also be applied in different locations to test whether the method can be generalized or is specific to Sidney Spit. It is anticipated that the accuracy will change with the introduction of new benthic types such as cobble, brighter or darker sand, and brown algae, which occurred in very small amounts at the study site.

If the mapping strategy shows resiliency to seasonal and tidal variation, there are many applications for the methodology. Historical imagery could be used to determine present and historical eelgrass distribution along the B.C. coast and establish a baseline for monitoring further change. IKONOS for example, has been acquiring imagery since January 1, 2000 and Landsat since the 1970s. Similarly, baseline distribution and subsequent monitoring could be carried out on a specific coastal area before and after a known possible disturbance threat, such as a newly constructed pier, shoreline development, recreational use, aquaculture, fish farms, point source pollution, or harvesting of reproductive eelgrass shoots from donor beds for transplant (Duarte et al., 2002; Marba et al., 2006; Burkholder et al., 2007; Diaz-Almela et al., 2008; Holmer et al., 2008; Apostolaki et al., 2009, Marion & Orth, 2010). Restoration sites can be targeted with the classification of historical imagery as well, as currently bare areas that previously sustained eelgrass beds can be identified. These areas have a high chance of success over randomly chosen areas because nutrient, current, and light conditions were once ideal to

sustain an eelgrass community and could perhaps do so again. This is especially important in remote areas where people haven't been observing change over time. Lastly, long term eelgrass distribution changes in response to climate change can be monitored. Since eelgrass is a key indicator of ecosystem health, remote mapping of eelgrass presents the opportunity to monitor the "pulse" of the coastal ecosystem. Closely monitoring the indicator species may enable forewarning and faster response to intercept larger scale disruption in its early stages.

A major threat to eelgrass proliferation is marine vessel anchoring because it creates scars in the beds that can take several years to fill in and can lead to decline in epifaunal species richness and abundance (Reed and Hovel, 2006). In an attempt to protect the large bed in the southern lagoon at Sidney Spit, a motor-vessel restriction areas has been designated to the south of the government dock, and mooring buoys have been installed along the sand spit. However, recreational boaters are still known to anchor elsewhere when the buoys are at capacity (personal observation, 2008) or even install their own mooring buoys for the duration of their stay (personal communications, Mayne Island Conservancy, 2010). Eelgrass classification maps can be used to detect additional regions where marine vessel anchoring is occurring within eelgrass beds. For example, the AISA image was acquired in August, during a time of peak recreational usage. The most accurate classification shows the majority of boats occurring over the deep sand area just north of the ferry dock, however thirteen boats are seen over eelgrass beds, particularly over the large bed on the sandbar directly west of the deep sand patch and over the bed just north of Hook Spit (Figure 4.13a).

The best combination of processing methods and classifier type can be selected on a project basis, as each management goal has a differing capacity for trade-off between accuracy and effort depending on time, staff, and budget allotment and whether automation is requisite. For instance if a minimum of 80% eelgrass mapping accuracy is required for management applications, as suggested by Andrefouet et al., (2003), this research indicates the following: Supervised classification of ELC or Tafkaa corrected AISA imagery is sufficient, as is LSU classification of ELC corrected AISA imagery. IKONOS imagery is only sufficient if using supervised classification. Fully automated (Tafkaa correction and LSU or SAM classifier) eelgrass mapping is insufficient for either sensor. Epiphyte presence/absence can be sufficiently delineated only with supervised classification of AISA imagery and lastly, LAI classification is not possible with sufficient accuracy.

The findings of this study were forwarded as recommendations for remote eelgrass mapping and monitoring within the Gulf Islands National Park Reserve. It is hoped that the findings can be applied to provide eelgrass distribution information to government and private agencies seeking to further understand coastal ecological dynamics.

Chapter 5

Conclusions

The goal of this research was to assess the feasibility and limitations of using various remote optical sensors - namely hyperspectral field measurement, airborne hyperspectral AISA, and multispectral satellite sensors IKONOS and Landsat ETM+ - to map the location and biophysical attributes of eelgrass at Sidney Spit, Gulf Islands National Park Reserve of Canada (GINPRC). To meet this objective, two components were addressed:

1. *Define key spectral variables that provide optimum separation between eelgrass and its associated benthic substrates, using in situ hyperspectral measurements and simulated IKONOS and Landsat 7ETM+ spectral response;*

2. *Evaluate the efficacy of these key variables in classification of the high spatial resolution imagery, AISA and IKONOS, at various levels of processing, to determine the processing methodology that offers the highest eelgrass mapping accuracy.*

As part of these objectives, the added-value mapping potential of eelgrass LAI, percent cover, and epiphyte type were also considered.

The first objective was carried out in Chapter 3 using *in situ* hyperspectral measurements acquired in August 2008 and IKONOS and Landsat 7ETM+ spectra simulated from these *in situ* measurements. The *in situ* measurements, acquired over all substrates, provided four datasets: above water spectra, below water spectral profiles, water-corrected (post acquisition) spectra and pure endmember spectra. The high spectral resolution of the four datasets and their location below the atmosphere allowed for detailed spectral characterization of substrates with limited interference from the atmosphere. The water-corrected spectra and endmembers allowed the same analysis with no interference from the water column. Unique spectral characteristics were

defined as spectral indices, which were defined as spectral slopes and ratios located in ranges of high variation among substrates. The second objective was accomplished in Chapter 4 using an AISA hyperspectral airborne image and an IKONOS multispectral satellite image, the indices from Chapter 3, and ground-truth data described in Chapter 2. The accuracy of eelgrass classification was tested on each image with five different classifiers (K-Means, Minimum Distance, Maximum Likelihood, Spectral Angle Mapper, and Linear Spectral Unmixing) at varying levels of image pre-processing (atmospheric, glint, and water column corrections), and in the cases of full spectral resolution or spectral indices only.

From the above water *in situ* data set, discriminant analysis identified spectral variables that enabled eelgrass classification accuracy of 98% when identifying six classes: shallow (< 3 m deep) eelgrass, deep (> 3 m) eelgrass, shallow sand, deep sand, shallow green algae, and spectrally deep water. The statistically selected variables were the slope from 500 – 530 nm, and the first derivatives at 566 nm, 580 nm, and 602 nm. The variables were located mainly in the green and red spectral region, thus capitalizing on differences in accessory pigment composition between eelgrass and algae, higher visible reflectance and red signature of sand, the unique features of epiphytes in the red region, and the higher transparency of water in this region. From the water corrected and endmember data sets, the ratios 566:600 and 566:710 enabled eelgrass classification accuracy of 96% when classifying the same six classes. The only source of confusion in all datasets was between green algae and eelgrass, presumably due to their similar pigment composition. This confusion was increased when manually "cleaned" eelgrass samples were added to the classification dataset. This suggests that the presence of epiphytes allow eelgrass to be more spectrally distinct, with the exception of confusion between biofouled eelgrass and senesced green algae. IKONOS and Landsat 7ETM+ simulated datasets performed similarly well, with 92% and 94% eelgrass classification accuracy respectively, however the significantly coarser spatial resolution of Landsat 7ETM+ would likely limit its efficacy in fine-scale ecosystem studies.

In Chapter 4, in the case of both AISA and IKONOS images it was found that the highest eelgrass classification accuracies were achieved with atmospheric correction, glint correction, optically deep water masking, and maximum likelihood (ML) classification of the predetermined indices. There was an exception in IKONOS regions deeper than three metres, which were better classified by the MD classifier. AISA achieved eelgrass producer and user accuracies of 85% for

eelgrass in less than 3 metres of water, and 93% for deeper areas. This was the most accurate eelgrass map produced by the study (Figure 5.1). IKONOS achieved eelgrass producer and user accuracies of 79% for shallow waters and over 82% for deep waters. Endmember classification also showed accuracies over 84% and 71% in AISA and IKONOS imagery respectively.

The ultimate goal of remote sensing is automation. Toward this goal, the radiative transfer modelling atmosphere correction *Tafkaa* was tested, along with the SAM and LSU classifiers, which both utilize a spectral endmember library as a lookup table. While *Tafkaa* performed as well as Empirical Line Calibration (ELC) in the best case scenario (ML classification), known issues of *Tafkaa* over-correction of the blue wavelengths created additional classification error in SAM and LSU. These errors are not seen in the ML classification, because the indices avoid the blue range. These findings indicate that automation of eelgrass mapping is possible if (1) an atmospheric correction that uses radiative transfer modelling can be found with less error in the blue range (the Brando & Dekker (2003) c-WOMBAT-c could be tested) or (2) limiting the analysis to the spectral range of 500 – 750 nm improves the accuracy.

Similar to the findings of Chapter 3, the largest source of confusion was between eelgrass and green algae. Some misclassification was found between exposed vegetation (sea asparagus and green algae) and eelgrass that was either exposed or very close to the surface, especially in the classifications that utilized a spectral library (SAM and LSU). This confusion was due to insufficiencies of the dataset as the boat could not be manoeuvred to collect spectra over exposed substrates. If additional spectra were collected over exposed substrates of all types, or if the endmember data were used in the spectral library, this confusion is likely to decrease.

The value-added classification of eelgrass LAI and epiphyte type produced poor results in all cases except epiphyte presence/absence. Classifications of three LAI classes resulted in producer accuracies of less than 55% for both images at all levels of processing. Classification of two LAI classes approached 79% accuracy but the accuracy was poorly distributed between classes. Two-class epiphyte presence/absence classification was successful in ML classification of the AISA image (total accuracy 87%) but less than 60% in all other cases. Further research into these value-added classifications should involve an increased number of ground-truth sites for training and testing. Rather than splitting LAI into classes, a regression analysis may provide more accurate results (Dierssen et al., 2003). LAI and epiphyte estimation may be more accurate

in water corrected imagery (Dierssen et al., 2003). This possibility could be tested on exposed areas or in a submerged area of less than 2.5m depth (e.g. the lagoon at low tide) corrected with the Maritorena et al (1994) water correction. Before water correction, the bathymetry layer should be corrected for eelgrass height in the areas where eelgrass beds are present.

Classification accuracies of *in situ* spectra (Chapter 3) were much higher than for AISA and IKONOS (Chapter 4) (compare Figures 3.2 / 3.7 with Figures 4.8 – 4.10). There are three possible reasons for this. First, the *in situ* spectral data are punctual. As such, a given *in situ* spectrum represents a small area of substrate with high homogeneity. In the imagery, a given spectrum represents a 2 x 2 m (AISA) or 4 x 4 m (IKONOS) area of substrate, introducing the opportunity for higher substrate heterogeneity and more spectral mixing, resulting in higher spectral variability. Second, the atmospheric column to be corrected for in the spectra of images is longer than that of the *in situ* spectra. The return trip of the signal was 1 m for *in situ* spectra, 1 km for AISA spectra, and 680 km for IKONOS. Because there is more attenuation to be accounted for in this longer atmospheric path length, more spectral uncertainty may be introduced in the corrected spectra. Further, the atmospheric correction methods applied make the assumption of homogeneous atmosphere for the entire scene, which may not always be the case. Third, the tide levels and current regimes are different between *in situ* and image acquisition, thus creating differences in the above water spectra. The higher tide level gives the images more influence of the water column and the differing current speeds alter orientation of submerged vegetation, and thusly the surface area detected by the sensor.

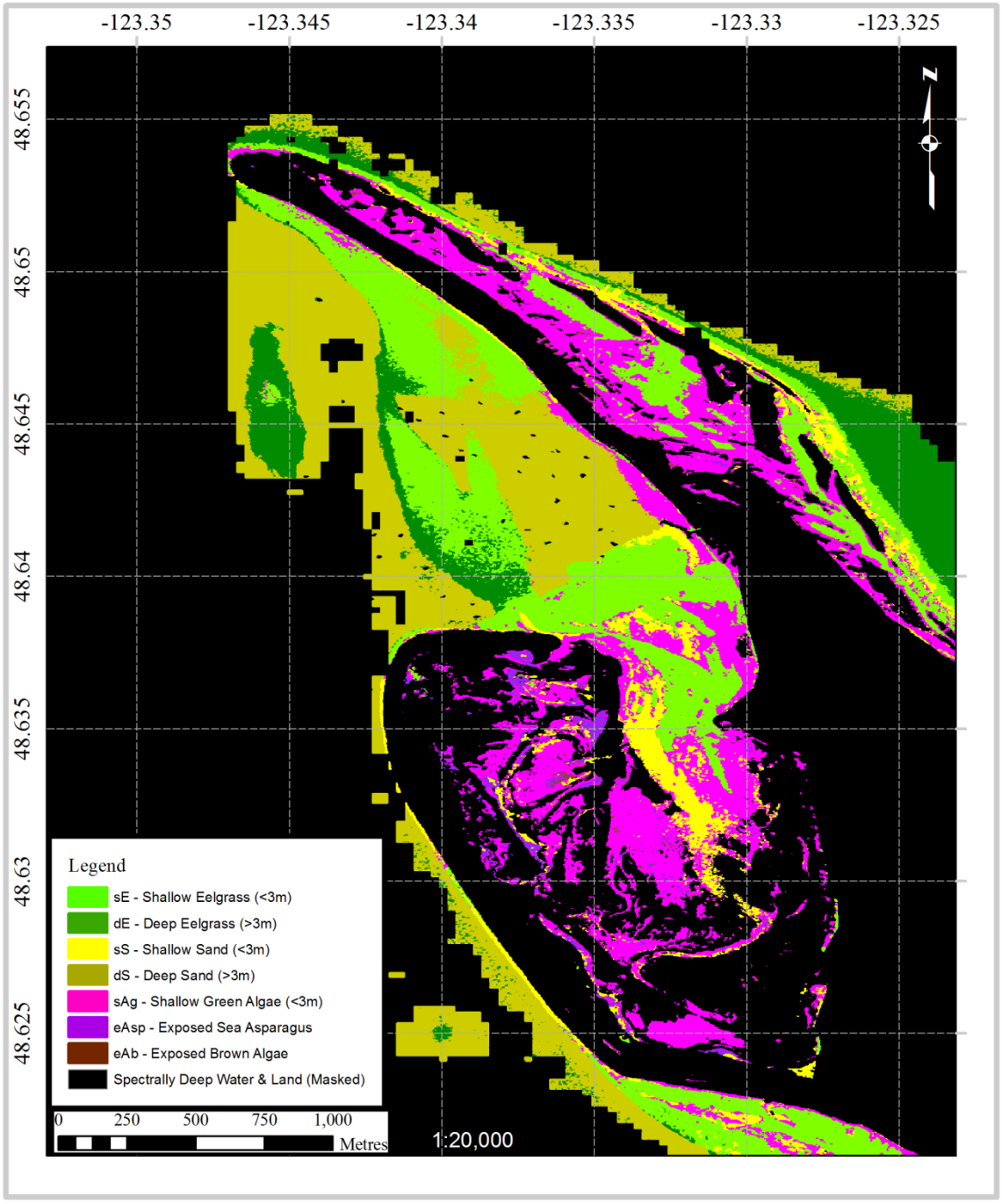

Figure 5.1 Most accurate eelgrass map produced in this study. Image processing steps were: atmospheric correction, glint correction, optically deep water masking, and maximum likelihood classification of the spectral variables: slope from 500 – 530 nm, and the first derivatives at 566 nm, 580 nm, and 602 nm. Eelgrass producer/ user accuracies are 85%/ 96% for shallow eelgrass and 98%/ 93% deep eelgrass. Total accuracy is 83.2%.

The following points should be considered in the application of this study's findings:

(1) Spatial resolution

IKONOS imagery was found to perform fairly well at eelgrass classification, but its 4 m x 4 m spatial resolution may be too coarse for application to fine scale ecosystem research and management. For instance patchiness has been shown to be a major factor in the biodiversity of eelgrass bed inhabitants and patches can occur in dimensions less than 4 m. IKONOS does however, offer fused panchromatic data at higher resolution (1 m x 1 m). This fused data has been found to produce lower classification accuracy but could alternatively be used as a source of additional information to refine the classification of the full resolution 4 m x 4 m image. Information, such as patchiness and texture, could be used to add confidence and strength to the classification by determining substrate confusions and manually resolving where patchiness occurs (Pasquilini, 2005).

(2) Kd variability:

The value of K_d changes with varying concentrations of suspended sediment, dissolved organic matter, and phytoplankton. If the water optical constituents in the water at the time of image acquisition are far different than the ones measured in this study (Table 3.2), the selected above water classification variables may be less effective. The classification of water corrected spectra may, however, remain reliable with fluctuating K_d, at least to the tested maximum of $K_d(440) = 0.82\ m^{-1}$, $K_d(550) = 0.72\ m^{-1}$, and $K_d(650) = 1.06\ m^{-1}$, and only areas shallower the 3 metres. Methods for deriving K_d values from image data exist (Boss and Zaneveld 2003) and could be used as input to the water column correction algorithm.

(3) Presence of brown algae:

Since very little brown algae was present at the Sidney Spit study site, it is not represented in the model. The efficacy of the model may change should it be used in an area with high occurrence of brown algae. Since the main differences between brown algae spp. and green vegetation is higher red and lower green reflectance, it is possible that the selected indices, located mainly in the green and red portion of the spectrum should capture the variation. However confusion may occur between brown algae and diatom epiphytes.

(4) Exposed eelgrass:

Due to the logistics of spectral acquisition from a boat, measurements of exposed eelgrass could not be obtained. The lack of exposed eelgrass samples in the statistical analysis lead to the selection of variables that were focussed on separating only submerged substrates. The consequences of applying these spectral variables in classification of imagery was some confusion between exposed eelgrass, eelgrass near the surface of the water, and exposed sea asparagus in the LSU and SAM classifications of AISA and IKONOS, and most markedly in MD classification of IKONOS. Fyfe (2003) recommends inclusion of a NIR band to aid in the separation of exposed vegetation. The variable 668:710 was found not to adversely affect the classification accuracy of submerged substrates in Chapter 3 and therefore could be added to the AISA variable set to test for improvements in exposed class separation. This ratio incorporates the NIR region and captures the red-edge, an important feature in identifying exposed vegetation. Similarly, the IKONOS NIR (805nm) band or the 665:805 ratio could be added to the IKONOS variable set for ML and MD classifications.

(5) Statistical analysis

Although MDA is robust to departures from multivariate normality, and in the case of this dataset, the departures were fairly small, it still remains that the results should be interpreted with more care (Williams, 1983; cited by Richardson et al., 2003). Therefore the MDA is used in this case for exploratory analysis rather than statistical testing. Additionally, the use of a stepwise variable selection method may have limited the final model results. Since stepwise analysis does not allow variables back into the model once they have been removed, it is likely that the model obtained is not the best possible. A neural network technique such as Tabusearch (Glover and Laguna, 1997) considers more variable combinations and would be more likely to arrive at the best model.

Sample sizes have been listed throughout the chapters and should be noted with scrutiny, especially for the LAI, percent cover, and epiphyte type classification within eelgrass in Chapter 3. For example, the sparse class in the percent cover model contained only four samples. This is likely the reason for the high classification accuracies of Chapter 3 versus the poor performance of the classifications when applied to the imagery in Chapter 4. Models could be improved upon by increasing the sample size and forming equal size classes.

(6) Tidal effects:

LAI estimation is more beneficial than percent cover estimation because it provides an absolute quantitative measure. It can be combined with leaf area-to-mass relationships to derive biomass, or with leaf growth rates to be translated into Net Primary Productivity (Dierssen et al., 2003), both which can be further integrated into carbon budget modelling to assess the impact of natural disturbances, climate change, and management strategies (National Resources Canada, 2010). Percent cover, on the other hand, fluctuates with tidal state. Eelgrass blades assume a vertical orientation at slack tide and become nearly parallel to the substrate in high tidal flux or when exposed on the surface. But the eelgrass bed orientation issue is two-fold. The extreme flattening of blades caused by a strong tidal current is expected to increase the at-sensor visible range reflectance, creating over-estimates of LAI when using a model developed for a slack tide. It is therefore especially important for effective temporal monitoring of eelgrass to always acquire imagery during the same tide level and current state under which the model was developed.

(6) Depth of detection

It is possible that a very low tide does not optimize LAI estimates and further research is required to determine this. However when considering only substrate detection, the area that can be effectively mapped depends on the depth of detection threshold of the sensor. Since this varies with water depth and attenuation coefficient, it is recommended that imagery be acquired during the lowest possible tide. In any case, all effort should be made to acquire imagery in the months when waters are clearest, and during a time when no major blooms are known to be occurring.

Even at low tide, confusion occurred between eelgrass, sand, and deep water in areas of the image that approached the depth threshold of substrate detection. This occurred in the classification of both images, but more so in the IKONOS image, owing to a slightly deeper tidal stage, but primarily to an order of magnitude higher detecting threshold (R_{rs}^{DT}) (Eq. 4.8). This error was reduced but not entirely eliminated by the masking of deep water. With spatial and temporal fluctuation of depth and K_d it is these subtidal classifications that will have the most variable accuracy. It is important however that reliable mapping techniques for temporal monitoring work over a range of conditions (Roelfsema, 2009). Toward this end, there are additional procedures that can be applied to further reduce error and increase reliability of

subtidal eelgrass mapping. For example, Roelfsema (2009) stratified their image data by depth and turbidity (> 3 m and turbid versus < 3 m and exposed). They performed image classification techniques on the shallow/exposed fraction, and manually digitized the deep and turbid areas based on local knowledge, ground-truthing, IKONOS fused higher resolution data (as discussed above), etc. Each manually digitized polygon was assigned a reliability level based on the amount and type of information used to derive it. Pe'eri et al. (2008) similarly applied manual expert guidance post-classification to separate green macro-algae from eelgrass. The methods of Roelfsema (2009) and Pe'eri et al. (2008) could be applied as a secondary step to the recommendations of our study.

(7) Eelgrass phenology:

Substrate discrimination in the remote sensing of vegetation is achievable as long as the species and substrates under study are spectrally distinct over space and time (Fyfe, 2003). For example, high classification accuracies at Sidney Spit are owed in part to the large spectral magnitude differences between eelgrass and sand. Classification of an area where substrates are darker and more closely resemble the reflectance of submerged eelgrass may not perform as well (Ackleson and Klemas, 1987). Likewise, plant phenology and water properties inevitably vary over time and among locations. With this in mind, it is important to note that the results of this study may be geographically and / or seasonally biased (Claustre and Maritorena, 2003). For example, classification at a time when eelgrass is largely senescent or sparse or when the water has a different K_d value may yield poorer accuracies. Further, it is anticipated that the accuracy will change with the introduction of new benthic types such as cobble, brighter or darker sand, and brown algae. It is therefore recommended that before applying our methodologies to conservation strategy, they be tested on data gathered at Sidney Spit over different seasons and at additional areas in the Gulf Islands National Park. This will strengthen the reliability of the procedure and confirm whether the models are local- and time-specific, or more widely applicable.

(8) Operator training

The findings of this study were forwarded as recommendations for remote eelgrass mapping and monitoring within the Gulf Islands National Park Reserve. It is hoped that the

findings can be applied to provide eelgrass distribution information to government and private agencies seeking to further understand coastal ecological dynamics. However it is cautioned that as with any new tool that aids policy decision, employee training and skill development take place before implementing the methodology presented here. A full understanding of possible sources of confusion enables some error to be avoided, and the unavoidable error to be considered in the final product. Implications of the final map product accuracy level and the difference between user and producer accuracies must be well understood when using the eelgrass spatial data in further analysis. An example of where this is important is in the detection of eelgrass distribution change. An area of change map created by subtraction of two eelgrass distribution images acquired at different times would contain the multiplicative error of the two images.

If the mapping strategy shows resiliency to seasonal and tidal variation, there are many applications for the methodology. Historical imagery could be used to determine historical eelgrass distribution. Eelgrass beds could be monitored for distribution change in response to climate change, or to introduction of a known disturbance threat, such as pier construction, shoreline development, boat anchoring, fish farming, point source pollution, or shoot harvesting from donor beds for transplant (Duarte et al., 2002; Marba et al., 2006; Burkholder et al., 2007; Diaz-Almela et al., 2008; Holmer et al., 2008; Apostolaki et al., 2009, Marion & Orth, 2010). Bare areas that previously sustained eelgrass could be targeted as restoration sites, especially in remote areas where there is little local historical knowledge. Since eelgrass is a key indicator of ecosystem health, remote mapping of eelgrass presents the opportunity to monitor the "pulse" of the coastal ecosystem. Closely monitoring the indicator species may enable forewarning and faster response to intercept larger scale disruption in its early stages.

Bibliography

Abileah, R. (2007). Mapping ocean currents with IKONOS. *IEEE Oceans, 1*, 1-5.

Ackleson, S. G., & Klemas, V. (1987). Remote sensing of submerged aquatic vegetation in lower Chesapeake Bay: a comparison of Landsat MSS to TM imagery. *Remote Sensing of Environment*, *22*, 235-248.

Adams, S. M. (1976). Feeding ecology of reef fish communities. *Transactions of the American Fisheries Society*, *105*(4), 514-519.

Andrefouet, S, Berkelmans, R., Odriozola, L., Done, T., Oliver, J., & Muller-Karger, F. (2002). Choosing the appropriate spatial resolution for monitoring coral bleaching events using remote sensing. *Coral Reefs*, *21*, 147-154.

Andrefouet, S, Kramer, P., Torres-Pulliza, D., Joyce, K., Hochberg, E., Garza-Perez, R., et al. (2003). Multi-site evaluation of IKONOS data for classification of tropical coral reef environments. *Remote Sensing of Environment*, *88*(1-2), 128-143.

Andrefouet, Serge, Muller-karger, F. E., Hochberg, E. J., Hu, C., & Carder, Kendall L. (2001). Change detection in shallow coral reef environments using Landsat 7 ETM + data. *Remote Sensing of Environment*, *78*, 150 - 162.

Antajan, E., & Gasparini, S. (2004). Assessment of Cryptophyceae ingestion by copepods using alloxanthin pigment: a caution. *Marine Ecology Progress Series*, *274*, 191-198.

Apostolaki, E. T., Marba, N., Holmer, M. Karakassis, I. (2009). Fish farming enhances biomass and nutrient loss in Posidonia oceanica (L.). *Estuarine Coastal and Shelf Science*, *81*, 390–400.

Apostolaki, E. T., Holmer, M., Marbà, N., & Karakassis, I. (2010). Degrading seagrass (Posidonia oceanica) ecosystems: a source of dissolved matter in the Mediterranean. *Hydrobiologia*, *649*(1), 13-23

Arar, E. J. (1997). Determination of Chlorophylls a and b and Identification of Other Pigments of Interest in Marine and Freshwater Algae Using High Performance Liquid Chromatography with Visible Wavelength Detection National Exposure Research Laboratory Office of Research a, (September).

Armstrong, R.A. (1993). Remote sensing of submerged canopies for biomass estimation. I*nternational Journal of Remote Sensing, 14,* 621-627.

Austin, R.W., and Petzold, T. (1981): The determination of the diffuse attenuation coefficient of sea water using the Coastal Zone Color Scanner. *In:* Gower, J.F.R. (Ed). Oceanography from Space, *Plenum Press,* 239–256.

Babin, M., Morel, A., Fournier-Sicre, V., Fell, F., Stramski, D. (2003). Light scattering properties of marine particles in coastal and open ocean waters as related to the particle mass concentration. *Limnology and Oceanography*, *48*(2), 843–859.

Bandos, T. V., Bruzzone, L., & Camps-Valls, G. (2009). Classification of Hyperspectral Images With Regularized Linear Discriminant Analysis. *IEEE Transactions on Geoscience and Remote Sensing*, *47*(3), 862-873.

Barnett, T.P., Adam, J.C., Lettenmaier, D.P. (2005) Potential impacts of a warming climate on water availability in snow-dominated regions. *Nature, 438,* 303–309.

Batiuk, R.A., Orth, R.J., Moore, K.A., Dennison, W.C., Stevenson, J.C., Staver, L., Carter, V., Rybicki, N., Hickman, R.E., Kollar, S., Bieber, S., Heasly, P., Bergstrom, P. (1992). Submerged aquatic vegetation habitat requirements and restoration targets: A technical synthesis. CBP/TRS 83/92. U.S. Environmental Protection Agency, Annapolis, Maryland.

Becker, B. L., Lusch, D. P., & Qi, J. (2005). Identifying optimal spectral bands from in situ measurements of Great Lakes coastal wetlands using second-derivative analysis. *Remote Sensing of Environment*, *97*, 238 - 248.

Bell JD, Westoby M (1986a) Importance of local changes in leaf height and density to fish and decapods associated with seagrasses. J Exp Mar Biol Ecol 104:249–274

Bell JD, Westoby M (1986b) Variation in seagrass height and density over a wide spatial scale: effects on common fish and decapods. J Exp Mar Biol Ecol 104:275–295

Berk, A. 1989. MODTRAN: A Moderate Resolution Model for LOWTRAN 7. *Hanscom Air Force Base, Massachusetts: U.S. Air Force Geophysical Laboratory (AFGL).*

Bintz, J.C., Nixon, S.W., Buckley, B.A., Granger, S.L. (2003). Impacts of temperature and nutrients on coastal lagoon plant communities. *Estuaries and Coasts 26,* 765–776.

Borg, J. A., Rowden, A. A., Attrill, M. J., Schembri, P. J., & Jones, M. B. (2006). Wanted dead or alive: high diversity of macroinvertebrates associated with living and "dead" Posidonia oceanica matte. *Marine Biology*, *149*(3), 667-677.

Boss, E., and Zaneveld, J.R.V. (2003). The effect of bottom substrate on inherent optical properties: Evidence of biogeochemical processes. *Limnology and Oceanography, 48,* 346-354.

Bouvet, G., Ferraris, J., & Serge, A. (2003). Evaluation of large-scale unsupervised classification of New Caledonia reef ecosystems using Landsat 7 ETM+ imagery. *Oceanologica Acta*, *26*, 281-290.

Brando, Vittorio E, Anstee, Janet M, Wettle, Magnus, & Dekker, Arnold G. (2009). A physics based retrieval and quality assessment of bathymetry from suboptimal hyperspectral data. *Remote Sensing of Environment*, *113*(4), 755-770.

Brando, Vittorio E, & Dekker, Arnold G. (2003). Satellite Hyperspectral Remote Sensing for Estimating Estuarine and Coastal Water Quality. *IEEE Transactions on Geoscience and Remote Sensing*, *41*(6), 1378-1387.

Burdick, D.M., Short, F.T., Wolf, J. (1993). An index to assess and monitor the progression of the wasting disease in eelgrass, *Zostera marina*. *Marine Ecology Progress Series, 94,* 83–90.

Burkholder, J., Tomasko, D., & Touchette, B. (2007). Seagrasses and eutrophication. *Journal of Experimental Marine Biology and Ecology*, *350*(1-2), 46-72.

Call, K. A., Hardy, J. T., & Wallin, D. O. (2003). Coral reef habitat discrimination using multivariate spectral analysis and satellite remote sensing. *International Journal of Remote Sensing*, *24*(13), 2627-2639.

Carder, K.L., Steward, R.G., Harvey, G.R., Ortner, P.B. (1989). Marine humic and fulvic acids: Their effects on remote sensing of ocean chlorophyll. *Limnology and Oceanography, 34,* 68-81.

Center for the Study of Earth from Space (CSES), 1999, Atmosphere Removal Program (ATREM), Version 3.1, User's Guide, University of Colorado, Boulder, 12 p.

Chauvaud, S., Bouchon, C., & Maniere, R. (1998). Remote sensing techniques adapted to high resolution mapping of tropical coastal marine ecosystems (coral reefs, seagrass beds and mangrove). *International Journal of Remote Sensing*, *19*(18), 3625-3639.

Chavez, P. (1988). An Improved Dark-Object Subtraction Technique for Atmospheric Scattering Correction of Multispectral Data. *Remote Sensing of Environment*, *24*, 459-479.

Chavez, P. S. (1996). Image-Based Atmospheric Corrections - Revisited and Improved. *Society*, *62*(9), 1025-1036.

Che, N. And Price, J.C. (1992). Survey of radiometric calibration results and methods for visible and near infrared channels of NOAA 7, 9 and 11 AVHRR. *Remote Sensing of Environment, 41*, 19–27.

Chen, Z., Hanson, J. D., Curran, P. J. (1991). The form of the relationship between suspended sediment concentration and spectral reflectance: Its implications for the use if Daedalus1268 data. *Remote Sensing Letters, 12*(1), 215-222.

Chen, R.F. and Gardner, G.B. (2004). High-resolution measurements of chromophoric dissolved organic matter in the Mississippi and Atchafalaya River plume regions. *Marine Chemistry, 89*(1-4), 103-125.

Cho, H. J., Kirui, P., & Natarajan, H. (2008). Test of Multi-spectral Vegetation Index for Floating and Canopy-forming Submerged Vegetation. *International Journal of Environmental Research and Public Health*, *5*(5), 477-483.

Christiansen, C., Christoffersen, H., Dalsgaard, J., Nornberg, P. (1981). Coastal and near-shore changes correlated with dieback in eelgrass (Zostera marina, L.). *Sediment. Geol. 28*, 163–173.

Ciraolo, G., Cox, E., Loggia, G. L., & Maltese, A. (2006). The classification of submerged vegetation using hyperspectral MIVIS data, *49*(1), 287-294.

Clark, C D, Ripley, H. T., Green, E P, Edwards, A. J., & Mumby, P J. (1997). Cover Mapping and measurement of tropical coastal environments with hyperspectral and high spatial resolution data. *International Journal of Remote Sensing*, *18*(2), 237-242.

Claustre, H. and Maritorena, S. (2003). The many shades of ocean blue. *Science, 302*, 1514-1515.

Clesceri, L.S., Greenberg, A.E., Eaton, A.D. (1998). 2540 D. Total suspended solids dried at 103-105°c. *In:* Clesceri, L. S.; Greenberg, A. E.; Eaton, A. D. (Ed.). Standard Methods for the Examination of Water and Wastewater, American Public Health Association, Washington, D.C. p. 2-57 - 2-58.

Congalton, R. and Green, K. (1999). Assessing the accuracy of Remote Sensing Data: Principles and Practices. *Roca Baton, Lewis.*

Conger, C. L., Hochberg, E. J., Fletcher, C. H., & Atkinson, M. J. (2006). Decorrelating Remote Sensing Color Bands from Bathymetry in Optically Shallow Waters. *IEEE Transactions on Geoscience and Remote Sensing*, *44*(06), 1655-1600.

Cottam, C., Lynch, J.J., Nelson, A.L. (1944). Food habits and management of American sea brant. *Journal of Wildlife Management, 8*, 36–56.

Cottam, C., Munro, D.A. (1954). Eelgrass status and environmental relations. *Journal of Wildlife Management, 18*, 449–460.

Cracknell, A.P. (1999). Remote sensing techniques in estuaries and coastal zones - An update. *International Journal of Remote Sensing, 20*(3), 485–496.

Curran, P.J., Dungan, J. L., Macler, B. A., Plummer, S. E. (1991). The effect of a red pigment on the relationship between red edge and chlorophyll concentration, *Remote Sensing of Environment, 35*, 69–*76.*

Darecki, M., and Stramski, D. (2004). An evaluation of MODIS and SeaWiFS bio-optical algorithms in the Baltic Sea. *Remote Sensing of Environment, 89*(3), 326−350

Davis, C.O. Bowles, J., Leathers, R.A., Korwan, D., Downes, T.V. Snyder, W.A., Rhea, W.J., Chen, W. (2002). Ocean PHILLS hyperspectral imager: Design, characterization, and calibration. *Optical Express, 10,* 210-221.

DeJong, V.N. and DeJong, D.J. (1992). Role of tide, light, and fisheries in the decline of Zostera marina L. in the Dutch Wadden Sea. *Netherlands Institute for Sea Research Publications Series 20,* 161-176

Dekker, A G, Brando, V E, & Anstee, J M. (2005). Retrospective seagrass change detection in a shallow coastal tidal Australian lake. *Remote Sensing of Environment*, *97*, 415−433.

Dekker, A, Malthus, T., Wijnen, M., & Seyhan, E. (1992). The effect of spectral bandwidth and positioning on the spectral signature analysis of inland waters. *Remote Sensing of Environment*, *41*, 211-225.

den Hartog, C. (1971). The dynamic aspect in the ecology of sea-grass communities. *Thalassia Jugoslavica,* 7, 101-12.

den Hartog, C. (1994). Suffocation of a littoral *Zostera* bed by *Enteromorpha radiata*. *Aquatic Botany, 47,* 21-28.

Dennison, W. C., Orth, Robert J, Moore, Kenneth A, Stevenson, J. C., Carter, V., Kollar, S., et al. (1993). Assessing Water Quality with Submersed Aquatic Vegetation: Habitat requirements as barometers of Chesapeake Bay health. *Bioscience*, *43*(2), 86-94.

Dennison, W. C. and Abal, E.G. (1999) Moreton Bay Study: A Scientific Basis for the Healthy Waterways Campaign, Brisbane, South East Queensland Regional Water Quality Management Strategy Team, 245p.

Diaz-Almela, E., N. Marba, E. Alvarez, Santiago, R., Holmer, M., Grau, A., Danovaro, R., Argyrou, M., Karakassis, I., Duarte, C.M. (2008). Benthic input rates predict seagrass (Posidonia oceanica) fish farm-induced decline. *Marine Pollution Bulletin, 56*: 1332–1342.

Dierssen, H. M., Zimmerman, R. C., Leathers, Robert A, Downes, T Valerie, Davis, Curtiss O, & Davis, C. (2003). Ocean color remote sensing of seagrass and bathymetry in the Bahamas Banks by high-resolution airborne imagery. *Limnology and Oceanography*, *48*(1), 444-455.

Drake, L. A., Dobbs, F. C., & Zimmerman, R. C. (2003). Effects of epiphyte load on optical properties and photosynthetic potential of the seagrasses Thalassia testudinum Banks ex Konig and Zostera marina L . *Limnology and Oceanography*, *48*(1, part 2), 456-463.

Duarte CM (1991). Allometric scaling of seagrass form and productivity. *Marine Ecology Progress Series, 77,* 289–300

Duarte, C. M., and Chiscano, C.M. (1999). Seagrass biomass and production: a reassessment. *Aquatic Botany, 65*, 159-174.

Duarte, C. M. (2002). The future of seagrass meadows. *Environmental Conservation, 29*(02), 192-206.

Environment Canada and Precision Identification. (2002). Methods for mapping and monitoring eelgrass habitat in British Columbia, Draft 4. Environment Canada internal report.

Efron, B. (1981). Nonparametric estimates of standard error: The jackknife, the bootstrap and other methods. *Biometrika, 68*, 589-599.

Esaias, W. E., Abbott, M. R., Barton, I., Brown, O. B., Campbell, J. W., Carder, K.L., et al. (1998). An overview of MODIS capabilities for ocean science observations. *IEEE Transactions on Geoscience and Remote Sensing, 36*(4), 1250-1265.

Fargion, G.S. and Mueller, J.L. (2000). Ocean optics protocols for satellite ocean color sensor validation, revision 2. *NASA Technical Memo. 209966, NASA Goddard Space Flight Center, Greenbelt, MD., 184 pp.*

Ferguson, R L, & Korfmacher, K. (1997). Remote sensing and GIS analysis of seagrass meadows in North Carolina, USA. *Aquatic bo, 58*, 241-258.

Ferguson, Randolph L, Wood, L. L., & Graham, D. B. (1993). Monitoring Spatial Change in Seagrass Habitat with Aerial Photography. *Photogrammetric Engineering & Remote Sensing, 59*(6), 1033 - 1038.

Ferwerda, J. G., Leeuw, J. D., Atzberger, C., & Vekerdy, Z. (2007). Satellite-based monitoring of tropical seagrass vegetation: Current techniques and future developments. *Hydrobiologia, 591*, 59-71.

Fisher, R.A. (1936). The use of multiple measurements in taxonomic problems. *Annual Eugenics, Part II, 7*, 179-188.

Fonseca, M., & Cahalan, J. (1992). A preliminary evaluation of wave attenuation by four species of seagrass. *Estuarine, Coastal and Shelf Science, 35*(6), 565-576.

Fornes, A., Basterretxea, G., Orfila, A., Jordi, A., Alvarez, A., & Tintore, J. (2006). Mapping Posidonia oceanica from IKONOS. *ISPRS Journal of Photogrammetry & Remote Sensing, 60*, 315 - 322.

Forster, R., & Jesus, B. (2006). Field spectroscopy of estuarine intertidal habitats. *International Journal of Remote Sensing, 27*(17), 3657-3669.

Freemantle, J. R., Pu, R., Miller, J. R. (1992). Calibration of imaging spectrometer data to reflectance using pseudo-invariant features. *Proceedings of the 15th Canadian Symposium on Remote Sensing (Toronto: Canadian Remote Sensing Society & Canadian Aeronautics and Space Institute)*, 452-455.

Fyfe, S. K. (2003). Spatial and temporal variation in spectral reflectance : Are seagrass species spectrally distinct? *Limnology and Oceanography*, *48*(1), 464-479.

Ganter, B. (2000). Seagrass (Zostera spp.) as food for brent geese (*Branta bernicla*): an overview. *Helgoland Marine Research*, *54*(2-3), 63-70.

Gao, B. -C., Heidebrecht, K. B., Goetz, A. F. H. (1993). Derivation of scaled surface reflectances from AVIRIS data, *Remote Sens. Environ., 44*, 165-178.

Gao, B.-cai, Montes, Marcos J, Ahmad, Z., & Davis, Curtiss O. (2000). Atmospheric correction algorithm for hyperspectral remote sensing of ocean color from space. *Applied Optics*, *39*(6), 887-896.

Gao, B.-C., Montes, Marcos J., Davis, Curtiss O., & Goetz, A. F. H. (2009). Atmospheric correction algorithms for hyperspectral remote sensing data of land and ocean. *Remote Sensing of Environment*, *113*, S17-S24. Elsevier Inc.

Gausman, H.W., (1982). Visible light reflectance, transmittance, and absorptance of differently pigmented cotton leaves. *Remote Sensing of the Environment, 13,* 233 – 238.

GeoEye. (2006). IKONOS imagery products guide. Accessed online at: http://www.glcf.umd.edu/library/guide/IKONOS_Product_Guide_jan06.pdf

GeoEye. (2008). IKONOS relative spectral response. Geoeye Resource Library White Papers. Accessed online at http://www.geoeye.com/CorpSite/resource/white-papers.aspx

Giesen, W. B. J. T., Katwijk, M. M. van, & Hartog, C. den. (1990). Eelgrass condition and turbidity in the Dutch Wadden Sea. *Aquatic Botany*, *37*, 71-85.

Gitelson, A., Garbuzov, G., Szilagyi, F., Mittenzwey, K.H., Karnieli, A, Kaiser, A. (1993). Quantitative remote sensing methods for real-time monitoring of inland waters quality. *International Journal of Remote Sensing, 14,* 1269–1295.

Gitelson, A. and Merzlyak, M.N. (1994). Spectral reflectance changes associated with autumn senescence of *Aesculus hippocastanum* L. and *Acer platanoides* L. leaves: Spectral features and relation to chlorophyll estimation. *Journal of Plant Physiology 143*, 286–292.

Glazer, A. N., Apell, G. S., Hixson, C. S., Bryant, D. A., Rimon, S., & Brown, D. M. (1976). Biliproteins of cyanobacteria and Rhodophyta: Homologous family of photosynthetic accessory pigments. *Proceedings of the National Academy of Sciences of the United States of America*, *73*(2), 428-431.

Glover, F. (1989). Tabu search—Part I. ORSA *J. Comput., 1,* 190.

Glover, F. (1990) Tabu search—Part II. ORSA *J. Comput., 2*, 4

Glover, F., Taillard, E., de Werra, D. (1993) A user's guide to tabu search. *Ann. Oper. Res., 41*, 3–28.

Goodman, J.A., Montes, M.J., Ustin, S.L. (2003). Applying Tafkaa for atmospheric correction of AVIRIS over coral ecosystems in the Hawai-ian Islands. *Presented at 12th AVIRIS/HYPERION Earth Science Workshop, Jet Propulsion Laboratory, Pasadena, California, February 25-28, 2003.*

Gordon, H.R., and Morel, A. (1983). Remote assessment of ocean color for interpretation of satellite visible imagery: A review. Springer-Verlag, New York, 44 pp.

Gordon, H. R. (2005). Normalized water-leaving radiance: revisiting the influence of surface roughness. *Applied Optics, 44*(2), 241–248.

Gower, Jim, Hu, C., Borstad, G., & King, S. (2006). Ocean Color Satellites Show Extensive Lines of Floating Sargassum in the Gulf of Mexico. *IEEE Transactions on Geoscience and Remote Sensing*, *44*(12), 3619-3625.

Green,E.P., Mumby, P.J., Edwards, A.J., Clark, C.D. (2000). Remote sensing handbook for tropical coastal management. *Coastal Management Sourcebooks 3, UNESCO Paris.316pp.*

Greve, T.M., Borum, J., Pedersen, O. (2003). Meristematic oxygen variability in eelgrass (Zostera marina). *Limnology and Oceanography, 48*, 210–216.

Gullstrom, M., Lunden, B., Bodin, M., Kangwe, J., Ohman, M., Matern, S., et al. (2006). Assessment of changes in the seagrass-dominated submerged vegetation of tropical Chwaka Bay (Zanzibar) using satellite remote sensing. *Estuarine, Coastal and Shelf Science*, *67*, 399-408.

Guzzi, R., Rizzi, R., & Zibordi, G. (1987). Atmospheric correction of data measured by a flying platform over the sea: elements of a model and its experimental validation. *Applied Optics*, *26*(15), 3043-3051.

Habeeb, R., Johnson, C., Wotherspoon, S., & Mumby, P. (2007). Optimal scales to observe habitat dynamics: a coral reef example. *Ecological Applications*, *17*(3), 641-647.

Heck KL Jr, Orth RJ (1980) Seagrass habitats: the roles of habitat complexity, competition and predation in structur- ing associated fish and motile macroinvertebrate assemblages. In: Kennedy VS (ed) Estuarine perspectives. Academic Press, New York, NY

Hedley, J D, & Mumby, P J. (2003). A remote sensing method for resolving depth and subpixel composition of aquatic benthos. *Limnology and Oceanography, 48*(1, part 2), 480-488.

Hedley, J D, Mumby, P J, Joyce, K. E., & Phinn, S R. (2004). Spectral unmixing of coral reef benthos under ideal conditions. *Coral Reefs, 23*, 60-73.

Hedley, J., Harborne, A., & Mumby, P. (2005). Simple and robust removal of sun glint for mapping shallow-water benthos. *International Journal of Remote Sensing, 26*, 2107-2112.

Heege, T., Bogner, A., & Pinnel, N. (2003). Mapping of submerged aquatic vegetation with a physically based process chain. *Proc. Remote Sensing, 5233*, 1-8.

Heiri, O., Lotter, A. F., & Lemcke, G. (2001). Loss on ignition as a method for estimating organic and carbonate content in sediments : reproducibility and comparability of results. *Journal of Paleolimnology*, 101-110.

Hemming, M. A., Duarte, C.M. (2000). Seagrass ecology. Cambridge University Press.

Hochberg, E., & Atkinson, M. (2003). Capabilities of remote sensors to classify coral,algae and sand as pure and mixed spectra. *Remote Sensing of Environment, 85*(2), 174-189.

Hochberg, E. J., Andréfouët, S., & Tyler, M. R. (2003). Sea Surface Correction of High Spatial Resolution Ikonos Images to Improve Bottom Mapping in Near-Shore Environments. *IEEE Transactions on Geoscience and Remote Sensing*, *41*(7), 1724-1729.

Holben B.N., Eck, T.F., Slutsker, I., Tanré, D., Buis, J.P., Setzer, A., Vermote, E., Reagan, J.A., Kaufman, Y., Nakajima, T., Lavenu, F., Jankowiak, I., Smirnov, A. (1998). AERONET - A federated instrument network and data archive for aerosol characterization, *Remote Sensing of the Environment, 66,* 1-16.

Holden, H., & Ledrew, E. (1998). Spectral discrimination of healthy and non-healthy corals based on cluster analysis, principal components analysis and derivative spectroscopy. *Remote Sensing of Environment*, *65*, 217-224.

Holden, H., & Ledrew, E. (1999). Hyperspectral identification of coral reef features. *International Journal of Remote Sensing*, *20*(13), 2545-2563.

Holmer, M., Argyrou, M., Dalsgaard, T., Danovaro, R., Diaz-Almela, E., Duarte, C.M., Frederiksen, M., Grau, A., Karakassis, I., Marba, N., Mirto, S., Perez, M., Pusceddu, A., Tsapakis, M. (2008). Effects of fish farm waste on Posidonia oceanica meadows: synthesis and provision of monitoring and management tools. *Marine Pollution Bulletin, 56*: 1618–1629.

Holt, T.J., Hartnoll, R.G., Hawkins, S.J. (1997). Sensitivity and vulnerability to man-induced change of selected communities: intertidal brown algal shrubs, *Zostera* beds and *Sabellaria spinulosa* reefs. *Peterbourough English Nature, Research Report No. 234*

Hooker, S. B., Zibordi, G., & Brown, J. W. (2004). Above-water radiometry in shallow coastal waters. *Applied Optics*, *43*(21), 4254-4268.

Hyland, S. J., Courtney, A.J. and Butler, C.T. (1989) Distribution of seagrass in the Moreton Region from Coolangatta to Noosa. Brisbane, Queensland Government Department of Primary Industries, 42p.

Hyndes, G. A., Kendrick, A. J. , Macarthur, L.D., Stewart, E. (2003). Differences in the species- and size-composition of fish assemblages in three distinct seagrass habitats with differing plant and meadow structure. *Marine Biology 142*, 1195–1206.

IOCCG. (2000). Remote sensing of ocean colour in coastal and other optically complex waters. In: Sathyendrannath, S. (Ed.), Reports of the International Ocean Colour Coordinating Group. No. 3, IOCCG, Dartmouth, Canada, 140 pp.

IPCC. (2007). Climate change 2007: the physical science basis. Contribution of Working Group I to the 4th assessment report of the Intergovernmental Panel on Climate Change. Cambridge University Press, Cambridge.

Irlandi, E.A., Ambrose, W.G.L., Orlando, B.A. (1995). Landscape ecology and the marine environment: how spatial configuration of seagrass habitat influences growth and survival of the bay scallop. *Oikos, 72,* 307–313.

Irlandi EA (1997) Seagrass patch size and survivorship of an infaunal bivalve. Oikos, 78, 511-518.

Jackson, J.B.C., Kirby, M.X., Berger, W.H., Bjorndal, K.A., Botsford, L.W., Bourque, B.J., Bradbury, R.H., Cooke, R., Erlandson, J., Estes, J.A., Hughes, T.P., Kidwell, S., Lange, C.B., Lenihan, H.S., Pandolfi, J.M., Peterson, C.H., Steneck, R.S., Tegner, M.J.,Warner, R.R. (2001). Historical overfishing and the recent collapse of coastal ecosystems. *Science 293,* 629-638.

Jeffrey, S.W., Mantoura, R.F.C., Wright, S.W., International Council of Scientific Unions. Scientific Committee on Oceanic Research.; Unesco. (1997). Phytoplankton pigments in oceanography: guidelines to modern methods. *UNESCO Publishing, Paris. 661pp.*

Jensen, J.R. (2007). Remote Sensing of the Environment: An Earth Resource Perspective, 2nd Ed., *Prentice Hall*, 592pp.

Johannessen, S.C., Macdonald, R.W., Paton, D.W. (2003). A sediment and organic carbon budget for the greater Strait of Georgia. *Estuarine, Coastal and Shelf Science, 56,* 845–860.

Johannessen, S.C., Masson, D., Macdonald, R.W. (2006). Distribution and cycling of suspended particles inferred from transmissivity in the Strait of Georgia, Haro Strait and Juan de Fuca Strait. *Atmosphere–Ocean, 44*, 17–27.

Johannessen, S. C., Potentier, G., Wright, C. A., Masson, D., & Macdonald, R. W. (2008). Water column organic carbon in a Pacific marginal sea (Strait of Georgia, Canada). *Marine environmental research*, *66 Suppl*, S49-61. Elsevier Ltd.

Johannessen, S., & Macdonald, R. (2009). Effects of local and global change on an inland sea: the Strait of Georgia, British Columbia, Canada. *Climate Research, 40*(November), 1-21.

Johansen, K., Roelfsema, C., & Phinn, S. (2008). Special feature - high spatial resolution remote sensing for environmental monitoring and management. *Journal of Spatial Science, 53*(1), 43-47.

Johnson, M. P., Edwards, M., Bunker, F., & Maggs, C. A. (2005). Algal epiphytes of Zostera marina : Variation in assemblage structure from individual leaves to regional scale. *Aquatic Botany, 82*, 12-26.

Johnson, S. W., Thedinga, J. F., Neff, A. D., Harris, P. M., Lindeberg, M. R., Maselko, J. M., et al. (2010). Fish Assemblages in Nearshore Habitats of Prince William Sound, Alaska. *Northwest Science, 84*(3), 266-280.

Jordan, C.F. (1969). Determination of leaf area index from quality of light on the forest floor. *Ecology, 50*, 663–666.

Kaufman, Y. J., & Remer, L. (1994). Detetion of forests using mid-IR reflectance: An application for aerosol studies. *IEEE Transactions on Geoscience and Remote Sensing, 32*(3), 672-683.

Karpouzli, E. & Malthus, T. (2003). The empirical line method for the atmospheric correction of IKONOS imagery. *International Journal of Remote Sensing, 24*, 1143–1150.

Kay, S., Hedley, John D., & Lavender, Samantha. (2009). Sun glint correction of high and low spatial resolution images of aquatic scenes: A review of methods for visible and near-infrared wavelengths. *Remote Sensing, 1*, 697-730.

Kirk, J.T.O. (1994). Light & Photosynthesis in Aquatic Ecosystems, University Press, Cambridge.

Kirk, J. T. O. (2003). The vertical attenuation of irradiance as a function of the optical properties of the water. *Limnology and Oceanography, 48*(1), 9-17.

Kirkman, H. (1996). Baseline and monitoring methods for seagrass meadows. *Journal of Environmental Management, 47*, 191-201.

Klein, A.G., and Isacks, B.L. (1997). Alpine glacial geomorphological studies in the Central Andes using Landsat Thematic Mapper images. *Glacial Geology and Geomorphology rp01/1998, 1-26.*

Kneizys, F. X., Shettle, E.P., Abreu, L.W., Chetwynd, J.H., Anderson, G.P., Gallery, W.O., Selby, J.E.A., Clough, S.A. (1988). Users Guide to LOWTRAN7. *Technical Report AFGL-TR-8-0177, Air Force Geophys. Lab., Bedford, MA.*

Komick, N. M., Costa, M. P. F., & Gower, J. (2009). Bio-optical algorithm evaluation for MODIS for western Canada coastal waters: An exploratory approach using in situ reflectance. *Remote Sensing of Environment, 113*(4), 794-804.

Kowalczuk, P., Olszewski, J., Darecki, M., Kaczmarek, S. (2005). Empirical relationships between coloured dissolved organic matter (CDOM) absorption and apparent optical properties in Baltic Sea waters. *International Journal of Remote Sensing, 26*(2), 345-370.

Kromkamp, J., De Brouwer, J. F. C., Blanchard, G. F., Forster, R. M., & Creach, V. (Eds.). (2006). Functioning of microphytobenthos in estuaries Amsterdam: Royal Netherlands Academy of Arts and Sciences.

Kruse, F. A., Lefkoff, A. B., Boardman, J. B., Heidebrecht, K. B., Shapiro, A. T., Barloon, P. J., and Goetz, A. F. H. (1993). The Spectral Image Processing System (SIPS) - Interactive Visualization and Analysis of Imaging spectrometer Data. *Remote Sensing of the Environment, 44,* 145 - 163.

Kutser, Tiit, Vahtmae, Ele, Roelfsema, Chris M, & Metsamaa, L. (2007). Photo-library method for mapping seagrass biomass. *Estuarine, c, 75,* 559-563.

Kutser, Tiit, Vahtmäe, E., & Metsamaa, L. (2006). Spectral library of macroalgae and benthic substrates in Estonian coastal waters. *Proc. Estonian. Acad. Sci. Biol. Ecol., 55*(4), 329-340.

Larkum, Anthony W.D., Robert J. Orth, and Carlos M. Duarte (Eds). (2006). Seagrasses: Biology, Ecology and Conservation. Springer.

Lathrop, R. G., Montesano, P., & Haag, S. (2006). A Multi-scale Segmentation Approach to Mapping Seagrass Habitats Using Airborne Digital Camera Imagery. *Photogrammetric Engineering & Remote Sensing, 72*(6), 665-675.

Lavender, S, Pinkerton, M., Moore, G, Aiken, J., & Blondeaupatissier, D. (2005). Modification to the atmospheric correction of SeaWiFS ocean colour images over turbid waters. *Continental Shelf Research, 25*(4), 539-555.

Leatherbarrow, K.E. (2006). Monitoring environmental impacts of recreational boat anchoring on eelgrass (*Zostera marina L.*) and benthic invertebrates in the Gulf Islands National Park Reserve of Canada. MSc Graduate Student Thesis, University of Victoria.

Lee, Z., Carder, K L, & Arnone, R. A. (2002). Deriving inherent optical properties from water color: a multiband quasi-analytical algorithm for optically deep waters. *Applied Optics, 41*(27), 5755-5772.

Li, M., Gargett, A., & Denman, K. (2000). What Determines Seasonal and Interannual Variability of Phytoplankton and Zooplankton in Strongly Estuarine Systems? Application to the semi-enclosed estuary of Strait of Georgia and Juan de Fuca Strait. *Estuarine, Coastal and Shelf Science, 50*(4), 467-488.

Lichtenthaler, H.K., Gitelson, A. and Lang, M. (1996). Non-destructive determination of chlorophyll content of leaves of a green and an aurea mutant of tobacco by reflectance measurements. *Journal of Plant Physiology, 148,* 483–193.

Liedtk, J., Roberts, A., Luternauer, J. (1995). Practical remote sensing of suspended sediment concentration. *Photogrammetric Engineering and Remote Sensing 61* (2), 167–175.

Lobitz, B., Guild, L., Armstrong, R., Montes, M, & Goodman, J. (2008). Pre-Processing 2005 AVIRIS Data for Coral Reef Analysis. *Proceedings of the 11th International Coral Reef Symposium, Ft. Lauderdale, Florida, 7-11, July 2008, Session number 17*.

Louchard, E. M., Reid, R. P., Stephens, F. C., Davis, C O, Leathers, R A, & Downes, T V. (2003). Optical remote sensing of benthic habitats and bathymetry in coastal environments at Lee Stocking Island, Bahamas: A comparative spectral classification approach. *Limnology and Oceanography*, *48*(1, part 2), 511-521.

Luczkovich, J.J., Uczkovich, J.J., Wagner, T.W., Michalek, J.L. Stoffle, R.W. (1993). Discrimination of coral reefs, seagrass meadows, and sand bottom types from space: a Dominican Republic case study. *Photogrammetric Engineering and Remote Sensing, 59*, 385-389.

Lunden, B. and Gullstrom, M. (2003). Satellite remote sensing for monitoring of vanishing seagrass in Swedish coastal waters. *Norwegian Journal of Geography 57*, 121-124.

Lyzenga, D. R. (1978). Passive remote sensing techniques for mapping water depth and bottom features. *Applied Optics, 17*(3), 379-384.

Lyzenga, D.R. (1981). Remote sensing of bottom reflectance and water attenuation parameters in shallow water using aircraft and Landsat data. *International Journal of Remote Sensing, 10*, 53-69.

Macleod, R.D. (1994). Using a Quantitative Accuracy Assessment to Compare Various Change Detection Techniques for Eelgrass Dis- tributions in Great Bay, NH with Landsat Thematic Mapper Data, M.S. Thesis, University of New Hampshire, Durham, New Hampshire, 149pp.

Macleod, R. D., & Congalton, R G. (1998). Quantitative comparison of change detection algorithms for monitoring eelgrass from remotely sensed data. *Photogrammetric Engineering and Remote Sensing*, *64*(3), 207-216.

Marba, N., Santiago, R., Diazalmela, E., Alvarez, E., & Duarte, C. (2006). Seagrass (Posidonia oceanica) vertical growth as an early indicator of fish farm-derived stress. *Estuarine, Coastal and Shelf Science*, *67*(3), 475-483.

Marion, S. R., & Orth, Robert J. (2008). Innovative techniques for large-scale seagrass restoration using Zostera marina (eelgrass) seeds. *Restoration Ecology*, *18*(4), 514-526.

Maritorena, S., Morel, A., & Gentili, B. (1994). Diffise reflectance of oceanic shallow waters: Influence of water depth and bottom albedo. *Limnology and Oceanography*, *39*(7), 1689-1703.

Maritorena, S., Morel, A., & Gentili, B. (2000). Determination of the fluorescence quantum yield by oceanic phytoplankton in their natural habitat. *Applied Optics*, *39*(36), 6725-6737.

Mather P.M. (1999). Computer processing of remotely sensed images: an introduction. *Second edition, John Wiley & Sons*

Mateo, M. A., Sanchez-Lizaso, J. L., Romero, J. (2003). Posidonia oceanica ‘‘banquettes’’: a preliminary assessment of the relevance for meadow carbon and nutrients budget. *Estuarine, Coastal and Shelf Science*, *56*, 85–90.

Mazzella, L. And Alberte, R.S. (1986). Light adaptation and the role of autotrophic epiphytes in primary production of the temperate seagrass, *Zostera marina* L. *Journal of Experimental Marine Biology and Ecology, 100,* 165-180.

Mazzella, L., Scipione, M. B., Buia, M.C. (1989). Spatio-temporal distribution of algal and animal communities in a Posidonia oceanica meadow. *Marine Ecology, 10*, 107–129.

McArdle, S. S., Miller, J. R., Freemantle, J. R.. (1992). Airborne image acquisition under cloud: preliminary comparisons with clear-sky scene radiance and reflectance imagery.

Meleder, V., Barille, L., Launeau, P., Carrere, V., Rince, Y. (2003). Spectrometric constraint in analysis of benthic diatom biomass using monospecific cultures. *Remote Sensing of Environment, 88,* 386−400.

McArdle, S. S., Miller, J. R., Freemantle, J. R.. (1992). Airborne image acquisition under cloud: preliminary comparisons with clear-sky scene radiance and reflectance imagery. *Proceedings of the 15th Canadian Symposium on Remote Sensing (Toronto: Canadian Remote Sensing Society & Canadian Aeronautics and Space Institute),* 446-449.

McGarigal, K., Cushman, S., Stafford, S. (2000). Multivariate statistics for wildlife and ecology research, *Springer, New York, USA*

Mishra, D. R., Narumalani, S., Rundquist, D., & Lawson, M. (2005). High-Resolution Ocean Color Remote Sensing of Benthic Habitats : A Case Study at Roatan Island, Honduras. *IEEE Transactions on Geoscience and Remote Sensing*, *43*(7), 1592-1604.

Mishra, D., Narumalani, S., Rundquist, D., & Lawson, M. (2006). Benthic Habitat Mapping in Tropical Marine Environments Using QuickBird Multispectral Data. *Photogrammetric Engineering & Remote Sensing*, *72*(9), 1037-1048.

Mobley, C. D. (1994). Light and water: Radiative transfer in natural waters. *Academic Press.*

Mobley, C. D. (1999). Estimation of the Remote-Sensing Reflectance from Above-Surface Measurements. *Applied Optics*, *38*(36), 7441-7455.

Mobley, C. D. and Sundman, L. K. (2000a). HYDROLIGHT 4.1 users' guide, WA London' Sequoia Scientific, Inc., 85pp.

Mobley, C. D. and Sundman, L. K. (2000b). HYDROLIGHT 4.1 technical documentation, WA Sequoia Scientific, Inc., 76pp

Montes, M.J., Gao, B., Davis, C.O. (2004b). Hyperspectral remote sensing of ocean colour: A comparison of Hyperion and AVIRIS. *in* Green, R.O. (ed) (2004). *Proceedings of the 13th JPL Airborne Earth Science Workshop,* JPL Publications.

Montes, Marcos, Gao, B.-cai, & Davis, Curtiss O. (2004a). *NRL Atmospheric Correction Algorithms for Oceans : Tafkaa User's Guide*. *Distribution* (pp. 1-39).

Montes, M.J., Gao, B., Davis, C.O., Moline, M, (2003). Analysis of AVIRIS data from LEO-15 using Tafkaa atmospheric correction. *NASA technical paper http://ntrs.nasa.gov/archive/nasa/casi.ntrs.nasa.gov/20050192437_2005194961.pdf*

Moore, K., & Wetzel, R. (2000). Seasonal variations in eelgrass (Zostera marina L.) responses to nutrient enrichment and reduced light availability in experimental ecosystems. *Journal of Experimental Marine Biology and Ecology*, *244*(1), 1-28.

Moore, Kenneth A., Wilcox, D. J., & Orth, Robert J. (2000). Analysis of the Abundance of Submersed Aquatic Vegetation Communities in the Chesapeake Bay. *Estuaries*, *23*(1), 115-127.

Moore, K.A., Jarvis, J.C. (2008). Environmental factors affecting recent summertime eelgrass diebacks in the lower Chesapeake Bay: implications for long-term persistence. *Journal of Coastal Research, 55,* 135–147.

Morel, A. and Maritorena, S. (2001). Bio-optical properties of oceanic waters: A reappraisal. *Journal of Geophysical Research, 106*(4), 7163-7180.

Morel, A., Gentili, B., Claustre, H., Babin, M., Bricaud, A., Ras, J., et al. (2007). Optical properties of the "' clearest '" natural waters. *Limnology and Oceanography*, *52*(1), 217-229.

Muehlstein, L.K. (1989). Perspectives on the wasting disease of eelgrass *Zostera marina*. *Disease of Aquatic Organisms, 7,* 211–221.

Muehlstein, L.K., Porter, D., Short, F.T. (1991). Labyrinthula zosterae sp. nov., the causative agent of wasting disease of eelgrass, *Zostera marina*. *Mycologia, 83,* 180–191.

Mueller, J.L., Fargion, G.S., McClain, C.R. (Eds). (2003). Ocean Optics Protocols For Satellite Ocean Color Sensor Validation, Revision 4, Volume IV. NASA, Goddard Space Flight Center, Greenbelt, MD.

Mumby, P J, & Edwards, A. J. (2002). Mapping marine environments with IKONOS imagery: enhanced spatial resolution can deliver greater thematic accuracy. *Remote Sensing of Environment*, *82*, 248-257.

Mumby, P J, Green, E P, Edwards, A. J., & Clarke, C. D. (1997). Coral reef habitat mapping: How much detail can remote sensing provide?. *Marine Biology*, *130*, 193-202.

Mumby, P. J., Green, E. P., Clark, C. D., & Edwards, a J. (1998). Digital analysis of multispectral airborne imagery of coral reefs. *Coral Reefs*, *17*(1), 59-69. Murphy, M. L., Johnson, S. W., & Csepp, D. J. (2000). A Comparison of Fish Assemblages in Eelgrass and Adjacent Subtidal Habitats Near Craig , Alaska. *Alaska Fishery Research Bulletin*, *7*, 11-21.

Murphy, R. J., Tolhurst, T. J., Chapman, M. G., & Underwood, A. J. (2004). Estimation of surface chlorophyll on an exposed mudflat using digital colour-infrared (CIR) photography. *Estuarine, Coastal and Shelf Science*, *59*, 625-638.

Murphy, R. J., Tolhurst, T. J., Chapman, M. G., & Underwood, A. J. (2005). Estimation of surface chlorophyll-a on an emersed mudflat using field spectrometry: accuracy of ratios and derivative-based approaches. *International Journal of Remote Sensing*, *26*(9), 1835-1859.

Murphy, R. J., Underwood, A. J., Pinkerton, M. H., & Range, P. (2005). Field spectrometry : New methods to investigate epilithic micro-algae on rocky shores. *Journal of Experimental Marine Biology and Ecology*, *325*, 111 - 124. Najjar, R. G., Pyke, C. R., Adams, M. B., Breitburg, D., Hershner, C., Kemp, M., et al. (2010). Potential climate-change impacts on the Chesapeake Bay. *Estuarine, Coastal and Shelf Science*, *86*(1), 1-20. Elsevier Ltd.

NASA. (2009). Chapter 8: ETM+ Calibration. *In:* Landsat 7 science data users handbook. Accessed online at: http://landsathandbook.gsfc.nasa.gov/handbook/handbook_htmls/chapter8/chapter8.html

Neckles, H.A., Wetzel, R.L., Orth, R.J. (1993) Relative effects of nutrient enrichment and grazing on epiphyte-macrophyte (Zostera marina L.) dynamics. *Oecologia, 93,* 285-295.

Nienhuis, P.H. (1983). Temporal and spatial patterns of eelgrass (Zostera marina L.) in a former estuary in the Netherlands, dominated by human activities. *Mar. Technol. Soc. J., 17,* 69–77.

Norris, J. G., & Wyllie-Echeverria, S. (1997). Estimating maximum depth distribution of seagrass using underwater videography. 4th Int. Conf. Remote Sens. Mar. Coastal Environ., Orlando, Florida, 17–19 March 1997, Vol. I (pp. 603–610).

Orth, R.J. (1976). The demise and recovery of eelgrass, *Zostera marina,* in the Chesapeake Bay, Virginia. *Aquatic Botany, 2,* 141-159.

Orth, R.J., and Moore, K.A. (1983). An unprecedented decline in submerged aquatic vegetation (Chesapeake Bay). *Science, 22,* 51-53.

Orth, R.K., Moore, K.A., Gordon, H.H. (1979) Distribution and abundance of submerged aquatic vegetation in the lower Chesapeake Bay, Virginia. U.S. EPA Final Report. 600/8-79-029/SAV1. 199 p.

Orth, Robert J., & Moore, Kenneth A. (1984). Distribution and Abundance of Submerged Aquatic Vegetation in Chesapeake Bay: An Historical Perspective. *Estuaries, 7*(4), 531-540.

Palacios, S.L., Zimmerman, R.C. (2007). Response of eelgrass *Zostera marina* to CO2 enrichment: possible impacts of climate change and potential for remediation of coastal habitats. *Marine Ecology Progress Series, 344,* 1–13.

Parks Canada. (2010). Sidney Spit (Sidney Island). Gulf Islands National Park Reserve of Canada. Accessed online at: http://www.pc.gc.ca/pn-np/bc/gulf/carte-map-nfl.aspx#a28

Pasqualini, V., Pergentmartini, C., Pergent, G., Agreil, M., Skoufas, G., Sourbes, L., et al. (2005). Use of SPOT 5 for mapping seagrasses: An application to Posidonia oceanica. *Remote Sensing of Environment, 94*(1), 39-45.

Pawlowicz, R., Allen, S., Lee, D.J., Harris, S., Halverson, M., Riche, O., Bird, T. (2003). STRATOGEM—The Strait of Georgia Ecosystem Project. *2003 Georgia Basin/Puget Sound Research Conference proceedings.*

Peneva, E., Griffith, J. A., & Carter, G. A. (2008). Seagrass Mapping in the Northern Gulf of Mexico using Airborne Hyperspectral Imagery: A Comparison of Classification Methods. *Journal of Coastal Research, 24*(4), 850-856.

Pe'eri, S., Morrison, J. R., Short, F., Mathieson, A., Brook, A., & Trowbridge, P. (2008). Macroalgae and eelgrass mapping in Great Bay Estuary using AISA hyperspectral imagery. *A final report to The New Hampshire Estuaries Project,* 148pp.

Penhale, P.A., Smith Jr.,W.O. (1977). Excretion of dissolved organic carbon by eelgrass (Zostera marina) and its epiphytes. *Limnol. Oceanogr. 22,* 400–407.

Penuelas, J.C., Gamon, J.A., Griffin, K.L., Field, C.B. (1993). Assessing community type, plant biomass, pigment composition, and photosynthetic efficiency of aquatic vegetation from spectral reflectance. *Remote Sensing of Environment, 46,* 110–118.

Penuelas, J.C., Filella, I., Gamon, J.A. (1995). Assessment of photosynthetic radiation use efficiency with spectral reflectance. *New Phytologist 131,* 291–296.

Phillips, R.C. and Lewis, R.L. (1983). Influence of environmental gradients on leaf widths and transplant success in North American seagrasses. *Marine Technology Society Journal, 17*:59- 68.

Phillips, R.C. (1984). The ecology of eelgrass meadows in the Pacific Northwest: a community profile. U.S. Fish and Wildlife Service FWS/OBS-84/24. 85p.

Philpot, W. (2007). Estimating Atmospheric Transmission and Surface Reflectance from a Glint-Contaminated Spectral Image. *IEEE Transactions on Geoscience and Remote Sensing, 45,* 448-457.

Phinn, S, Dekker, A, Brando, V, & Roelfsema, C. (2005). Mapping water quality and substrate cover in optically complex coastal and reef waters: An integrated approach. *Marine Pollution Bulletin, 51*, 459−469.

Phinn, Stuart, Roelfsema, Chris, Dekker, Arnold, Brando, Vittoro, & Anstee, J. (2008). Remote Sensing of Environment Mapping seagrass species , cover and biomass in shallow waters: An assessment of satellite multi-spectral and airborne hyper-spectral imaging systems in Moreton Bay (Australia). *Remote Sensing of Environment, 112*, 3413-3425.

Precision Identification. (2002). Eelgrass mapping review. Internal report prepared for Environment Canada, September 2002.

Purkis, S. J. (2005). A "Reef-Up" approach to classifying coral habitats from IKONOS imagery. *IEEE Transactions on Geoscience and Remote Sensing*, *43*(6), 1375-1390.

Rasmussen, E. (1977). The wasting disease of eelgrass (*Zostera marina*) and its effects on environmental factors and fauna. *In*: McRoy, C.P., Helfferich, C. (eds). Seagrass ecosystems – a scientific perspective. Marcel Dekker, New York, pp 1–51.

Reed, B., & Hovel, K. (2006). Seagrass habitat disturbance: how loss and fragmentation of eelgrass Zostera marina influences epifaunal abundance and diversity. *Marine Ecology Progress Series, 326*, 133-143.

Richards, J.A. (1999). Remote Sensing Digital Image Analysis, *Springer-Verlag, Berlin, p. 240.*

Richards, J. And Jia, X. (2006). Chapter 10: *Feature* Reduction. *In:* Remote sensing digital image analysis: an introduction. 4th Ed. (Springer)

Richardson, A. J. and Wiegand, C. L. (1977). Distinguishing vegetation from soil background information. *Photogramm. Eng. Remote Sens. 43,* 1541-1552.

Richardson, A.D., Berlyn, G.P., Duigan, S.P. (2003). Reflectance of Alaskan black spruce and white spruce in relation to elevation and latitude. *Tree Physiology, 23,* 537–544.

Richardson, Andrew D, Reeves, J. B., & Gregoire, T. G. (2004). Multivariate Analyses of Visible/Near Infrared (VIS/NIR) Absorbance Spectra Reveal Underlying Spectral Differences among Dried, Ground Conifer Needle Samples from Different Growth Environments. *New Phytologist*, *161*(1), 291-301.

Robinson, C., & Martel, G. (2007). The status of eelgrass meadow (Zostera marina) health during August 2004-2006 in the new Gulf Islands National Park Reserve of Canada. *WSNC Technical Report for Western and Northern Canada Service Centre – Parks Canada*, 59pp.

Robinson, C. L. K., & Yakimishyn, J. (2005). Monitoring for the Ecological Integrity of Eelgrass Beds (Zostera marina) in Canada ' s Coastal National Parks of British Columbia. *Parks Canada Resource Conservation technical report (internal document)*, 1-89.

Roelfsema, C, Phinn, S, Dennison, W., Dekker, a, & Brando, V. (2006). Monitoring toxic cyanobacteria Lyngbya majuscula (Gomont) in Moreton Bay, Australia by integrating satellite image data and field mapping. *Harmful Algae*, *5*(1), 45-56.

Roelfsema, C. M., Phinn, S. R., Udy, N., & Maxwell, P. (2009). An Integrated Field and Remote Sensing Approach for Mapping Seagrass Cover, Moreton Bay, Australia. *Journal of Spatial Science*, *54*(1), 45-62.

Rouse, J.W., Haas, R.H., Schell, J.A., Deering, D.W. (1973). Monitoring vegetation systems in the great plains with ERTS. *Third ERTS Symposium, NASA SP-351, vol. 1, NASA, Washington DC*, 309-317.

Rowan, K.S. (1989). Photosynthetic Pigments of Algae. Cambridge University Press

Ruddick, K. G., Cauwer, V. D., Park, Y.-je, & Moore, Gerald. (2006). Seaborne measurements of near infrared water-leaving reflectance: The similarity spectrum for turbid waters. *Limnology and Oceanography*, *51*(2), 1167-1179.

Salita JT, Ekau W, Saint-Paul U (2003) Field evidence on the influence of seagrass landscapes on fish abundance in Bolinao, northern Philippines. Mar Ecol Prog Ser 247: 183–195

Sathyendranath, S. (2000). Remote Sensing of Ocean Colour in Coastal, and Other Optically-Complex, Waters. *IOCCG Report 3, International Ocean-Colour Coordinating Group, Dartmouth, Canada.*

Satlantic Inc. (2003a). Operation manual for the HyperSAS. Satlantic Document #SAT-DN-00212 Revision A.

Satlantic Inc. (2003b). Operation manual for the OCR-3000 (MiniSpec). Satlantic document #SAT-DN-0069 Revision D.

Schweizer, D., Armstrong, R. A., & Posadal, J. (2005). Remote sensing characterization of benthic habitats and submerged vegetation biomass in Los Roques Archipelago National Park , Venezuela. *International Journal of Remote Sensing*, *26*(12), 2657-2667.

Seager, S., Turner, E. L., Schafer, J. and Ford, E. B. (2005). Vegetation's Red Edge: A possible Spectroscopic Biosignature of Extraterrestrial Plants. *Astrobiology 5*(3), 372-390.

Sewell, A. T., Norris, J.G., Wyllie-Echeverria, S., Skalski, J.R. (2001) Eelgrass monitoring in Puget Sound: Overview of the Submerged Vegetation Monitoring Program. *Puget Sound Research 2001, Puget Sound Water Quality Action Team, P.O.Box 40900, Olympia, WA 98504- 0900.*

Shi, W., & Wang, M. (2007). Detection of turbid waters and absorbing aerosols for the MODIS ocean color data processing. *Remote Sensing of Environment*, *110*, 149 – 161.

Short., F.T., and Coles, R.G. (2001). Global seagrass research methods. Elsevier.

Short, F.T., Muehlstein, L.K., Porter, D. (1987). Eelgrass wasting disease: cause and recurrence of a marine epidemic. *Biological Bulletin, 173,* 557–562

Short, F. T., & Wyllie-Echeverria, S. (1996). Natural and human-induced disturbance of seagrasses. *Environmental Conservation*, *23*(01), 17-27.

Short, F.T., Neckles, H.A. (1999). The effects of global climate change on seagrasses. *Aquatic Botany, 63,* 169–196.

Smith, G.M. and Milton, E.J. (1999) The use of the empirical line method to calibrate remotely sensed data of reflectance. *International Journal of Remote Sensing, 20,* 2653–2662.

Spectral Imaging. (2008). AISA DUAL Hyperspectral Sensor. Accessed online at: http://www.channelsystems.ca/documents/AISADualver1-07.pdf

Stevens, T. and Connolly, R.M. (2005) Local- scale mapping of benthic habitats to access representation in marine protected area, Marine and Freshwater Research, 56, pp. 111- 123.

Stevenson, J.C., Staver, L.W., Staver, K.W. (1993). Water quality associated with survival of submersed aquatic vegetation along an estuarine gradient. *Estuaries, 16,* 346–361.

Story, M., & Congalton, Russell G. (1986). Accuracy Assessment : A User ' s Perspective. *Photogrammetric Engineering and Remote Sensing*, *52*(3), 397-399.

Strittholt, J.R., Frost, P.A. (1996) Determining abundance and distribution of eelgrass (*Zostera marina*) in Tillamook Bay Estuary, Oregon Using Multispectral Airborne Imagery. *Prepared for Tillamook Bay National Estuary Project, Garibaldi, Oregon 97118. Prepared under Cooperative Agreement #CE990292-1 with the U.S. Environmental Protection Agency.*

Su, H., Karna, D., Fraim, E., Fitzgerald, M., Dominguez, R., Myers, J. S., et al. (2006). Evaluation of Eelgrass Beds Mapping Using a High-Resolution Airborne Multispectral Scanner. *Photogrammetric Engineering & Remote Sensing*, *72*(7), 789-797.

Teillet, P.M., Slater, P.N., Ding, Y., Santer, R.P., Jackson, R.D., Moran, M.S. (1990). Three methods for the absolute calibration of the NOAA AVHRR sensors in-flight. *Remote Sensing of Environment, 31,* 105–120.

Thistle, M. E., Schneider, D. C., Gregory, R. S., & Wells, N. J. (2010). Fractal measures of habitat structure: maximum densities of juvenile cod occur at intermediate eelgrass complexity. *Marine Ecology Progress Series, 405,* 39-56.

Thom, R.M. (1996). CO2-Enrichment effects on eelgrass (*Zostera marina L*.) and bull kelp (*Nereocystis luetkeana*). *Water, Air, & Soil Pollution, 88,* 383–391.

Thorhaug, A., Richardson, A D, & Berlyn, G. P. (2007). International Journal of Remote Spectral reflectance of the seagrasses : Thalassia testudinum, Halodule wrightii, Syringodium filiforme and five marine algae. *International Journal of Remote Sensing*, *28*(7), 1487-1501.

Tou, J. T. and Gonzalez, R. C. (1974). Pattern Recognition Principles, *Addison-Wesley Publishing Company, Reading, Massachusetts.*

Twardowski, M. S., Donaghay, P. L. (2001). Separating in situ and terrigenous sources of absorption by dissolved materials in coastal waters. *Journal of Geophysical Research, 106* (C2), 2545–2560.

Ungar, S. G. (1997). Technologies for future Landsat missions. *Photogrammetric Engineering & Remote Sensing, 63,* 901−905.

USGS. (2010). Landsat missions. Accessed online at: http://landsat.usgs.gov/

Vahtmae, E, Kutser, T, Martin, G., & Kotta, J. (2006). Feasibility of hyperspectral remote sensing for mapping benthic macroalgal cover in turbid coastal waters—a Baltic Sea case study. *Remote Sensing of Environment, 101*(3), 342-351.

Vermote, E., Tanre, D., Deuze, J. L., Herman, M., & Morcrette, J. J. (1997). Second Simulation of the Satellite Signal in the Solar Spectrum, 6S: An overview. *IEEE Transactions on Geoscience and Remote Sensing*, *35*(3), 675-686.

Viollier, M., Belsher, T. and Loubersac, L. (1985). Signatures spectrales des objets du littoral. Proceedings of the 3rd International Colloquium Spectral Signatures of Objects in Remote Sensing, 16–20 December 1985 SP-247 (Les Arcs: ESA), pp. 253–256. *In* Murphy, R.J.,

Tolhurst, T.J., Chapman, M.G., Underwood, A.J. (2005) Estimation of surface chlorophyll-a on an emersed mudflat using field spectrometry: accuracy of ratios and derivative-based approaches, *International Journal of Remote Sensing*, *26*(9), 1835-1859.

Vergeer, L.H.T., den Hartog, C. (1994). Omnipresence of Labyrinthulaceae in seagrass. *Aquatic Botany, 48,* 1–20.

Wang, M. H. (2006). Effects of ocean surface reflectance variation with solar elevation on normalized water-leaving radiance. *Applied Optics, 45*(17), 4122–4128.

Werdell, P. J., & Roesler, C. S. (2003). Remote assessment of benthic substrate composition in shallow waters using multispectral reflectance. *Limnology and Oceanography*, *48*(1), 557-567.

Wettle, M, Brando, V E, & Dekker, A G. (2004). A methodology for retrieval of environmental noise equivalent spectra applied to four Hyperion scenes of the same tropical coral reef. *Remote Sensing of Environment*, *93*, 188−197.

Whitmarsh, J. and Govindjee (1999). The Photosynthetic Process. *In:* Concepts in Photobiology: Photosynthesis and Photomorphogenesis. Edited by G.S. Singhal, G. Renger, K-D. Irrgang, S. Sopory and Govindjee. Narosa Publishers/Kluwer Academic Publishers. pp. 11-51.

Williams, B.K. (1983). Some observations on the use of discriminant analysis in ecology. *Ecology, 64*, 1283-1291.

Yakimishyn, J., & Robinson, C. (2005). Epiphyte Photo Index (EPI) Development and Application for Evaluating Epiphyte Loads on Eelgrass (Zostera marina) in Pacific Rim National Park Reserve of Canada. *Parks Canada internal report*, 13pp.

Young, E.L. (1937). Notes on the *Labyrinthula* parasite of eelgrass *Zostera marina*. *Bulletin of the Mount Desert Island Biological Laboratory*, p 33–35

Young, P. C. and Kirkman, H. (1975). The seagrass communities of Moreton Bay, Queensland, Australia. *Aquatic Botany*, *1*, 191-202.

Young, A. (1982). Raleigh scattering: Questions of terminology are resolved during a historical excursion through the physics of light-scattering by gas molecules. *Physics Today*, *82*.

Zacharias, M., Niemann, O., & Borstad, G. (1992). An assessment and classification of a multispectral bandset for the remote sensing of intertidal seaweeds. Canadian Journal of Remote Sensing, 18(4), 263–274.

Zainal, A., Dalby, D. H., Robinson, I. S. (1993). Monitoring marine ecological changes in the east coast of Bahrain with Landsat TM. *Photogrammetric Engineering and Remote Sensing, 59,* 415–421.

Zharikov, Y., Skilleter, G.A., Loneragan, N.R., Taranto, T. and Cameron, B.E. (2005) Mapping and characterising subtropical estuarine landscapes using aerial photography and GIS for potential application in wildlife conservation and management, Biological Conservation, 125, pp. 87–100.

Zimmerman, R. C. (2003). A biooptical model of irradiance distribution and photosynthesis in seagrass canopies. *Limnology and Oceanography*, *48*(1), 568-585.

Appendix A

Ancillary Figures and Tables

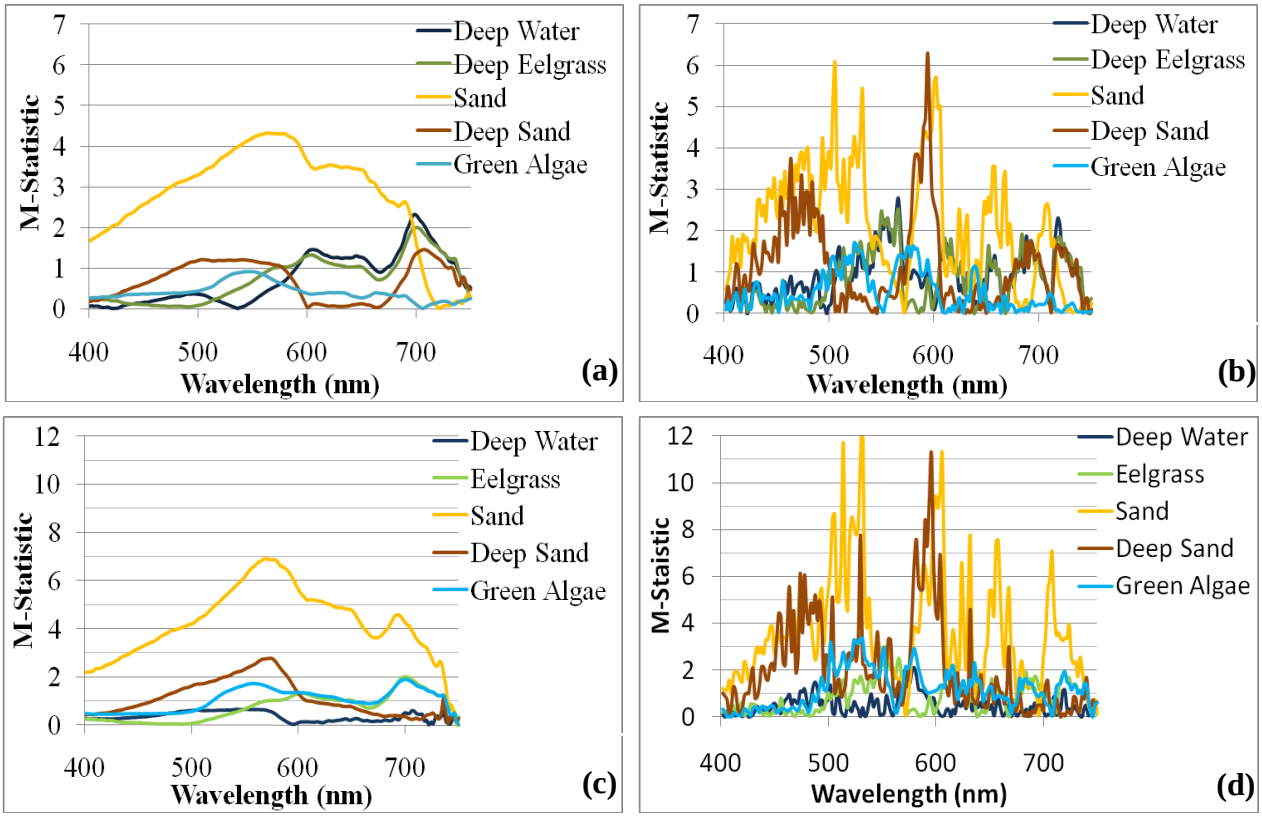

Figure 6.1 M-statistic results for the above-water dataset describing the separability of each benthic class and (a) shallow eelgrass (<3m) original $R_{rs}(0+)$ data; (b) shallow eelgrass $R_{rs}(0+)$ first derivative data; (c) deep eelgrass (>3m) original $R_{rs}(0+)$ data; and (d) deep eelgrass $R_{rs}(0+)$ first derivative data. An M-statistic > 1 indicates good separation (Kaufman and Remer, 1994). Note generally higher discerning ability of first derivative values.

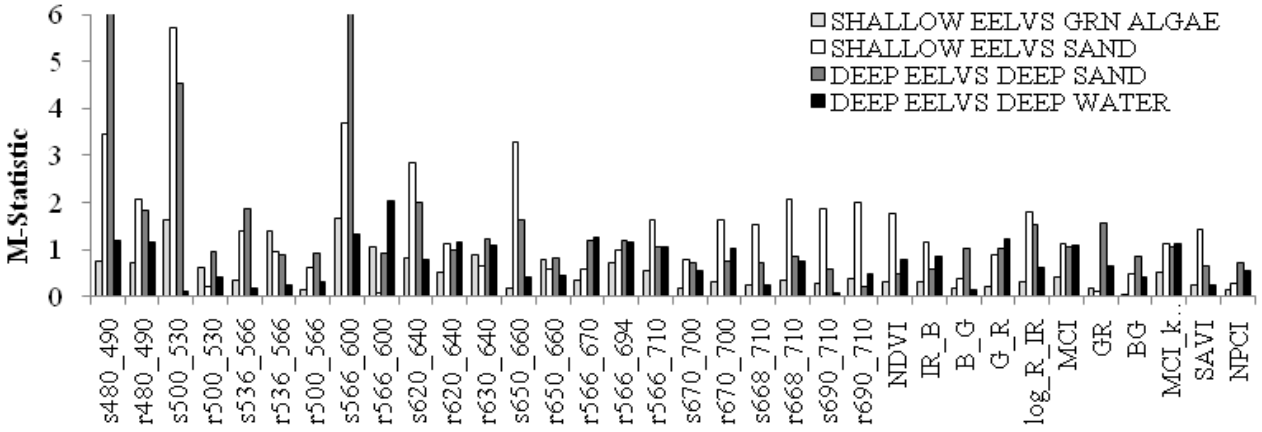

Figure 6.2 M-Statistic results of above water dataset indices for the shallow (< 3 m) dataset (white and light grey bars) and the deep (> 3 m) dataset (dark grey and black bars).

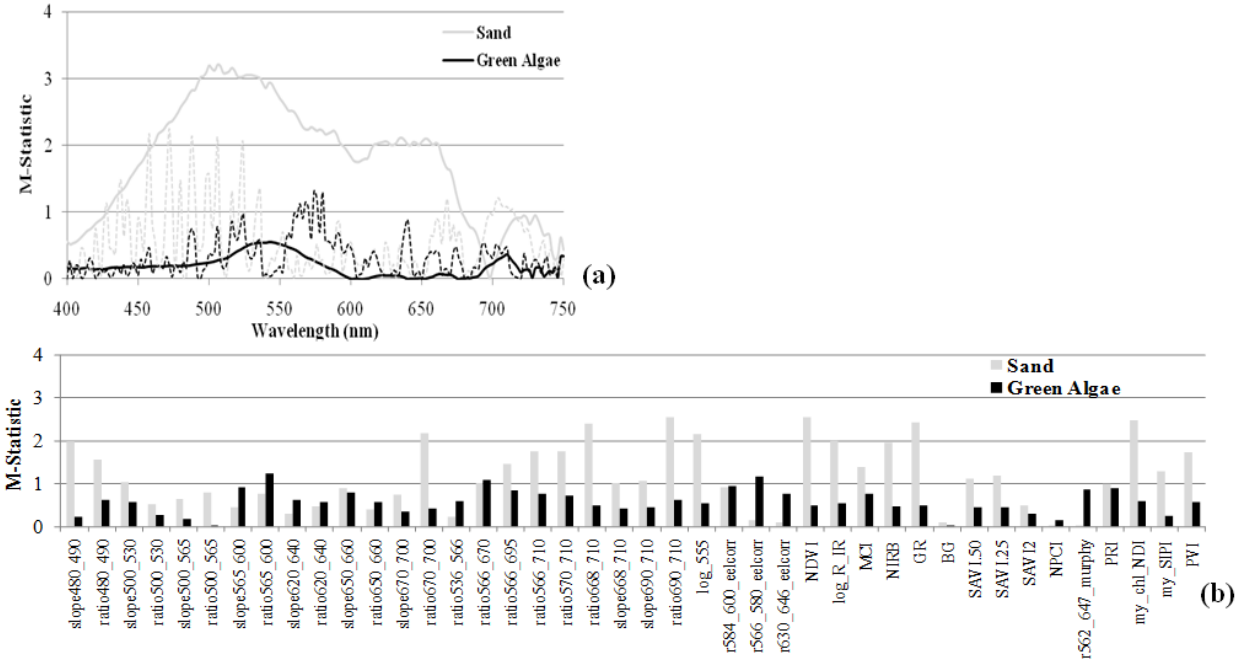

Figure 6.3 M-statistic results of water column corrected data set (a) original and first derivative data and (b) indices for separating eelgrass from sand and green algae. Thick lines represent the original water corrected data and thin lines represent the first derivative water corrected data.

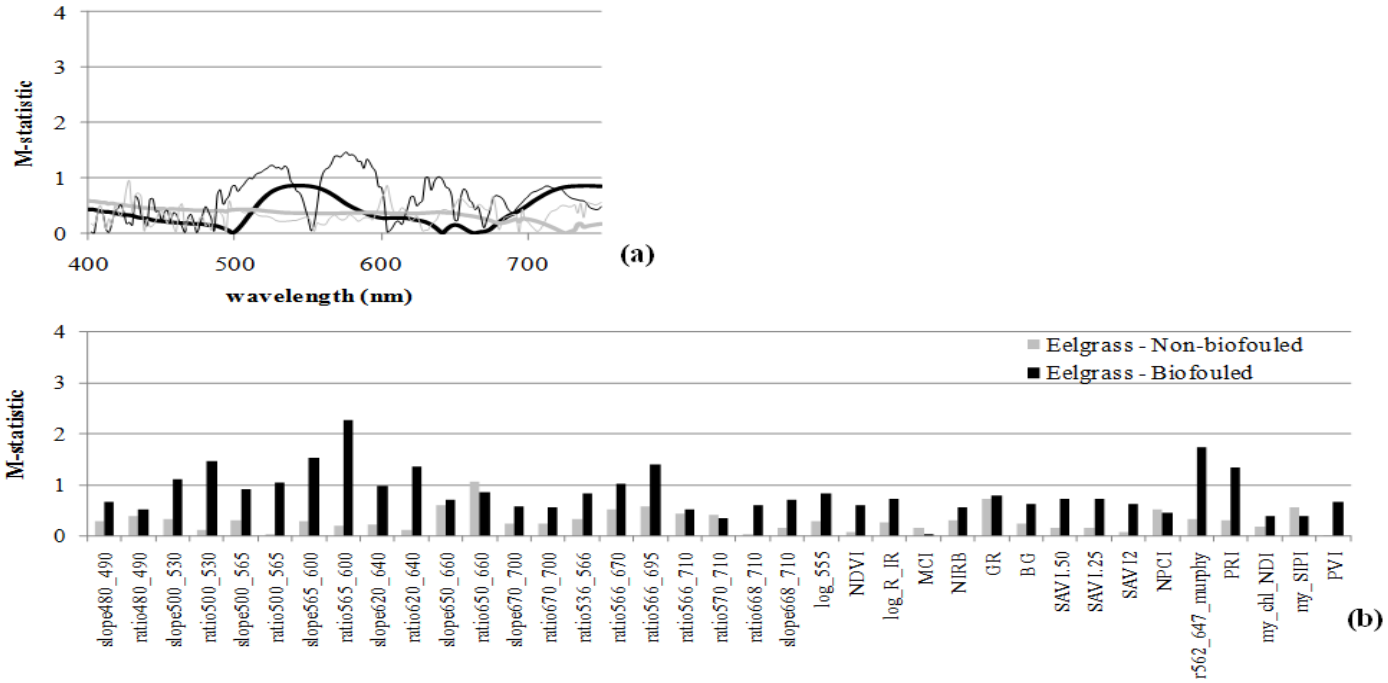

Figure 6.4 M-statistic results of endmember data set (a) original and first derivative data and (b) indices, for separating green algae from biofouled eelgrass (black) and non-biofouled (manually cleaned) eelgrass (grey). Thick lines represent the original Rrs endemember spectra, thin lines represent the first derivative spectra, and bars represent spectral indices. Note difficulty (M<1) of separating non-biofouled eelgrass from green algae.

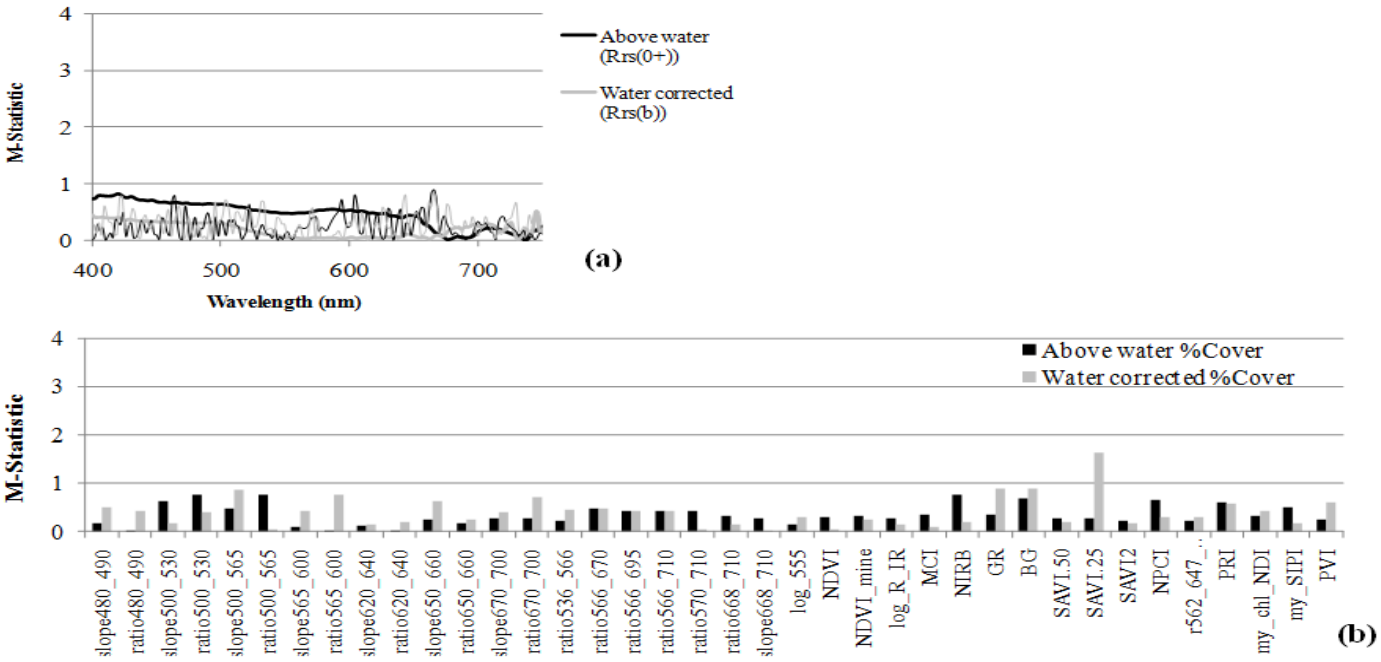

Figure 6.5 M-statistic results for separating Sparse (20-70% cover) and Dense (> 70% cover) percent cover classes in shallow (< 3 m) eelgrass using (a) the original $R_{rs}^{(0+)}$ data (thick lines) and first derivative $R_{rs}^{(0+)}$ (thin lines) data; and (b) indices. Results are shown for both above water data ($R_{rs}^{(0+)}$) and water corrected data (R_{rs}^{b}).

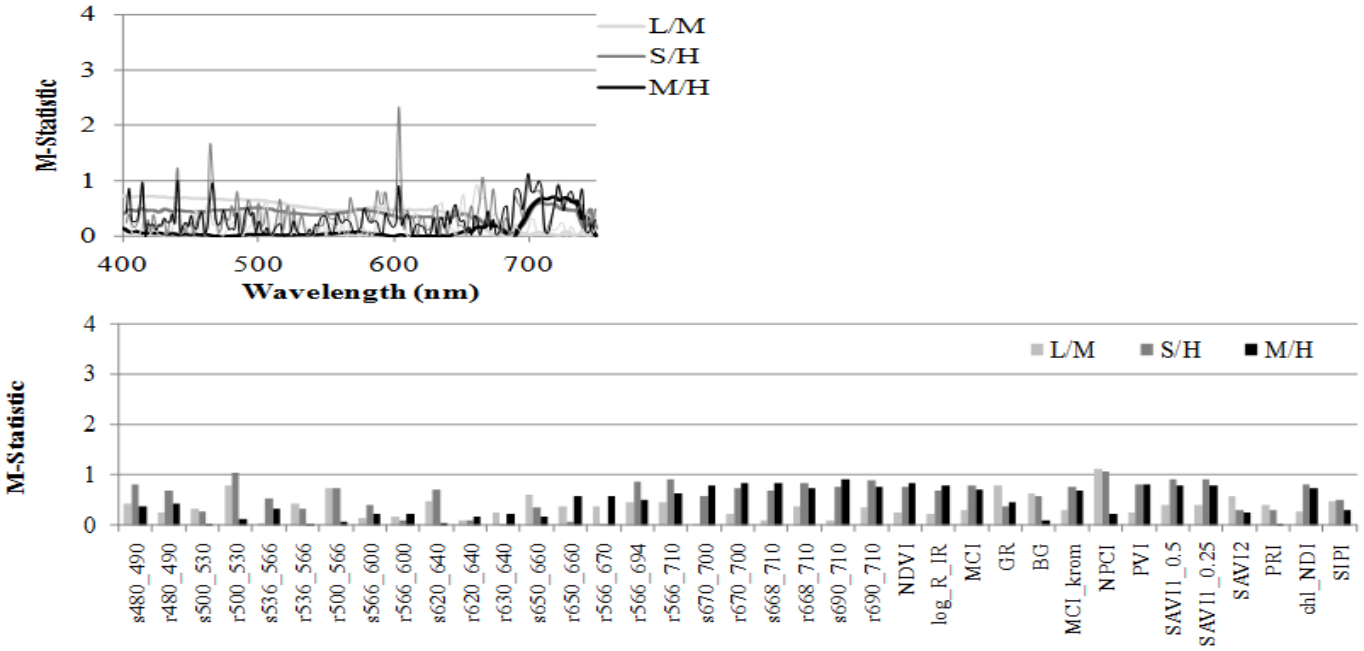

Figure 6.6 M-statistic results of the above water dataset for the separation of three LAI classes in shallow (<3m) eelgrass using (a) the original Rrs(0+) data (thick lines) and first derivative Rrs(0+) (thin lines) data; and (b) indices. L/M = Low vs. Medium LAI, L/H = Low vs. High LAI, and M/H = Medium vs. High LAI classes. An M-statistic > 1 indicates good separation (Kaufman and Remer, 1994). Note higher discerning ability of first derivative values.

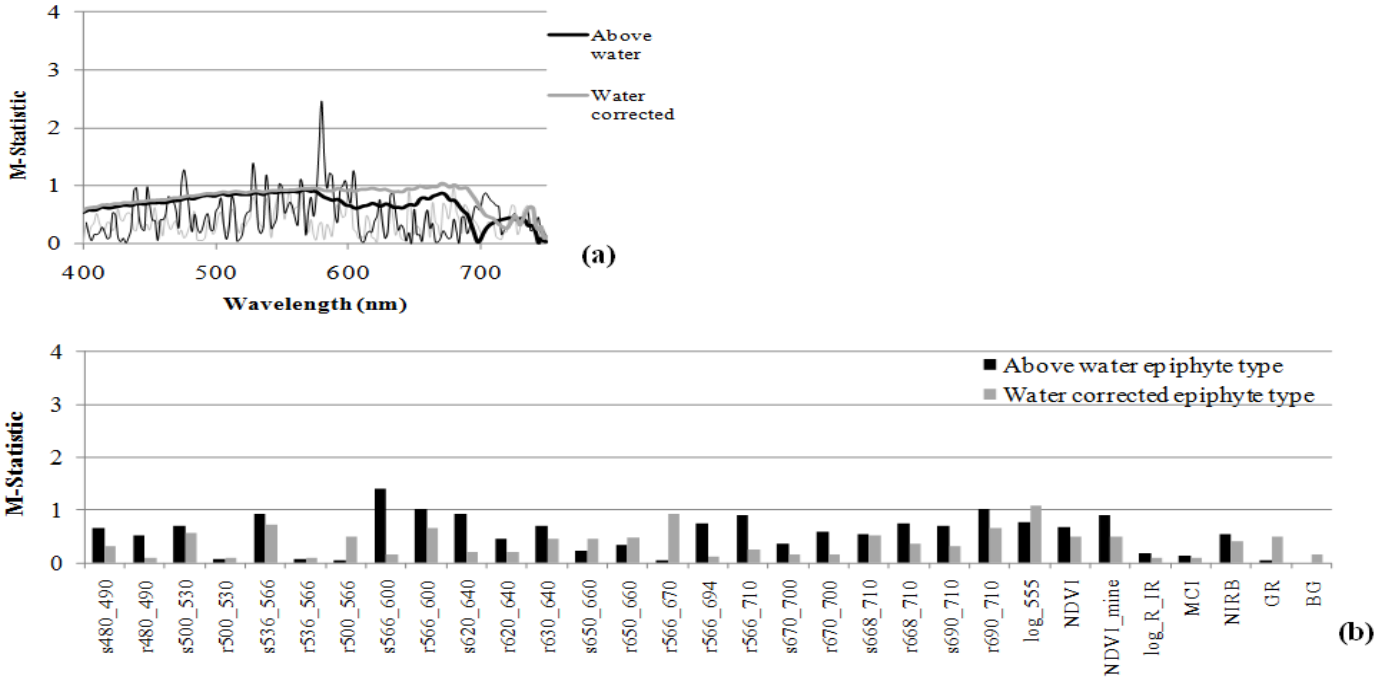

Figure 6.7 M-statistic results between epiphyte type classes (diatom and red algae) in shallow (<3m) eelgrass for above water data and water corrected data (a) original and first derivative data and (b) indices.

Appendix B

Chromophoric Dissolved Organic Matter (CDOM) Measurements

Stn	$a_{CDOM}(440)$ (m^{-1})	Mean (m^{-1})	Std. (m^{-1})	CV (%)
1A	0.241			
1B	0.186	0.242	0.056	23
1C	0.298			
2B	0.253	0.268	0.021	8
2C	0.283			
3A	0.220			
3B	0.170	0.210	0.035	17
3C	0.239			
4A	0.265	0.246	0.027	11
4B	0.227			
6A	0.252			
6B	0.233	0.251	0.017	7
6C	0.267			
7A	0.243			
7B	0.225	0.228	0.014	6
7C	0.215			
9A	0.241			
9B	0.199	0.229	0.027	12
9C	0.248			
14A	0.214	0.206	0.011	5
14B	0.198			
15A	0.221			
15B	0.190	0.212	0.019	9
15C	0.223			
16A	0.352	0.327	0.036	11
16B	0.301			
22A	0.249			
22B	0.262	0.253	0.008	3
22C	0.249			
24A	0.216			
24B	0.244	0.232	0.014	6
24C	0.235			
27A	0.226			
27B	0.210	0.218	0.008	4

27C	0.218			
31A	0.315			
31B	0.209	0.256	0.054	21
31C	0.243			
35A	0.245			
35B	0.225	0.243	0.018	7
35C	0.260			
37A	0.197			
37B	0.217	0.199	0.017	8
37C	0.183			
38A	0.211			
38B	0.259	0.257	0.045	18
38C	0.301			
41A	0.252			
41B	0.289	0.278	0.023	8
41C	0.294			
45A	0.277	0.275	0.004	1
45B	0.272			
46A	0.278			
46B	0.276	0.280	0.005	2
46C	0.285			
49A	0.206			
49B	0.224	0.215	0.009	4
49C	0.215			
50A	0.217			
50B	0.153	0.184	0.032	17
50C	0.181			
51A	0.183			
51B	0.158	0.207	0.066	32
51C	0.282			
52A	0.214			
52B	0.223	0.220	0.005	2
52C	0.221			
54A	0.171			
54B	0.214	0.194	0.022	11
54C	0.198			
56A	0.376			
56B	0.337	0.330	0.051	15
56C	0.276			
BLANK1	0.064	n/a	n/a	n/a
BLANK2A	0.029			
BLANK2B	0.039	0.046	0.021	45
BLANK2C	0.069			
BLANK3A	0.038			
BLANK3B	0.019	0.047	0.013	27
BLANK3C	0.083			

Appendix C

Chlorophyll-a (Chl-a) and Accessory Pigments Measurements

Stn.	chl-a	chl-b	chl-c2	chl-c3	Fucoxanthin	Diadino	Peridinin	β-carotene	19' but fuco	19' hex fuco	Alloxanthin	Zeaxanthin
1	2.0823	0.0417	0.3013	0.0683	0.6447	0.1047	0.404	0.0217	#NAME?	n.a.	0.0250	0.0237
2	2.2270	0.0845	0.3385	0.0660	0.6880	0.1500	0.537	0.0280	0.0515	n.a.	0.0340	0.0330
3	1.5500	0.0383	0.2450	0.0503	0.4710	0.0850	0.328	n.a.	0.0377	n.a.	0.0207	0.0323
4	5.6230	0.0720	0.6540	0.1510	2.5310	0.2820	0.517	0.0710	0.0450	n.a.	0.0470	0.0800
6	1.7937	0.1007	0.1437	0.0350	0.4437	0.0570	0.144	0.0355	0.0333	n.a.	0.0197	0.0503
7	1.7495	0.1555	0.1970	0.0355	0.6415	0.0820	0.192	0.0350	0.0400	n.a.	0.0575	0.0650
9	1.4253	0.0200	0.1897	0.0427	0.4297	0.0633	0.257	0.0133	0.0313	n.a.	0.0207	0.0313
14	2.4310	0.0344	0.3813	0.0751	0.7415	0.1686	0.572	0.0200	0.0868	0.0230	0.0194	0.0307
15	2.2417	0.0607	0.3483	0.0677	0.6687	0.1447	0.546	0.0203	0.0310	n.a.	0.0223	0.0263
16	2.7070	0.2690	0.1745	0.0305	0.9290	0.0810	0.040	0.0945	n.a.	n.a.	0.2705	0.1290
22	2.7277	0.0513	0.3910	0.0990	0.8520	0.1043	0.301	0.0293	0.0693	n.a.	0.0230	0.0243
24	1.9842	0.0328	0.3498	0.0882	0.6563	0.1095	0.326	0.0194	0.0361	n.a.	0.0213	0.0217
27	2.1030	0.0577	0.2963	0.0647	0.7637	0.0893	0.243	0.0237	0.0197	n.a.	0.0293	0.0290
31	2.2000	0.0537	0.3297	0.0690	0.8180	0.0977	0.273	0.0273	0.0363	n.a.	0.0307	0.0260
35	3.0610	0.0737	0.3973	0.0807	1.0243	0.1213	0.335	0.0443	0.0000	n.a.	0.0407	0.0310
37	1.9963	0.0410	0.2787	0.0607	0.6970	0.0690	0.203	0.0283	0.0230	n.a.	0.0307	0.0287
38	3.3277	0.0967	0.3493	0.0423	1.4967	0.1300	0.058	0.1240	0.0000	n.a.	0.1590	0.1513
41	1.7407	0.0683	0.1933	0.0323	0.8153	0.0580	0.035	0.0403	n.a.	n.a.	0.1520	0.0760
45	7.2260	0.2057	0.7317	0.1797	2.7997	0.2767	0.410	0.1337	0.0390	n.a.	0.0580	0.0893
46	3.3230	0.1287	0.3263	0.0630	1.3907	0.1140	0.117	0.0617	n.a.	n.a.	0.0770	0.0980
49	1.8426	0.0525	0.2111	0.0496	0.5504	0.0542	0.144	0.0223	0.0203	n.a.	0.0357	0.0422
50	1.6460	0.0537	0.1837	0.0277	0.7010	0.0410	0.041	0.0153	n.a.	n.a.	0.0257	0.0220
51	1.6307	0.0557	0.1817	0.0300	0.7097	0.0493	0.044	0.0183	n.a.	0.0260	0.0293	0.0247
52	1.2790	0.1430	0.1257	0.0173	0.5940	0.0520	n.a.	0.0300	n.a.	n.a.	0.1003	0.0710
54	1.8773	0.1253	0.2093	0.0383	0.7917	0.0563	0.038	0.0210	n.a.	0.0370	0.0370	0.0413
56	1.7070	0.1203	0.1990	0.0260	0.9253	0.0657	0.029	0.0453	n.a.	n.a.	0.0343	0.0890

Appendix D

Total Suspended Matter (TSM) Measurements

Stn.	TSM ($g\ m^{-3}$)	Mean ($g\ m^{-3}$)	Std. ($g\ m^{-3}$)	CV (%)
1A	2.84000			
1B	3.06000	2.84333	0.21502	8
1C	2.63000			
2A	3.68000			
2B	3.46000	4.28333	1.24042	29
2C	5.71000			
3A	3.32000			
3B	1.83000	2.57667	0.74501	29
3C	2.58000			
4A	3.66000			
4B	4.18000	3.95000	0.26514	7
4C	4.01000			
6A	3.58000			
6B	3.64000	3.60667	0.03055	1
6C	3.60000			
7A	7.22000			
7B	4.39000	5.73667	1.41994	25
7C	5.60000			
9A	3.96000			
9B	4.86000	4.36667	0.45622	10
9C	4.28000			
14A	1.76000			
14B	2.58000	2.36667	0.53304	23
14C	2.76000			
15A	5.06000	4.45500	0.85560	19
15B	3.85000			
16A	5.84000	6.17500	0.47376	8
16C	6.51000			
DI blank 1	0.01000			
DI blank 2	-0.05000	0.01000	0.06000	600
DI blank 3	0.07000			
22A	3.93000			
22B	3.31000	3.56000	0.32696	9
22C	3.44000			
24A	3.20000	3.16875	1.01830	1
24B	3.13750			
27A	4.83000			
27B	3.83000	3.99333	0.76814	19
27C	3.32000			
31A	2.73000			
31B	2.57000	2.56667	0.16503	6

31C	2.40000			
35A	3.15000	3.57500	0.60104	17
35B	4.00000			
37A	3.11000			
37B	2.54000	2.80000	0.28827	10
37C	2.75000			
38A	6.40000			
38B	6.35000	6.23333	0.24664	4
38C	5.95000			
41A	5.15000			
41B	4.79000	4.91333	0.20502	4
41C	4.80000			
45A	4.95000			
45B	3.79000	3.84667	1.07612	28
45C	2.80000			
46A	6.59000			
46B	4.73000	5.61000	0.93402	17
46C	5.51000			
49A	4.25000			
49B	5.72826	4.56609	1.04077	23
49C	3.72000			
DI blank 4	1.74000			
DI blank 5	1.28000	1.15000	0.66461	58
DI blank 6	0.43000			
50A	2.07000			
50B	3.43000	3.15667	0.97905	31
50C	3.97000			
51A	3.19000			
51B	2.49000	2.97000	0.41617	14
51C	3.23000			
52A	4.08000	5.38667	2.16865	1
52B	4.19000			
54A	5.34000			
54B	5.17000	4.83000	0.74101	15
54C	3.98000			
56A	5.41000			
56B	5.36000	5.83667	0.78271	13
56C	6.74000			
BLANK7	-0.13000			
BLANK8	-0.15000	-0.13667	0.01155	-8
BLANK9	-0.13000			

Appendix E

Spatial Distribution of Water Optical Constituents

Spatial distribution of CDOM, TSM, Chlorophyll-a, and pigment composition at the study site Class ranges were defined by natural breaks.

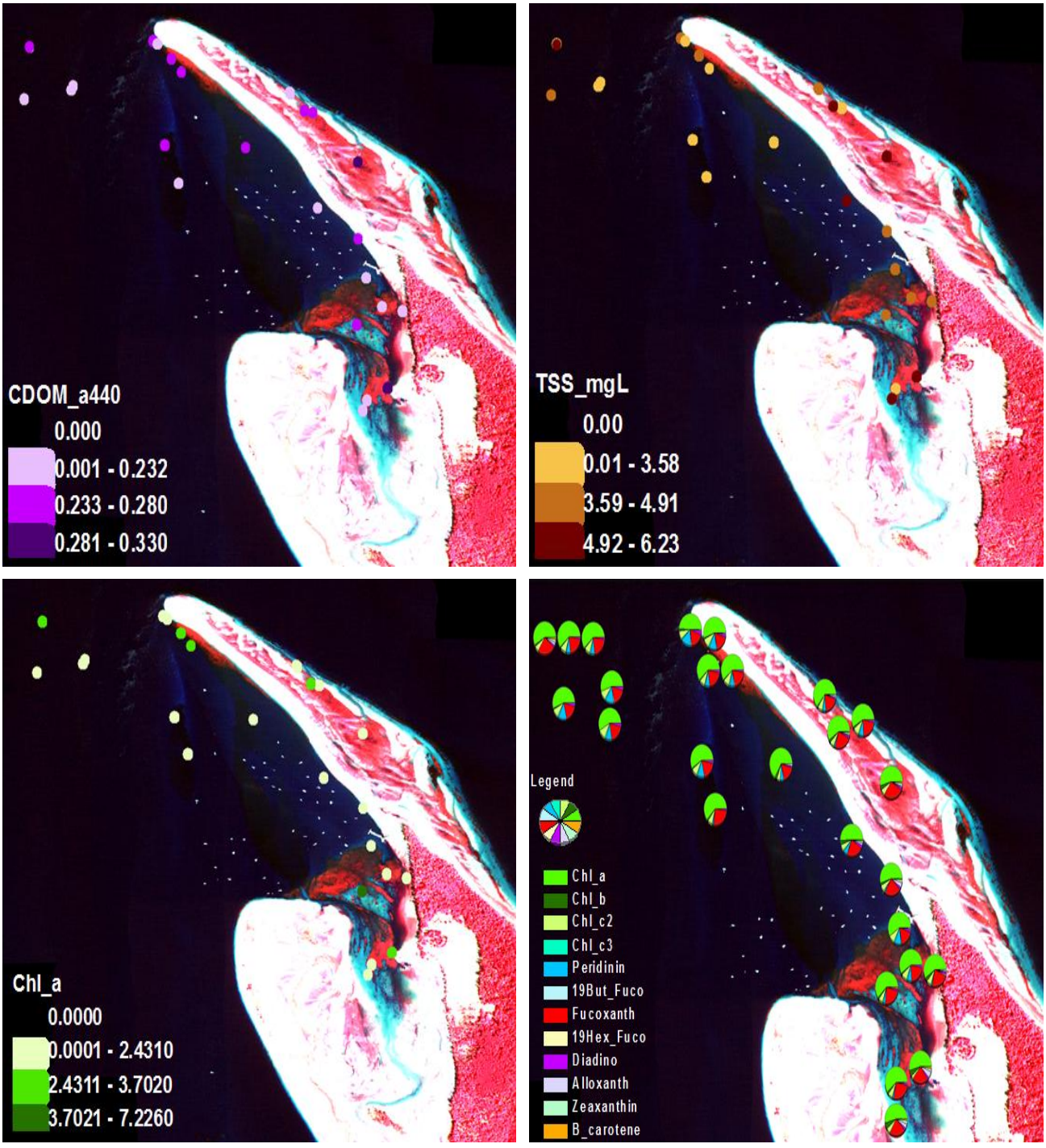

Appendix F

Tafkaa Input: Parameter and AISA / IKONOS Header Files

Tafkaa input parameters: AISA

tafkaa_input_image_name =
F:\Image_Processing\AISA\AISA\AtCorr_tafkaa\input_files\AISA_Lmask_797_BIL_MovAve_MovAve_resize_um_integer.dat

; Image parameters
tafkaa_sample_range = { }
tafkaa_line_range = { }

; Environmental parameters
tafkaa_ground_elevation = 0.000000

; Gaseous (absorption feature) parameters
tafkaa_atmo_model = mid latitude summer
tafkaa_atmo_gasses = {H2O, O3, O2, NO2}
tafkaa_atmo_ozone = 0.284000
tafkaa_atmo_no2_scale = 1.0
tafkaa_use_prev_atmo_trans = 0
tafkaa_atmo_clmwvap = 1.8835
tafka_h2o_enter_inputs = 0

; Aerosol parameters
tafkaa_interp_sensor_altitude = true
tafkaa_geometry = 0
tafkaa_aerosol_model = coastal-a
tafkaa_aerosol_rh = 50%
tafkaa_aerosol_tau550 = 0.156400
tafkaa_wind_speed = 2.000000
tafkaa_aerosol_method = -1
;tafka_aerosol_weights = {0, 0, 0, 0., 0., 0., 0., 0., 0., 1., 1., 1., 1.}

; Mask parameters
tafkaa_use_wee_masks = {none}

; Lookup table location and output parameters
tafkaa_data_directory =
C:\NEW_TAFKAA_Jul13_2010\NRL_Tools\Complete_Tafkaa_Distribution\LSF\
tafkaa_output_type = rrs

tafkaa_output_root_name =
F:\Image_Processing\AISA\AISA\AtCorr_tafkaa\AISA_rafmoveave_tafkaa_elev1.0_coast-a
tafkaa_output_scale_factor = 100000

Header File: AISA

ENVI
description = {Spectral Math Result, Exp = [fix(s1)] [Fri Jul 23 01:28:28 2010]}
samples = 1500
lines = 2694
bands = 171
header offset = 0
file type = ENVI Standard
data type = 2
interleave = bil
sensor type = AISA
byte order = 0
map info = {Geographic Lat/Lon, 1.0000, 1.0000, -123.36197138, 48.66506472,
2.7138336215e-005, 1.7985162940e-005, North America 1983, units=Degrees}
default bands = {108,65,20}
wavelength units = Micrometers
band names = { (band names) }
wavelength = {0.408800, 0.410900, 0.413000, 0.415200, 0.417300, 0.419400, 0.421500,
0.423700, 0.425800, 0.427900, 0.430100, 0.432200, 0.434300, 0.436500, 0.438700, 0.440900,
0.443100, 0.445400, 0.447600, 0.449800, 0.452000, 0.454300, 0.456500, 0.458700, 0.461000,
0.463200, 0.465400, 0.467600, 0.469900, 0.472100, 0.474300, 0.476500, 0.478800, 0.481000,
0.483200, 0.485400, 0.487700, 0.489900, 0.492100, 0.494300, 0.496600, 0.498800, 0.501000,
0.503200, 0.505500, 0.507700, 0.509900, 0.512100, 0.514400, 0.516600, 0.518800, 0.521000,
0.523300, 0.525500, 0.527700, 0.529900, 0.532200, 0.534400, 0.536600, 0.538800, 0.541100,
0.543300, 0.545500, 0.547800, 0.550100, 0.552400, 0.554700, 0.557000, 0.559300, 0.561700,
0.564000, 0.566300, 0.568600, 0.570900, 0.573200, 0.575500, 0.577800, 0.580100, 0.582400,
0.584700, 0.587000, 0.589400, 0.591700, 0.594000, 0.596300, 0.598600, 0.600900, 0.603200,
0.605500, 0.607800, 0.610100, 0.612400, 0.614800, 0.617100, 0.619400, 0.621700, 0.624000,
0.626300, 0.628600, 0.630900, 0.633200, 0.635500, 0.637800, 0.640100, 0.642500, 0.644800,
0.647100, 0.649400, 0.651700, 0.654000, 0.656300, 0.658600, 0.660900, 0.663200, 0.665500,
0.667900, 0.670200, 0.672500, 0.674800, 0.677100, 0.679400, 0.681700, 0.684000, 0.686300,
0.688700, 0.691000, 0.693300, 0.695600, 0.697900, 0.700200, 0.702500, 0.704900, 0.707200,
0.709500, 0.711800, 0.714200, 0.716500, 0.718800, 0.721100, 0.723400, 0.725800, 0.728100,
0.730400, 0.732700, 0.735000, 0.737400, 0.739700, 0.742000, 0.744300, 0.746700, 0.749000,
0.751300, 0.753700, 0.756000, 0.758400, 0.760800, 0.763100, 0.765500, 0.767900, 0.770200,
0.772600, 0.775000, 0.777300, 0.779700, 0.782000, 0.784400, 0.786800, 0.789100, 0.791500,
0.793900, 0.796200}
fwhm = { 0.0100, ... }
acquisition date = DATE(dd-mm-yyyy): 16-08-2008
gps start time = UTC Time : 18:12:39.8113
gps stop time = UTC TIME: 18:13:24.0000

gps starting point = {48.665825, -123.356850}
gps ending point = {48.637703, -123.356911}
rectification = range-based
image_scale_factor = { 100.00 }
image_center_date = {2008, 8, 16}
image_center_time = {18, 00, 00.000}
image_center_long = {123.341631195, 0.0, 0.0}
image_center_long_hem = W
image_center_lat = {48.6408477, 0.0, 0.0}
image_center_lat_hem = N
image_center_zenith_ang = {0, 0, 0.000}
image_center_azimuth_ang = {0, 0, 0.000}
sensor_altitude = 1.0

Tafkaa input parameters - IKONOS

tafkaa_input_image_name =
F:\Image_Processing\IKONOS_IKONOS_RADIANCE_conversion\IKONOS_L&TreeMask_RADIANCE_(Gebreslasie2009)_integer_x100

; Image parameters
tafkaa_sample_range = { }
tafkaa_line_range = { }

; Environmental parameters
tafkaa_ground_elevation = 0.000000

; Gaseous (absorption feature) parameters
tafkaa_atmo_model = mid latitude summer
tafkaa_atmo_gasses = {H2O, O3, O2, NO2}
tafkaa_atmo_ozone = 0.349000
tafkaa_atmo_no2_scale = 2.0
tafkaa_use_prev_atmo_trans = 0
tafkaa_atmo_clmwvap = 1.6012
tafkaa_h2o_enter_inputs = 0

; Aerosol parameters
tafkaa_interp_sensor_altitude = true
tafkaa_geometry = 0
tafkaa_aerosol_model = coastal-a
tafkaa_aerosol_rh = 50%
tafkaa_aerosol_tau550 = 0.135238
tafkaa_wind_speed = 2.000
tafkaa_aerosol_method = -1
;tafka_aerosol_weights = {0, 0, 0, 0., 0., 0., 0., 0., 0., 1., 1., 1., 1.}

; Mask parameters
tafkaa_use_which_masks = { none }

; Lookup table location and output parameters
tafkaa_data_directory =
C:\NEW_TAFKAA_Jul13_2010\NRL_Tools\Complete_Tafkaa_Distribution\LSF\
tafkaa_output_type = rrs
tafkaa_output_root_name =
F:\Image_Processing\IKONOS\AtCorr_tafkaa\Results\IKONOS_tafkaa_Oct20_2010
tafkaa_output_scale_factor = 100000

Header File: IKONOS

ENVI
description = {Spectral Math Result, Exp = [fix(s1*100)] [Wed Oct 20 01:41:04 2010]}
samples = 500
lines = 684
bands = 4
header offset = 0
file type = ENVI Standard
data type = 2
interleave = bil
sensor type = IKONOS
byte order = 0
x start = 442
map info = {Geographic Lat/Lon, 1.0000, 1.0000, -123.36200049, 48.68100000,
1.1111000000e-004, 1.1111000000e-004, North America 1983, units=Degrees}
wavelength units = Micrometers
band names = { (band names) }
wavelength = {0.480000, 0.550000, 0.665000, 0.805000}
fwhm = {0.071300, 0.088600, 0.065800, 0.0954000}
image_scale_factor = { 100.00 }
image_center_date = {2008, 8, 31}
image_center_time = {19, 14, 00.000}
image_center_long = {123.3342785, 0.0, 0.0}
image_center_long_hem = W
image_center_lat = {48.6430559, 0.0, 0.0}
image_center_lat_hem = N
image_center_zenith_ang = {15.19, 0, 0.000}
image_center_azimuth_ang = {127.89, 0, 0.000}
sensor_altitude = 680

Appendix G

Numerical Classification Accuracy Results (%)

AISA - DW Masked - Shallow Eelgrass (< 3 m) Accuracies

	K-Means		MD		ML		SAM		LSU	
	P	**U**	**P**	**U**	**P**	**U**	**P**	**U**	**P**	**U**
1-AISA_Raw	67.3	79.9	54.5	88.3	-	-	-	-	-	-
2-AISA_ELC_GC	71.7	79.8	73.9	86.2	84.8	95.6	33.5	57.7	87.6	84.2
3-AISA_ELC_GC_WC	-	-	7.8	95.7	22.3	80.7	7.9	70.8	9.2	31.1
4-AISA_GC_Tafk	54.6	55.5	49.4	88.7	82.7	95.0	19.2	57.7	50.2	100.0

AISA - DW Masked - Deep Eelgrass (> 3 m) Accuracies

	K-Means		MD		ML		SAM		LSU	
	P	**U**	**P**	**U**	**P**	**U**	**P**	**U**	**P**	**U**
1-AISA_Raw	98.2	42.4	88.5	97.1	-	-	-	-	-	-
2-AISA_ELC_GC	76.1	64.7	71.7	90.0	98.2	92.5	91.2	94.5	100.0	**85.0**
3-AISA_ELC_GC_WC	-	-	-	-	-	-	-	-	-	-
4-AISA_GC_Tafk	0	0	88.5	97.1	98.2	92.5	92.0	26.8	0.0	0.0

IKONOS - Shallow Eelgrass (< 3 m) Accuracies **Producer/User Accuracy**

	K-Means		MD		ML		SAM		LSU	
	P	**U**	**P**	**U**	**P**	**U**	**P**	**U**	**P**	**U**
6-IKONOS_Raw	48.6	59.6	43.7	81.1	-	-	-	-	-	-
8-IKONOS_GC_ELC	66.9	83.4	79.8	79.6	79.2	81.1	72.5	68.8	71.2	84.7
9-IKONOS_GC_Tafk	50.2	65.4	71.9	70.7	77.8	82.7	86.7	65.2	83.9	70.1

IKONOS - Deep Eelgrass (> 3 m) Accuracies Producer/User Accuracy

	K-Means		MD		ML		SAM		LSU	
	P	**U**	P	U	P	U	P	U	P	U
6-IKONOS_Raw	0.0	0.0	90.9	90.9	-	-	-	-	-	-
8-IKONOS_GC_ELC	90.9	37.7	81.8	85.7	100.0	59.0	90.9	29.0	70.8	73.9
9-IKONOS_GC_Tafk	90.9	76.9	90.9	83.3	100.0	59.0	100.0	41.8	82.6	59.4

AISA TOTAL ACCURACY

	K-Means	MD	ML	SAM	LSU
AISA_Raw	59.6	56.7	-	-	-
AISA_ELC_GC	65.4	62.8	83.2	34.9	79.6
AISA_ELC_GC_WC	-	24.5	42.5	7.5	7.5
AISA_GC_Tafkaa	44.1	53.8	81.6	14.4	35.3

	K-Means	MD	ML	SAM	LSU
IKONOS_Raw	41.1	46.6	-	-	-
IKONOS_ELC_GC	57.1	66.9	70.8	53.1	55.0
IKONOS_GC_Tafkaa	40.2	57.0	69.1	53.6	53.0

LAI (AISA) **Producer/User Accuracy**

	K-Means		MD		ML	
	P	U	P	U	P	U
Fine LAI - Low	43.86	55.56	80.61	40.51	81.63	39.41
Fine LAI - Med	51.18	52.43	59.06	44.3	74.27	48.29
Fine LAI - High	63.87	53.8	43.09	87.33	32.24	91.59
TOTAL	53.5		54.3		53.2	

LAI - 2Classes (AISA) **Producer/User Accuracy**

	K-Means		MD		ML	
	P	U	P	U	P	U
Coarse LAI - Low	86.84	48.53	71.88	43.27	90.63	25.24
Coarse LAI - High	71.39	94.58	28.13	56.73	9.38	74.76
TOTAL	75.1		60.3		78.5	

LAI (IKONOS) **Producer/User Accuracy**

	K-Means		MD		ML	
	P	U	P	U	P	U
Fine LAI - Low	62.5	23.08	88.9	30.8	53.9	30.4
Fine LAI - Med	21.21	93.33	7.9	31.3	39.1	51
Fine LAI - High	63.04	51.79	50	55.6	21.6	25
TOTAL	42.6		37.7		37	

LAI - 2Classes (IKONOS) **Producer/User Acc**

	K-Means		MD		ML	
	P	U	P	U	P	U
Coarse LAI - Low	9.52	7.14	85.2	31.1	55.6	36.6
Coarse LAI - High	75.93	81.19	51.4	93.1	74.5	86.4
TOTAL	65.1		58.3		70.5	

EPI - 3 Classes (AISA)	Producer/User Accuracy					
	K-Means		MD		ML	
	P	U	P	U	P	U
diatom epi	46.93	62.77	1.4	27.9	43.2	86.4
Smithora epi	27.08	31.97	63.6	27.9	56	29.2
epi absent	51.08	33.22	36.9	26.2	76.9	79
TOTAL	43.7		25.7		58.3	

EPI - 2 Classes (AISA)	Producer/User Accuracy					
	K-Means		MD		ML	
	P	U	P	U	P	U
epi present	34.31	40.46	51.4	80	80	100
epi absent	51.18	44.63	76.9	46.9	100	73.6
TOTAL	42.9		60.6		**87.2**	

EPI - 3 Classes (IKONO	Producer/User Accuracy					
	K-Means		MD		ML	
	P	U	P	U	P	U
diatom epi	63.27	58.49	70.6	29.3	-	-
Smithora epi	66.67	35.29	36.4	35.6	-	-
epi absent	0	0	15.2	62.5	-	-
TOTAL	44.7		35.1		-	

EPI - 2 Classes (IKONO	Producer/User Accuracy					
	K-Means		MD		ML	
	P	U	P	U	P	U
epi present	75	64.56	34.4	51.2	-	-
epi absent	3.45	5.56	39.4	24.5	-	-
TOTAL	53.6		36.2		-	

University of Victoria

Partial Copyright License

Title of Thesis: Mapping of Eelgrass, *Zostera marina*, at Sidney Spit, Gulf Islands National Park Reserve of Canada, Using High Spatial Resolution Remote Imagery

Author: _____

Jennifer D. O'Neill

January 5, 2011